THE MINISTRY OF SCIENCE AND HIGHER EDUCATION OF THE RUSSIAN FEDERATION

ST. PETERSBURG STATE POLYTECHNICAL UNIVERSITY JOURNAL

Physics and Mathematics

VOLUME 16, No. 2, 2023

Peter the Great St. Petersburg
Polytechnic University
2023

**ST. PETERSBURG STATE POLYTECHNICAL UNIVERSITY JOURNAL.
PHYSICS AND MATHEMATICS**

JOURNAL EDITORIAL COUNCIL

A.I. Borovkov – vice-rector for perspective projects;
V.A. Glukhikh – full member of RAS;
D.A. Indeitsev – corresponding member of RAS;
V.K. Ivanov – Dr. Sci.(phys.-math.), prof.;
A.I. Rudskoy – full member of RAS, deputy head of the editorial council;
R.A. Suris – full member of RAS;
A.E. Zhukov – corresponding member of RAS, deputy head of the editorial council.

JOURNAL EDITORIAL BOARD

V.K. Ivanov – Dr. Sci. (phys.-math.), prof., SPbPU, St. Petersburg, Russia, – editor-in-chief;
A.E. Fotiadi – Dr. Sci. (phys.-math.), prof., SPbPU, St. Petersburg, Russia, – deputy editor-in-chief;
V.M. Kapralova – Candidate of Phys.-Math. Sci., associate prof., SPbPU, St. Petersburg, Russia, – executive secretary;
V.I. Antonov – Dr. Sci. (phys.-math.), prof., SPbPU, St. Petersburg, Russia;
I.B. Bezprozvanny – Dr. Sci. (biology), prof., The University of Texas Southwestern Medical Center, Dallas, TX, USA;
A.V. Blinov – Dr. Sci. (phys.-math.), prof., SPbPU, St. Petersburg, Russia;
A.S. Cherepanov – Dr. Sci. (phys.-math.), prof., SPbPU, St. Petersburg, Russia;
D.V. Donetski – Dr. Sci. (phys.-math.), prof., State University of New York at Stony Brook, NY, USA;
D.A. Firsov – Dr. Sci. (phys.-math.), prof., SPbPU, St. Petersburg, Russia;
A.S. Kheifets – Ph.D., prof., Australian National University, Canberra, Australia;
O.S. Loboda – Candidate of Phys.-Math. Sci., associate prof., SPbPU, St. Petersburg, Russia;
J.B. Malherbe – Dr. Sci. (physics), prof., University of Pretoria, Republic of South Africa;
V.M. Ostryakov – Dr. Sci. (phys.-math.), prof., SPbPU, St. Petersburg, Russia;
V.E. Privalov – Dr. Sci. (phys.-math.), prof., SPbPU, St. Petersburg, Russia;
E.M. Smirnov – Dr. Sci. (phys.-math.), prof., SPbPU, St. Petersburg, Russia;
A.V. Solov'yov – Dr. Sci. (phys.-math.), prof., MBN Research Center, Frankfurt am Main, Germany;
A.K. Tagantsev – Dr. Sci. (phys.-math.), prof., Swiss Federal Institute of Technology, Lausanne, Switzerland;
I.N. Toptygin – Dr. Sci. (phys.-math.), prof., SPbPU, St. Petersburg, Russia.

The journal is included in the List of leading peer-reviewed scientific journals and other editions to publish major findings of theses for the research degrees of Doctor of Sciences and Candidate of Sciences.

The publications are presented in the VINITI RAS Abstract Journal and Ulrich's Periodical Directory International Database.

The journal is published since 2008 as part of the periodical edition 'Nauchno-tekhnicheskie vedomosti SPb-GPU'.

The journal is registered with the Federal Service for Supervision in the Sphere of Telecom, Information Technologies and Mass Communications (ROSKOMNADZOR). Certificate ПИ № ФС77-52144 issued December 11, 2012.

The journal is distributed through the CIS countries catalogue, the «Press of Russia» joint catalogue and the «Press by subscription» Internet catalogue. The subscription index is **71823.**

The journal is in the **Web of Science** (Emerging Sources Citation Index), **Scopus**, the **Russian Science Citation Index** (RSCI) and the **Directory of Open Access Journals** (DOAJ) databases.

© Scientific Electronic Library (http://www.elibrary.ru).

No part of this publication may be reproduced without clear reference to the source.

The views of the authors may not represent the views of the Editorial Board.

Address: 195251 Politekhnicheskaya St. 29, St. Petersburg, Russia.

Phone: (812) 294-22-85.
http://ntv.spbstu.ru/physics

© Peter the Great St. Petersburg Polytechnic University, 2023

МИНИСТЕРСТВО НАУКИ И ВЫСШЕГО ОБРАЗОВАНИЯ РОССИЙСКОЙ ФЕДЕРАЦИИ

НАУЧНО-ТЕХНИЧЕСКИЕ ВЕДОМОСТИ

САНКТ-ПЕТЕРБУРГСКОГО ГОСУДАРСТВЕННОГО ПОЛИТЕХНИЧЕСКОГО УНИВЕРСИТЕТА

Физико-математические науки

ТОМ 16, № 2

2023

Санкт-Петербургский политехнический
университет Петра Великого
2022

НАУЧНО-ТЕХНИЧЕСКИЕ ВЕДОМОСТИ САНКТ-ПЕТЕРБУРГСКОГО ГОСУДАРСТВЕННОГО ПОЛИТЕХНИЧЕСКОГО УНИВЕРСИТЕТА. ФИЗИКО-МАТЕМАТИЧЕСКИЕ НАУКИ

РЕДАКЦИОННЫЙ СОВЕТ ЖУРНАЛА

Боровков А.И., проректор по перспективным проектам;
Глухих В.А., академик РАН;
Жуков А.Е., чл.-кор. РАН – зам. председателя;
Иванов В.К., д-р физ.-мат. наук, профессор;
Индейцев Д.А., чл.-кор. РАН;
Рудской А.И., академик РАН – зам. председателя;
Сурис Р.А., академик РАН.

РЕДАКЦИОННАЯ КОЛЛЕГИЯ ЖУРНАЛА

Иванов В.К., д-р физ.-мат. наук, профессор, СПбПУ, СПб., Россия, – главный редактор;
Фотиади А.Э., д-р физ.-мат. наук, профессор, СПбПУ, СПб., Россия, – зам. главного редактора;
Капралова В.М., канд. физ.-мат. наук, доцент, СПбПУ, СПб., Россия, – ответственный секретарь;
Антонов В.И., д-р физ.-мат. наук, профессор, СПбПУ, СПб., Россия;
Безпрозванный И.Б., д-р биол. наук, профессор, Юго-Западный медицинский центр Техасского университета, Даллас, США;
Блинов А.В., д-р физ.-мат. наук, профессор, СПбПУ, СПб., Россия;
Донецкий Д.В., д-р физ.-мат. наук, профессор, университет штата Нью-Йорк в Стоуни-Брук, США;
Лобода О.С., канд. физ.-мат. наук, доцент, СПбПУ, СПб., Россия;
Малерб Й.Б., Dr.Sc. (Physics), профессор, университет Претории, ЮАР;
Остряков В.М., д-р физ.-мат. наук, профессор, СПбПУ, СПб., Россия;
Привалов В.Е., д-р физ.-мат. наук, профессор, СПбПУ, СПб., Россия;
Смирнов Е.М., д-р физ.-мат. наук, профессор, СПбПУ, СПб., Россия;
Соловьёв А.В., д-р физ.-мат. наук, профессор, Научно-исследовательский центр мезобионаносистем (MBN), Франкфурт-на-Майне, Германия;
Таганцев А.К., д-р физ.-мат. наук, профессор, Швейцарский федеральный институт технологий, Лозанна, Швейцария;
Топтыгин И.Н., д-р физ.-мат. наук, профессор, СПбПУ, СПб., Россия;
Фирсов Д.А., д-р физ.-мат. наук, профессор, СПбПУ, СПб., Россия;
Хейфец А.С., Ph.D. (Physics), профессор, Австралийский национальный университет, Канберра, Австралия;
Черепанов А.С., д-р физ.-мат. наук, профессор, СПбПУ, СПб., Россия.

Журнал с 2002 г. входит в Перечень ведущих рецензируемых научных журналов и изданий, в которых должны быть опубликованы основные результаты диссертаций на соискание ученых степеней доктора и кандидата наук.

Сведения о публикациях представлены в Реферативном журнале ВИНИТИ РАН, в международной справочной системе «Ulrich's Periodical Directory».

С 2008 года выпускается в составе сериального периодического издания «Научно-технические ведомости СПбГПУ».

Журнал зарегистрирован Федеральной службой по надзору в сфере информационных технологий и массовых коммуникаций (Роскомнадзор). Свидетельство о регистрации ПИ № ФС77-52144 от 11 декабря 2012 г.

Распространяется по Каталогу стран СНГ, Объединенному каталогу «Пресса России» и по Интернет-каталогу «Пресса по подписке». Подписной индекс **71823**.

Журнал индексируется в базе данных **Web of Science** (Emerging Sources Citation Index), **Scopus**, а также включен в базы данных **«Российский индекс научного цитирования»** (РИНЦ), размещенную на платформе Научной электронной библиотеки на сайте http://www.elibrary.ru, и **«Directory of Open Access Journals»** (DOAJ)

При перепечатке материалов ссылка на журнал обязательна.

Точка зрения редакции может не совпадать с мнением авторов статей.

Адрес редакции и издательства:
Россия, 195251, Санкт-Петербург, ул. Политехническая, д. 29.
Тел. редакции (812) 294-22-85.
http://ntv.spbstu.ru/physics

© Санкт-Петербургский политехнический университет Петра Великого, 2023

Contents

Condensed matter physics

Pavlov A. V., Stukova E. V., Baryshnikov S. V. *Phase transitions of caesium nitrate embedded in porous alumina films* 9

Simulation of physical processes

Gamzaev Kh. M., Gamzaeva N. Kh. *Numerical identification of the chemical reaction rate constant in the ideal displacement model* 19

Atom physics and physics of clusters and nanostructures

Ipatov A. N., Kupriianov G. A. *The plasmon resonance in the cadmium selenide semiconductor nanocrystals with different doping types* 27

Physical electronics

Pomozov T. V., Muradymov M. Z., Tkach E. A. *The efficiency of a focusing system based on thin diaphragms in the ion source with a corona discharge* 52

Physical materials technology

Nagpure P. A., Kherde N. D., Barde W. S. *Synthesis and PL study of $Sr_3(VO_4)_2$:Eu^{3+} phosphor for W-LED application* 61

Tretyakov A.A., Kapralova V.M., Sapurina I.Yu., Sudar N.T., Shishov M.A. *Electric and thermoelectric properties of a coordination polymer based on phenazine ligands and silver* 68

Bekpulatov I. R., Loboda V. V., Normuradov M. T., Donaev B. D., Turapov I. Kh. *Formation of Mn_4Si_7 films by magnetron sputtering and a wide range of their thermoelectric properties* 78

Shirinov G. M., Donaev S. B., Umirzakov B. Y., Loboda V. V. *Emission, optical and electrical properties of GaInP/GaP nanofilms* 89

Biophysics and medical physics

Alaa N., Walid S., Ola Z., Noha K. *Determination of conditions for obtaining radioactivity of nitrogen-13 isotope for medical use by NX2 dense plasma focus device* 98

Nuclear physics

Lobanov A. A., Berdnikov Ya. A., Mitrankov Iu. M. *Machine learning models to determine unobservable centrality-related parameter values for a wide range of nuclear collisions at the energy of 200 GeV* 111

Lobanov A. A., Berdnikov A. Ya., Mitrankova M. M. *Machine learning models to find unobservable centrality-related parameter values in collisions of different nuclei in the initial energy range from 40 to 200 GeV* 121

Theoretical Physics

Akintsov N. S., Nevecheria A. P., Martynov A. A. *The motion of an uncharged relativistic particle: an analysis of its integrable motion integrals dynamics* 132

Mathematics

Berdnikov A. S., Solovyev K. V. *A numerical algorithm for constructing polynomials deviating least from zero with a given weight* 146

Содержание

Физика конденсированного состояния

Павлов А. В., Стукова Е. В., Барышников С. В. *Фазовые переходы нитрата цезия, внедренного в пористые оксидные пленки алюминия* 9

Математическое моделирование физических процессов

Гамзаев Х. М., Гамзаева Н. Х. *Численная идентификация константы скорости химической реакции в модели идеального вытеснения* 19

Атомная физика, физика кластеров и наноструктур

Ипатов А. Н., Куприянов Г. А. *Плазмонный резонанс в полупроводниковых нанокристаллах селенида кадмия с различным типом легирования* 27

Физическая электроника

Помозов Т. В., Мурадымов М. З., Ткач Е. А. *Эффективность фокусирующей системы на основе тонких диафрагм в ионном источнике с коронным разрядом* 52

Физическое материаловедение

Нагпуре П. А., Херде Н. Д., Барде В. С. *Синтез и фотолюминесцентное исследование люминофора* $Sr_3(VO_4)_2:Eu^{3+}$ *с целью применения в белых светоизлучающих диодах (статья на английском языке)* 61

Третьяков А. А., Капралова В. М., Сапурина И. Ю., Сударь Н. Т., Шишов М. А. *Электрические и термоэлектрические свойства координационного полимера на основе феназиновых лигандов и серебра* 68

Бекпулатов И. Р., Лобода В. В., Нормурадов М. Т., Донаев Б. Д., Турапов И. Х. *Получение пленок* Mn_4Si_7 *методом магнетронного распыления и широкий спектр их термоэлектрических свойств (статья на английском языке)* 78

Ширинов Г. М., Донаев С. Б., Умирзаков Б. Е., Лобода В. В. *Эмиссионные, оптические и электрофизические свойства нанопленок GaInP/GaP (статья на английском языке)*..... 89

Биофизика и медицинская физика

Алаа Н., Валид С., Ола З., Ноха К. *Определение условий получения радиоактивности изотопа азот-13, требуемой для медицинского применения, при использовании устройства плазменной фокусировки NX2 (статья на английском языке)*..... 98

Ядерная физика

Лобанов А. А., Бердников Я. А., Митранков Ю. М. *Модели машинного обучения для определения значений ненаблюдаемых параметров, связанных с центральностью, для широкого спектра ядерных столкновений при энергии 200 ГэВ* 111

Лобанов А. А., Бердников А. Я., Митранкова М. М. *Модели машинного обучения для нахождения значений ненаблюдаемых параметров, описывающих с центральность, при столкновениях различных ядер в энергетическом диапазоне от 40 до 200 ГэВ* 121

Теоретическая физика

Акинцов Н. С., Невечеря А. П., Мартынов А. А. *Анализ динамики интегрируемых интегралов движения незаряженной релятивистской частицы (статья на английском языке)*..... 132

Математика

Бердников А. С., Соловьев К. В. *Численный алгоритм для конструирования многочленов, наименее отклоняющихся от нуля с заданным весом* 146

CONDENSED MATTER PHYSICS

Original article
DOI: https://doi.org/10.18721/JPM.16201

PHASE TRANSITIONS OF CESIUM NITRATE EMBEDDED IN NANOPOROUS ALUMINA FILMS

A.V. Pavlov[1], *E.V. Stukova*[1]✉, *S.V. Baryshnikov*[2]

[1] Amur State University, Blagoveshchensk, Russia

[2] Blagoveshchensk State Pedagogical University, Blagoveshchensk, Russia

✉ lenast@bk.ru

Abstract. In order to make material with improved properties, nanocomposites based on nanoporous Al_2O_3 films (having different pore sizes) filled with ferroelectric, namely, cesium nitrate $CsNO_3$, have been fabricated, and their electrophysical charactistics have been investigated. The film surfaces were tested by electron microscopy. Temperature dependences of the effective permittivity ε′ and of the third harmonic coefficient were measured for the nanocomposites. The phase-transition points were determined by the maximum value of the $d\varepsilon'/dT$ derivative. The reduction in pore was found to lead to a decrease in the Curie temperature (by more than30 K) and a phase transition blur. This phenomenon is associated with the influence of intrinsic size effects.

Keywords: ferroelectric, cesium nitrate, permittivity, phase transition, nanocomposite

Citation: Pavlov A. V., Stukova E. V., Baryshnikov S. V., Phase transitions of cesium nitrate embedded in nanoporous alumina films, St. Petersburg State Polytechnical University Journal. Physics and Mathematics. 16 (2) (2023) 9–18. DOI: https://doi.org/10.18721/JPM.16201

This is an open access article under the CC BY-NC 4.0 license (https://creativecommons.org/licenses/by-nc/4.0/)

Научная статья
УДК 537.226.4
DOI: https://doi.org/10.18721/JPM.16201

ФАЗОВЫЕ ПЕРЕХОДЫ НИТРАТА ЦЕЗИЯ, ВНЕДРЕННОГО В НАНОПОРИСТЫЕ ПЛЕНКИ ОКСИДА АЛЮМИНИЯ

А. В. Павлов[1], *Е. В. Стукова*[1]✉, *С. В. Барышников*[2]

[1] Амурский государственный университет, г. Благовещенск, Россия;

[2] Благовещенский государственный педагогический университет, г. Благовещенск, Россия

✉ lenast@bk.ru

Аннотация. С целью создания материала с улучшенными сегнетоэлектрическими свойствами были изготовлены нанокомпозиты на основе нанопористых пленок Al_2O_3 (с разным размером пор), заполненных сегнетоэлектриком – нитратом цезия $CsNO_3$, и изучены их электрофизические свойства. Поверхность пленок контролировалась методом электронной микроскопии. Были измерены температурные зависимости эффективной диэлектрической проницаемости ε′ и коэффициента третьей гармоники для нанокомпозитов. Температура фазовых переходов определялась по максимальному значению производной $d\varepsilon'/dT$. Обнаружено, что уменьшение размера пор ведет к снижению температуры Кюри (более, чем на 30 K) и размытию фазового перехода, что связано с влиянием собственных размерных эффектов.

© Pavlov A. V., Stukova E. V., Baryshnikov S. V., 2023. Published by Peter the Great St. Petersburg Polytechnic University.

Ключевые слова: сегнетоэлектрик, нитрат цезия, диэлектрическая проницаемость, фазовый переход, нанокомпозит

Ссылка для цитирования: Павлов А. В., Стукова Е. В., Барышников С. В. Фазовые переходы нитрата цезия, внедренного в нанопористые пленки оксида алюминия // Научно-технические ведомости СПбГПУ. Физико-математические науки. 2023. Т. 16. № 2. С. 9–18. DOI: https://doi.org/10.18721/ JPM.16201

Статья открытого доступа, распространяемая по лицензии CC BY-NC 4.0 (https://creativecommons.org/licenses/by-nc/4.0/)

Introduction

Composite materials based on porous nanoscale matrices, such as opal, porous glass, metal oxide films, etc., filled with ferroelectrics, are of interest for practical application in diverse nanoelectronics devices [1–3]. The properties of the particles of materials embedded in the matrices are crucial due to a pronounced size effect, as well as the interaction of such inclusions with the walls of the matrix pores; these particles generally have different properties than bulk ferroelectrics. Analysis of experimental data indicates that the size effects are particularly noticeable near structural ferroelectric phase transitions for nanocomposites synthesized by embedding ferroelectrics into nanoporous matrices.

Polar nanoscale structures obtained by introducing ferroelectric particles into the pores of the Al_2O_3 oxide film were considered in [4–11]. It was reported in [4, 5] that stabilization of the ferroelectric phase was detected in a nanoscale composite of Rochelle salt $KNaC_4H_4O_6{\cdot}4H_2O$ embedded in a porous Al_2O_3 film. The ferroelectric phase persists in the composite up to the decomposition temperature of the Rochelle salt (328 K), which in turn is higher than the Curie temperature (about 30 degrees) for the phase transition of the Rochelle salt (297 K). It was discovered in [6] that an increase in the ferroelectric phase is observed for a Rochelle salt composite in a porous Al_2O_3 matrix, due to a simultaneous decrease in the Curie temperature for the first phase transition (255 K), accompanied by an increase in the Curie temperature of the second phase transition (297 K). Shifts in the phase transition temperature were observed in the porous matrices for KNO_3 [8], TGS [4], $SC(NH_2)_2$ [7], $NaNO_2$ [9], KIO_3 [10], C_6H_{16} NBr [11] and a number of other ferroelectric nanocomposites.

Cesium nitrate $CsNO_3$ has ferroelectric properties with a Curie temperature T_C = 425 K. Spontaneous polarization of cesium nitrate is small ranging to, according to different data, from 2 μC/cm^2 [12] to 3.23 μC/cm^2 [13]. Several studies considered the ferroelectric properties of composite structures based on cesium nitrate [14,15]. In particular, a cesium nitrate nanocomposite, a porous glass, was obtained and studied in [15]. Surface mechanical stresses for cesium nitrate particles embedded in glass pores, arising in the nanocomposite from the matrix led to an increase in the Curie temperature of the composite by 3 K. Moreover, the study discovered that the temperature hysteresis of the phase transition expanded by 9 K in this nanocomposite.

This paper reports on the study of the third harmonic coefficient and permittivity of nanocomposites obtained by embedding cesium nitrate $CsNO_3$ particles into nanoporous Al_2O_3 films with pore sizes of 300 and 240 nm.

Samples and experimental procedure

Cesium nitrate has a trigonal lattice structure with the parameters a = 10.950 E and c = 7.716 E at room temperature [12]. At T = 427 K, cesium nitrate transforms into the cubic phase with the lattice parameter a = 8.980 E. Notably, unlike potassium nitrate, the temperature history does not affect the nature of the structural phase transition in cesium nitrate.

Nanocomposites were obtained using chemically pure cesium nitrate and nanoporous aluminum oxide films (manufactured by TopMembranes Technology, China). The size of the cells was 450 nm, the thickness of the films was 50 μm. Two types of films with different pore diameters were used in the experiment: 300 and 240 nm. Fig. 1 shows electronic micrographs of the surfaces of the studied Al_2O_3 films.

© Павлов А. В., Стукова Е. В., Барышников С. В., 2023. Издатель: Санкт-Петербургский политехнический университет Петра Великого.

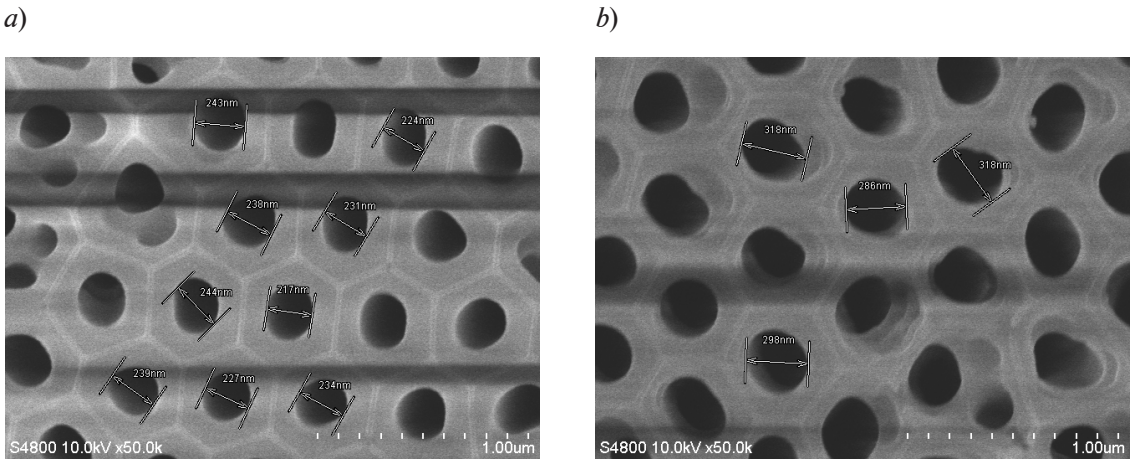

Fig. 1. SEM images of Al_2O_3 films with pore sizes of 330 nm (*a*) and 240 nm (*b*)

Cesium nitrate was introduced into the pores from a saturated solution of $CsNO_3$ at a temperature of 343–353 K. The solubility of cesium nitrate is significantly lower than that of other nitrates, so the pore filling degrees after 5 cycles of embedding and drying were about 15% and 12%, respectively, for films with pore sizes of 300 and 240 nm. Cylindrical samples of polycrystalline cesium nitrate were used as reference (their diameter and thickness were 10.0 and 1.5 mm, respectively); the samples were obtained by pressing at $8 \cdot 10^3$ kg/cm^2.

An E7-25 digital LCR meter was used to measure the effective permittivity. Methods of nonlinear dielectric spectroscopy were used to detect the polar phase in cesium nitrate. A harmonic signal with a frequency of 2 kHz was applied to the sample, and multi-frequency signals were monitored and recorded on a computer. The presence of a polar phase can be determined by the amplitude and temperature course of the latter signals. The electric field strength of the main signal was approximately 10 V/mm for bulk samples and about 10^4 V/mm for films.

The third harmonic coefficient ($\gamma_{3\omega} = U_{3\omega}/U_{\omega}$) was taken for further analysis, which is the most sensitive to the appearance of a ferroelectric state. The technique for measuring nonlinear dielectric properties is described in detail in [15, 16].

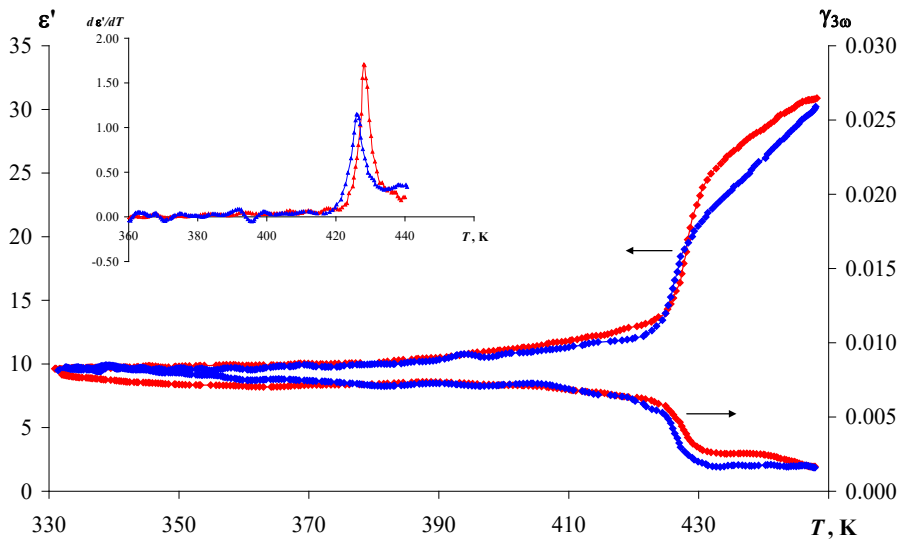

Fig. 2. Temperature dependences of permittivity and third harmonic coefficient for bulk $CsNO_3$ sample under heating and cooling (red and blue symbols, respectively)
The inset shows the temperature dependences for the variation rate of permittivity under the given conditions

Experimental results and discussion

The graphs in Figs. 2 and 3 represent the temperature dependences of permittivity and the third harmonic coefficient for bulk cesium nitrate and a nanocomposite sample based on a porous oxide film with embedded cesium nitrate with a pore size of 300 nm. The temperature of the phase transitions determined from the maximum value of the derivative $d\varepsilon'/dT$ is 428 K under heating and 426 K under cooling. The third harmonic coefficient exhibits anomalies at the same temperatures, evidencing that the $CsNO_3$ sample makes a transition from the ferroelectric to the paraelectric phase.

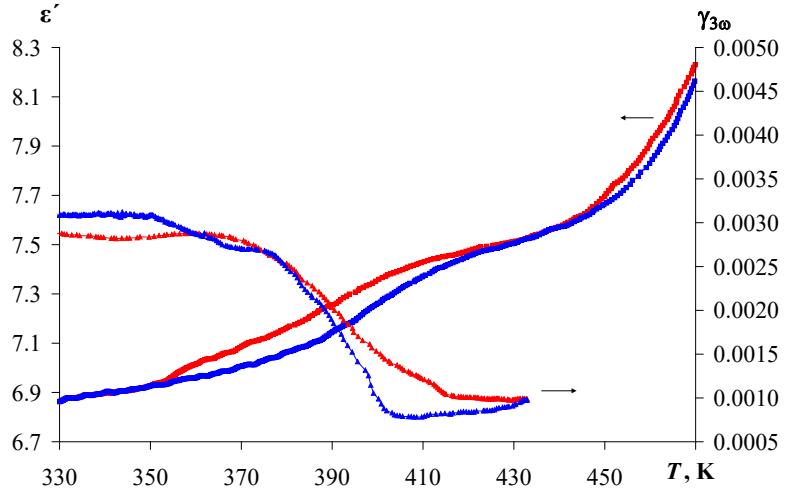

Fig. 3. Temperature dependences of permittivity and the third harmonic coefficient for $CsNO_3/Al_2O_3$ nanocomposite sample with nanoporous film pore size of 300 nm under heating and cooling (red and blue symbols, respectively)

As follows from the graphs in Fig. 3 that the phase transition is significantly smeared for the nanocomposite sample. Despite this, the anomalies on the $\gamma_{3\omega}(T)$ dependence can be used to estimate the temperatures at which spontaneous polarization disappears and appears in cesium nitrate. These temperatures are 416 K under and 405 K under cooling for a film with 300 nm pores. Thus, an increase in the temperature hysteresis of the phase transition from 2 to 11 K is observed.

The third harmonic signal of the $CsNO_3/Al_2O_3$ nanocomposite with a film pore size of 240 nm was at the noise level due to a lower proportion of cesium nitrate. The phase transition was even more smeared, but the transition temperature, determined by the maximum of the derivative $d\varepsilon'/dT$, shifted towards the low-temperature region (Fig. 4). As can be seen in the graphs, the phase transition temperature for a film with a pore size of 240 nm is about (393±1) K under heating and about (387±1) K under cooling.

The smearing and shift in the phase transition temperature towards lower temperatures was previously detected in $Ba_xSr_{1-x}TiO_3$ thin films, which the authors explained by the presence of non-switchable dielectric "dead layers" in the films [17, 18] caused by pinning of the domain walls, i.e., shielding of the internal field with a depleted layer [19–23]. A decrease in the Curie temperature and a smearing in the phase transition were also observed for DTGS in Al_2O_3 films with pores of 300 and 100 nm [24], where this was attributed to intrinsic size effects. A similar situation likely happens for the $CsNO_3/Al_2O_3$ composite (300 and 240 nm).

The decrease in the phase transition temperature in $CsNO_3$ embedded in Al_2O_3 film corresponds to the predictions made by the theoretical Landau and Ising models [25–27]. These models adopt the concept of correlation volume determining the number of ordered dipoles necessary for inducing ferroelectricity. Strong interactions along the polar axis and less strong ones perpendicular to it lead to anisotropy of the correlation volume.

A decrease in the phase transition temperature with a decrease in particle sizes was predicted in earlier studies [25–27]. These assumptions were derived from the theoretical Landau and Ising models based on the concept of correlation volume, determining the number of ordered dipoles, which produces a ferroelectric state.

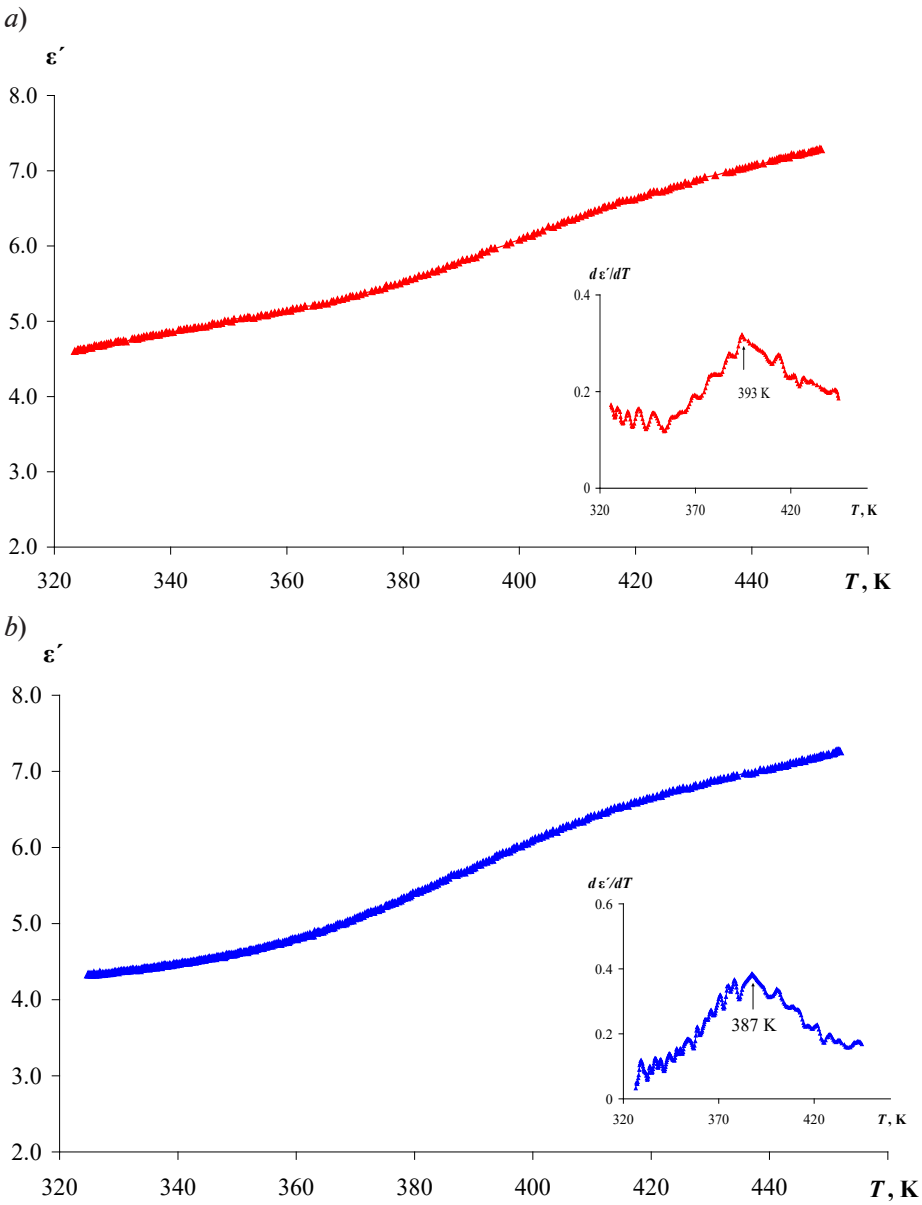

Fig. 4. Temperature dependences of permittivity for $CsNO_3/Al_2O_3$sample with the film pore size of 240 nm under heating (*a*) and under cooling (*b*). The corresponding temperature dependences $d\varepsilon'/dT$ are shown in the insets

The experimental data we obtained for $CsNO_3$ embedded in Al_2O_3 film confirm that these predictions are correct. A possible interpretation of our results is that anisotropy appears in the correlation volume because strong interactions are directed along the polar axis, and less strong ones are perpendicular to it.

As particle sizes decrease below the critical value, the balance between the long-range and the short-range forces is disrupted and the ferroelectric state is destabilized; a paraelectric phase is consequently formed. These models suggest that the phase transition temperature shifts deep into the ferroelectric phase as the sizes of isolated spherical or cylindrical nanoparticles decrease. The results obtained for isolated small particles of barium titanate can serve as a confirmation for this explanation (see [28] and references therein).

Interactions between polar particles and pore walls, as well as dipole-dipole interactions between particles in adjacent pores can influence the temperature of the ferroelectric phase transition, along with its intrinsic size effect [28–33]. The directions of the dipole moments of particles located in adjacent pores of the matrix can contribute to both an increase and a decrease in the Curie temperature.

The influence of mechanical stresses on the ferroelectric properties of nanoparticles was considered in [29–31]. It was established that the interaction of the embedded substance with the matrix walls, geneally leads to an increase in the temperature of the ferroelectric phase transition. For this reason, it can be assumed that the role of mechanical stresses in the $CsNO_3/Al_2O_3$ nanocomposite is minimal as the pores are only partially filled (by no more than 12–15%). On the other hand, the low level of spontaneous polarization and the considerable distances between the pores weaken the influence of dipole-dipole interaction. Thus, we can exclude the effect of mechanical stresses and the role of dipole-dipole interaction on the variation in the phase transition temperature of the $CsNO_3/Al_2O_3$ composite. However, if we assume that the particles of the embedded substance exist in the pores as a system of small crystallites whose dimensions are significantly smaller than the diameter of the pores, then we can hypothesize that the decrease in the phase transition temperature in $CsNO_3/Al_2O_3$ is due to the intrinsic size effect.

Ferroelectric nanoparticles embedded into matrix materials are characterized by a significant smearing of the phase transition maximum, as discussed in a number of theoretical studies. This phenomenon can be attributed to a wide range of cause related to non-uniform distribution of elastic strains and internal electric fields. Similar processes are typical for disordered ferroelectric structures and solid solutions. A gradual transition from the disordered to the ordered phase is observed in a wide temperature range called the Curie region. This region is characterized by a gradual change in such ferroelectric properties as spontaneous polarization, piezoelectric moduli, anomalous specific heat capacity, and others.

Conclusion

The results of dielectric studies of cesium nitrate particles embedded in nanoporous aluminum oxide films suggest that a decrease in the pore size leads to a decrease in the Curie temperature and a smearing of the phase transition, which is most likely due to intrinsic size effects.

REFERENCES

1. **Stadlober B., Zirkl M., Irimia-Vladu M.,** Route towards sustainable smart sensors: ferroelectric polyvinylidene fluoride-based materials and their integration in flexible electronics, Chem. Soc. Rev. 48(6) (2019) 1787–1825.

2. **Jin R. B., Cai N., Huang Y., et al.,** Theoretical investigation of a spectrally pure-state generation from isomorphs of KDP crystal at near-infrared and telecom wavelengths, Phys. Rev. Appl. 11 (3) (2019) 034067.

3. **Kasap S., Capper P.** (Eds.), Springer handbook of electronic and photonic materials, Springler-Verlag US, New York, 2007.

4. **Rogazinskaya O. V., Milovidova S. D., Sidorkin A. S., et al.,** Properties of nanoporous aluminum oxide with with triglycine sulfate and Rochelle salt inclusions, Phys. Solid State. 51 (7) (2009) 1518–1520.

5. **Yadlovker D., Berger S.,** Uniform orientation and size of ferroelectric domains, Phys. Rev. B. 71 (18) (2005) 184112.

6. **Baryshnikov S. V., Stukova E. V., Milinskiy A. Yu., et al.,** Ferroelectricity in Rochelle salt nanoparticles confined to porous alumina, Ferroelectrics. 396 (1) (2010) 3–9.

7. **Milinskii A. Y., Baryshnikov S. V., Antonov A. A.,** Phase transitions of $SC(NH_2)_2$ferroelectricsin Al_2O_3-based nanoporous matrices, Phys. Solid State. 59 (9) (2017) 1783–1788.

8. **Rogazinskaya O. V., Sidorkin A. S., Popravko N. G., et al.,** Dielectric and repolarization properties of nanocomposites based on porous matrix with sodium nitrite, Ferroelectrics. 469 (1) (2014) 138–143.

9. **Alekseeva O. A., Naberezhnov A. A., Stukova E. V., et al.,** Temperature range broadening of the ferroelectric phase in KNO_3 nanoparticles embedded in the pores of the nanoporous Al_2O_3 matrix, Ferroelectrics. 574 (1) (2921) 8–15.

10. **Milinskii A. Y., Baryshnikov S. V.,** Phase transitions of KIO_3ferroelectrics in Al_2O_3-based nanoporous matrices,Phys. Solid State. 60 (3) (2018) 549–552.

11. **Milinskiy A. Yu., Baryshnikov S. V., Egorova I. V., et al.,** Dielectric properties of an organic ferroelectrics of bromide diisopropylammonium embedded into the pores of nanosized Al_2O_3 films, J. Phys. Condens. 31 (48) (2019) 485704.

12. **Lucas B. W.,** The structure (neutron) of phase II cesium nitrate at 298 K, $CsNO_3$, Acta Crystallogr. C. Struct. Chem. C39(12) (1983)1591–1594.

13. **Nautiyal A., Sekhar K. C., Pathak N. P., Nath R.,** Study of ferroelectric properties of spray pyrolysis deposited cesium nitrate films, Thin Solid Films. 518 (24, Suppl,) (2010) e143–e145.

14. **Rao M. V. M., Reddy S. N., Chary A. S.,** Enhancement of DC ionic conductivity in dispersed solid electrolyte system $CsNO_3$: γ-Al_2O_3, Phys. B Condens. 389(2) (2007) 292–295.

15. **Milinskiy A. Y., Baryshnikov S. V., Chernechkin I. A.,** Dielectric and thermal properties of cesium nitrate–porous glass nanocomposite, Russ. Phys. J. 65 (9) (2023) 1431–1435.

16. **Ikeda S., Kominami H., Koyama K., Wada Y. J.,** Nonlinear dielectric constant and ferroelectric-to-paraelectric phase transition in copolymers of vinylidenefluoride and trifluoroethylene, J. Appl. Phys. 62 (8) (1987) 3339–3342.

17. **Vendik O. G., Zubko S. P.,** Ferroelectric phase transition and maximum dielectric permittivity of displacement type ferroelectrics ($Ba_xSr_{1-x}TiO_3$), J. Appl. Phys. 88 (9) (2000) 5343–5350.

18. **Lookman A., Bowman R. M., Gregg J. M., et al.,** Thickness independence of true phase transition temperatures in barium strontium titanate films. J. Appl. Phys. 96 (1) (2004) 555–562.

19. **Larsen P. K., Dormans G. J. M., Taylor D. J., van Yeldhoven P. J.,** Ferroelectric properties and fatigue of $PbZr_{0.51}Ti_{0.49}O_3$ thin films of varying thickness: Blocking layer model, J. Appl. Phys. 76 (4) (1994) 2405–2413.

20. **Miller S. L., Nasbv R. D., Schwank J. R., et al.,** Device modeling of ferroelectric capacitors,J. Appl. Phys. 68 (12) (1990) 6463–6471.

21. **Tagantsev A. K., Landivar M., Colla E., Setter N.,** Identification of passive layer in ferroelectric thin films from their switching parameters, J. Appl. Phys. 78 (4) (1995) 2623–2630.

22. **Lebedev N. I., Sigov A. S.,** Surface inhomogeneties and coercive field of thin ferroelectric film, Integr. Ferroelectr. 4 (1) (1994) 21–24.

23. **Tagantsev A. K.,** Size effects in polarization switching in ferroelectric thin films, Integr. Ferroelectr. 16 (1–4) (1997) 237–244.

24. **Stukova E., Baryshnikov S., Baryshnikova T., Solnyshkin A.,** Linear and non-linear dielectric properties of DTGS in porous Al_2O_3 films, Ferroelectrics. 543 (1) (2019) 184–190.

25. **Zhong W. L., Wang Y. G., Zhang P. L., Qu B. D.,** Phenomenological study of the size effect on phase transitions in ferroelectric particles, Phys. Rev. B. 50 (2) (1994) 698–703.

26. **Wang Y. G., Zhong W. L., Zhang P. L.,** Size driven phase transition in ferroelectric particles, Solid State Commun. 90 (5) (1994) 329–332.

27. **Wang C. L., Xin Y., Wang X. S., Zhong W. L.,** Size effects of ferroelectric particles described by the transverse Ising model,Phys. Rev. B. 62 (17) (2000) 11423–11427.

28. **Sedykh P., Michel D.,** Ferroelectric phase transition in barium titanate nanoparticles, Phys. Rev. B. 79 (13) (2009) 134119.

29. **Shchukin V. A., Bimberg D.,** Spontaneous ordering of nanostructures on crystal surfaces, Rev. Modern Phys. 71 (4) (1999) 1125–1171.

30. **Morozovska A. N., Glinchuk M. D., Eliseev E. A.,** Phase transitions induced by confinement of ferroic nanoparticles, Phys. Rev. B. 76 (1) (2007) 014102.

31. **Morozovska A. N., Eliseev E. A., Glinchuk M. D.,** Size effects and depolarization field influence on the phase diagrams of cylindrical ferroelectric nanoparticles, Phys. B. Cond. 387 (1–2) (2007) 358–366.

32. **Charnaya E. V., Pirozerskii A. L., Tien C., Lee M. K.,** Ferroelectricity in an array of electrically coupled confined small particles, Ferroelectrics. 350 (1) (2007) 75–80.

СПИСОК ЛИТЕРАТУРЫ

1. **Stadlober B., Zirkl M., Irimia-Vladu M.** Route towards sustainable smart sensors: ferroelectric polyvinylidene fluoride-based materials and their integration in flexible electronics // Chemical Society Reviews. 2019. Vol. 48. No. 6.Pp. 1787–1825.

2. **Jin R. B., Cai N., Huang Y., Hao X.-Y., Wang S., Li F., Song H.-Zh., Zhou Q., Shimizu R.** Theoretical investigation of a spectrally pure-state generation from isomorphs of KDP crystal at near-infrared and telecom wavelengths // Physical Review Applied. 2019. Vol. 11. No. 3. P. 034067.

3. **Kasap S., Capper P.** (Eds.) Springer handbook of electronic and photonic materials. New York: Springler-Verlag, US, 2007. 1407 p.

4. **Рогазинская О. В., Миловидова С. Д., Сидоркин А. С., Чернышев В. В., Бабичева Н. Г.** Свойства нанопористого оксида алюминия с включениями триглицинсульфата и сегнетовой соли // Физика твердого тела. 2009. Т. 7 № .51. С. 1432–1430.

5. **Yadlovker D., Berger S.** Uniform orientation and size of ferroelectric domains // Physical Review B. 2005. Vol. 71. No. 18. P. 184112.

6. **Baryshnikov S. V., Stukova E. V., Milinskiy A. Yu., Charnaya E. V., Tien C.** Ferroelectricity in Rochelle salt nanoparticles confined to porous alumina // Ferroelectrics. 2010. Vol. 396. No. 1. Pp. 3–9.

7. **Милинский А. Ю., Барышников С. В., Антонов А. А.** Исследование фазовых переходов сегнетоэлектрика $SC(NH_2)_2$ в нанопористых матрицах на основе Al_2O_3 // Физика твердого тела. 2017. Т. 59. № 9. С. 1759–1764.

8. **Rogazinskaya O. V., Sidorkin A. S., Popravko N. G., Milovidova S. D., Naberezhnov A. A., Grokhotova E. V.** Dielectric and repolarization properties of nanocomposites based on porous matrix with sodium nitrite // Ferroelectrics. 2014. Vol. 469. No. 1. Pp. 138–143.

9. **Alekseeva O. A., Naberezhnov A. A., Stukova E. V., Baryshnikov S. V., Franz A.** Temperature range broadening of the ferroelectric phase in KNO_3nanoparticles embedded in the pores of the nanoporous Al_2O_3 matrix // Ferroelectrics. 2021. Vol. 574. No. 1. Pp. 8–15.

10. Милинский **А.** Ю., Барышников С. В. Исследование фазовых переходов сегнетоэлектрика KIO_3 в нанопористых матрицах на основе пленок Al_2O_3 // Физика твердого тела. 2018. Т. 60. № 3. С. 543–546.

11. **Milinskiy A. Yu., Baryshnikov S. V., Egorova I. V., Charnaya E. V., Nguyen H. T.** Dielectric properties of an organic ferroelectrics of bromide diisopropylammonium embedded into the pores of nanosized Al_2O_3 films // Journal of Physics: Condensed Matter. 2019. Vol. 31. No. 48. P. 485704.

12. **Lucas B. W.** The structure (neutron) of phase II cesium nitrate at 298 K, $CsNO_3$ // Acta Crystallographica. Section C: Structural Chemistry. 1983. Vol. C39. Part 12. Pp. 1591–1594.

13. **Nautiyal A., Sekhar K. C., Pathak N. P., Nath R.** Study of ferroelectric properties of spray pyrolysis deposited cesium nitrate films // Thin Solid Films. 2010. Vol. 518. No. 24, Supplement. Pp. e143–e145.

14. **Rao M. V. M., Reddy S. N., Chary A. S.** Enhancement of DC ionic conductivity in dispersed solid electrolyte system $CsNO_3$:γ-Al_2O_3 // Physica B: Condensed Matter. 2007. Vol. 389.No. 2. Pp. 292–295.

15. Милинский **А.** Ю., Барышников С. В., Чернечкин **И.** А. Диэлектрические и тепловые свойства нанокомпозита нитрат цезия – пористое стекло // Известия высших учебных заведений. Физика. 2022. Т. 65. № 9. С. 15–19.

16. **Ikeda S., Kominami H., Koyama K., Wada Y. J.** Nonlinear dielectric constant and ferroelectric-to-paraelectric phase transition in copolymers of vinylidenefluoride and trifluoroethylene // Journal of Applied Physics. 1987. Vol. 62. No. 8. Pp. 3339–3342.

17. **Vendik** O. **G., Zubko S. P.** Ferroelectric phase transition and maximum dielectric permittivity of displacement type ferroelectrics ($Ba_xSr_{1-x}TiO_3$) // Journal of Applied Physics. 2000. Vol. 88. No. 9. Pp. 5343–5350.

18. **Lookman A., Bowman R. M., Gregg J. M., Kut J., Rios S., Dawber M., Ruediger A., Scott J. F.** Thickness independence of true phase transition temperatures in barium strontium titanate films // Journal of Applied Physics. 2004. Vol. 96. No. 1. Pp. 555–562.

19. **Larsen P. K., Dormans G. J. M., Taylor D. J., van Yeldhoven P. J.** Ferroelectric properties and fatigue of $PbZr_{0.51}Ti_{0.49}O_3$ thin films of varying thickness: Blocking layer model // Journal of Applied Physics. 1994. Vol. 76. No. 4. Pp. 2405–2413.

20. **Miller S. L., Nasbv R. D., Schwank J. R., Rodgers M. S., Dressendorfer P. V.** Device modeling of ferroelectric capacitors // Journal of Applied Physics. 1990. Vol. 68. No. 12. Pp. 6463–6471.

21. **Tagantsev A. K., Landivar M., Colla E., Setter N.** Identification of passive layer in ferroelectric thin films from their switching parameters // Journal of Applied Physics. 1995. Vol. 78. No. 4. Pp. 2623–2630.

22. **Lebedev N. I., Sigov A. S.** Surface inhomogeneties and coercive field of thin ferroelectric film // Integrated Ferroelectrics. 1994. Vol. 4. No. 1. Pp. 21–24.

23. **Tagantsev A. K.** Size effects in polarization switching in ferroelectric thin films // Integrated Ferroelectrics. 1997. Vol. 16. No 1–4. Pp. 237–244.

24. **Stukova E., Baryshnikov S., Baryshnikova T., Solnyshkin A.** Linear and non-linear dielectric properties of DTGS in porous Al_2O_3 films // Ferroelectrics. 2019. Vol. 543. No. 1. Pp. 184–190.

25. **Zhong W. L., Wang Y. G., Zhang P. L., Qu B. D.** Phenomenological study of the size effect on phase transitions in ferroelectric particles // Physical Review B. 1994. Vol. 50. No. 2. Pp. 698–703.

26. **Wang Y. G., Zhong W. L., Zhang P. L.** Size driven phase transition in ferroelectric particles // Solid State Communications. 1994. Vol. 90. No 5. Pp. 329–332.

27. **Wang C. L., Xin Y., Wang X. S., Zhong W. L.** Size effects of ferroelectric particles described by the transverse Ising model // Physical Review B. 2000. Vol. 62. No. 17. Pp. 11423–11427.

28. **Sedykh P., Michel D.** Ferroelectric phase transition in barium titanate nanoparticles // Physical Review B. 2009. Vol. 79. No. 13. P. 134119.

29. **Shchukin V. A., Bimberg D.** Spontaneous ordering of nanostructures on crystal surfaces // Review of Modern Physics. 1999. Vol. 71. No. 4. Pp. 1125–1171.

30. **Morozovska A. N., Glinchuk M. D., Eliseev E. A.** Phase transitions induced by confinement of ferroic nanoparticles // Physical. Review. B. 2007. Vol. 76. No. 1. P. 014102.

31. **Morozovska A. N., Eliseev E. A., Glinchuk M. D.** Size effects and depolarization field influence on the phase diagrams of cylindrical ferroelectric nanoparticles // Physica B: Condensed Matter. 2007. Vol. 387. No. 1–2. Pp. 358–366.

32. **Charnaya E. V., Pirozerskii A. L., Tien C., Lee M. K.** Ferroelectricity in an array of electrically coupled confined small particles // Ferroelectrics. 2007. Vol. 350. No. 1. Pp. 75–80.

THE AUTHORS

PAVLOV Aleksei V.
Amur State University
21 Ignatievskoe Ave., Blagoveshchensk, 675027, Russia
katal75@yandex.ru
ORCID: 0000-0002-7287-2006

STUKOVA Elena V.
Amur State University
21 Ignatievskoe Ave., Blagoveshchensk, 675027, Russia
lenast@bk.ru
ORCID: 0000-0002-7981-7456

BARYSHNIKOV Sergey V.
Blagoveschensk State Pedagogical University
104 Lenin St., Blagoveshchensk, 675000, Russia
svbar2003@list.ru
ORCID: 0000-0002-3362-8975

СВЕДЕНИЯ ОБ АВТОРАХ

ПАВЛОВ Алексей Владимирович – *аспирант кафедры физики Амурского государственного университета.*
675027, Россия, Амурская область, г. Благовещенск, Игнатьевское шоссе, 21
katal75@yandex.ru
ORCID:0000-0002-7287-2006

СТУКОВА Елена Владимировна – *доктор физико-математических наук, профессор кафедры физики Амурского государственного университета.*
675027, Россия, Амурская область, г. Благовещенск, Игнатьевское шоссе, 21
lenast@bk.ru
ORCID:0000-0002-7981-7456

БАРЫШНИКОВ Сергей Васильевич – *доктор физико-математических наук, профессор кафедры физического и математического образования Благовещенского государственного педагогического университета.*
675000, Россия, Амурская область, г. Благовещенск, ул. Ленина, 104
svbar2003@list.ru
ORCID:0000-0002-3362-8975

Received 09.03.2023. Approved after reviewing 12.04.2023. Accepted 12.04.2023.
Статья поступила в редакцию 09.03.2023. Одобрена после рецензирования 12.04.2023. Принята 12.04.2023.

© Peter the Great St. Petersburg Polytechnic University, 2023

SIMULATION OF PHYSICAL PROCESSES

Original article
DOI: https://doi.org/10.18721/JPM.16202

NUMERICAL IDENTIFICATION OF THE CHEMICAL REACTION RATE CONSTANT IN THE IDEAL DISPLACEMENT MODEL

Kh. M. Gamzaev✉, *N. Kh. Gamzaeva*

Azerbaijan State Oil and Industry University, Baku, Azerbaijan

✉ xan.h@rambler.ru

Abstract. A chemical-technological process of a second-order reaction in a chemical reactor of an ideal displacement, described by a nonlinear partial differential equation of the first order has been considered. Within the framework of the proposed model, the inverse problem of determining the rate constant of a chemical reaction was defined. In this case, an additional condition was set regarding the reagent concentration at the outlet from the reactor. To solve the inverse problem, its discrete analogue was constructed and a special representation was proposed for solving the resulting system of linear algebraic equations. As a result, an explicit formula for determining the approximate value of the rate constant of a chemical reaction was obtained. The possibilities of the proposed numerical method were illustrated by numerical calculations on model problems.

Keywords: chemical reactor of ideal displacement, chemical reaction rate constant, identification problem, coefficient inverse problem

Citation: Gamzaev Kh. M., Gamzaeva N. Kh., Numerical identification of the chemical reaction rate constant in the ideal displacement model, St. Petersburg State Polytechnical University Journal. Physics and Mathematics. 16 (2) (2023) 19–26. DOI: https://doi.org/10.18721/JPM.16202

This is an open access article under the CC BY-NC 4.0 license (https://creativecommons.org/licenses/by-nc/4.0/)

Научная статья
УДК 681.5:519.63
DOI: https://doi.org/10.18721/JPM.16202

ЧИСЛЕННАЯ ИДЕНТИФИКАЦИЯ КОНСТАНТЫ СКОРОСТИ ХИМИЧЕСКОЙ РЕАКЦИИ В МОДЕЛИ ИДЕАЛЬНОГО ВЫТЕСНЕНИЯ

Х. М. Гамзаев✉, *Н. Х. Гамзаева*

Азербайджанский государственный университет нефти и промышленности, г. Баку, Азербайджан

✉ xan.h@rambler.ru

Аннотация. Рассматривается химико-технологический процесс реакции второго порядка в химическом реакторе идеального вытеснения, описываемый нелинейным дифференциальным уравнением в частных производных первого порядка. В рамках предложенной модели поставлена обратная задача по определению константы скорости химической реакции. При этом задается дополнительное условие относительно концентрации реагента на выходе из реактора. Для решения поставленной обратной задачи строится ее дискретный аналог и предлагается специальное представление для решения полученной системы линейных алгебраических уравнений. В результате получена явная формула для определения приближенного значения константы скорости химической реакции. Возможности предложенного численного метода иллюстрируются численными расчетами на модельных задачах.

© Gamzaev Kh. M., Gamzaeva N. Kh., 2023. Published by Peter the Great St. Petersburg Polytechnic University.

Ключевые слова: химический реактор идеального вытеснения, константа скорости химической реакции, задача идентификации, коэффициентная обратная задача

Ссылка для цитирования: Гамзаев Х. М., Гамзаева Н. Х. Численная идентификация константы скорости химической реакции в модели идеального вытеснения // Научно-технические ведомости СПбГПУ. Физико-математические науки. 2023. Т. 16. № 2. С. 19–26. DOI: https://doi.org/10.18721/ JPM.16202

Статья открытого доступа, распространяемая по лицензии CC BY-NC 4.0 (https://creativecommons.org/licenses/by-nc/4.0/)

Introduction

The main element in any chemical engineering system is the chemical reactor where chemical processes occur to obtain a specific reagent with the given properties. Diverse types of chemical reactors with widely different designs are used in chemical engineering [1–3]. However, the kinetics of the process occurring in the reactor is mainly determined by the flow regime of the reaction medium and the thermal conditions in the reactor. For this reason, chemical reactors are classified by based on critical flow regimes: perfect displacement and perfect mixing in isothermal, adiabatic or polythermal conditions.

Mathematical modeling methods are widely used to study the operation of chemical reactors [4–6]. An important step in modeling the processes running in chemical reactors is to provide the models with the necessary quantitative information, i.e., identifying the parameters of mathematical models.

In general, the parameters of a mathematical model quantitatively characterize certain properties of a chemical engineering process. Notably, the parameters of all mathematical models of chemical engineering processes are mainly determined based on experimental studies, which can be complicated for a number of reasons. Statements and techniques for solving inverse problems [7–9] are therefore introduced to identify the parameters of mathematical models in chemical engineering processes.

This paper proposes a numerical method based on solving the inverse problem of perfect displacement in a chemical reactor to identify the rate constant of a second-order chemical reaction.

Problem statement and solution method

Consider a chemical reactor with perfect displacement, which is a tubular apparatus with a large ratio of the length of the tube to its diameter. Reagents are continuously supplied to the reactor, and the resulting flow moves in full displacement mode in a single direction along the length of the reactor. It is assumed that the reaction medium is not mixed along the reactor, as well as along its cross-section, and the parameter values of the reaction medium along the cross-section are the same. The reactor operates in isothermal mode, and a second-order reaction occurs when a certain distribution of reagent concentrations participating in the reaction is established along the length of the reactor.

A mathematical model for the transformation of one of the reagents as a result of a second-order chemical reaction occurring in a given chemical reactor with perfect displacement can be represented as a first-order nonlinear partial differential equation:

$$\frac{\partial C(x,t)}{\partial t} + \nu(t)\frac{\partial C(x,t)}{\partial x} + kC^2(x,t) = 0,\ 0 < x < l,\ 0 < t \le T, \tag{1}$$

where $C(x,t)$ is the concentration of the given reagent; $v(t)$ is the flow rate in the reactor; k is the rate constant of the chemical reaction; l is the length of the chemical reactor; x is the coordinate along which the reaction flow moves; t is the time.

Suppose that the initial and boundary conditions are given for Eq. (1)

© Гамзаев Х. М., Гамзаева Н. Х., 2023. Издатель: Санкт-Петербургский политехнический университет Петра Великого.

$$C(x,0)=\varphi(x), 0\le x\le l, \tag{2}$$

$$C(0,t)=p(t),\ 0\le t\le T. \tag{3}$$

Evidently, if we set the functions $v(t)$, $\varphi(t)$, $p(t)$ and the value of the constant k, then by solving problem (1)–(3) we can find the function $C(x,t)$, i.e., the distribution of the reagent concentration along the length of the reactor.

Now let us assume the rate constant k is also unknown along with the function $C(x,t)$. Instead, an additional condition is set for the concentration of the reagent at the outlet of the reactor:

$$C(l,t)=r(t),\ 0\le t\le T. \tag{4}$$

The problem consists in finding the function $C(x,t)$ and the parameter k satisfying Eq. (1) and conditions (2)–(4).

The formulated problem (1)–(4) belongs to the class of coefficient inverse problems of mathematical physics [9–11]. Notably, the existence of a solution and unique solvability of coefficient inverse problems for partial differential equations have been studied in [12, 13].

Assuming the existence of a solution and the unambiguous solvability of the coefficient inverse problem (1)–(4), we construct its discrete analogue by the method of difference approximation. For this purpose, we introduce a uniform space-time difference grid in a rectangular region $\{0 \le x \le l,\ 0 \le t \le T\}$

$$\overline{\omega}=\left\{(x_i,t_j): x_i=i\Delta x,\ t_j=j\Delta t,\ i=0,1,2,...,n, j=0,1,2,...,m\right\},$$

where $\Delta x = l/n$ is the step of the difference grid with respect to the variable x, $\Delta t = T/m$ is the step of the difference grid with respect to time t.

A linear difference problem as a discrete analogue of problem (1)–(4) is obtained using explicit-implicit time approximations. To do this, the convective term in Eq. (1) is approximated implicitly, and the nonlinear term $kC^2(x,t)$ describing the course of the chemical reaction is approximated explicitly over time. As a result, we obtain the following system:

$$\frac{C_i^j-C_i^{j-1}}{\Delta t}+v^j\frac{C_i^j-C_{i-1}^j}{\Delta x}+k(C_i^{j-1})^2=0,\quad i=1,2,...,n-1, \tag{5}$$

$$C_0^j=p^j, \tag{6}$$

$$C_n^j=r^j,\quad j=1,2,...,m, \tag{7}$$

$$C_i^0=\varphi_i, \tag{8}$$

where $C_i^j\approx C(x_i,t_j),\ \nu^j=\nu(t_j),\ p^j=p(t_j),\ \varphi_i=\varphi(x_i),\ r^j=r(t_j)$.

Apparently, the discrete analogue of problem (1)–(4) is a system of linear algebraic equations where the unknowns are the rate constant of the chemical reaction k and C_i^j, $i = 1, 2, ..., n - 1$, $j = 1, 2, ..., m$, i.e., the approximate values of the required function $C(x,t)$ in the nodes of the difference grid ω.

To solve the resulting system of equations (5)–(8), we introduce decomposition of this system into mutually independent subsystems, each of which can be solved independently of the other subsystem [9, 12]. Then the solution of the system of equations (5)–(8) for each fixed value of $j = 1, 2, ..., m$ can be represented as

$$C_i^j = U_i^j + kW_i^j, \quad i = 0,1,2,...,n, \tag{9}$$

where U_i^j, W_i^j and k are unknown variables.

Substituting relation (9) into Eq. (5), we obtain:

$$\frac{U_i^j + kW_i^j - C_i^{j-1}}{\Delta t} + \nu^j \frac{U_i^j + kW_i^j - U_{i-1}^j - kW_{i-1}^j}{\Delta x} + k(C_i^{j-1})^2 = 0,$$

or

$$\left[\frac{U_i^j - C_i^{j-1}}{\Delta t} + \nu^j \frac{U_i^j - U_{i-1}^j}{\Delta x}\right] + k\left[\frac{W_i^j}{\Delta t} + \nu^j \frac{W_i^j - W_{i-1}^j}{\Delta x} + (C_i^{j-1})^2\right] = 0.$$

Furthermore, substituting relation (9) into Eq. (6), we obtain

$$U_0^j + kW_0^j = p^j.$$

Since the variables U_i^j, W_i^j are arbitrary, we obtain the following independent systems of linear algebraic equations with respect to the variables U_i^j, W_i^j from the last two relations:

$$\frac{U_i^j - C_i^{j-1}}{\Delta t} + \nu^j \frac{U_i^j - U_{i-1}^j}{\Delta x} = 0, \quad i = 1,2,...,n, \tag{10}$$

$$U_0^j = p^j; \tag{11}$$

$$\frac{W_i^j}{\Delta t} + \nu^j \frac{W_i^j - W_{i-1}^j}{\Delta x} + (C_i^{j-1})^2 = 0, \quad i = 1,2,...,n, \tag{12}$$

$$W_0^j = 0, \quad j = 1,2,...,m \tag{13}$$

Evidently, the solutions to the system of linear equations (10), (11) and (12), (13) can be found by the recurrent formulas

$$U_i^j = \frac{C_i^{j-1} + U_{i-1}^j v^j \Delta t / \Delta x}{1 + v^j \Delta t / \Delta x}, \quad i = 1,2,...,n, \ U_0^j = p^j; \tag{14}$$

$$W_i^j = \frac{W_{i-1}^j \nu^j \Delta t / \Delta x - (C_i^{j-1})^2 \Delta t}{1 + v^j \Delta t / \Delta x}, \quad i = 1,2,...,n, \ W_0^j = 0, \ j = 1,2,...,m. \tag{15}$$

Substituting relation (9) into additional condition (7) produces the following equality:

$$U_n^j + kW_n^j = r^j.$$

We then obtain a formula for calculating the value of the parameter k for each fixed value of $j = 1, 2, ..., m$:

$$k = \frac{r^j - U_n^j}{W_n^j}. \tag{16}$$

Thus, the variables k and C_i^j ($i = 1, 2, ..., n - 1$, $j = 1, 2, ..., m$) from the system of linear algebraic equations (5)–(8) are determined by constructing the following computational algorithm.

Step 1. Solutions of a system of linear algebraic equations (10), (11) and (12), (13) are determined for a fixed value of the time layer j by recurrent formulas (14) and (15).

Step 2. The approximate value of the required parameter k is determined by Eq. (16).

Step 3. The values of variables C_i^j, $i = 1, 2, ..., n$ are calculated by Eq. (9).

Step 4. This calculation technique is repeated in each subsequent layer.

Results of numerical calculations

The proposed numerical method was tested with various simulation problems to establish its practical applicability. Numerical experiments were carried out by the following algorithm.

I. The solution of the system of linear algebraic equations (5)–(8) is determined for the given values of the variables k, v^j, p^j, φ_i:

$$C_i^j = \frac{C_i^{j-1} + C_{i-1}^j v^j \Delta t / \Delta x - k(C_i^{j-1})^2 \Delta t}{1 + v^j \Delta t / \Delta x},$$

$$i = 1, 2, .., n,\ j = 1, 2, ..., m,$$

$$C_i^0 = \varphi_i,\ C_0^j = p^j.$$

II. The values of the variable r^j, defined as $r^j = C_n^j$, are taken as input data to reconstruct the value of the parameter k by the proposed computational algorithm.

Numerical experiments were carried out on a space-time difference grid with steps $\Delta t = 1$ s, $\Delta t = 5$ s, $\Delta x = 0.04$ m for the following exact values of the rate constant: $k = 0.25$, 0.55 m^3/(kg·s).

The following data were used for the remaining parameters of model (1)–(4):

$$\varphi(x) = 0.1 \text{ kg/m}^3,\ p(t) = 0.8 \text{ kg/m}^3,\ v = 0.4 \text{ m/s},\ l = 2 \text{ m}.$$

Perturbed input data were also used along with unperturbed input data in the numerical experiments.

The following ratio was used to perturbate the input data r^j

$$\tilde{r}^j = r^j + \delta \xi^j r^j,$$

where ξ^j is a random variable modeled with a random number sensor; δ is the error level of the input data ($\delta = 0.02$ was used).

The results of numerical experiments conducted with unperturbed and perturbed input data are given in Table.

Analyzing the results, we can conclude that the value of the required rate constant is reconstructed exactly if unperturbed input data are used, regardless of the time step of the difference grid Δt, (second and third columns in Table). However, perturbed input data where the error is random affect the accuracy of reconstructing the value of the required constant (the remaining columns in Table). The reconstruction error of the required rate constant value depends on the time step of the difference grid Δt. It follows from the data in Table that the relative reconstruction errors of $k_e = 0.25$ and 0.55 m^3/(kg·s) exceed 10% and 6.5%, respectively, for the time step $\Delta t = 1$ s. However, the maximum relative reconstruction errors of $k_e = 0.25$ and 0.55 m^3/(kg·s) do not exceed 3.5 and 2.2%, respectively, for the step $\Delta t = 5$ s.

Table

Numerical search for value of rate constant k with variable input data

t, s	Calculated k, m^3/(kg·s), with different input data					
	Unperturbed		Perturbed			
	k_e = 0.25 m^3/(kg·s)	k_e = 0.55 m^3/(kg·s)	k_e = 0.25 m^3/(kg·s)		k_e = 0.55 m^3/(kg·s)	
			Δt = 1 s	Δt = 5 s	Δt = 1 s	Δt = 5 s
5	0.250	0.550	0.235	0.250	0.532	0.545
10			0.245	0.250	0.543	0.544
15			0.276	0.242	0.584	0.545
20			0.261	0.247	0.563	0.542
25			0.249	0.247	0.548	0.546
30			0.266	0.244	0.570	0.542
35			0.226	0.246	0.515	0.540
40			0.263	0.248	0.579	0.544
45			0.225	0.246	0.515	0.544
50			0.246	0.246	0.542	0.538

Preset parameters: k_e is the exact value of the constant k, t is the time, Δt is the step on the space-time difference grid.

The results of numerical experiments indicate that the time step of the difference grid Δt acts as a regularization parameter (self-regularization) [8, 9], so that the reconstruction accuracy of the required constant increases with increasing Δt.

Analysis of the obtained results confirms that self-regularization can be used to reduce the influence of the error in the input data on the reconstruction accuracy of the required rate constant, therefore making the proposed computational algorithm more robust against input data errors.

Conclusion

We considered the problem of identifying the rate constant of a second-order chemical reaction occurring in a perfect displacement reactor. We adopted a numerical method based on discretization and special decomposition to solve the resulting system of linear algebraic equations. This method allows to determine the rate constant of a chemical reaction with a sufficiently high accuracy. The proposed numerical method can also be used to identify the hydrodynamic parameters of the flow in a perfect displacement chemical reactor.

REFERENCES

1. **Komissarov Yu. A., Gordeyev L. S, Vent D. P.,** Protsessy i apparaty khimicheskoy tekhnologii [Processes and units of equipment of chemical technology], Khimiya Publishing, Moscow, 2011 (in Russian).

2. **Kutepov A. M., Bondareva T. N., Berengarten M. B.,** Obshchaya khimicheskaya tekhnologiya [General chemical technology], Akademkniga, Moscow (in Russian).

3. **Zakgeim A. Yu.,** Obshchaya khimicheskaya tekhnologiya: vvedeniye v modelirovaniye khimiko-tekhnologicheskikh protsessov [General chemical technology: Introduction to modeling of chemical processes], Logos, Moscow, 2009 (in Russian).

4. **Kafarov V. V., Glebov M. B.,** Matematicheskoye modelirovaniye osnovnykh protsessov khimicheskikh proizvodstv [Mathematical modeling of the main processes of chemical production]. Higher School Publisher, Moscow, 1991 (in Russian).

5. **Usheva N. V., Moyzes O. E., Mityanina O. E., Kuzmenko E. A.,** Matematicheskoye modelirovaniye khimiko-tekhnologicheskikh protsessov [Mathematical modeling of chemical technological processes], Tomsk Polytechnical University Publishing, Tomsk, 2014 (in Russian).

6. **Gumerov A. M.,** Matematicheskoye modelirovaniye khimiko-tekhnologicheskikh protsessov [Simulation of chemical technological processes], Lan Publishing, Moscow, 2014 (in Russian).

7. **Kabanikhin S. I.,** Inverse and ill-posed problems, Walter de Gruyter, Berlin, 2011.

8. **Alifanov O. M.,** Inverse heat transfer problems, Springer-Verlag, Berlin, 2011.

9. **Samarskii A. A., Vabishchevich P. N.,** Numerical methods for solving inverse problems of mathematical physics, Walter de Gruyter, Berlin, 2008.

10. **Vabishchevich P. N., Klibanov M. V.,** Numerical identification of the leading coefficient of a parabolic equation, Differ. Equ. 52 (7) (2016) 855–862.

11. **Gamzayev Kh. M.** A numerical method for solving the coefficient inverse problem for diffusion-convection-reaction equation, Tomsk State Univ. J. Math. Mech. (50) (2017) 67–78 (in Russian).

12. **Prilepko A. I., Volkov N. P.,** Inverse problems for determining the parameters of a nonstationary kinetic transport equation from additional information on the traces of the unknown function, Differ. Uravn. 24 (1) (1988) 136–146 (in Russian).

13. **Prilepko A. I., Orlovsky D. G., Vasin I. A.,** Methods for solving inverse problems in mathematical physics (Monographs and textbooks in pure and applied mathematics. Vol. 231), Marcel Dekker, Inc., New York, 2000.

14. **Gamzaev Kh. M., Huseynzade S. O., Gasimov G. G.,** A numerical method for solving identification problem for the lower coefficient and the source in the equation convection – reaction, Cybernetics and Systems Analysis 54 (6) (2018) 971–976.

СПИСОК ЛИТЕРАТУРЫ

1. **Комиссаров Ю. А., Гордеев Л. С, Вент Д. П.** Процессы и аппараты химической технологии. М.: Химия, 2011. 1230 с.

2. **Кутепов А. М., Бондарева Т. Н., Беренгартен М. Б.** Общая химическая технология. М.: Академкнига, 2007. 528 с.

3. **Закгейм А. Ю.** Общая химическая технология: введение в моделирование химико-технологических процессов. М.: Логос, 2009. 304 с.

4. **Кафаров, В. В., Глебов М. Б.** Математическое моделирование основных процессов химических производств. М.: Высшая школа, 1991. 400 с.

5. **Ушева Н. В., Мойзес О. Е., Митянина О. Е., Кузьменко Е. А.** Математическое моделирование химико-технологических процессов. Томск: Изд-во Томского политехнического университета, 2014. 140 с.

6. **Гумеров А. М.** Математическое моделирование химико-технологических процессов. М.: Изд-во «Лань», 2014. 176 с.

7. **Кабанихин С. И.** Обратные и некорректные задачи. 2-е изд., перераб. Новосибирск: Сибирское научное изд-во, 2009. 457 с.

8. **Алифанов О. М.** Обратные задачи теплообмена. М.: Машиностроение, 1988. 280 с.

9. **Самарский А. А., Вабищевич П. Н.** Численные методы решения обратных задач математической физики. 3-е изд. М.: Изд-во ЛКИ, 2009. 480 с.

10. **Вабищевич П. Н., Клибанов М. В.** Вычислительная идентификация старшего коэффициента параболического уравнения // Дифференциальные уравнения. 2016. Т. 52. № 7. С. 896–903.

11. **Гамзаев Х. М.** Численный метод решения коэффициентной обратной задачи для уравнения диффузии – конвекции – реакции // Вестник Томского государственного университета. Математика и механика. 2017. № 50. С. 67–78.

12. **Прилепко А. И., Волков Н. П.** Обратные задачи определения параметров нестационарного кинетического уравнения переноса по дополнительной информации о следах искомой функции // Дифференциальные уравнения. 1988. Т. 24. № 1. С. 136–146.

13. **Prilepko A. I., Orlovsky D. G., Vasin I. A.** Methods for solving inverse problems in mathematical physics (Monographs and textbooks in pure and applied mathematics. Vol. 231). New York: Marcel Dekker, Inc., 2000. 744 p.

14. **Gamzaev Kh. M., Huseynzade S. O., Gasimov G. G.** A numerical method for solving identification problem for the lower coefficient and the source in the equation convection – reaction // Cybernetics and Systems Analysis. 2018. Vol. 54. No. 6. Pp. 971–976.

THE AUTHORS

GAMZAEV Khanlar M.
Azerbaijan State Oil and Industry University
20 Azadlig Ave., Baku, AZ1010, Azerbaijan
xan.h@rambler.ru
ORCID: 0000-0002-1228-7892

GAMZAEVA Nusaba Kh.
Azerbaijan State Oil and Industry University
20 Azadlig Ave., Baku, AZ1010, Azerbaijan
hemzeyevanusaba90@mail.ru
ORCID: 0000-0002-4618-6643

СВЕДЕНИЯ ОБ АВТОРАХ

ГАМЗАЕВ Ханлар Мехвали оглу – *доктор технических наук, профессор кафедры общей и прикладной математики Азербайджанского государственного университета нефти и промышленности.*
AZ 1010, Азербайджан, г. Баку, пр. Азадлыг, 20
xan.h@rambler.ru
ORCID: 0000-0002-1228-7892

ГАМЗАЕВА Нушаба Ханлар гызы – *преподаватель кафедры нефтехимической технологии и промышленной экологии Азербайджанского государственного университета нефти и промышленности.*
AZ 1010, Азербайджан, г. Баку, пр. Азадлыг, 20
hemzeyevanusaba90@mail.ru
ORCID: 0000-0002-4618-6643

Received 16.02.2023. Approved after reviewing 02.04.2023. Accepted 02.04.2023.
Статья поступила в редакцию 16.02.2023. Одобрена после рецензирования 02.04.2023. Принята 02.04.2023.

© Peter the Great St. Petersburg Polytechnic University, 2023

ATOM PHYSICS AND PHYSICS OF CLUSTERS AND NANOSTRUCTURES

Original article
DOI: https://doi.org/10.18721/JPM.16203

THE PLASMON RESONANCE IN THE CADMIUM SELENIDE SEMICONDUCTOR NANOCRYSTALS WITH DIFFERENT DOPING TYPES

A. N. Ipatov[1, 2], *G. A. Kupriianov*[1]✉

[1] Peter the Great St. Petersburg Polytechnic University, St. Petersburg, Russia;

[2] Alferov University of RAS, St. Petersburg, Russia

✉ henryweis3@gmail.com

Abstract. The effect of the type of doping (surface (I) or bulk (II) doping) on the character of the dipole plasmon mode in semiconductor CdSe nanocrystals has been studied. It was found that in case I (donors located on the surface of the nanocrystal) the collective mode had a rotational character and only the angular degrees of freedom were excited. On the contrary, in case II the charge of the dopant impurities was distributed throughout the system and plasmon excitation was the oscillation of delocalized charge carriers in the direction normal to the surface. It was shown that the position of the resonance line was determined not only by the concentration of free charges, but also by the character of their collective motion determining by the type of doping.

Keywords: semiconductor nanocrystal, cadmium selenide, doping, plasmon resonance, multiparticle excitation

Citation: Ipatov A. N., Kupriianov G. A., The plasmon resonance in the cadmium selenide semiconductor nanocrystals with different doping types, St. Petersburg State Polytechnical University Journal. Physics and Mathematics. 16 (2) (2023) 27–51. DOI: https://doi.org/10.18721/JPM.16203

This is an open access article under the CC BY-NC 4.0 license (https://creativecommons.org/licenses/by-nc/4.0/)

© Ipatov A. N., Kupriianov G. A., 2023. Published by Peter the Great St. Petersburg Polytechnic University.

Научная статья
УДК 538.9
DOI: https://doi.org/10.18721/JPM.16203

ПЛАЗМОННЫЙ РЕЗОНАНС В ПОЛУПРОВОДНИКОВЫХ НАНОКРИСТАЛЛАХ СЕЛЕНИДА КАДМИЯ С РАЗЛИЧНЫМ ТИПОМ ЛЕГИРОВАНИЯ

А. Н. Ипатов[1, 2], *Г. А. Куприянов*[1] ✉

[1] Санкт-Петербургский политехнический университет Петра Великого, Санкт-Петербург, Россия;

[2] Академический университет им. Ж.И. Алфёрова РАН, Санкт-Петербург, Россия

✉ henryweis3@gmail.com

Аннотация. Исследовано влияние типа легирования (поверхностное (I) либо объемное (II)) на характер дипольной плазмонной моды в полупроводниковых нанокристаллах CdSe. Установлено, что в I случае (доноры расположены на поверхности нанокристалла) коллективная мода имеет вращательный характер и возбуждаются только угловые степени свободы. Напротив, во II случае заряд легирующих примесей распределен по всему объему системы и плазмонное возбуждение – суть колебание делокализованных носителей заряда в направлении нормали к поверхности. Показано, что положение резонансной линии обусловлено не только концентрацией свободных зарядов, но и характером их коллективного движения, который определяется типом легирования.

Ключевые слова: полупроводниковый нанокристалл, селенид кадмия, легирование, плазмонный резонанс, многочастичное возбуждение

Ссылка для цитирования: Ипатов А. Н., Куприянов Г. А. Плазмонный резонанс в полупроводниковых нанокристаллах селенида кадмия с различным типом легирования // Научно-технические ведомости СПбГПУ. Физико-математические науки. 2023. Т. 16. № 2. С. 27–51. DOI: https://doi.org/10.18721/ JPM.16203

Статья открытого доступа, распространяемая по лицензии CC BY-NC 4.0 (https://creativecommons.org/licenses/by-nc/4.0/)

Introduction

Recent decades have seen rapid advances in nanotechnology, nanoelectronics and nanophotonics, with the pressing need for novel materials whose physical and chemical properties differ from those of the corresponding bulk components. A burgeoning field is quantum plasmonics focused on studying the quantum properties of light and the mechanisms of its interaction with matter at the nanoscale level [1–3]. A distinct characteristic of nanoscale conducting particles is the presence of dipole resonances in their optical spectra [2, 4–8]. In particular, doped semiconductor nanocrystals are a promising class of materials [4, 5, 9–15]. Importantly, the position of the resonance line in the spectra of semiconductor nanoparticles depends not only on the concentration of carriers, but also on the doping method, which can be provisionally defined as either bulk or surface [16–20]. In the first case, the charge density of free carriers is distributed over the entire volume of the crystal and is at the same time neutralized by the charge of dopant impurities, while in the second case, free carriers are injected into the bulk of the semiconductor nanoparticle by donors/acceptors located on its surface [21, 22]. In the case of bulk-doped semiconductor nanoparticles [18–20, 23], a dipole plasmon can be described in the adiabatic approximation [24, 25] as a quasi-particle making harmonic oscillations of a system of delocalized electrons as a whole relative to the center of the positively charged core in the direction normal to its surface.

© Ипатов А. Н., Куприянов Г. А., 2023. Издатель: Санкт-Петербургский политехнический университет Петра Великого.

On the other hand, it was established in [26, 27] that the situation turns out to be fundamentally different for surface-doped nanocrystals. The characteristics of the electronic configuration induced by the surface doping mechanism generate excitation states of only angular degrees of freedom in the collective dipole mode upon interaction with an external electromagnetic field. The motion of electrons in the radial direction is not included, and the electrons oscillate tangentially with respect to the boundary of the system within a relatively thin spherical layer. The described phenomenon is similar to dipole plasmon oscillations in fullerenes [28–30].

The goal of the study was to detect and analyze the influence of the doping type, the number of delocalized charge carriers, as well as the geometric dimensions of the system on the nature of multiparticle excitations in the electron system of doped semiconductor nanocrystals, focusing on cadmium selenide CdSe nanocrystals.

Our approach to analysis of the phenomenon is based on a self-consistent quantum mechanical description of multiparticle excitations in a system of delocalized charge carriers. Calculations of the system's ground state were carried out in the Hartree–Fock approximation, taking into account the nonlocal interparticle exchange interaction. For comparison, the calculations were complemented by calculations performed in the local density approximation; the photoabsorption spectra of nanocrystals containing a different number of free charge carriers were obtained within the random phase approximation (RPA) both with nonlocal (RPAE) and local (RPAX) exchange interactions [31, 32].

Theoretical approach

We examine *n*-doped CdSe nanocrystals in a dielectric environment with different types of doping, as, according to the approach to the problem outlined in [19, 20], it determines the form of effective external potential where delocalized charge carriers move, and, accordingly, their distribution across the bulk of the nanocrystal.

Consider an electroneutral system of interacting fermions related by the Coulomb interaction. Negative particles in the conduction band are referred to as electrons with an effective mass m_e from now on.

The total Hamiltonian of the described system is an operator of the total energy of a system of N electrons interacting with each other by means of the Coulomb potential V in the external potential $U_{ext}(\mathbf{r})$, whose radial dependence is determined by the doping type:

$$\hat{H} = \sum_{i}^{N} \frac{\hat{\mathbf{p}}_i}{2m_e} + \sum_{i}^{N} U_{ext}(r_i) + \frac{1}{2}\sum_{i,j}^{N} V(\mathbf{r}_i, \mathbf{r}'_j). \tag{1}$$

Since the motion of electrons within the nanoparticle bulk is limited by the edge of the conduction band near the surface [13], we describe $U_{ext}(\mathbf{r})$ as a spherical potential well, whose geometric parameter R is determined by the dimensions set for the nanocrystal and the profile by the selected type of doping. The Coulomb pair interaction between electrons at points $\mathbf{r}_a$ and $\mathbf{r}_b$ is shielded due to polarization of both the semiconductor material itself and the environment, so that the multipole expansion of the interparticle interaction potential at $r_i, r_j < R$ can be written as follows [33, 34]:

$$V(\mathbf{r}_i, \mathbf{r}_j) = \sum_{LM} \frac{V_L}{2L+1} Y_{LM}(\mathbf{r}_i) Y^*_{LM}(\mathbf{r}_j),$$
$$V_L = \frac{4\pi e^2}{\varepsilon_1}\left(\frac{r_<^L}{r_>^{L+1}} + \frac{(\varepsilon_1 - \varepsilon_2)(L+1)(r_i r_j)^L}{(L\varepsilon_1 + (L+1)\varepsilon_2)R^{2L+1}}\right), \tag{2}$$

where $r_{>,<}$ are the largest and the smallest of the radii $r_{i,j}$, respectively; ε_1, ε_2 are the permittivity of nanocrystal materials and its surrounding environment, respectively; L, M are the total angular momentum and its projection, respectively; Y_{LM}, Y^*_{LM} are complex conjugate spherical functions; $\mathbf{r}_i$, $\mathbf{r}_j$ are the radius vectors of interacting particles.

It was assumed in the numerical calculations that the dielectric constant of cadmium selenide is equal to its value for the corresponding bulk material: $\varepsilon_1 = 6.25$, and the permittivity of the nanoparticle environment was chosen typical for a number of experimental and theoretical works [19, 21, 22]: $\varepsilon_2 = 2.25$. For comparison with some conclusions drawn in [19], numerical calculations were carried out at a value of $R = 2$ nm.

Importantly, since the effective electron mass of the electrons in cadmium selenide is relatively small relative to the mass of the free electron, namely $m_e = 0.11\ m_0$, and the effective Bohr radius a_0 turns out to be larger than the radius of the considered nanoparticles R,

$$a_0 = h^2\varepsilon_1/m_e e^2 = 3 \text{ nm},$$

this is fundamentally different from the situation with ZnO nanocrystals whose optical properties were discussed in [21, 22, 26, 27].

The interparticle interaction in the ground state of the system was described using, the Hartree–Fock (HF) approximation where the single-particle wave functions of the electrons $\phi(\mathbf{r}_i)$ satisfy the self-consistent equations [35–37]:

$$-\frac{\hbar^2\Delta_i}{2m_e}\phi_i(\mathbf{r}_i) + \left(U_{ext}(\mathbf{r}_i) + U_H(\mathbf{r}_i) + U_x(\mathbf{r}_i)\right)\phi_i(\mathbf{r}_i) = E_i\phi_i(\mathbf{r}_i), \tag{3}$$

where E_i are single-particle electron energies, $U_H(\mathbf{r})$ is the corresponding Hartree potential.

In the case of a system with filled shells, they are written as [37]

$$U_H(\mathbf{r}) = \int V(\mathbf{r},\mathbf{r}')\rho_e(\mathbf{r}')d\mathbf{r}', \tag{4}$$

where the bulk electron density

$$\rho_e(\mathbf{r}) = 2\sum_i \phi_i^*(\mathbf{r})\phi_i(\mathbf{r})$$

is calculated by summing over all filled single-particle states.

In this case, the contribution of the nonlocal exchange potential $U_x(\mathbf{r})$ is defined as

$$U_x(\mathbf{r})\phi_i(\mathbf{r}) = -e^2\sum_j \int \frac{\phi_j^*(\mathbf{r}')\phi_i(\mathbf{r}')d\mathbf{r}'}{|\mathbf{r}-\mathbf{r}'|}\phi_j(\mathbf{r}). \tag{5}$$

The computational results were compared with the corresponding values obtained in the local density approximation (LDA), implying that single-particle wave functions of electrons $\phi_i(\mathbf{r})$ satisfy the Kohn–Sham equations [38], where, unlike Eq. (3), local exchange potentials $U_x(\mathbf{r})$ are used in the Dirac–Slater approximation [38]:

$$U_x(\mathbf{r}) = -\left(e^2/\varepsilon_1\right)\left(3\rho_e(\mathbf{r})/\pi\right)^{1/3}. \tag{6}$$

In the case of spherically symmetric systems with closed electron shells and isotropic angular dependencies p($\mathbf{r}$) and $U_{ext}(\mathbf{r})$, the collective index i is equal to $i = (n,l,m,\sigma)$, where n is the radial quantum number; l, m are the orbital angular momentum and its projection; σ is the spin projection, while the actual single-particle wave functions are written as the product of the radial, angular and spin components [39]:

$$\phi_{nlm\sigma}(\mathbf{r}) = \frac{P_{nl}(r)}{r}Y_{lm}(\theta,\varphi)\chi_\sigma. \tag{7}$$

The random phase approximation with nonlocal exchange interaction was used to describe multielectron correlations. The wave function of the excited state $|\Phi_k\rangle$ is represented within this approach as a superposition of single-particle excitations of the particle–vacancy type:

$$\left|\Phi_k\right\rangle = \sum_{im}\left(X_{im}^{(k)}\hat{a}_m^+\hat{a}_i + Y_{im}^{(k)}\hat{a}_i^+\hat{a}_m\right)\left|\Phi_0\right\rangle, \tag{8}$$

where $|\Phi_0\rangle$ is the ground state of the complex; $\hat{a}^+$, $\hat{a}$ are single-particle operators of creation and annihilation; the indices i, m are used (here and below) to denote filled and unfilled single-particle states of the electronic subsystem; the coefficients $X_{im}^{(k)}$, $Y_{im}^{(k)}$ are the forward-in-time and backward-in-time amplitudes, respectively (determining the contributions of the corresponding particle–vacancy pair to the multiparticle excited state (8)).

The excited states of a multiparticle system with filled shells possessing spherical symmetry are characterized in the Russell–Saunders (LS) coupling approximation by the total angular momentum L and its projection M [41], therefore all single-particle particle–vacancy excitations have the same multipole in superposition (8).

To describe the optical properties of the given complexes, it is sufficient to consider only dipole transitions from the ground state $|\Phi_0\rangle$ to excited multiparticle states $|\Phi_k\rangle$ with $L = 1$, $M = 0$.

The amplitude coefficients $\mathbf{X}^{(k)}$ and $\mathbf{Y}^{(k)}$ in superposition (8) are determined by solving the RPAE matrix equation:

$$\mathbf{U}\mathbf{Z}^{(k)} = \hbar\Omega_k\mathbf{Z}^{(k)}, \tag{9}$$

where Ω_k are the eigenvalues of the matrix $\mathbf{U}$,

$$\mathbf{U} = \begin{pmatrix} \mathbf{A} & \mathbf{B} \\ -\mathbf{B}^* & -\mathbf{A}^* \end{pmatrix}, \ \mathbf{Z}^{(k)} = \begin{pmatrix} \mathbf{X}^{(k)} \\ \mathbf{Y}^{(k)} \end{pmatrix}. \tag{10}$$

The elements of Hermitian matrices $\mathbf{A}$, $\mathbf{B}$ are expressed in terms of single-particle energies E_i and Coulomb matrix elements of interparticle pair interaction, which are expressed as

$$\left\langle\alpha\beta\,|\,V\,|\,\gamma\eta\right\rangle = \delta_{\sigma_\alpha\sigma_\gamma}\delta_{\sigma_\beta\sigma_\eta}\int\varphi_\alpha^*(\mathbf{r})\varphi_\beta^*(\mathbf{r}')V(\mathbf{r},\mathbf{r}')\varphi_\gamma(\mathbf{r})\varphi_\eta(\mathbf{r}')d\mathbf{r}d\mathbf{r}', \tag{11}$$

with single-particle functions obtained by solving Eqs. (3), where the potential $V(\mathbf{r},\mathbf{r}')$ is determined from expansion (2).

Matrices $\mathbf{A}$ and $\mathbf{B}$ relate the single-particle excitations inside the electronic system [31, 37]:

$$\begin{gathered} A_{im,jn} = \delta_{ij}\delta_{mn}(E_n - E_i) + \left\langle in\,|\,U\,|\,mj\right\rangle, \\ B_{im,jn} = \left\langle ij\,|\,U\,|\,mn\right\rangle \end{gathered} \tag{12}$$

and include both direct (Hartree) and nonlocal exchange interactions, i.e.,

$$\left\langle\alpha\beta\,|\,U\,|\,\gamma\eta\right\rangle = 2\left\langle\alpha\beta\,|\,V\,|\,\gamma\eta\right\rangle + \left\langle\alpha\beta\,|\,V\,|\,\eta\gamma\right\rangle, \tag{13}$$

where the multiplier 2 before the direct component in this equality appears as a result of summation over spin variables.

The term containing the nonlocal exchange interaction in Eq. (13) was replaced by a matrix element in calculations of the excited states of the system in the random phase approximation with local exchange kernel (RPAX) [38],

$$\left\langle\alpha\beta\,|\,U\,|\,\gamma\eta\right\rangle = 2\left\langle\alpha\beta\,|\,V\,|\,\gamma\eta\right\rangle + \left\langle\alpha\beta\,|\,V_x\,|\,\gamma\eta\right\rangle, \tag{14}$$

where

$$V_x(\mathbf{r},\mathbf{r}') = \frac{\delta U_x\left[\rho(\mathbf{r})\right]}{\delta\rho(\mathbf{r})}\delta(\mathbf{r}-\mathbf{r}'), \tag{15}$$

(here the local exchange potential U_x is determined in accordance with expression (6)).

Positive eigenvalues Ω_k are the energies of transitions between the ground state $|\Phi_0\rangle$ and correlated excited states $|\Phi_k\rangle$. The energy spectra of excited states and the corresponding wave functions obtained by solving Eqs. (9), (10) allow to describe the processes associated with excitation of the system under various external influences. In particular, the response of the system to an external electromagnetic field is determined by the spectrum of dipole excitations.

The oscillator strengths f_k for dipole transitions between the ground and the kth excited state are equal to

$$f_k = 2m_e D_k^2 \Omega_k, \tag{16}$$

and satisfy the Thomas–Reich–Kuhn sum rule [37], i.e., $\sum_k f_k = N$.

Dipole matrix elements D_k (in the length form) are calculated by summing over all single-particle excitations [35, 36, 40]:

$$D_k = \sum_{im} \left(X_{im}^{(k)} d_{im} + Y_{im}^{(k)} d_{mi} \right), \tag{17}$$

where $d_{\alpha\beta} = \langle\alpha|z|\beta\rangle$ are the single-particle dipole amplitudes for the particle–vacancy pair.

The amplitude coefficients $\mathbf{X}^{(k)}$ and $\mathbf{Y}^{(k)}$ are normalized in accordance with the condition from [37], namely,

$$\sum_{im} \left(\left| X_{im}^{(k)} \right|^2 - \left| Y_{im}^{(k)} \right|^2 \right) = 1. \tag{18}$$

Results and discussion

Free charge carriers in semiconductor nanoparticles form electron shells regardless of the doping mechanism [42, 43]. On the other hand, it was established in [19], analyzing the distribution of electron densities of the ground states in cadmium selenide and cadmium sulfide nanocrystals (CdSe and CdS), that the type of doping determines the shell structure and its filling order, and, therefore, the density distribution of free charge carriers in the crystal bulk.

Coulomb repulsion between free electrons under surface doping shifts them towards the outer boundary of the system, and the characteristics of the electronic configuration induced by the surface doping mechanism ensure that only the angular degrees of freedom are excited during the formation of a collective dipole mode due to interaction with an external electromagnetic field. The motion of electrons in the radial direction is not included, since there is no effective restoring force acting on delocalized electrons from the positively charged core [26].

On the contrary, bulk-doped semiconductor nanocrystals are characterized by a more uniform distribution of electron density throughout the bulk, and the oscillation of free charges is translational in nature, similar to the situation in metal nanoparticles.

Surface doping

The step potential model [44, 45], replacing the potentials of individual atoms with an effective potential where delocalized conduction electrons move [46–48], implies that the electrons are strongly confined in their motion within the bulk of the nanoparticle under surface-type doping.

An example of surface-type doping is the method for photodoping nanocrystals used in [21, 22].

In this case, the external potential can be represented as a spherical potential well with impermeable walls [19, 22, 26]:

$$U_{ext}(r) = \begin{cases} -\dfrac{Ne^2}{\varepsilon_2 R}, & 0 < r < R, \\ -\dfrac{Ne^2}{\varepsilon_2 R} + U_0, & r > R, \end{cases} \tag{19}$$

where U_0 is some phenomenological parameter with the same order of magnitude as the electron work function of the semiconductor bulk material.

Calculations of the ground state of systems with closed electron shells with a different number of electrons N indicate that the distribution of electron density in surface-doped nanocrystals is considerably non-uniform, shifted towards the surface (see Fig. 1), which is qualitatively consistent with the predictions made in [19] based on the results of calculations performed in accordance with the density functional theory. This is due both to interelectronic Coulomb repulsion and to the peculiarities of the electronic structure of the system.

In the ground state, initial filling of electron shells with maximum orbital moments occurs, producing the following structure:

$$1s^2 2p^6 3d^{10} \ldots n_{\max} l_{\max}^{2(2l_{\max}+1)},$$

that is, all single-particle wave functions (7) of closed shells at $N \lesssim 10^2$ correspond to radial quantum numbers $n_r = n - l = 1$, for which the radial parts of the wave functions $P_{nl}(r)$ have no roots.

This electronic structure corresponds to the 'magic' numbers N for systems with closed electronic shells:

$$N = 2\left(l_{\max} + 1\right)^2,$$

where $l_{\max}$ is the angular momentum of the highest occupied molecular orbital (HOMO).

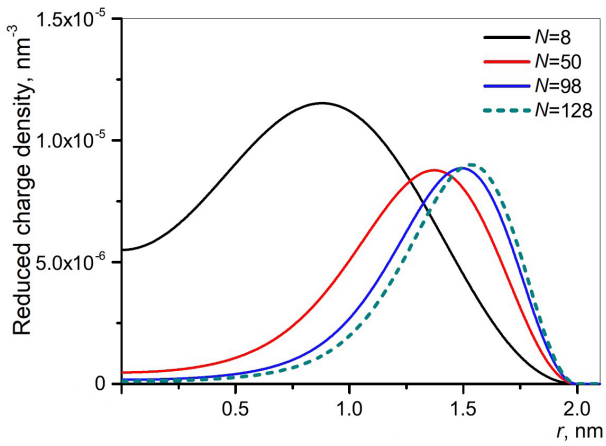

Fig. 1. Distributions of reduced electron charge density $\rho_e(r)/N$ in the bulk of surface-doped CdSe crystal for different numbers of electrons N

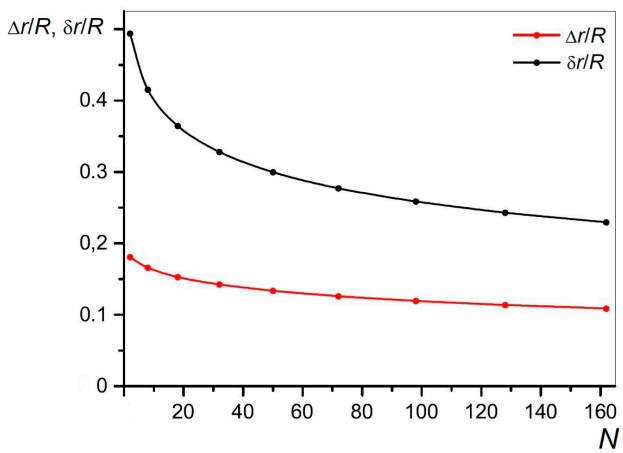

Fig. 2. Reduced displacement of the average radius of electronic system $\Delta r = \langle r \rangle / R$ and reduced effective width of electron layer $\delta r = \sqrt{\langle r^2 \rangle - \langle r \rangle^2}/R$ in the bulk of surface-doped CdSe crystal as functions of number of electrons

Fig. 2 shows the displacement ratio of the average electron radius to the nanocrystal radius $\Delta r = R - \langle r \rangle / R$ and the reduced effective width of electron density distribution $\delta r = \sqrt{\langle r^2 \rangle - \langle r \rangle^2}/R$. It can be seen that the dispersion of electron radius decreases with increasing number of electrons N, and the electronic system acquires a relatively narrow radial distribution, which determines its optical properties. At the same time, the distribution functions $\rho_e(r)$ calculated in the Hartree–Fock approximation (3) and using the local Dirac exchange potential (6) turned out to be almost identical for all selected values of N.

It was hypothesized in [19] that the dipole resonance observed in the photoabsorption spectrum of CdSe nanocrystals is transformed with an increase in the number of free charge carriers in the system from an excited state whose parameters are determined by size quantization into plasmon-type excitation, even with a relatively small crystal radius (R = 2 nm). Indeed, the harmonic plasmon resonance of rotational type also dominated in the spectra of dipole excitations of photodoped ZnO nanocrystals [21, 22] with a similar radial distribution of electron density. The collective nature of this resonance has been well described both within the quantum fluid oscillation model and within the quantum mechanical approach based on RPAE [26, 27].

However, the situation with cadmium selenide is radically different. As established in [27], a necessary condition for harmonic oscillations of electron density by the rotational plasmon type is that the size of the nanoparticle exceed the value of the effective Bohr radius a_0, which was satisfied for all nanoparticles considered in [21, 22]. On the other hand, this condition is not satisfied for CdSe nanocrystals, since R = 2 nm.

In view of this difference, we conducted an analysis of the optical properties of CdSe nanocrystals, which is presented below. The analysis provided conclusions about the nature of the dominant dipole resonance in CdSe photoabsorption spectra.

As established in the next section, the contribution to the collective excited state described by the wave function $|\Psi_k\rangle$ (see Eq. (8)) for nanoparticles with a uniform distribution of electron density, such as bulk-doped semiconductor nanocrystals, produces a sufficiently large number of particle–vacancy pairs, and the distribution of oscillator strengths in the optical spectrum is obtained as a result of numerical solutions of Eq. (10) taking into account the contribution of all single-particle excitations.

However, the situation is fundamentally different for surface-doped nanocrystals. Calculations indicate that a dominant expansion term appears in superposition (8) due to effective separation of the radial and angular motion of electrons, corresponding to the dipole transition between single-particle states on the lowest unoccupied (LUMO) and the highest occupied (HOMO) molecular orbitals with the excitation energy Δ:

$$\Delta = E_{\text{LUMO}} - E_{\text{HOMO}}.$$

In other words, only the states with the smallest radial quantum numbers n_r = 1 participate in the photoabsorption process, and only the transition between HOMO and LUMO electronic levels with the maximum angular moments $l_{\max}$ and $l_{\max}$ + 1, respectively, is effectively allowed for dipole excitations, while correlations between HOMO-LUMO single-particle excitation and other electron–hole pairs are negligible. This allows to describe the plasmon mode using the two-level model (proposed in [27]), where all single-particle transitions appear to be negligible, with the exception of the single HOMO-LUMO excitation.

In this case, the RPAE equation (10) is reduced to a system of two linear equations:

$$\begin{aligned} &\left(\Delta + V_{TF} - \hbar\Omega\right) X + V_{TR} Y = 0, \\ &\left(\Delta + V_{TR} + \hbar\Omega\right) Y + V_{TF} X = 0, \end{aligned} \tag{20}$$

where $V_{TF} = \langle in|v|mj\rangle$ is the forward-in-time matrix element between two single-particle particle–hole dipole excitations; $V_{TR} = \langle ij|v|mn\rangle$ is the backward-in-time matrix element between the ground state and the two-particle–two-hole excitation.

In the case of local exchange interaction (15), these matrix elements turn out to be equal to each other, $V_{TF} = V_{TR} = V$, and the RPAX 2×2 system of equations (20) has a simple analytical solution:

$$\hbar\Omega = \sqrt{\Delta^2 + 2\Delta V}, \tag{21}$$

$$X = \frac{\hbar\Omega + \Delta}{2\sqrt{\hbar\Omega\Delta}}, \; Y = -\frac{\hbar\Omega - \Delta}{2\sqrt{\hbar\Omega\Delta}}. \tag{22}$$

As already mentioned, [19] discussed the transformation of dipole resonance in CdSe nanocrystals from size quantization to classical plasmon oscillations with increasing number of charge carriers in the system, even with its relatively small geometric dimensions (R = 2 nm). As demonstrated in [26, 27], the influence of Coulomb interaction determining the contribution of interparticle correlations to the collective excited state can be estimated by a dimensionless parameter written using the notations in Eq. (20) in the form:

$$\lambda = \Delta^2 / 2\Delta V = \Delta / 2V.$$

In the classical limit, with the system sizes significantly exceeding the Bohr radius, i.e., $R \gg a_0$, the Coulomb interaction dominates, and $\lambda \ll 1$. Conversely, in the size quantization mode, when $R \ll a_0$, the frequency Ω is mainly determined by the single-particle energy Δ ($\lambda \gg 1$). At the same time, analyzing Eq. (21), we can see that taking into account Coulomb correlations $2\Delta V$ causes the plasmon resonance to shift towards higher values compared with the energy of single-particle excitation Δ. Importantly, the shift of the excitation energy is not accompanied by any transformation of the wave function $|\Psi_v\rangle$, since it contains only electron–hole HOMO-LUMO pairs, which does not contradict the collective nature of this excited state. Indeed, superposition (8) contains a large number of terms, although the radial quantum numbers $n_r = 1$ and angular momenta $l_h = l_p - 1$ remain fixed, and summation is carried out over the angular momentum projections. Thus, the dipole excited state can be regarded as a collective mode if the number of free electrons in the filled HOMO shell participating in oscillatory motion is sufficiently large: $2(2l_{max} + 1) \gg 1$.

Another important parameter that allows to estimate the contribution of Coulomb correlations to excitation of the dipole mode is the ratio of the backward-in-time and forward-in-time amplitudes (Y and X, respectively):

$$\frac{Y}{X} = -\frac{\hbar\Omega - \Delta}{\hbar\Omega + \Delta} = -\frac{\sqrt{\Delta + 2V} - \sqrt{\Delta}}{\sqrt{\Delta + 2V} + \sqrt{\Delta}}. \tag{23}$$

In the case of small sizes of nanocrystals, when $R \ll a_0$ ($\lambda \gg 1$), the role of Coulomb correlations is negligible, $X \simeq 1$, $Y \ll 1$, because the energy of interelectronic interaction is small compared with the kinetic energy of electrons localized near an impenetrable potential barrier at the particle surface. The role of these correlations is especially important in the case of CdSe nanocrystals considered, when the effective mass of charge carriers is small compared with the free electron mass.

The approximation of independent single-particle electronic states describes both the ground state and the spectrum of dipole excitations sufficiently well in this size quantization mode. In another limiting case, at $R \gg a_0$ ($\lambda \ll 1$), the interelectronic interaction plays a significant role, which is confirmed by the relation $X \simeq -Y \simeq 1$. The increase in the back-in-time amplitude points to significant influence of Coulomb correlations in the ground state $|0\rangle$. The transformation of the uncorrelated ground state of the system formed from filled single-particle electronic states below the Fermi level into a correlated multiparticle ground state consists in simultaneous production of excited electron–hole pairs, corresponding in the case of a two-level model to transitions between single-particle HOMO and LUMO states. This transformation leads both to a noticeable shift in the excitation energy $\hbar\Omega$ and to a change in the dipole matrix element D that is the transition from the ground state to $|0\rangle$ the collective excited state $|1\rangle$. According to Eq. (21), Coulomb correlations lead to a significant increase in the transition energy $\hbar\Omega$ compared with its single-particle value Δ. Their ratio can be estimated as $\hbar\Omega/\Delta \simeq 2V/\Delta \simeq 1/\lambda$.

At the same time, as follows from Eq. (16), the dipole matrix element itself decreases. Since the ratio $X \simeq -Y$ holds true in the presence of correlations, the two terms on the right-hand side of this equation compensate for each other, which leads to a decrease in the multiparticle matrix element D compared with its single-particle value d. According to Eq. (21), the sum of the amplitudes X and Y is equal to

$$X + Y = \sqrt{\frac{\Delta}{\hbar\Omega}}. \tag{24}$$

Thus, a simultaneous decrease in the dipole matrix element and an increase in the transition energy $|0\rangle \to |1\rangle$ preserve the value of the oscillator strength, i.e.,

$$f = \frac{2m_e\Omega}{\hbar}|D|^2 = \frac{2m_e\Delta}{\hbar^2}|d|^2 = \frac{2}{3}N. \tag{25}$$

The strength of the transition oscillator $|0\rangle \to |1\rangle$ is 2/3 of the sum rule, which is a characteristic sign that this transition describes the contribution of the rotational dipole plasmon to the optical spectrum of the system. This conclusion is based on the property of the rotational mode: it includes only the angular motion of electrons; the radial degrees of freedom remain unexcited.

For the same reason, the square frequency of rotational plasmon is 2/3 of the square frequency of translational plasma oscillations observed in the case of bulk-type doping.

As an example, Fig. 3 shows the distribution of oscillator strengths in the vicinity of the dipole resonance for CdSe nanocrystal containing 98 delocalized electrons (N = 98) with a closed shell configuration

$$1s^2 2p^6 3d^{10} 4f^{14} 5g^{18} 6h^{22} 7i^{26}$$

and the maximum orbital moment $l_{\max}$ = 6 for the HOMO orbital. The figure illustrates the computational results obtained within the RPAE approximation by solving Eq. (10) with a complete set of particle–vacancy pairs. For comparison, the dashed line in the same figure shows the spectral position of the oscillator strength corresponding to the two-level model (20) for the HOMO → LUMO $7i \to 8j$ transition. The thin red line roughly corresponds to the profile of the photoabsorption cross section, generated by artificially broadening the spectral lines with Lorentzian profiles at a width of 0.2Ω. The energy position of the dominant resonance line on the spectrum (numbered 1) coincides with the analytical solution (21) with high accuracy, confirming the hypothesis that the resonance mode can be described as a correlated excited state including only transitions between HOMO and LUMO orbitals taking into account summation over all possible angular momentum projections.

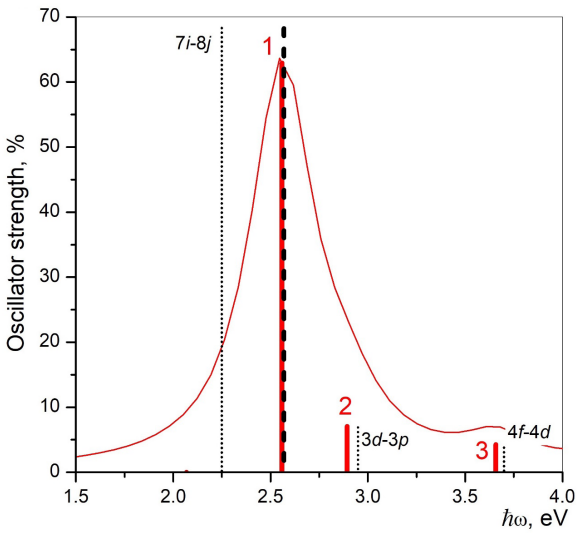

Fig. 3. Energy distribution of oscillator strengths in the vicinity of dipole resonance in CdSe nanocrystal (N = 98) according to different models: RPAE and single-particle Hartree–Fock approximations (bold solid red and dotted black lines, respectively), the two-level model (bold dashed black line). The spectral lines are numbered: k = 1, 2, 3

Notably, the oscillator strength includes 2/3 of the sum rule with a sufficiently high accuracy in both cases, allowing to classify the resonance mode as purely rotational oscillations. The graph in Fig. 3 also shows the oscillator strength, calculated in the single-particle approximation. According to Eq. (21), the shift of the resonance line 1 towards higher energies compared with the initial position of the energy $\Delta_{7i\to 8j}$, indicates the contribution of interparticle correlations to the formation of the resonance mode and confirms its collective nature. Dipole transitions whose lines are numbered 2 and 3 (containing 6 and 5% of the sum rule, respectively) correspond to transitions with excitation of radial degrees of freedom and bear a single-particle nature, judging by the small difference in their energies from the values in the Hartree–Fock approximation.

As an addition to analysis of the dipole spectrum in Fig. 3, Fig. 4 shows for comparison the radial distribution of electron density for the ground state of the system $\rho_e(r)$ and the radial distributions of transition density for spectral lines 1, 2 and 3, illustrating the fundamental difference between the two types of excited states. The given radial distributions for lines 1, 2 and 3 are defined as

$$\rho_{tr}^{(k)}(r) = \sum_{im}\left(X_{im}^{(k)}\phi_i(r)\phi_m^*(r) + Y_{im}^{(k)}\phi_i^*(r)\phi_m(r)\right). \tag{26}$$

The same graph (see Fig. 4) shows the density of the dipole transition for the two-level model, which in this case is defined as

$$\langle HOMO \,|\, LUMO\rangle = P_{7i}(r)P_{8j}(r).$$

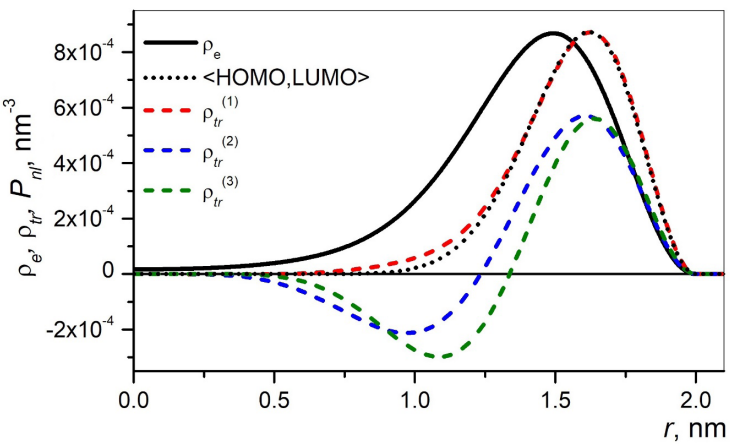

Fig. 4. Radial distributions of electron density $\rho_e(r)$ and transition density $\rho^{(k)}_{tr}(r)$ for spectral lines with k = 1, 2, 3 (see Fig. 3), as well as the overlap of wave functions $P_{nl}(r)$ for molecular orbitals $1i_{(HOMO)}$ and $1j_{(LUMO)}$

As seen from the presented dependences, the transition density of resonance line 1 almost completely coincides with the data of the two-level model and is concentrated on the outer boundary of the electron density distribution, while the densities of single-particle transitions 2 and 3 are more evenly distributed throughout the entire bulk of the system, since they correspond to excitation of radial degrees of freedom.

On the other hand, in our opinion, the transformation of resonant dipole mode in CdSe nanocrystals as the number of electrons increases with relatively small geometric dimensions of the system cannot be characterized as a transition from the quantum to the classical mode, as suggested in [19]. Despite the increase in the shift of the position of the resonance line relative to the energy of the single-particle transition Δ observed in Fig. 5,*a*, the values of the parameter λ and the amplitude ratio $-Y/X$ (see Fig. 5, *b*, *c*) obtained for all $N \lesssim 10^2$ still do not satisfy the

conditions $\lambda \ll 1$ and $X \simeq -Y \simeq 1$, characteristic of classical plasmon oscillation, when the energy of the Coulomb interelectronic interaction prevails in the correlated multiparticle excitation over the single-particle energy of size quantization Δ. This is a consequence of the relatively small effective electron mass in the CdSe and, accordingly, the large effective Bohr radius. While the relative increase in the back-in-time amplitude observed in Fig. 5,*c* indicates a corresponding increase in the contribution of Coulomb correlations to the ground state $|\Phi_0\rangle$ as the number of particles N increases, it turns out to be insufficient for transition to the classical oscillations of the electronic system.

In this case, the transition of resonant excitations from the quantum to the classical mode is achieved by increasing the geometric dimensions of the nanocrystal so that at least the condition $R > a_0$ is satisfied. Fig. 6 shows the dependences for the main parameters of the resonant excited state on the radius R in a nanocrystal containing 98 electrons ($N = 98$) for the resonance mode corresponding to spectral line 1 in Fig. 3. Evidently, the transition of the rotational plasmon mode to the classical regime in the case of CdSe is achieved at values of R above 6 nm, i.e., at least for $R \gtrsim a_0$.

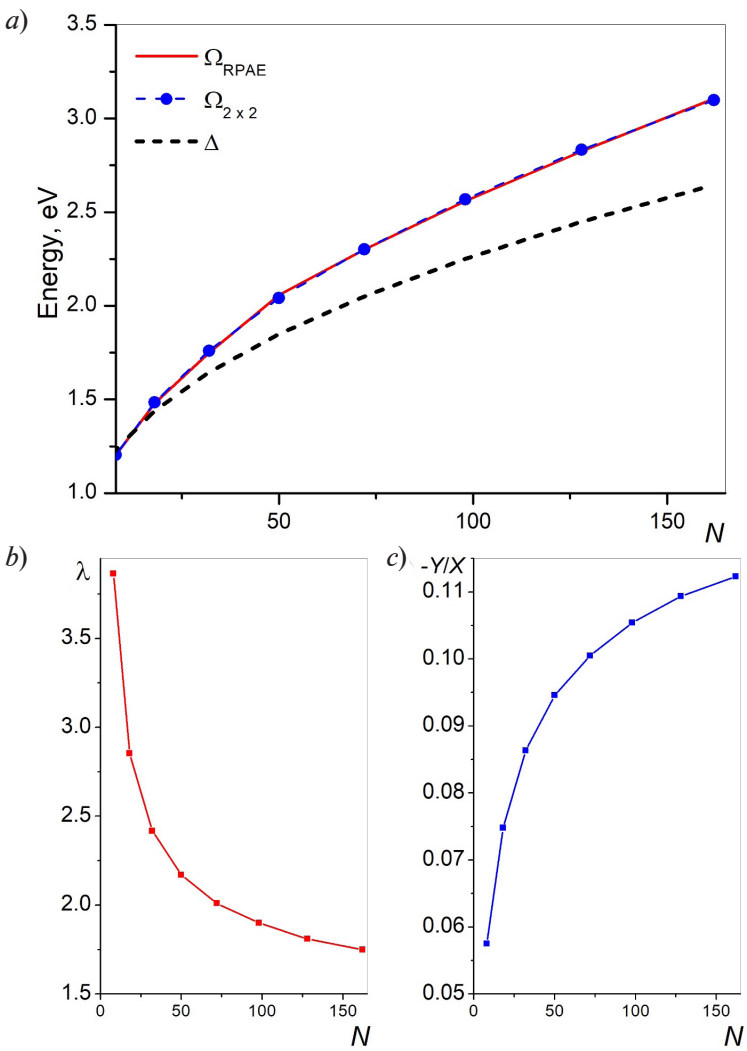

Fig. 5. Main parameters of resonant excited state in a nanocrystal as functions of the number of electrons N: plasmon energies $\hbar\Omega$ obtained in different approximations (*a*); parameter λ (*b*) and amplitude ratios $-Y/X$ (*c*).
RPAE approximations, two-level model (2×2) and one-particle approximation (Δ) (Fig. 5,*a*) are used

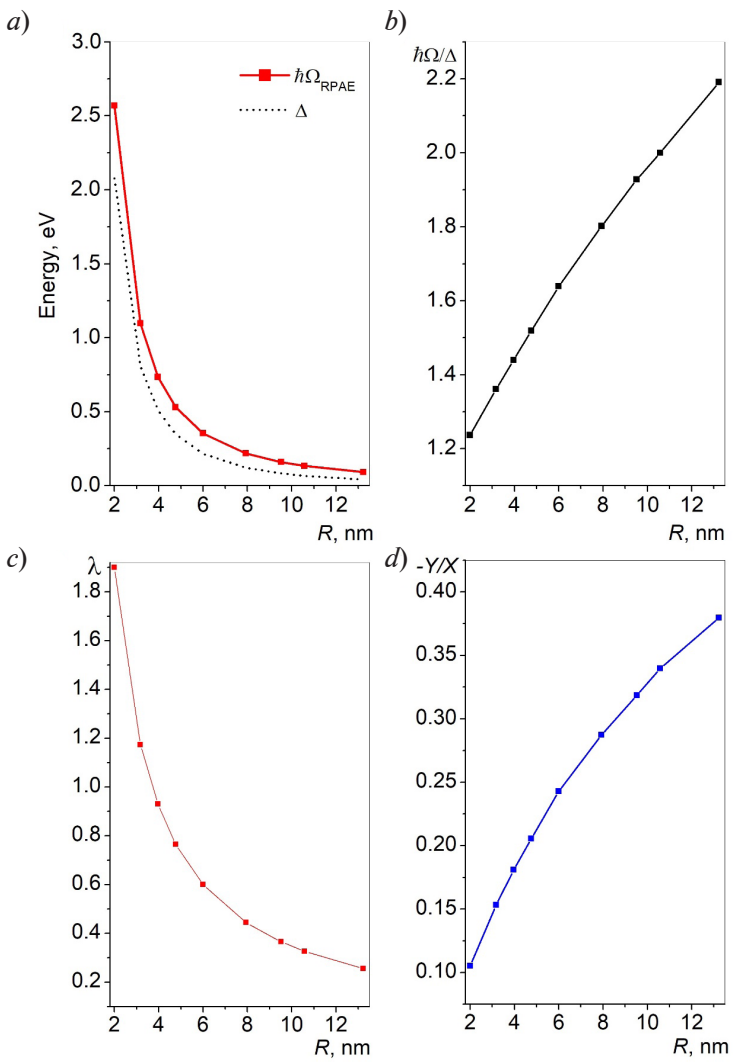

Fig. 6. Main parameters of resonant excited state in CdSe nanocrystal ($N = 98$) as function of potential well radius R: dipole resonance energy $\hbar\Omega$ and energy difference of single-particle levels Δ (*a*), ratio $\hbar\Omega/\Delta$ (*b*), parameter λ (*c*) and ratio $-Y/X$ for resonant line 1 (see Fig. 3) (*d*)

Bulk doping

In the case of bulk doping of semiconductor nanocrystals, the positive charge is assumed to be uniformly distributed throughout the entire bulk of the system [19] and the external potential it generates within the model used should take the form of the potential of a uniformly charged sphere with the charge $Z = Ne$ in a dielectric environment:

$$U_{ext}(r) = \begin{cases} \dfrac{Ne^2}{2\varepsilon_1 R^3}\left(r^2 - \left(1 + \dfrac{2\varepsilon_1}{\varepsilon_2}\right)R^2\right), & 0 < r < R, \\ -\dfrac{Ne^2}{\varepsilon_2 r} + U_0, & r > R. \end{cases} \tag{27}$$

Transformation of the external potential in the case of bulk-type doping compared with the surface-type leads to a significant change in the structure of the electronic shells of the system, their filling order and, consequently, the distribution of electron density in the bulk of the

nanocrystal. The calculations show that the order of shell filling in bulk-doped systems both in the Hartree–Fock approximation and using the local exchange potential (6) should be similar to this order for delocalized electrons in clusters of alkali metal atoms within the jellium model [6, 9, 46, 49, 50], when delocalized conduction electrons move in the field of the effective potential of a uniformly charged ion core. Thus, the electronic structure of the ground state of a bulk-doped nanocrystal containing 124 electrons is written as follows:

$$1s^2 2p^6 3d^{10} 2s^2 4f^{14} 3p^6 5g^{18} 4d^{10} 6h^{22} 3s^2 7i^{26} 4p^6.$$

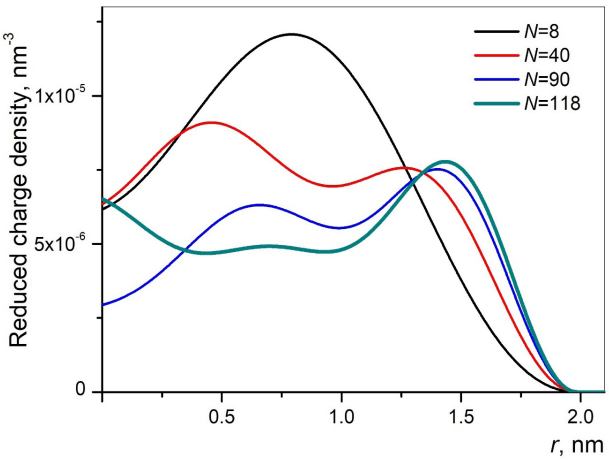

Fig. 7. Reduced radial distributions of electron density $\rho_e(r)/N$ in bulk-doped CdSe nanocrystals with a different number of electrons N

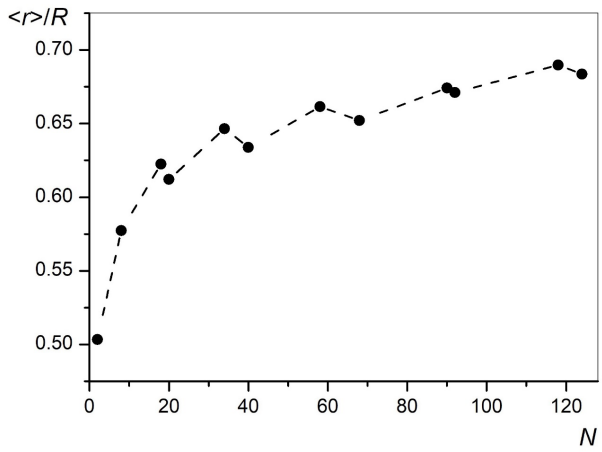

Fig. 8. Ratio of average radius of electronic system to radius of nanocrystal $\langle r\rangle/R$ as function of system particle number

In other words, unlike the situation with surface-type doping discussed in the previous section, as shells are filled, orbitals whose radial wave functions $P_{nl}(r)$ have no roots alternate with orbitals whose wave functions have roots, which, in turn, leads to a more uniform distribution of electron density $\rho_e(r)$ over the bulk of the system (Fig. 7). Fig. 8 shows a noteworthy non-monotonic dependence of the average radius of the electronic system on the number of particles. The reason why steps appear, accompanied by a slow increase in $\langle r\rangle$, is that the filled shells alternately have radial wave functions $P_{nl}(r)$ with no roots, characterized by greater average radii, and wave functions with roots (this was not observed in the case of surface-doped systems).

As in the case of surface doping, the resonance mode dominates in the spectrum of dipole excitations of bulk-doped nanocrystals; its frequency significantly shifted relative to the positions of the frequencies of single-particle transitions.

Fig. 9 shows the distributions of oscillator strengths in the CdSe crystal with 90 electrons ($N = 90$) and the ground state configuration

$$1s^2 2p^6 3d^{10} 2s^2 4f^{14} 3p^6 5g^{18} 4d^{10} 6h^{22}$$

in the vicinity of dipole resonance, calculated in the random phase approximation both taking into account the nonlocal exchange interaction (RPAE) and the local exchange potential (15) (RPAX). It should be noted that unlike surface doping, in the case of bulk doping, electrons under dipole resonance move in the direction normal to the system surface with minor deviations in the distribution of electron density relative to its ground state. On the other hand, oscillations of the electronic system under surface-type doping have a compressive nature, with significant variation in the charge density occurring during motion [27]. As established above, the reason for this is that only angular (rotational) degrees of freedom participate in excitation of the collective mode under surface-type doping.

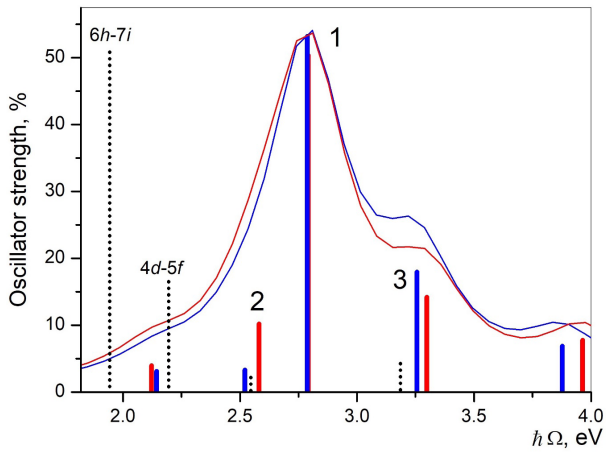

Fig. 9. Energy distributions of oscillator strengths in the vicinity of dipole resonance in the spectrum of bulk-doped CdSe nanocrystal ($N = 90$) obtained in different approximations: RPAE and RPAX (vertical red and blue segments, respectively), single-particle Hartree–Fock approximation (vertical black dotted lines).
The spectral lines are numbered: $k = 1, 2, 3$

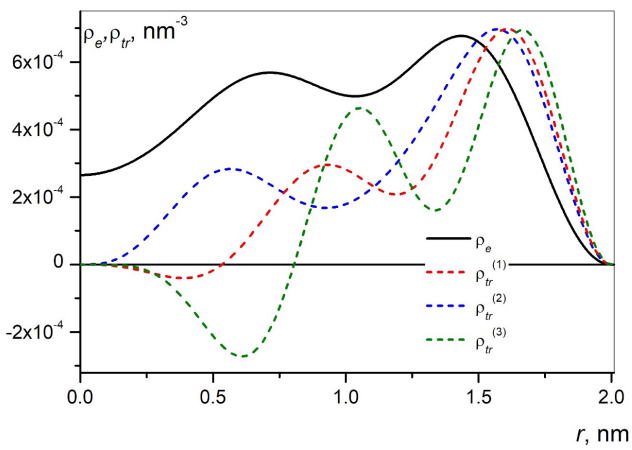

Fig. 10. Radial distributions of electron density $\rho_e(r)$ and transition density $\rho_{tr}^{(k)}(r)$ for spectral lines with $k = 1, 2, 3$ (see Fig. 9)

The motion of electrons in the direction normal to the system surface in the case of bulk doping is due to the fact that an effective restoring force acting on delocalized electrons arises in the parabolic potential generated by the bulk distribution of the positive charge in the nanocrystal.

Within the adiabatic approximation [24, 25], such collective excitation is identical in nature to the surface plasmon in the spectra of metal clusters [6, 9, 46] and can be described as harmonic oscillations in the center of mass of an electron cloud in the parabolic potential of a positively charged core. At the same time (see Fig. 9), pronounced fragmentation is observed in the resonance line due to the interaction of the harmonic mode with single-particle excitations. In contrast with the situation discussed in the previous section, a difference appeared in the position of the lateral maxima, associated with different exchange potentials, preserving an almost unchanged position of the central peak and its oscillator strength. This result confirms the link between the fragmentation of the resonance line and the interparticle interaction involving the exchange component.

Fig. 10 shows the radial distributions of electron density of the ground state $\rho_e(r)$ and the density of dipole transitions for the spectral lines numbered in Fig. 9. Importantly, the transition density dramatically differs from zero over the entire bulk of the system for all three spectral lines, including the main one numbered 1. This means that at least several particle–vacancy pairs participate in the formation of collective modes (8) and the two-level model (20) is no longer applicable.

The table gives the values of the forward-in-time and backward-in-time amplitudes for the main single-particle transitions that contribute to the corresponding lines in the spectrum of excited states in a cadmium selenide nanocrystal with the number of electrons $N = 90$, shown in Fig. 9. As can be seen from the data in the table, all three dipole perturbations (including the main resonance line 1 with an energy of $\hbar\Omega = 2.8$ eV and an oscillator strength of approximately 52% of the sum rule) are linear combinations (8), where the main contribution is made by two single-particle transitions: $6h \to 7i$ and $4d \to 5f$. The influence of other particle–vacancy pairs turned out to be insignificant. Judging by the amplitude ratios $-Y/X \sim 1$, correlations in the ground states play a significant role in all cases, so we can conclude that all three lines can be regarded as the result of fragmentation of one harmonic mode.

Table

Calculated amplitudes of the main single-particle transitions contributing to spectrum of excited states in CdSe nanocrystal (see Fig. 9)

Spectral line	Amplitudes, arb. units, or their ratios for transition					
	$6h \to 7i$			$4d \to 5f$		
	X	$-Y$	$-Y/X$	X	$-Y$	$-Y/X$
1	0.60	0.12	0.20	0.54	0.07	0.13
2	0.36	0.05	0.14	0.44	0.04	0.09
3	0.22	0.05	0.23	0.15	0.03	0.20

Notations: X, Y are the forward-in-time and backward-in-time amplitudes, respectively. Note. The number of electrons in the electron shell was assumed to be $N = 90$.

Fig. 11,*a* shows the $\hbar\Omega_{\mathrm{RPAE}}$ dependences for the energy of the resonance mode on the number of delocalized electrons, calculated in the random phase approximation with a full basis of single-particle excitations, as well as the computational results obtained within the two-level model for transitions with the maximum oscillator strength $\Omega_{2\times2}$ and the energy of the corresponding single-particle transitions Δ depending on the number of electrons in bulk-doped CdSe nanocrystals. In contrast to the situation with surface-type doping, where, according to the data presented in Fig. 5, the results obtained by the two-level model and the calculations taking into account the full basis virtually coincided, there is a significant discrepancy between these approaches for any number of electrons in the system. This confirms the significant influence

of correlations between single-particle channels on the formation of a collective excited state (8). This influence is also confirmed by the observation that the frequency Ω_{RPAE} is increased by almost two times compared with the frequency of the single-particle transition Δ, while the amplitude ratio $-Y/X$ for the main dipole transitions is higher by more than two times (compared with the results in Fig. 5,*a*). Recall that this ratio serves as an indicator of correlations in the ground state.

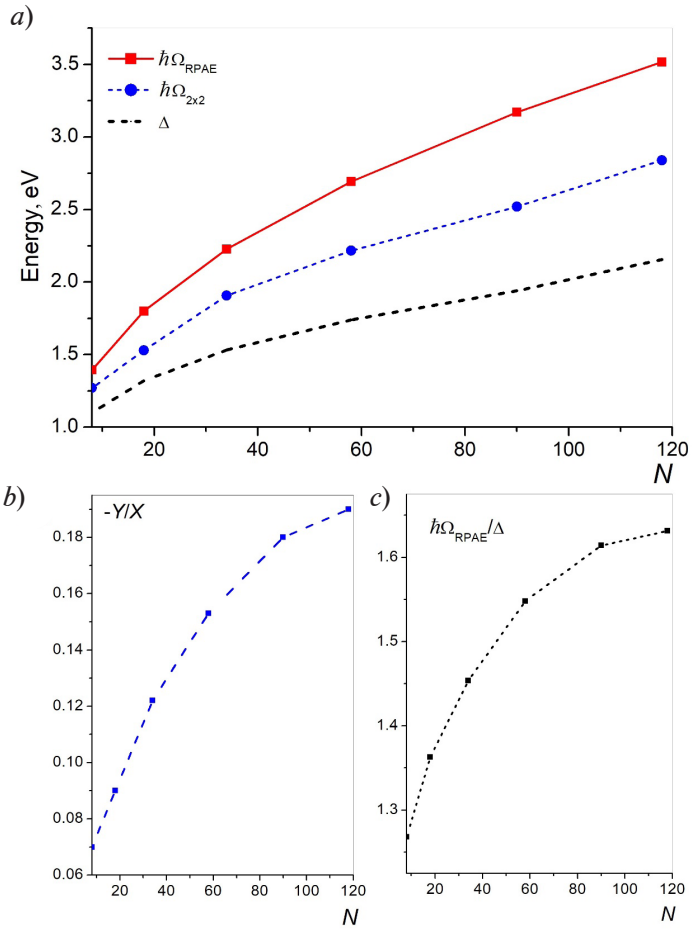

Fig. 11. Main parameters of resonant excited state in bulk-doped CdSe nanocrystal as function of number of electrons N: dipole resonance frequencies Ω obtained in different approximations (*a*); amplitude ratios $-Y/X$ (*b*) and ratios $\hbar\Omega_{RPAE}/\Delta$ (*c*). RPAE approximations, two-level model (2 × 2) and one-particle approximation (Δ) were used (Fig. 11,*a*)

Thus, the collective dipole mode in CdSe nanocrystals with bulk-type doping exhibits all the properties of a correlated multiparticle excited state. Therefore, it can be described as a surface plasmon resonance, even though the condition $X \simeq -Y \simeq 1$ is not satisfied for the considered case when $R = 2$ nm at $N \lesssim 10^2$.

As in the case of surface doping, the collective resonance mode increasingly approaches the classical plasmon in its properties with an increase in the geometric dimensions of the bulk-doped nanocrystal. Fig. 12,*a* shows the dependences for the energy of the resonant excited state $\hbar\Omega_{RPAE}$ and the differences of single-particle energy levels Δ for the single-particle transition $6h \to 7i$ (HOMO → LUMO) on the radius R in a nanocrystal containing $N = 90$ electrons for the resonance mode corresponding to line 1 in Fig. 9,*a*. Fig. 12,*a* also shows the analytical radial dependence of the classical frequency of plasma oscillations Ω_{cl} for a conducting sphere in a dielectric environment; the graph is plotted by the formula [12]:

$$\Omega_{cl} = \sqrt{\frac{3e^2 N}{m\left(\varepsilon_1 + 2\varepsilon_2\right) R^3}}. \tag{28}$$

As seen from this graph, there is still a noticeable discrepancy between the frequency of the dipole resonance obtained by quantum mechanical calculations and by the classical estimate at $R = 2$ nm. However, its magnitude decreases rapidly, a transition from the quantum regime of plasma oscillations to the classical one can be assumed to be already made at $R \gtrsim 4$ nm, when the influence of interparticle interaction in the electronic system prevails over the effects of size quantization, and the ground state in this case is a highly correlated system. This is also evidenced by the dependences presented in Fig. 12,*b* and *c* for the ratios of energies and amplitudes for the electronic transition making the main contribution to the sum (8).

Thus, we can conclude that the conditions for the transition of collective dipole excitation from the quantum regime to the classical one largely depend not only on the geometric dimensions of the nanocrystal and the number of free charge carriers, but also on the doping type; in the case of bulk doping, the transition is observed at relatively smaller values of the system radius.

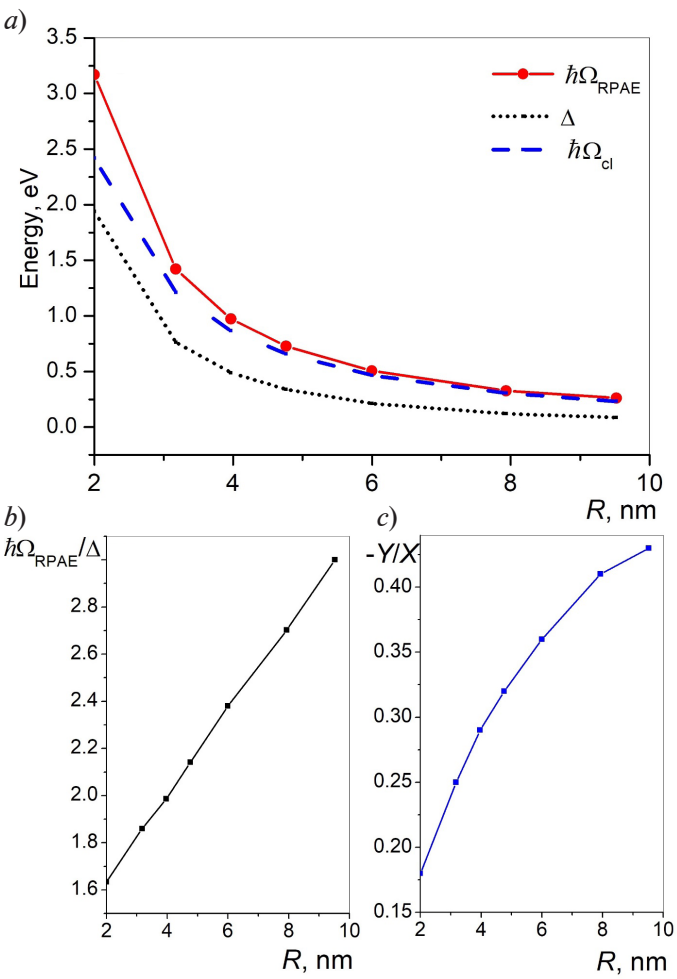

Fig. 12. Radial dependences for main parameters of the resonant excited state in bulk-doped CdSe nanocrystal ($N = 90$): dipole resonance energies $\hbar\Omega$ according to different models (*a*), as well as $\hbar\Omega_{\mathrm{RPAE}}/\Delta$ (*b*) and amplitude $-Y/X$ (*c*) ratios. RPAE and single-particle (Δ) approximations are used; the figure also shows the corresponding values of the classical plasmon resonance frequency Ω_{cl} (see Fig. 12,*a*)

Conclusion

The paper theoretically investigated the optical properties of semiconductor nanocrystals with different types of doping. We considered cadmium selenide (CdSe) nanocrystals containing different numbers of delocalized charge carriers. The interaction processes of electrons with each other and with an external electromagnetic field were described using a theoretical approach based on the Hartree–Fock approximation and the random phase approximation taking into account exchange interactions (RPAX). For comparison, the results are also presented for calculations in the local density approximation with the Dirac–Slater potential.

It was found that a dominant resonance line is observed in the optical spectra of nanocrystals obtained using both approaches; its position practically does not depend on the method chosen for describing the exchange interaction between electrons for all the given particle numbers in the system. The excited state corresponding to the resonant dipole transition has a collective nature in both surface and bulk doping mechanisms, as evidenced by the significant contribution of multiparticle correlations to the generation of the wave function.

In the case of surface doping, the electronic structure of the ground state has a largely non-uniform distribution of charge density, when the maximum of the distribution function is shifted to the surface of the nanocrystal, which, in turn, determines the nature of the oscillations of the dipole resonance mode.

Analyzing the distribution of oscillator strengths in the vicinity of the resonance line, as well as the corresponding dipole amplitudes and the density distribution of dipole transitions, we found that the oscillations of electron density in the collective mode are rotational in nature, with only angular degrees of freedom excited, while the motion in the radial direction is practically frozen, since there is no restoring force (directed along the normal to the surface) acting on charge carriers in the external potential.

This conclusion is further corroborated by the results obtained within the two-level model that describes the dipole resonance under surface doping as a correlated excited state composed of particle–vacancy pairs including only transitions between HOMO and LUMO orbitals for all possible angular momentum projections. Calculations indicate that the resonance frequency values obtained taking into account all possible single-particle transitions and within the two-level model turn out to be nearly identical for all CdSe nanocrystals considered containing from 8 to 162 delocalized electrons. Since the relationship between the rotational mode and single-particle excitations involving radial degrees of freedom is weak, the resonance line is virtually not fragmented. It was also found for relatively small system sizes, when the radius of the nanocrystal turns out to be less than the effective Bohr radius, that the resonance mode still does not make a transition from size quantization mode to classical plasmon oscillations with an increase in the number of electrons, even despite the increasing contribution of interelectron Coulomb interaction. The tendency towards transition to classical mode is manifested only when the radius of the system is increased to the size of the effective Bohr radius, with the rotational character of oscillatory motion preserved.

As established by the calculations, the electronic structure of the ground state turns out to be significantly different for bulk doping compared with surface-doped systems. In this case, the radial distribution of electron density over the bulk of the nanocrystal becomes more uniform, and the parabolic nature of the positively charged core induces a radially directed restoring force acting on the electrons. Therefore, the collective excited state can be described as harmonic oscillations of the electron cloud as a whole in the direction normal to the surface of the system with minor deviations in the density distribution compared with the ground state.

Thus, in the case of bulk doping, the dipole resonance can be described as a collective translational mode where, in contrast with surface doping, several single-particle dipole transitions are correlated simultaneously. This is confirmed by the fact that the results obtained by the two-level model differ significantly from those taking into account the full single-particle basis, and the difference increases as the number of particles in the system increases. In addition, the interaction of the harmonic mode with single-particle excited states leads to fragmentation of the resonance line, since the degrees of freedom of the oscillatory electronic system are not separated in this situation. Quantum effects also make the largest contributions to forming the collective mode at relatively small sizes of nanocrystals, however, the transition to the classical plasmon oscillation mode occurs at smaller radii of the system than with the surface type of doping. As a result, the

dipole oscillations of the electron cloud can be described as a plasmon mode even at sizes comparable to the effective Bohr radius. The frequency of this mode tends to the classical frequency of plasma oscillations in a spherical conductor.

Thus, it can be concluded that the optical spectrum of semiconductor nanocrystals is dominated by a resonant dipole mode regardless of the method used for doping. The nature of the mode in question is determined by the size of the system itself, as well as the type and degree of doping, i.e., the number of delocalized charge carriers. As the geometric dimensions of the electronic system (primarily) and the number of its electrons increase, a power-law transition of the collective excited state occurs from the size quantization mode to classical plasmon oscillatory motion of this system. In this case, the nature of motion depending on the number of excited degrees of freedom is determined by the electronic structure of the ground state. In turn, the electronic structure of this state is formed in accordance with the distribution of the positive charge potential, i.e., with the doping type.

REFERENCES

1. **Klimov V. V.,** Nanoplasmonics, Jenny Stanford Publishing, New York, 2014.
2. **Bozhevolniy S. I.**, **Martin-Moreno L., Garcia-Vidal F.** (Eds.), Quantum plasmonics (Springer Series in Solid-State Sciences. Vol. 185), Springer International Publishing, Cham, Switzerland, 2017.
3. **Enoch S., Bonod N.,** Plasmonics: From basics to advanced topics. (Springer Series in Optical Sciences. Vol. 167), Springer-Verlag, Heidelberg, Berlin, 2012.
4. **Tame M. S., McEnery K. R., Özdemir Ş. K., et al.,** Quantum plasmonics, Nat. Phys. 9 (June) (2013) 329–340.
5. **Scholl J. A., Koh A. L., Dionne J. A.,** Quantum plasmon resonances of individual metallic nanoparticles, Nature. 483 (22 March) (2012) 421–427.
6. **Brack M.,** The physics of simple metal clusters: Self-consistent jellium model and semiclassical approaches, Rev. Mod. Phys. 65 (3) (1993) 677–732.
7. **Harb M., Rabilloud F., Simon D., et al.,** Optical absorption of small silver clusters: Ag_n (n = 4–22), J. Chem. Phys. 129 (19) (2008) 194108.
8. **Xuan F., Guet C.,** Core-polarization-corrected random-phase approximation with exchange for dipole surface plasmons in silver clusters, Phys. Rev. A. 94 (4) (2016) 043415.
9. **Kreibig U., Vollmer M.,** Optical properties of metallic clusters (Springer Series in Materials Science. Vol. 65), Springer-Verlag, Heidelberg, Berlin, 1995.
10. **Kreibig U., Zacharias P.,** Surface plasma resonances in small silver and gold particles, Z. Physik. 231 (2) (1970) 128–143.
11. **Kriegel I., Scotognella F., Manna L.,** Plasmonic doped semiconductor nanocrystals: Properties, fabrication, applications and perspectives, Phys. Rep. 674 (28 February) (2017) 1–52.
12. **Klimov V. I.,** Nanocrystal quantum dots, Second edition, CRC Press, Boca Raton, Florida, USA, 2010.
13. **Monreal R. C., Antosiewicz T. J., Appel S. P.,** Competition between surface screening and size quantization for surface plasmons in nanoparticles, New J. Phys. 15 (8) (2013) 083044.
14. **Scotognella F., Della Valle G., Kandada A. R. S., et al.,** Plasmonics in heavily-doped semiconductor nanocrystals, Eur. Phys. J. B. 86 (4) (2013) 154.
15. **Xie Y., Carbone L., Nobile C., et al.** Metallic-like stoichiometric copper sulfide nanocrystals: Phase- and shape-selective synthesis, near-infrared surface plasmon resonance properties, and their modeling, ACS Nano. 7 (8) (2013) 7352–7369.
15. **Xie Y., Carbone L., Nobile C., et al.** Metallic-like stoichiometric copper sulfide nanocrystals: Phase- and shape-selective synthesis, near-infrared surface plasmon resonance properties, and their modeling // ACS Nano (The American Chemical Society). 2013. Vol. 7. No. 8. Pp. 7352–7369.
16. **Routzahn A. L., White S. L., Fong L.-K., Jain P. K.,** Plasmonics with doped quantum dots, Isr. J. Chem. 52 (11–12) (2012) 983–991.
17. **Luther J. M., Jain P. K., Ewers T., Alivisators A. P.,** Localized surface plasmon resonances arising from free carriers in doped quantum dots, Nat. Mater. 10 (May) (2011) 361–366.
18. **Faucheaux J. A., Stanton A. L. D., Jain P. K.,** Plasmon resonances of semiconductor nanocrystals: Physical principles and new opportunities, J. Phys. Chem. Lett. 5 (6) (2014) 976–985.

19. **Zhang H., Kulkarni V., Prodan E., et al.,** Theory of quantum plasmon resonances in doped semiconductor nanocrystals, J. Phys. Chem. C. 118 (29) (2014) 16035–16042.

20. **Lounis S. D., Runnerstrom E. L., Bergerud A., et al.,** Influence of dopant distribution on the plasmonic properties of indium tin oxide nanocrystals, J. Am. Chem. Soc. 136 (19) (2014) 7110–7116.

21. **Schimpf A. M., Thakkar N., Gunthardt C. E., et al.,** Charge-tunable quantum plasmons in colloidal semiconductor nanocrystals, ACS Nano. 8 (1) (2014) 1065–1072.

22. **Schimpf A. M., Gunthardt C. E., Rinehart J. D., et al.,** Controlling carrier densities in photochemically reduced colloidal ZnO nanocrystals, J. Am. Chem. Soc. 135 (44) (2013) 16569–16577.

23. **Liu X., Swihart M. T.,** Heavily-doped colloidal semiconductor and metal oxide nanocrystals, an emerging new class of plasmonic nanomaterials, Chem. Soc. Rev. 43 (11) (2014) 3908–3920.

24. **Gerchikov L. G., Guet C., Ipatov A. N.,** Multiple plasmons and anharmonic effects in small metallic clusters, Phys. Rev. A. 66 (5) (2002) 053202.

25. **Ipatov A. N., Gerchikov L. G., Guet C.,** Resonant photoabsorption of metallic clusters in a strong laser field, Comput. Mater. Sci. 35 (3) (2006) 347–353.

26. **Ipatov A. N., Gerchikov L. G., Guet C.,** Plasmon resonance in photoabsorption of colloidal highly doped ZnO nanocrystals, Nanoscale Res. Lett. 13 (1) (2018) 297.

27. **Ipatov A. N., Gerchikov L. G.,** Rotational dipole plasmon mode in nanoscale semiconductor particles, J. Exp. Theor. Phys., 132 (6) (2021) 922–940.

28. **Yabana K., Bertsch G. F.,** Electronic structure of C_{60} in a spherical basis, Phys. Scr. 48 (5) (1993) 633–637.

29. **Ju N., Bulgac A., Keller J. W.,** Excitation of collective plasmon states in fullerenes, Phys. Rev. B. 48 (12) (1993) 9071–9079.

30. **Ostling P., Apell P., Rosén A.,** Theory for collective resonances of the C_{60} molecule, Europhys. Lett. 21 (5) (1993) 539–544.

31. **Madjet M., Guet G., Johnson W. R.,** Comparative study of exchange-correlation effects on electron and optical properties of alkali-metal clusters, Phys. Rev. A. 51 (2) (1995) 1327–1339.

32. **Mukherjee D.,** Applied many-body methods in spectroscopy and electronic structure, Springer, NY, 1992.

33. **Serra Ll., Garcias F., Navarro J., et al.,** Electronic surface excitations of cavities in metals, Phys. Rev. B. 46 (15) (1992) 9369–9379.

34. **Varshalovich D. A., Moskalev A. N., Khersonskii V. K.,** Quantum theory of angular momentum, World Scientific, Singapore, 1988.

35. **Ipatov A. N., Gerchikov L. G.** Many-particle correlations in microscopic electron-hole droplets, J. Phys. B. – At. Mol. Opt. 47 (18) (2014) 185101.

36. **Gerchikov L. G., Ipatov A. N.,** Collective excitations in the optical spectra of nanoscale exciton and electron-positron droplets, J. Exp. Theor. Phys. 119 (5) (2014) 891–901.

37. **Amusia M. Y., Chernysheva L.V.,** Computation of atomic processes. A handbook for the atom programs, CRC Press, Boca Raton, 1997.

38. **Dreizler R. M., Gross E. K. U.,** Density functional theory: An approach to the quantum many-body problem, Springer, Berlin, 1990.

39. **Landau L. D., Lifshitz E. M.,** Quantum mechanics. Non-relativistic theory. (Course of theoretical physics. Vol. 3), Pergamon Press, Oxford, London, New York, Paris, 1965.

40. **Ipatov A. N., Gerchikov L. G.,** Stability and properties of finite Fermi-systems with different masses, J. Exp. Theor. Phys. 118 (1) (2014) 93–103.

41. **Sobel'man I. I.**, Introduction to the theory of atomic spectra (International Series in Natural Philosophy, Vol. 40), Pergamon Press, Oxford, UK, 1972.

42. **Banin U., Cao Y., Katz D., Millo O.,** Identication of atomic-like electronic states in indium arsenide nanocrystal quantum dots, Nature. 400 (5 August) (1999) 542–544.

43. **Kouwenhoven L. P., Austing D. G., Tarucha S.,** Few electron quantum dots, Rep. Progr. Phys. 64 (6) (2001) 701–736.

44. **Bimberg D., Grundmann M., Ledentsov N. N.,** Quantum dot heterostructures, John Wiley & Sons, Chichester, 1999.

45. **Shelawati T., Nurisya M. S., Kar Tim C., Mazliana A. K.,** Effects of step-potential on confinement strength of strain-induced type-I core–shell quantum dots, Superlattices Microstruct. 131 (July) (2019) 95–103.

46. **Guet C., Johnson W. R.,** Dipole excitations of closed-shell alkali-metal clusters, Phys. Rev. B. 45 (19) (1992) 11283–11287.

47. **Ekardt W.,** Size-dependent photoabsorption and photoemission of small metal particles, Phys. Rev. B. 31 (10) (1985) 6360–6370.

48. **Beck D. E.,** Self-consistent calculation of the eigen frequencies for the electronic excitations in small jellium spheres, Phys. Rev. B. 35 (14) (1987) 7325–7333.

49. **Haberland H.** Clusters of atoms and molecules. Theory, experiment, and clusters of atoms (Springer Series in Chemical Physics. Chemical, Vol. 52), Springer, Berlin, Heidelberg, 1994.

50. **De Heer W. A.,** The physics of simple metal clusters: Experimental aspects and simple models, Rev. Mod. Phys. 65 (3) (1993) 611–676.

СПИСОК ЛИТЕРАТУРЫ

1. **Климов В. В.** Наноплазмоника. М.: Физматлит, 2009. 480 с.

2. **Bozhevolniy S. I., Martin-Moreno L., Garcia-Vidal F.** (Eds.) Quantum plasmonics. (Springer Series in Solid-State Sciences. Vol. 185). Cham, Switzerland: Springer International Publishing, 2017. 327 p.

3. **Enoch S., Bonod N.** Plasmonics: From basics to advanced topics. (Springer Series in Optical Sciences. Vol. 167). Heidelberg, Berlin: Springer-Verlag, 2012. 321 p.

4. **Tame M. S., McEnery K. R.,** Özdemir **Ş. K., Lee J., Maier S. A., Kim M. S.** Quantum plasmonics // Nature Physics. 2013. Vol. 9. June. Pp. 329–340.

5. **Scholl J. A., Koh A. L., Dionne J. A.** Quantum plasmon resonances of individual metallic nanoparticles // Nature. 2012. Vol. 483. 22 March. Pp. 421–427.

6. **Brack M.** The physics of simple metal clusters: Self-consistent jellium model and semiclassical approaches // Reviews of Modern Physics. 1993. Vol. 65. No. 3. Pp. 677–732.

7. **Harb M., Rabilloud F., Simon D., Rydlo A., Lecoultre S., Conus F., Rodrigues V., Félix C.** Optical absorption of small silver clusters: Ag_n (n = 4–22) // The Journal of Chemical Physics. 2008. Vol. 129. No. 19. P. 194108.

8. **Xuan F., Guet C.** Core-polarization-corrected random-phase approximation with exchange for dipole surface plasmons in silver clusters // Physical Review A. 2016. Vol. 94. No. 4. P. 043415.

9. **Kreibig U., Vollmer M.** Optical properties of metallic clusters. (Springer Series in Materials Science. Vol. 65). Heidelberg, Berlin: Springer-Verlag, 1995. 535 p.

10. **Kreibig U., Zacharias P.** Surface plasma resonances in small silver and gold particles // Zeitschrift für Physik. 1970. Vol. 231. No. 2. Pp. 128–143.

11. **Kriegel I., Scotognella F., Manna L.** Plasmonic doped semiconductor nanocrystals: Properties, fabrication, applications and perspectives // Physics Reports. 2017. Vol. 674. 28 February. Pp. 1–52.

12. **Klimov V. I.** Nanocrystal quantum dots. Second edition. Boca Raton, Florida, USA: CRC Press, 2010. 485 p.

13. **Monreal R. C., Antosiewicz T. J., Appel S. P.** Competition between surface screening and size quantization for surface plasmons in nanoparticles // New Journal of Physics. 2013. Vol. 15. No. 8. P. 083044.

14. **Scotognella F., Della Valle G., Kandada A. R. S., Zavelani-Rossi M., Longhi S., Lanzani G., Tassone F.** Plasmonics in heavily-doped semiconductor nanocrystals // The European Physical Journal B. 2013. Vol. 86. No. 4. P. 154.

15. **Xie Y., Carbone L., Nobile C., et al.** Metallic-like stoichiometric copper sulfide nanocrystals: Phase- and shape-selective synthesis, near-infrared surface plasmon resonance properties, and their modeling // ACS Nano (The American Chemical Society). 2013. Vol. 7. No. 8. Pp. 7352–7369.

16. **Routzahn A. L., White S. L., Fong L.-K., Jain P. K.** Plasmonics with doped quantum dots // Israel Journal of Chemistry. 2012. Vol. 52. No. 11–12. Pp. 983–991.

17. **Luther J. M., Jain P. K., Ewers T., Alivisators A. P.** Localized surface plasmon resonances arising from free carriers in doped quantum dots // Nature Materials. 2011. Vol. 10. May. Pp. 361–366.

18. **Faucheaux J. A., Stanton A. L. D., Jain P. K.** Plasmon resonances of semiconductor nanocrystals: Physical principles and new opportunities // The Journal of Physical Chemistry Letters. 2014. Vol. 5. No. 6. Pp. 976–985.

19. **Zhang H., Kulkarni V., Prodan E., Nordlander P., Govorov A. O.** Theory of quantum plasmon resonances in doped semiconductor nanocrystals // The Journal of Physical Chemistry. C. 2014. Vol. 118. No. 29. Pp. 16035–16042.

20. **Lounis S. D., Runnerstrom E. L., Bergerud A., Nordlund D., Milloron D. J.** Influence of dopant distribution on the plasmonic properties of indium tin oxide nanocrystals // Journal of the American Chemical Society. 2014. Vol. 136. No. 19. Pp. 7110–7116.

21. **Schimpf A. M., Thakkar N., Gunthardt C. E., Masiello D. J., Gamelin D. R.** Charge-tunable quantum plasmons in colloidal semiconductor nanocrystals // ACS Nano (The American Chemical Society). 2014. Vol. 8. No. 1. Pp. 1065–1072.

22. **Schimpf A. M., Gunthardt C. E., Rinehart J. D., Mayer J. M., Gamelin D. R.** Controlling carrier densities in photochemically reduced colloidal ZnO nanocrystals // Journal of the American Chemical Society. 2013. Vol. 135. No. 44. Pp. 16569–16577.

23. **Liu X., Swihart M. T.** Heavily-doped colloidal semiconductor and metal oxide nanocrystals, an emerging new class of plasmonic nanomaterials // Chemical Society Reviews. 2014. Vol. 43. No. 11. Pp. 3908–3920.

24. **Gerchikov L. G., Guet C., Ipatov A. N.** Multiple plasmons and anharmonic effects in small metallic clusters // Physical Review A. 2002. Vol. 66. No. 5. P. 053202.

25. **Ipatov A. N., Gerchikov L. G., Guet C.** Resonant photoabsorption of metallic clusters in a strong laser field // Computational Materials Science. 2006. Vol. 35. No. 3. Pp. 347–353.

26. **Ipatov A. N., Gerchikov L. G., Guet C.** Plasmon resonance in photoabsorption of colloidal highly doped ZnO nanocrystals // Nanoscale Research Letters. 2018. Vol. 13. No. 1. P. 297.

27. **Ипатов А. Н., Герчиков Л. Г.** Вращательная дипольная плазмонная мода в наноразмерных полупроводниковых частицах // Журнал экспериментальной и теоретической физики. 2021. Т. 159. № 6. С. 1047–1069.

28. **Yabana K., Bertsch G. F.** Electronic structure of C_{60} in a spherical basis // Physica Scripta. 1993. Vol. 48. No. 5. Pp. 633 –637.

29. **Ju N., Bulgac A., Keller J. W.** Excitation of collective plasmon states in fullerenes // Physical Review B. 1993. Vol. 48. No. 12. Pp. 9071–9079.

30. **Ostling P., Apell P., Rosén A.** Theory for collective resonances of the C_{60} molecule // Europhysics Letters. 1993. Vol. 21. No. 5. Pp. 539–544.

31. **Madjet M., Guet G., Johnson W. R.** Comparative study of exchange-correlation effects on electron and optical properties of alkali-metal clusters // Physical Review A. 1995. Vol. 51. No. 2. Pp. 1327–1339.

32. **Mukherjee D.** Applied many-body methods in spectroscopy and electronic structure. New York, USA: Springer, 1992. 299 p.

33. **Serra Ll., Garcias F., Navarro J., Barberán N., Barranco M., Pi M.** Electronic surface excitations of cavities in metals // Physical Review B. 1992. Vol. 46. No. 15. Pp. 9369–9379.

34. **Варшалович Д. А., Москалев А. Н., Херсонский В. К.** Квантовая теория углового момента. Ленинград: Наука, 1975. 439 с.

35. **Ipatov A. N., Gerchikov L. G.** Many-particle correlations in microscopic electron-hole droplets // Journal of Physics B: Atomic, Molecular and Optical Physics. 2014. Vol. 47. No. 18. P. 185101.

36. **Герчиков Л. Г., Ипатов А. Н.** Коллективные возбуждения в оптических спектрах наноразмерных экситонных и электрон-позитронных капель // Журнал экспериментальной и теоретической физики. 2014. Т. 5 № .146. С. 1025–1014.

37. **Амусья М. Я., Чернышева Л. Я.,** Яржемский **В. Г.** Поглощение фотонов, рассеяние электронов, распад вакансий. Атомные данные. СПб.: Наука, 2010. 314 с.

38. **Dreizler R. M., Gross E. K. U.** Density functional theory: An approach to the quantum many-body problem. Berlin: Springer, 1990. 302 p.

39. **Ландау Л. Д., Лифшиц Е. М.** Теоретическая физика. В 10 тт. Т. 3. Квантовая механика (нерелятивистская теория). -4е изд., испр. М.; Наука. Гл. ред. физ.-мат. лит-ры, 1989. 768 с.

40. **Ипатов А. Н., Герчиков Л. Г.** Стабильность и свойства конечных Ферми-систем, содержащих частицы разной массы // Журнал экспериментальной и теоретической физики. 2014. Т. 1 № .145. С. 119–108.

41. **Собельман И. И.** Введение в теорию атомных спектров. М.: Наука. Главная редакция физ.-мат. лит-ры, 1977. 320 с.

42. **Banin U., Cao Y., Katz D., Millo O.** Identication of atomic-like electronic states in indium arsenide nanocrystal quantum dots // Nature. 1999. Vol. 400. 5 August. Pp. 542–544.

43. **Kouwenhoven L. P., Austing D. G., Tarucha S.** Few electron quantum dots// Reports on Progress in Physics. 2001. Vol. 64. No. 6. Pp. 701–736.

44. **Bimberg D., Grundmann M., Ledentsov N. N.** Quantum dot heterostructures. Chichester: John Wiley & Sons, 1999. 338 p.

45. **Shelawati T., Nurisya M. S., Kar Tim C., Mazliana A. K.** Effects of step-potential on confinement strength of strain-induced type-I core–shell quantum dots // Superlattices and Microstructures. 2019. Vol. 131. July. Pp. 95–103.

46. **Guet C., Johnson W. R.** Dipole excitations of closed-shell alkali-metal clusters // Physical Review B. 1992. Vol. 45. No. 19. Pp. 11283–11287.

47. **Ekardt W.** Size-dependent photoabsorption and photoemission of small metal particles // Physical Review B. 1985. Vol. 31. No. 10. Pp. 6360–6370.

48. **Beck D. E.** Self-consistent calculation of the eigen frequencies for the electronic excitations in small jellium spheres // Physical Review B. 1987. Vol. 35. No. 14. Pp. 7325–7333.

49. **Haberland H.** Clusters of atoms and molecules. Theory, experiment, and clusters of atoms (Springer Series in Chemical Physics. Chemical, Vol. 52), Berlin, Heidelberg: Springer, 1994. 422 p.

50. **De Heer W. A.** The physics of simple metal clusters: Experimental aspects and simple models // Reviews of Modern Physics. 1993. Vol. 65. No. 3. Pp. 611–676.

THE AUTHORS

IPATOV Andrei N.
Peter the Great St. Petersburg Polytechnic University;
Alferov University of RAS
29 Politechnicheskaya St., St. Petersburg, 195251, Russia
andrei_ipatov@mail.ru

KUPRIIANOV Genrikh A.
Peter the Great St. Petersburg Polytechnic University
29 Politechnicheskaya St., St. Petersburg, 195251, Russia
henryweis3@gmail.com

СВЕДЕНИЯ ОБ АВТОРАХ

ИПАТОВ Андрей Николаевич – *доктор физико-математических наук, профессор кафедры физики Санкт-Петербургского политехнического университета Петра Великого и профессор кафедры физики и технологии наногетероструктур Санкт-Петербургского академического университета им. Ж. И. Алфёрова РАН.*
195251, Россия, г. Санкт-Петербург, Политехническая ул., 29
andrei_ipatov@mail.ru

КУПРИЯНОВ Генрих Александрович – *ассистент кафедры физики Санкт-Петербургского политехнического университета Петра Великого.*
195251, Россия, г. Санкт-Петербург, Политехническая ул., 29
henryweis3@gmail.com

Received 31.03.2023. Approved after reviewing 21.04.2023. Accepted 21.04.2023.
Статья поступила в редакцию 31.03.2023. Одобрена после рецензирования 21.04.2023. Принята 21.04.2023.

PHYSICAL ELECTRONICS

Original article
DOI: https://doi.org/10.18721/JPM.16204

THE EFFICIENCY OF A FOCUSING SYSTEM BASED ON THIN DIAPHRAGMS IN THE ION SOURCE WITH A CORONA DISCHARGE

T. V. Pomozov✉, *M. Z. Muradymov*, *E. A. Tkach*

Institute for Analytical Instrumentation of RAS, St. Petersburg, Russia

✉ tim-kor@mail.ru

Abstract. In this work, a charged particle beam transport in an ion source with a corona discharge, the source being equipped with a focusing system based on thin diaphragms in the standing gas and at atmospheric pressure, has been studied experimentally. The efficiency of the ion beam transportation through the focusing system was shown to depend on the distance between the corona needle and the diaphragm system, on the potential difference between the diaphragms of the focusing system and on the value of the corona discharge current. The results of comparing the efficiency of the ion beam transport in the ion source with using the focusing system and without it are presented. The use of the focusing system allowed to increase several times the current entering the collector through the diaphragm of the smallest diameter, and to raise the current entering the plane of this diaphragm by an order of magnitude.

Keywords: ion source, mass spectrometer, corona discharge, focusing system, ion transport

Funding: The research was partially funded within the Research Work 0074-2019-0009 being a part of The State Assignment 075-00780-19-02 of the Ministry of Science and Higher Education of the Russian Federation to the Institute for Analytical Instrumentation of Russian Academy of Sciences.

Citation: Pomozov T. V., Muradymov M. Z., Tkach E. A., The efficiency of a focusing system based on thin diaphragms in the ion source with a corona discharge, St. Petersburg State Polytechnical University Journal. Physics and Mathematics. 16 (2) (2023) 52–60. DOI: https://doi.org/10.18721/JPM.12604

This is an open access article under the CC BY-NC 4.0 license (https://creativecommons.org/licenses/by-nc/4.0/)

Научная статья
УДК 621.384.8
DOI: https://doi.org/10.18721/JPM.16204

ЭФФЕКТИВНОСТЬ ФОКУСИРУЮЩЕЙ СИСТЕМЫ НА ОСНОВЕ ТОНКИХ ДИАФРАГМ В ИОННОМ ИСТОЧНИКЕ С КОРОННЫМ РАЗРЯДОМ

Т. В. Помозов✉, *М. З. Мурадымов*, *Е. А. Ткач*

Институт аналитического приборостроения РАН, Санкт-Петербург, Россия

✉ tim-kor@mail.ru

Аннотация. Проведено экспериментальное исследование транспортировки пучка заряженных частиц в ионном источнике с коронным разрядом с фокусирующей системой на основе тонких диафрагм в стоячем газе при атмосферном давлении. Показано, что

© Pomozov T. V., Muradymov M. Z., Tkach E. A., 2023. Published by Peter the Great St. Petersburg Polytechnic University.

эффективность транспортировки ионного пучка через систему фокусировки зависит от расстояния от коронирующего острия до системы диафрагм, разности потенциалов между диафрагмами фокусирующей системы и величины тока коронного разряда. Представлены результаты сравнения эффективности транспортировки ионного пучка в ионном источнике с фокусирующей системой и без нее. Использование фокусирующей системы позволяет в несколько раз увеличить ток, приходящий на коллектор через диафрагму наименьшего диаметра, и повысить на порядок ток, приходящий на плоскость этой диафрагмы.

Ключевые слова: ионный источник, масс-спектрометр, коронный разряд, фокусирующая система, транспортировка ионов

Финансирование. Работа выполнена частично в рамках НИОКТР FFZM-2022-0009, входящей в состав Государственного задания Министерства науки и высшего образования Российской Федерации № 075-00761-22-00 для ИАП РАН.

Ссылка для цитирования: Помозов Т. В., Мурадымов М. З., Ткач Е. А. Эффективность фокусирующей системы на основе тонких диафрагм в ионном источнике с коронным разрядом // Научно-технические ведомости СПбГПУ. Физико-математические науки. 2023. Т. 16. № 2. С. 52–60. DOI: https://doi.org/10.18721/ JPM.16204

Статья открытого доступа, распространяемая по лицензии CC BY-NC 4.0 (https://creativecommons.org/licenses/by-nc/4.0/)

Introduction

Atmospheric pressure ionization sources have long been widespread in mass spectrometry for solving problems of organic and bioorganic chemistry, pharmacology, proteomics, ecology, and so on [1–3].

The sensitivity of a mass spectrometer depends on the transport efficiency of the ion source with atmospheric pressure injecting ions into the high-vacuum mass analyzer through a gas interface consisting of a differential pumping system (DPS) with ion optics. While ion losses are observed at all stages of the DPS, the maximum losses of the ion beam occur during transition from the region with atmospheric pressure through the nozzle to the first stage of the DPS and can amount to two orders of magnitude or more of the total current of the ion source [4].

A promising technique reducing ion losses is to focus the ion beam onto the nozzle. Such focusing was carried out in [5] by placing a hemispherical grid electrode between the spray capillary and the nozzle. This solution had a number of drawbacks, in particular, limited transparency of the grids and distortion of the field structure due to deposition of microdrops. The ion beam in the experiments in [6–8] was focused by an additional electrode (aperture) installed in front of the nozzle; the thickness-to-diameter ratio of the aperture ranged from 1 to 5.

However, the numerical simulations of ion trajectories in electrostatic fields in dense gas indicate that focused ion beam systems based on thin apertures have the best potential in terms of focusing efficiency (the above ratio should be several tens). Theoptical setup of such a focusing system is considered in [9], proposing an electrode configuration based on thin apertures (0.1 mm thick) with decreasing opening diameters. The reason why the thinnest possible apertures were chosen is that the system has more pronounced focusing properties due to the absence of local defocusing regions in the aperture channels.

In this paper, we experimentally considered the procedure for increasing the transport efficiency of an ion beam using a focusing system based on thin apertures in a source with a corona discharge in a stagnant gas. This is intended to improve the transport efficiency by focusing the ions in an electrostatic field. The aperture of the focusing system with the smallest diameter becomes a nozzle separating the atmospheric pressure region from the first stage of the SDO in the gas interface of the mass spectrometer.

© Помозов Т. В., Мурадымов М. З., Ткач Е. А., 2023. Издатель: Санкт-Петербургский политехнический университет Петра Великого.

Ion optics of focusing system based on thin apertures in source with corona discharge

The ion optics of the experimentally investigated focusing system based on thin apertureus in a source with corona discharge source is shown in Fig. 1. The setup consists of a corona point (needle), four thin apertures (d_1–d_4) 0.1 mm thick with decreasing opening sizes and a planar electrode serving as a collector. The sizes of aperture openings, in descending order, are 4.00 mm; 2.65 mm; 1.20 mm and 0.50 mm. The distances between the thin apertures and the distance between the last aperture and the collector are 1 mm. A potential U_n is applied to the corona point to ignite the discharge, and some pulling potential U_c is applied to the collector. Aperture *4*, which has the smallest diameter, separates the region with atmospheric pressure from the first stage of the DPS and acts as the nozzle.

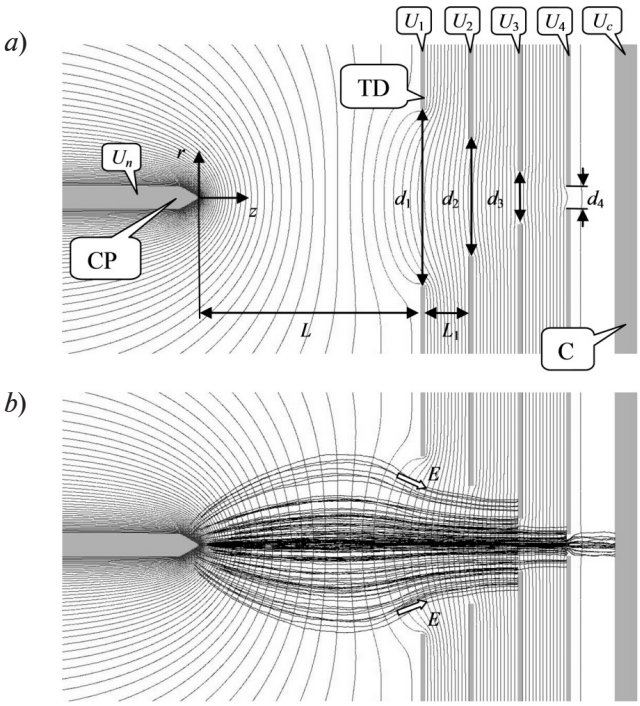

Fig. 1. Ion optics of focusing system based on thin apertures (*a*); trajectories of positively charged ions (*b*):
corona point (needle) CP, set of thin apertures TD (d_1–d_4), collector C; equipotential lines of the electrostatic field E in the plane passing through the optical axis. Geometrical and electrical parameters of the setup: L = 5 mm, L_1 = 1 mm, d_1 = 4 mm, d_2 = 2.65 mm, d_3 = 1.2 mm, d_4 = 0.5 mm, U_n = 7 kV, U_1 = 3 kV, U_2 = 2 kV, U_3 = 1 kV, U_4 = 0 V, U_c = −1 kV. The thickness of the apertures *1–4* is 0.1 mm

If the same potential difference between adjacent apertures $\Delta U < 0$ ($\Delta U = U_{i+1} - U_i$, $i = 1 - 3$) is applied for positively charged ions, the system in question has focusing properties, since the electrostatic field strength in the gaps between adjacent apertures increases due to a decrease in aperture diameters. Fig. 1 also shows the equipotential lines of the electrostatic field in a plane passing through the optical axis, as well as the trajectories of positively charged ions; the geometric and electrical parameters of the ion optical setup and their values are given in the caption.

Numerical simulation of the electrostatic field and trajectories of charged particles in a dense gas (air) under normal conditions (T = 300 K, p = 760 Torr) without taking into account the effects introduced by the space charge was carried out in the SIMION 8.0 software package [10] using statistical diffusion simulation (SDS) [11], a user program that is part of the package Positive nitrogen ions (m = 14 u) with an initial spherical spatial distribution (d = 1.5 mm) were taken as a model beam.

Notably, the focusing properties of the given ion optical setup depend on the magnitude of the potential difference ΔU applied between thin apertures: the focusing properties are enhanced with increasing ΔU, and weaken with decreasing ΔU. The computations for the ion optical setup considered indicate that the proportion of ions entering the collector is about 4.2%, and about 27% in the plane of the aperture with the smallest diameter (d_4 = 0.5 mm).

Experimental setup

Fig. 2 shows the experimental setup constructed to study the transport efficiency of the ion beam in a source with a focusing system.

The setup incorporates the ion optics of the focusing system described above, consisting of a corona point (needle) *7*, a coaxially arranged system of thin apertures *1–4* 0.1 mm thick and a collector *5*. The diameter of the opening in the first aperture (*1*) is 4 mm, 2.65 mm in the second (*2*), 1.2 mm in the third (*3*), 0.5 mm in the fourth (*4*). All the apertures are insulated from each other and from collector *5* by ceramic inserts *6* 1 mm thick. Electrodes *1–3* and *5*, *7* of the experimental setup have independent power supply from regulated highly stable high-voltage power supplies *20–24*. Zero potential is applied to aperture *4*.

All electrodes of the system are also connected to electrometer amplifiers with gain coefficients from $10^{-6}$to 10^{-8}A/V, allowing to measure the current flowing through the electrodes. The corona point is mounted on a platform with a mechanical drive allowing to vary the distance from the point to the nearest aperture of the focusing system.

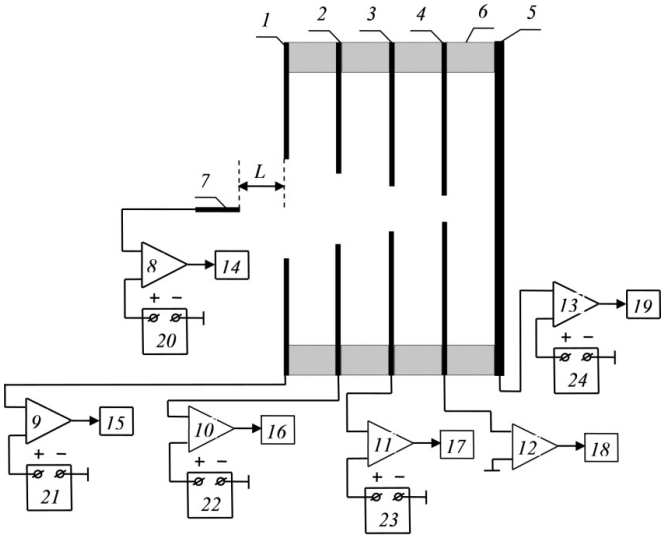

Fig. 2. Experimental setup with ion beam focusing in a system of thin apertures:
thin apertures *1–4*, collector *5*, ceramic inserts *6*, corona point (needle) *7*, electrometers *8–13*, digital current meters 14–19, highly stable high-voltage power supplies *20–24*. Thin apertures are 0.1 mm thick, ceramic inserts are 1 mm thick

Computational results and discussion

The experiment was aimed at studying ion beam transport in the system described above (see Figs. 1 and 2) with varying electrical and geometric parameters, namely:

ΔU is the value of the potential difference between the apertures,

I_d is the corona discharge current,

L is the distance from the corona point to the nearest aperture.

The current balance condition in the system was monitored during all experimental measurements; the condition is satisfied if the discharge current is equal to the sum of the currents flowing into the apertures and the collector. The obtained experimental dependences were reproduced with sufficient accuracy (<10%) in independent series of measurements.

Fig. 3, *a* and *b* shows the current in the collector I_c and the sum of the currents in the fourth apperture and the collector $I_4 + I_c$ as functions of collector potential U_c at different potential differences ΔU between the apertures for a positive corona discharge current $I_d = 1$ μA and a distance $L = 6$ mm. The collector potential was varied in the range from 0 to −1000 V, and ΔU in the range from −300 to −900 V. In practice, the maximum value of $\Delta U = -900$ V was limited by the condition of electrical breakdown between the apertures at atmospheric pressure.

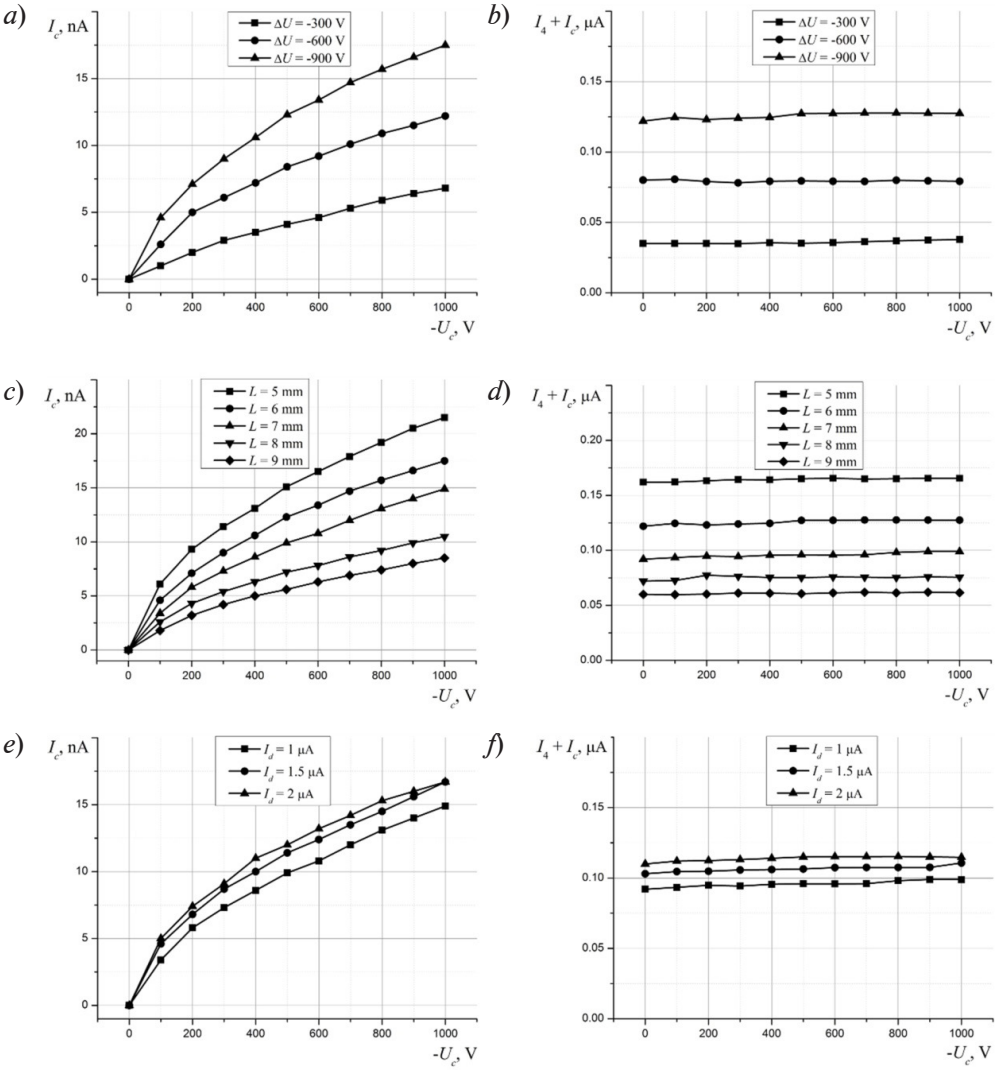

Fig. 3. Current characteristics of ion source with focusing system for varied parameters ΔU (*a*, *b*), L (*c*, *d*) and I_d (*e*, *f*).
The figure shows the dependences for the collector current I_c (*a*, *c*, *e*) and the sum of currents $I_4 + I_c$ (*b*, *d*, *f*) on the collector potential U_c at fixed $I_d = 1$ μA and $L = 6$ mm (*a*, *b*), $\Delta U = -900$ V and $I_d = 1$ μA (*c*, *d*), $\Delta U = -900$ V and $L = 7$ mm (*e*, *f*)

Analyzing the obtained experimental results, we found that the potential difference between the apertures ΔU has a significant effect on the redistribution of currents in the apertures of the system, which is consistent with the results of numerical simulation. If the potential difference between the apertures ΔU is increased, the focusing properties of the system are enhanced: the currents I_1 and I_2 flowing into the first and second apertures decrease, while the currents I_3 and I_4 flowing into the third and fourth apertures as well as the current I_c flowing into the collector, increase. An increase in the potential difference ΔU from −300 to −900 V allows to achieve an increase in the current in the collector I_c by about 2.5 times and the sum of the currents flowing into aperture *4* and collector $I_4 + I_c$, by about 3.5 times for the collector voltage $U_c = -1000$ V.

We should also note that varying the collector voltage has no apparent effect on the redistribution of current between the first three apertures, only affecting the redistribution of current between the fourth aperture and the collector.

Fig. 3, *c* and *d* shows the current in the collector I_c and the sum of currents in the fourth aperture and collector $I_4 + I_c$ as functions of collector potential U_c for different distances L from the corona point to the first aperture at the corona discharge current $I_d = 1$ μA and the potential difference between the apertures of the focusing system $\Delta U = -900$ V. As follows from the dependences presented, the transport efficiency of the ion beam to the fourth aperture and to the collector deteriorates with increasing L: the maximum values of the collector current I_c and the sum of currents $I_4 + I_c$ decrease by about 2.5 times with increasing distance from the corona point to the apertures from 5 to 9 mm. This effect is explained by an increase in the length of the defocusing segment of the field in the vicinity of the ion source when the corona point is removed from the aperture system.

Fig. 3, *e* and *f* shows the experimental dependences for currents I_c and $I_4 + I_c$ on the collector potential U_c for different values of the corona discharge current I_d. If the corona discharge current is increased by two times from 1 to 2 μA, the current in the collector I_c and the sum of the currents $I_4 + I_c$ increase in absolute magnitude but very slightly (by 1.15 times). However, the ratios of currents I_c and $I_4 + I_c$ to the corona discharge current I_d fall by about 1.7 times. The observed deterioration in the transport efficiency of the ion beam with an increase in the corona discharge current is undoubtedly due to enhanced space charge effects, accompanied by spatial broadening of the ion beam.

It is logical to compare the beam transport efficiency in a corona discharge ion source with a focusing system to that in a source without a focusing system. For this purpose, the focusing system with thin apertures was modified by replacing ceramic inserts between the apertures with PTFE gaskets 0.1 mm thick. A quasiplanar concentric-ring counterelectrode under zero potential was thus constructed from the initial aperture system. The modified experimental setup is shown in Fig. 4.

The beam transport efficiencies in the initial (see Fig. 2) and the modified (Fig. 4) system were compared at equal distances L from the corona point to the nearest apertures. Fig. 5 shows a comparison of the currents in the collector I_c and the sum of the currents $I_4 + I_c$ in the ion source with a focusing system (for $\Delta U = -900$ V, which provided the maximum possible focusing effect) and without it for different values of the corona discharge current I_d and distances L from the corona point to the nearest aperture. These experimental results point to a noticeable increase in the magnitude of the current I_c flowing from the collector in the setup with a focused beam which increases by 3.0–3.7 times (depending on the experimental conditions). The sum of the currents $I_4 + I_c$ flowing into the fourth aperture and collector in the focusing geometry exceeds that for an ion source without focusing by about an order of magnitude (by 8.3–11.1 times).

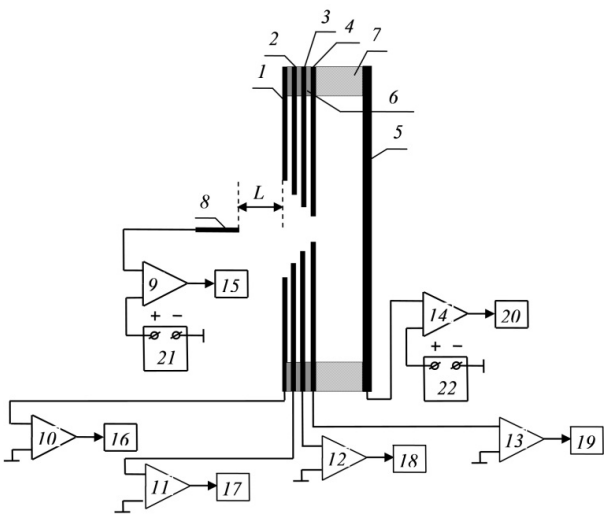

Fig. 4. Modified experimental setup with quasiplanar counterelectrode:
thin apertures *1–4*, collector *5*, PTFE gaskets *6*, ceramic *7*, corona point (needle) *8*, electrometers *9–14*, digital current meters *15–20*, highly stable high-voltage power supplies *21* and *22*.
Thin apertures and PTFE gaskets are 0.1 mm thick, the ceramic insert is 1 mm thick

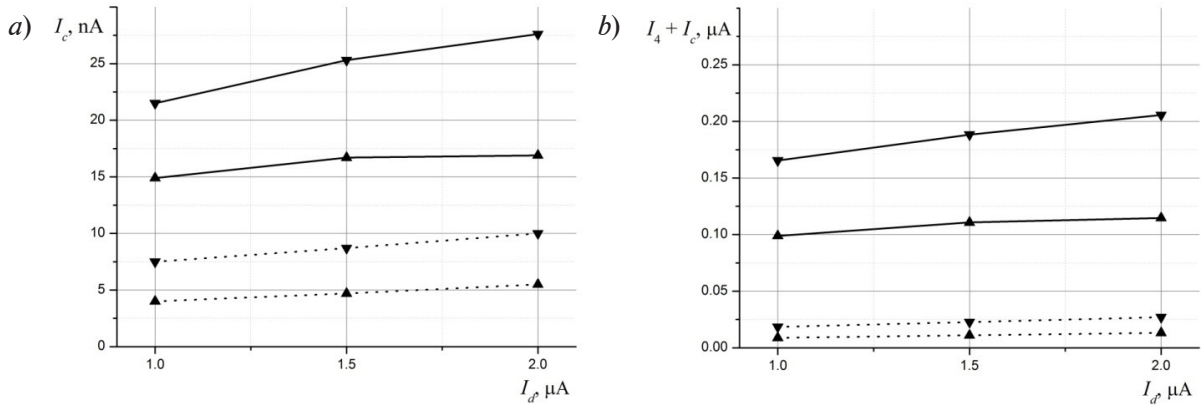

Fig. 5. Comparison for dependences of current in the collector I_c (*a*) and sum of currents $I_4 + I_c$ (*b*) in the ion source on discharge current I_d obtained with the focusing system ($\Delta U = -900$ V, solid lines) and without it (dotted lines) at distances $L = 7$ mm (▲) and 5 mm (▼)

In general, the focusing system in the ion source with corona discharge allows transporting up to 2% of the corona discharge current to the collector through the aperture with the smallest diameter (aperture 4) and up to 15% of the discharge current to the plane of aperture 4 in stagnant gas.

Conclusion

We experimentally studied the properties of a focusing system based on thin apertures in an ion source with corona discharge (the system is proposed in [9]). We obtained the experimental dependences characterizing the influence of the system's geometric and electrical parameters on the efficiency of ion transport. This efficiency increases with an increase in the potential difference between the apertures and decreases with an increase in the corona discharge current and the distance from the corona needle to the aperture system. Comparing the efficiency of ion transport in ion sources with and without a focusing system shows that focusing the ion beam produces a threefold increase in the collector current and an increase by about an order of magnitude in the sum of currents flowing into the aperture with the smallest diameter and the collector. This proves that the correct approach was taken to configure the geometry of the focusing system.

A logical extension of this paper is a study into ion beam transport in an aperture system accounting for gas flow in the vicinity of the inlet nozzle of the gas interface in the mass spectrometer.

REFERENCES

1. **Gall L. N., Bazenov A. N., Shkurov V. A., et al.,** ERIAD (ESI) mass spectrometry as a new method of isotopic and elemental analysis, Mass-Spectrometriya. 4 (1) (2007) 11–18 (in Russian).

2. **Lebedev A. T.,** Mass spectrometriya v organicheskoy khimii [Mass spectrometry in organic chemistry], Publishing House BINOM, Knowledge Laboratory, Moscow, 2003 (in Russian).

3. **Covey T. R., Thomson B. A., Schneider B. B.,** Atmospheric pressure ion sources, Mass Spectrom. Rev. 28 (6) (2009) 870–897.

4. **Willoughby R.C., Sheehan E.W., Fries D.** Transmission of ions through laminated conductance pathways from atmospheric pressure, lcms.com/products/pdf/ion_conductane_asms_2004_abstract.pdf. Accessed December 01, 2022.

5. **Sheehan E.W., Willoughby R.C.** Apparatus and method for focusing ions and charged particles at atmospheric pressure, United State Patent, No. 6744041B2 (2004).

6. **Andreyeva A. D., Muradymov M. Z., Kurnin I. V., Gall L. N.,** An electrostatic focusing effect in the gas dynamical interface of the mass spectrometer, Nauchnoye Priborostroeniye. 16 (3) (2006) 80–87 (in Russian).

7. **Kuzmin D. A., Muradymov M. Z., Krasnov N. V., et al.,** Transport of ions in sources with ionization at atmospheric pressure. I. Substantive geometry, Nauchnoye Priborostroeniye. 27 (4) (2017) 8–16 (in Russian).

8. **Arseniev A. N., Kurnin I. V., Krasnov N. V., et al.,** Optimization of ion transport from atmospheric pressure ion sources, Int. J. Ion Mobil. Spectrom. 22 (1) (2019) 31–38.

9. **Pomozov T. V., Krasnov N. V.,** Influence of features of the electric field in the diaphragm system on the transportation of the flow of charged particles at atmospheric pressure, Nauchnoye Priborostroeniye. 31 (3) (2021) 3–9 (in Russian).

10. **Manura D. J., Dahl D. A.,** SIMIONTM 8.0 User Manual, Sci. Instrument Services, Inc., Idaho Nat. Lab., 2006.

11. **Appelhans A. D., Dahl D. A.,** SIMION ion optics simulations at atmospheric pressure, Int. J. Mass Spectrom. 244 (1) (2005) 1–14.

СПИСОК ЛИТЕРАТУРЫ

1. **Галль Л. Н., Баженов А. Н., Шкуров В. А., Бабаин В. А., Галль Н. Р.** Масс-спектрометрия ЭРИАД как новый метод изотопного и элементного анализа // Масс-спектрометрия. 2007. Т. 4. № 1. С. 11–18.

2. **Лебедев А. Т.** Масс-спектрометрия в органической химии. М: БИНОМ. Лаборатория знаний, 2003. 494 с.

3. **Covey T. R., Thomson B. A., Schneider B. B.** Atmospheric pressure ion sources // Mass Spectrometry Reviews. 2009. Vol. 28. No. 6. Pp. 870–897.

4. **Willoughby R.C., Sheehan E.W., Fries D.** Transmission of ions through laminated conductance pathways from atmospheric pressure. Режим доступа: http://www.lcms.com/products/pdf/ion_conductane_asms_2004_abstract.pdf (Дата обращения: 01.12.2022).

5. **Sheehan E.W., Willoughby R.C.** Apparatus and method for focusing ions and charged particles at atmospheric pressure. United State Patent No. 6744041B2 (2004).

6. **Андреева А. Д., Мурадымов М. З., Курнин И. В., Галль Л. Н.** Электростатическая фокусировка ионов в газодинамических интерфейсах масс-спектрометров // Аналитическое приборостроение. 2006. Т. 16. № 3. С. 80–87.

7. **Кузьмин Д. А., Мурадымов М. З., Краснов Н. В., Помозов Т. В., Арсеньев А. Н.** Транспортировка ионов в источниках с ионизацией при атмосферном давлении. I. Субстантивная геометрия // Научное приборостроение. 2017. Т. 27. № 4. С. 8–16.

8. **Arseniev A. N., Kurnin I. V., Krasnov N. V., Muradymov M. Z., Yavor M. I., Pomozov T. V., Krasnov M. N.** Optimization of ion transport from atmospheric pressure ion sources // International Journal for Ion Mobility Spectrometry. 2019. Vol. 22. No. 1. Pp. 31–38.

9. **Помозов Т. В., Краснов Н. В.** Влияние особенностей электрического поля в системе диафрагм на транспортировку потока заряженных частиц при атмосферном давлении // Научное приборостроение. 2021. Т. 31. № 3. С. 3–9.

10. **Manura D. J., Dahl D. A.** SIMIONTM 8.0 User Manual. Sci. Instrument Services, Inc., Idaho Nat. Lab., 2006.

11. **Appelhans A. D., Dahl D. A.** SIMION ion optics simulations at atmospheric pressure // International Journal of Mass Spectrometry. 2005. Vol. 244. No. 1. Pp. 1–14.

THE AUTHORS

POMOZOV Timofey V.
Institute for Analytical Instrumentation of the Russian Academy of Sciences
31–33, Ivan Chernykh St., St. Petersburg, 198095, Russia
tim-kor@mail.ru
ORCID: 0000-0001-8925-7600

MURADYMOV Marat Z.
Institute for Analytical Instrumentation of the Russian Academy of Sciences
31–33, Ivan Chernykh St., St. Petersburg, 198095, Russia
m.muradymov@gmail.com
ORCID: 0000-0002-7969-496X

TKACH Egor A.
Institute for Analytical Instrumentation of the Russian Academy of Sciences
31–33, Ivan Chernykh St., St. Petersburg, 198095, Russia
egorka765@gmail.com
ORCID: 0009-0003-8001-7469

СВЕДЕНИЯ ОБ АВТОРАХ

ПОМОЗОВ Тимофей Вячеславович – *кандидат физико-математических наук, старший научный сотрудник Института аналитического приборостроения Российской академии наук.*
198095, Россия, г. Санкт-Петербург, ул. Ивана Черных, 31–33
tim-kor@mail.ru
ORCID: 0000-0001-8925-7600

МУРАДЫМОВ Марат Зарифович – *старший научный сотрудник Института аналитического приборостроения Российской академии наук.*
198095, Россия, г. Санкт-Петербург, ул. Ивана Черных, 31–33
m.muradymov@gmail.com
ORCID: 0000-0002-7969-496X

ТКАЧ Егор Андреевич – *аспирант Института аналитического приборостроения Российской академии наук.*
198095, Россия, г. Санкт-Петербург, ул. Ивана Черных, 31–33
egorka765@gmail.com
ORCID: 0009-0003-8001-7469

Received 21.12.2022. Approved after reviewing 09.02.2023. Accepted 09.02.2023.
Статья поступила в редакцию 21.12.2022. Одобрена после рецензирования 09.02.2023. Принята 09.02.2023.

© Peter the Great St. Petersburg Polytechnic University, 2023

PHYSICAL MATERIALS TECHNOLOGY

Original article
DOI: https://doi.org/10.18721/JPM.16205

SYNTHESIS AND PL STUDY OF $Sr_3(VO_4)_2:Eu^{3+}$ PHOSPHOR FOR W-LED APPLICATION

P. A. Nagpure✉, *N. D. Kherde* , *W. S. Barde*

Shri Shivaji Science College, Amravati, Maharashtra, India

✉ nagpurepa@yahoo.co.in

Abstract. In the present paper, a single host phosphor for a white light emitting diode (W-LED) $Sr_3(VO_4)_2:Eu^{3+}$, prepared by the co-precipitation method and combustion one, has been reported. Formation of the compound was confirmed by studying the X-ray diffraction pattern. The photoluminescence (PL) properties were studied by fluorescence spectrophotometer F-7000. The $Sr_3(VO_4)_2:Eu^{3+}$ exhibited a broad emission band covering the entire visible region centered at 520 nm wavelength and a sharp peak at 613 nm, when excited by 350 nm. The excitation spectrum at 520 nm emission wavelength was found to be suitable for pc-W-LED application.

Keywords: strontium vanadate, co-precipitation, combustion, X-ray diffraction pattern, photoluminescence spectroscopy, W-LED

Citation: Nagpure P. A., Kherde N. D., Barde W. S., Synthesis and PL study of $Sr_3(VO_4)_2:Eu^{3+}$ phosphor for W-LED application, St. Petersburg State Polytechnical University Journal. Physics and Mathematics. 16 (2) (2023) 61–67. DOI: https://doi.org/10.18721/JPM.16205

This is an open access article under the CC BY-NC 4.0 license (https://creativecommons.org/licenses/by-nc/4.0/)

Научная статья
УДК 678.046.82
DOI: https://doi.org/10.18721/JPM.16205

СИНТЕЗ И ФОТОЛЮМИНЕСЦЕНТНОЕ ИССЛЕДОВАНИЕ ЛЮМИНОФОРА $Sr_3(VO_4)_2:Eu^{3+}$ С ЦЕЛЬЮ ПРИМЕНЕНИЯ В БЕЛЫХ СВЕТОИЗЛУЧАЮЩИХ ДИОДАХ

П. А. Нагпуре✉, *Н. Д. Херде*, *В. С. Барде*

Научный колледж Шри Шиваджи, г. Амравати, штат Махараштра, Индия

✉ nagpurepa@yahoo.co.in

Аннотация. В статье исследован люминофор $Sr_3(VO_4)_2:Eu^{3+}$, перспективный для создания белого светоизлучающего диода (W-LED) на основе этого одного соединения. Образцы данного материала были получены двумя способами: соосаждения и сжигания. Образование требуемого вещества было подтверждено рентгенографически. Практически важные свойства объекта изучались методом фотолюминесцентной спектроскопии. В спектрах соединения обнаружены широкая эмиссионная полоса, охватывающая всю видимую область спектра с центром на длине волны 520 нм, а также острый пик на 613 нм. В спектрах возбуждения люминесценции наблюдалась широкая полоса с центром на длине волны 350 нм. Представлена соответствующая диаграмма энергетических уровней. Полученные экспериментальные результаты привели к заключению, что метод соосаждения предпочтителен, а фотолюминесцентные свойства полученного люминофора удобны для создания штучных белых светоизлучающих диодов.

© Nagpure P. A., Kherde N. D., Barde W. S., 2023. Published by Peter the Great St. Petersburg Polytechnic University.

Ключевые слова: ванадат стронция, соосаждение, метод сжигания, фотолюминесценция, белый светоизлучающий диод

Ссылка для цитирования: Нагпуре П. А., Херде Н. Д., Барде В. С. Синтез и фотолюминесцентное исследование люминофора Sr3(VO4)2:Eu3+ с целью применения в белых светоизлучающих диодах // Научно-технические ведомости СПбГПУ. Физико-математические науки. 2023. Т. 16. № 2. С. 61–67. DOI: https://doi.org/10.18721/JPM.16205

Статья открытого доступа, распространяемая по лицензии CC BY-NC 4.0 (https://creativecommons.org/licenses/by-nc/4.0/)

Introduction

White light emitting diodes (W-LEDs) have been found wide use especially for solid state lighting and backlight of liquid crystal display (LCD), traffic signals. W- LEDs have a number of advantages such as long lifetime and lack of pollutant, higher energy efficiency, compactness and reduced power consumption [1]. In a W-LED, white light can be produced either by combining a blue LED with a yellow phosphor or combining the ultraviolet light emitting diodes (UV-LED) with a blend of blue, green and red phosphors. White light emission resulted from a single-phase phosphor compared to combination of two or three phosphors expected to give high luminous efficiency, because it reduces the probability of multiphosphor reabsorption of emission colors [2].

In recent years, vanadates have been used in many high-technology fields, such as biological materials, electrochemistry, optical lasers, catalysis, etc. [3] Luminescence materials have been widely studied and used in white light emitting diodes and flat-panel displays (FPDs), such as $YVO_4:Eu^{3+}$, etc. [4]. At ambient pressure orthovanadates exhibit oxygen ionic conductivity and high electronic conductivity, i. e., the migration of electrons between V^4- and V^5-centers, but electronic conduction is absent in isostructural orthophosphates and orthoarsenates [5]. Vanadates with general formula $M_3(VO_4)_2$ (M = Ca, Sr, Ba) have been proved to be good candidates for the luminescent hosts, because they have strong absorption band in the UV region and then transfer the energy to rare-earth activator ions efficiently due to good match of energy levels in the wide region and strong interaction between states of $[VO_4]^{3-}$ and rare-earth ions. In addition to this, vanadates have the self-activated emitting properties and better chromaticity [6]. $[VO_4]^{3-}$ group consists of the central metal vanadium ion coordinated by four oxygen ligands in the tetrahedral symmetry and is known to be an efficient luminescent center with broad band emissions from 400 to more than 700 nm with UV or near-UV light excitation [7]. Vanadium oxides have different complex groups of ortho-, meta- and pyrovanadates. Vanadates generally show a short wavelength of the optical absorption edge. This makes them suitable as hosts to accommodate active rare-earth ions [8]. The ytterbium ions Yb^{3+} doped with $Sr_3(VO_4)_2$ provide characteristic near-infrared (NIR) emission in the range of 970 – 1050 nm which are suitable to get rid of the spectral mismatch problem of c-Si solar cells [9].

In the present work, photoluminescence of $Sr_3(VO_4)_2:Eu^{3+}$ phosphor synthesized by co-precipitation and combustion methods has been studied in the context of its application as W-LED phosphor.

Experimental part

Strontium nitrate $Sr(NO_3)_2$ (99.9% A.R.), europim oxide Eu_2O_3 (99.9% A.R.) and ammonium vanadate NH_4VO_4 (99.9% A.R.), all from Sigma Aldrich, were used.

Synthesis. The synthesis of phosphor Sr3–x(VO4)2:(Eu3+)x, was attempted using two methods: co-precipitation one and combustion one.

Co-precipitation method. The phosphors $Sr_{3-x}(VO_4)_2:(Eu^{3+})_x$ (x = 0.002, 0.005, 0.010) were synthesized by co-precipitation method (Fig. 1). The precursors $Sr(NO_3)_2$ (99.9% A.R.), Eu_2O_3 (99.9% A.R.) and NH_4VO_4 (99.9% A.R.) were weighed in proper stoichiometric ratio and used for synthesis of the phosphor. The starting chemicals NH_4VO_4 (99.9% A.R.) were dissolved in the double distilled water and heated on a hot plate at about 100 °C. The nitric acid HNO_3 was added drop by drop in Eu_2O_3 and a DD water mixture in separate beaker was so as to convert it into

© Нагпуре П. А., Херде Н. Д., Барде В. С., 2023. Издатель: Санкт-Петербургский политехнический университет Петра Великого.

$Eu(NO_3)_3$. The hot solution of NH_4VO_4 then added drop wise to the aqueous transparent mixture of nitrates with constant stirring. The entire homogenous solution was then placed on the hot plate maintained at a temperature of 90 °C for slow evaporation of water. The dried precipitate was finally crushed and heated at 800 °C for 1 hour and 950 °C for 2 hours in order to get white crystalline powder of $Sr_{3-x}(VO_4)_2:(Eu^{3+})_x$ (x = 0.002, 0.005, 0.010).

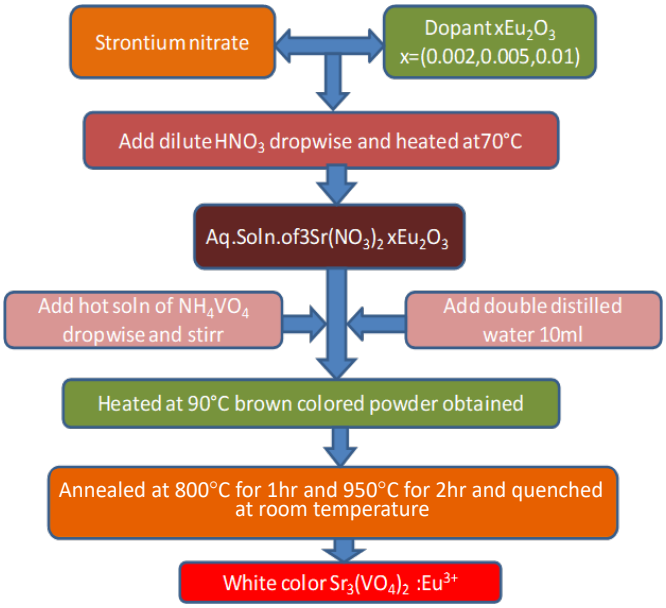

Fig. 1. Flow chart of synthesis of $Sr_{3-x}(VO_4)_2:(Eu^{3+})_x$ via co-precipitation method

Combustion method. The stoichiometric amount of precursors, namely, strontium nitrate $Sr(NO_3)_2$, ammonium vanadete NH_4VO_3, urea and Eu_2O_3 converted to $Eu(NO_3)_3$ (x = 0.002, 0.005, 0.010) were taken in a china clay basin and few drops of DD water added to the mixture. This mixture was heated at 90 °C till the precursors dissolved completely, then it was kept into the preheated furnace at 900 °C, and then warmed for 5 min. The self-heat generating redox reaction was completed in 2 min and the fine powder of $Sr_3(VO_4)_2:Eu^{3+}$ was obtained (Fig. 2). This raw powder was sintered for 2 hours at 950 °C and quenched to room temperature.

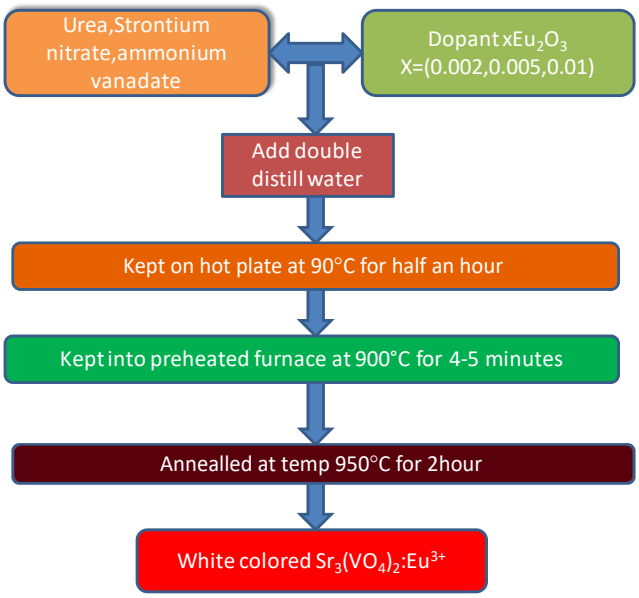

Fig. 2. Flow chart of synthesis of $Sr_{3-x}(VO_4)_2:(Eu^{3+})_x$ via combustion method

Characterizations. Formation of the required phase of the compound was confirmed by the X-ray diffraction pattern. The photoluminescence (PL) properties were studied using Hitachi (F-7000) fluorescence spectrophotometer.

Results and discussion

X-ray diffraction (XRD) analysis. The formation of $Sr_3(VO_4)_2$ host in the crystalline phase synthesized by both co-precipitation and combustion methods was confirmed by XRD pattern taken from Rigaku miniflex II X-ray diffractometer with scan rate of 2.000°/min and CuK_α (k = 0.15406 nm) radiation in the range from 10° to 90° (see Fig. 3). The XRD pattern for $Sr_3(VO_4)_2$ agreed with the ICDD file (01-081-1844) very well.

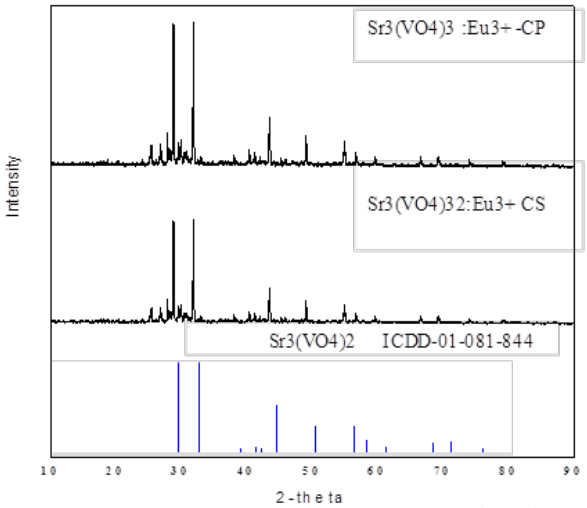

Fig. 3. X-ray diffraction pattern of $Sr_3(VO_4)_2$:Eu^{3+}

Photoluminescence characterization. The photoluminescence (PL) emission and excitation spectrum of $Sr_3(VO_4)_2$:Eu^{3+} phosphor synthesized by co-precipitation and combustion methods are shown in Fig. 4. For the both cases the nature of emission spectra are almost the same but there is a slight difference in the excitation spectra. The emission spectrum exhibits a green broad band centered at 520 nm which is attributed to $^3T_{1,2} \rightarrow {}^1A_1$ transition of $[VO_4]^{3-}$ group, and with a sharp peak at 613 nm in the red region corresponding to a characteristic $^5D_0 \rightarrow {}^7F_2$ transition of Eu^{3+} [10, 11].

The PL emission spectra of the phosphor shows maximum intensity for 0.002 mol doping of Eu when synthesized by the co-precipitation method and for 0.001 mol doping of Eu when synthesized by the combustion one. The overall intensity of PL emission is greater for the phosphor synthesized by the co-precipitation method than that for the phosphor synthesized by the combustion one.

Fig. 5. presents the simplified energy level diagrams of $[VO_4]^{3-}$ group and Eu^{3+} ion and emission transition processes in the $Sr_3(VO_4)_2$:Eu^{3+} phosphor as well.

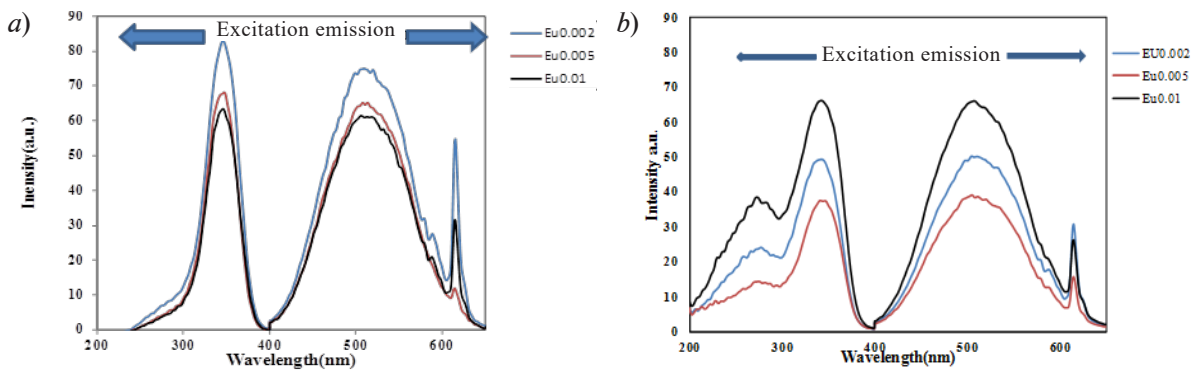

Fig. 4. Photoluminescence excitation and emission spectra of $Sr_{3-x}(VO_4)_2$: $(Eu^{3+})_x$ synthesized by co-precipitation (a) and combustion (b) methods

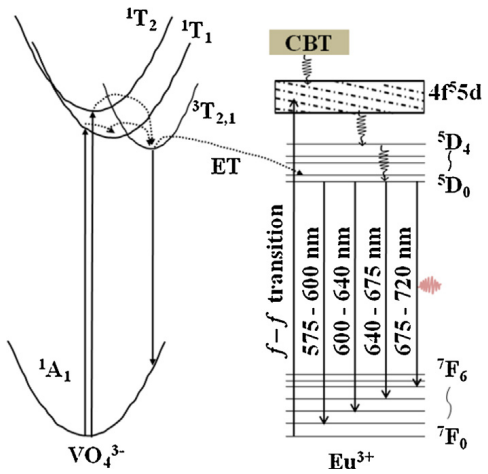

Fig. 5. The simplified energy level diagrams of $[VO_4]^{3-}$ group and Eu^{3+} ion and emission transition (ET) processes in the $Sr_3(VO_4)_2$:Eu^{3+} phosphor

Summary

A series of $Sr_3(VO_4)_2$:Eu^{3+} phosphors were successfully synthesized by co-precipitation and combustion methods. The XRD patterns confirmed the pure crystalline phase of $Sr_3(VO_4)_2$. The photoluminescence excitation spectra showed the broad excitation band with maximum at 350 nm. The photoluminescence emission spectra showed the broad band (400 – 650 nm) with a maximum at 520 nm attributed to the $^3T_{1,2} \rightarrow {}^1A_1$ transitions of $[VO_4]^{3-}$ group and a sharp peak at 613 nm attributed to the $^5D_0 \rightarrow {}^7F_2$ transition of Eu^{3+}. The co-precipitation method was found to be suitable and efficient for synthesis of $Sr_3(VO_4)_2$:Eu^{3+}.

The photoluminescence spectra of the $Sr_3(VO_4)_2$:Eu^{3+} exhibited a potential application of the prepared phosphor in energy-efficient solid-state lighting, optoelectronic devices and organic composite solar cells.

REFERENCES

1. **Chung D. N., Hieu D. N., Thao T. T., et al.,** Synthesis and characterization of Ce-doped $Y_3Al_5O_{12}$ (YAG : Ce) nanopowders used for solid-state lighting, J. Nanomater. 2014 (25 May) (2014) 571920.

2. **Bajaj N. S., Koparkar K. A., Nagpure P. A., Omanwar S. K.,** Red and blue emitting borate phosphor excited by near ultraviolet light, J. Optics. 46 (2) (2017) 91–94.

3. **Zhang Z., Tang W. J.,** Energy transfer and tunable luminescence of Na_2(Y, Eu)$Mg_2V_3O_{12}$ phosphors for white LED applications, Mater. Res. Bull. 73 (January) (2016) 351–356.

4. **Erdei S., Rodriguez N. M., Ainger F. W., et al.,** Luminescent characteristics and morphology of Eu^{3+}:YVO4 phosphor powders prepared by HCR and flux techniques, J. Mater. Chem. 8 (1) (1998) 99–103.

5. **Grzechnik A., McMillan P. F.,** High-pressure X-ray diffraction of $Sr_3(VO_4)_2$ and $Ba_3(VO_4)_2$, Physica B. Condens. 252 (4) ((1998) 268–273.

6. **Cao R., Peng D., Xu H., et al.,** Synthesis and luminescence properties of $Sr_3(VO_4)_2$:Eu^{3+} phosphor and emission enhancement by co-doping Li^+-ion, Optik. 127 (19) (2016) 7896–7901.

7. **Sheetal, Taxak V. B., Khatkar S. P.,** Synthesis and luminescent properties of $M_2V_2O_7$: Eu (M = Sr, Ba) nanophosphors, J. Fluoresc. 22 (3) (2012) 891–897.

8. **Shinde K. N., Singh R.,** Vanadate phosphors for energy efficient lighting. Ch. 12, In book: Tiwari A., Valykh S. (Eds.), Advanced Energy Materials, John Wiley & Sons, Oxford (UK), 2014.

9. **Sawala N. S., Bajaj N. S., Omanwar S. K.,** Near-infrared quantum cutting in Yb^{3+} ion doped strontium vanadate, Infrared Phys. Technol. 76 (May) (2016) 271–275.

10. **Cao R., Peng D., Xu H., Luo Z., Ao H., Guo S., Fu J.,** Synthesis and luminescence properties of $Sr_3(VO_4)_2$:Eu^{3+} phosphor and emission enhancement by co-doping Li^+ ion // Optik. Vol. 127. No. 19. Pp. 7896–7901.

11. **Bedyal A. K., Kumar V., Swart H. C.,** Charge compensated derived enhanced red emission from $Sr_3(VO_4)_2$:Eu^{3+} nanophosphors for white light emitting diodes and flat panel displays, J. Alloys Compd. 709 (30 June) (2017) 362–372.

СПИСОК ЛИТЕРАТУРЫ

1. **Chung D. N., Hieu D. N., Thao T. T., Truong V., Dinh N. N.** Synthesis and characterization of Ce-doped $Y_3Al_5O_{12}$ (YAG : Ce) nanopowders used for solid-state lighting // Journal of Nanomaterials. 2014. Vol. 2014. 25 May. P. 571920 (7 p).

2. **Bajaj N. S., Koparkar K. A., Nagpure P. A., Omanwar S. K.** Red and blue emitting borate phosphor excited by near ultraviolet light // Journal of Optics. 2017. Vol. 46. No. 2. Pp. 91–94.

3. **Zhang Z., Tang W. J.** Energy transfer and tunable luminescence of Na_2(Y, Eu)$Mg_2V_3O_{12}$ phosphors for white LED applications // Materials Research Bulletin. 2016. Vol. 73. January. Pp. 351–356.

4. **Erdei S., Rodriguez N. M., Ainger F. W., et al.** Luminescent characteristics and morphology of Eu^{3+}:YVO4 phosphor powders prepared by HCR and flux techniques // Journal of Materials Chemistry. 1998. Vol. 8. No. 1. Pp. 99–103.

5. **Grzechnik A., McMillan P. F.** High-pressure X-ray diffraction of $Sr_3(VO_4)_2$ and $Ba_3(VO_4)_2$ // Physica B: Condensed Matter. 1998. Vol. 252. No. 4. Pp. 268–273.

6. **Cao R., Peng D., Xu H., Luo Z., Ao H., Guoa S., Fu J.** Synthesis and luminescence properties of $Sr_3(VO_4)_2$:Eu^{3+} phosphor and emission enhancement by co-doping Li^+-ion // Optik. 2016. Vol. 127. No. 19. Pp. 7896–7901.

7. **Sheetal, Taxak V. B., Khatkar S. P.** Synthesis and luminescent properties of $M_2V_2O_7$: Eu (M = Sr, Ba) nanophosphors // Journal of Fluorescence. 2012. Vol. 22. No. 3. Pp. 891–897.

8. **Shinde K. N., Singh R.** Vanadate phosphors for energy efficient lighting. Chapter 12 // Tiwari A., Valykh S. (Eds.). Advanced Energy Materials. Oxford, UK: John Wiley & Sons, 2014. 616 p.

9. **Sawala N. S., Bajaj N. S., Omanwar S. K.** Near-infrared quantum cutting in Yb^{3+} ion doped strontium vanadate // Infrared Physics & Technology. 2016. Vol. 76. May. Pp. 271–275.

10. **Cao R., Peng D., Xu H., Luo Z., Ao H., Guo S., Fu J.** Synthesis and luminescence properties of $Sr_3(VO_4)_2$:Eu^{3+} phosphor and emission enhancement by co-doping Li^+ ion // Optik. Vol. 127. No. 19. Pp. 7896–7901.

11. **Bedyal A. K., Kumar V., Swart H. C.** Charge compensated derived enhanced red emission from $Sr_3(VO_4)_2$:Eu^{3+} nanophosphors for white light emitting diodes and flat panel displays // Journal of Alloys and Compounds. 2017. Vol. 709. 30 June. Pp. 362–372.

THE AUTHORS

NAGPURE Pankaj A.
Shri Shivaji Science College, Amravati
Shivaji Nagar, Morshi Road, Amravati, 444603, India
nagpurepa@yahoo.co.in
ORCID: 0000-0001-6767-1907

KHERDE Nivedita D.
Shri Shivaji Science College, Amravati
Shivaji Nagar, Morshi Road, Amravati, 444603, India
niveditaholey@gmail.com

BARDE Waman S.
Shri Shivaji Science College, Amravati
Shivaji Nagar, Morshi Road, Amravati, 444603, India
wamanbarde81@gmail.com

СВЕДЕНИЯ ОБ АВТОРАХ

НАГПУРЕ Панкадж А. – *Ph.D., доцент кафедры физики Научного колледжа Шри Шиваджи, г. Амравати, штат Махараштра, Индия.*
Shivaji Nagar, Morshi Road, Amravati, 444603, India
nagpurepa@yahoo.co.in
ORCID: 0000-0001-6767-1907

ХЕРДЕ Ниведита Д. – *сотрудник кафедры физики Научного колледжа Шри Шиваджи, г. Амравати, штат Махараштра, Индия.*
Shivaji Nagar, Morshi Road, Amravati, 444603, India
niveditaholey@gmail.com

БАРДЕ Ваман С. – *Ph.D., адьюнкт-профессор кафедры физики Научного колледжа Шри Шиваджи, г. Амравати, штат Махараштра, Индия.*
Shivaji Nagar, Morshi Road, Amravati, 444603, India
wamanbarde81@gmail.com

Received 11.10.2022. Approved after reviewing 27.12.2023. Accepted 27.12.2023.
Статья поступила в редакцию 11.10.2022. Одобрена после рецензирования 27.12.2023. Принята 27.12.2023.

© Peter the Great St. Petersburg Polytechnic University, 2023

Original article
DOI: https://doi.org/10.18721/JPM.16206

ELECTRIC AND THERMOELECTRIC PROPERTIES OF COORDINATION POLYMER BASED ON PHENAZINE LIGANDS AND SILVER

A. A. Tretyakov[1], *V. M. Kapralova*[1]✉, *I. Yu. Sapurina*[2], *N. T. Sudar*[1], *M. A. Shishov*[1, 2]

[1] Peter the Great St. Petersburg Polytechnic University, St. Petersburg, Russia;

[2] Institute of Macromolecular Compounds of RAS, St. Petersburg, Russia

✉ kapralova2006@yandex.ru

Abstract. The paper presents the results of an experimental study of the electric conductivity and thermoelectric properties of a new coordination polymer (CP) based on phenazine ligands (Phz) and silver (Ag) synthesized by a one-step method. This method produces phenazine by oxidative dimerization of aniline under the action of $AgNO_3$ followed by release of metal nanoparticles and subsequent self-organization of Phz with excess $AgNO_3$ into the CP. The used method of the Phz-Ag synthesis was found to make possible obtaining CP with conductivity of about 1300 S/cm commensurable with the modern record value for CPs. The obtained experimental data led to the conclusion that the studied CP Phz-Ag possesses a metallic type of conductivity. A physical mechanism of forming this property was put forward.

Keywords: polymer composite, nanocomposite, thermal properties, coordination polymer, phenazine ligand

Funding: This work was funded by State Assignment for Basic Research (project FSEG-2023-0016).

Citation: Tretyakov A. A., Kapralova V. M., Sapurina I. Yu., Sudar N. T., Shishov M. A., Electric and thermoelectric properties of coordination polymer based on phenazine ligands and silver, St. Petersburg State Polytechnical University Journal. Physics and Mathematics. 16 (2) (2023) 68–77. DOI: https://doi.org/10.18721/JPM.16206

This is an open access article under the CC BY-NC 4.0 license (https://creativecommons.org/licenses/by-nc/4.0/)

© Tretyakov A. A., Kapralova V. M., Sapurina I. Yu., Sudar N. T., Shishov M. A., 2023. Published by Peter the Great St. Petersburg Polytechnic University.

Научная статья
УДК 538.95
DOI: https://doi.org/10.18721/JPM.16206

ЭЛЕКТРИЧЕСКИЕ И ТЕРМОЭЛЕКТРИЧЕСКИЕ СВОЙСТВА КООРДИНАЦИОННОГО ПОЛИМЕРА НА ОСНОВЕ ФЕНАЗИНОВЫХ ЛИГАНДОВ И СЕРЕБРА

А. А. Третьяков[1], *В. М. Капралова*[1]✉, *И. Ю. Сапурина*[2]
Н. Т. Сударь[1], *М. А. Шишов*[1, 2]

[1] Санкт-Петербургский политехнический университет Петра Великого,

Санкт-Петербург, Россия;

[2] Институт высокомолекулярных соединений РАН, Санкт-Петербург, Россия

✉ kapralova2006@yandex.ru

Аннотация. В статье представлены результаты экспериментального исследования электропроводности и термоэлектрических свойств нового координационного полимера (КП) на основе феназиновых лигандов (Phz) и серебра (Ag), синтезированного одностадийным методом. Этот метод позволяет получать феназин путем окислительной димеризации анилина под действием $AgNO_3$ с выделением наночастиц металла и последующей самоорганизацией Phz с избытком $AgNO_3$ в КП. Установлено, что использованный метод синтеза Phz-Ag позволяет получать КП с проводимостью примерно 1300 С/см, что соизмеримо с современным рекордным значением для КП. Полученные экспериментальные данные позволили заключить, что новый КП обладает металлическим типом проводимости. Предложен физический механизм формирования этого свойства.

Ключевые слова: полимерный композит, феназиновый лиганд, координационный полимер, термоэлектрические свойства

Финансирование: Работа выполнена в рамках Государственного задания на проведение фундаментальных исследований (код темы FSEG-2023-0016).

Ссылка для цитирования: Третьяков А. А., Капралова В. М., Сапурина И. Ю., Сударь Н. Т., Шишов М. А. Электрические и термоэлектрические свойства координационного полимера на основе феназиновых лигандов и серебра // Научно-технические ведомости СПбГПУ. Физико-математические науки. 2023. Т. 16. № 2. С. 68–77. DOI: https://doi.org/10.18721/ JPM.16206

Статья открытого доступа, распространяемая по лицензии CC BY-NC 4.0 (https://creativecommons.org/licenses/by-nc/4.0/)

Introduction

In recent years, considerable attention has been paid to the study of coordination polymers (CPs), which are organized metal-organic frameworks [1–4] consisting of organic ligands and transition metal atoms or ions. Organic ligands contain various functional groups (carboxylate, pyridine, azole, etc.) that include electron-donor atoms (O, N, S), which, due to donor-acceptor bonding, provide the ligand interaction with the transition metal. CPs are capable of forming one-, two-, or three-dimensional crystalline structures, the design of which is very diverse.

The electrical conductivity of CP varies over a wide range. Most of them are dielectrics with conductivity of 10^{-14}–10^{-4} S/cm, but there are known CPs with significant conductivity of semiconductor and metallic types [3]. For example, the specific conductivity of a CP based on benzene-hexathiol ligands and copper, prepared as a film at the interface of two immiscible solvents, is approximately 1500 S/cm [5].

© Третьяков А. А., Капралова В. М., Сапурина И. Ю., Сударь Н. Т., Шишов М. А., 2023. Издатель: Санкт-Петербургский политехнический университет Петра Великого.

Elucidating the reasons for the high conductivity of CP is an important physical task. As noted above, CPs demonstrating metallic conductivity have now been synthesized. There is no band gap in these CPs and the charge carriers fill the states up to the Fermi level [6]. However, so far, the most effective way to increase the electrical conductivity of CPs is the inclusion of metal atoms into the intermolecular space of these polymers, which can form conducting clusters that provide the through conductivity of CP samples [7].

A variety of electrophysical properties of CPs determines a wide range of their practical applications. CPs can be used to produce porous materials with given physicochemical parameters of the available intermolecular volume [5], so CPs can be applied as organic frameworks for lithium storage in modern rechargeable batteries [8]. CPs with high electrical conductivity are considered to be promising materials for fabricating conductive channels in field-effect transistors [9]. The possibility of using CPs as detecting materials in new sensor devices is currently under discussion [10].

Thus, the synthesis of novel CPs with high conductivity and unique physical and chemical properties seems to be an urgent task, and the study of the electrophysical properties of such polymers is of significant scientific and practical relevance.

The authors of [11] developed a method for the one-step synthesis of a new CP based on phenazine ligands (Phz) and silver (Ag). It involved the synthesis of phenazine by oxidative dimerization of aniline under the action of silver nitrate and subsequent extraction of metal Ag-nanoparticles. As a result, the self-assembly of phenazine ligands into a crystalline organometallic framework occurred through interaction with an excess of $AgNO_3$. In the Phz-Ag combination silver performs two functions: silver ions serve as binding elements for the ligands, and metallic silver clusters play the role of guest elements, which, according to the authors of [11], will determine the high conductivity of the material.

This paper is aimed at finding out the nature of the conductivity of this CP synthesized by the one-step mechanism, which can be based on the electric impedance and thermoelectric data for this CP.

Materials and Methods

The synthesis of the Phz-Ag composition was carried out under normal conditions in the volume of the aqueous-organic phase as a unified process. It began with the formation of the Phz molecule by oxidative dimerization of aniline under the action of silver nitrate $AgNO_3$ with the subsequent release of two reduced silver atoms [12]. The relevant chemical reaction is as follows:

In parallel, the process of self-organization of Phz and excess $AgNO_3$ occurred with the

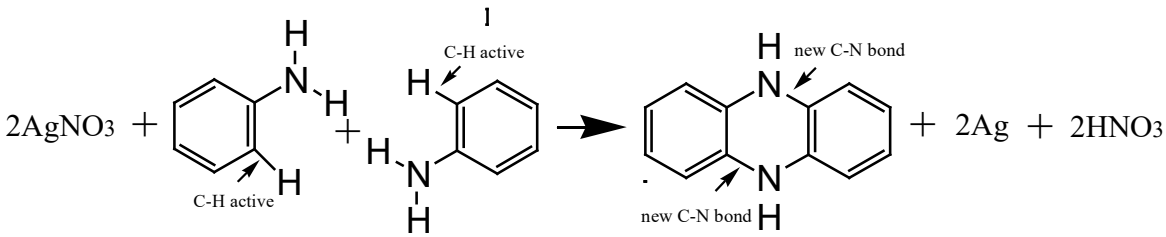

formation of a crystalline organometallic matrix and saturation of the matrix with silver metal nanoparticles. The resulting product was filtered out, washed with water, and dried under normal conditions. When dried, it was a yellowish-brown powder.

A study of the product composition showed that its organic part (60% C, 13% N, 3.3% H, 19.8% O) coincides well with the formula of the oxidized phenazine molecule containing NO_3-group as the counterion, and the silver content is 63–65 wt.%. The general formula of the product can be represented as $Ag_{3.5}$ (Phz^+ NO_3^-).

The composition and morphology of the Phz-Ag samples were examined using a Carl Zeiss Supra 55 VP scanning electron microscope (SEM).

Fig. 1 shows SEM image of Phz-Ag CP. We can see (Fig. 1,*a*) that the aggregate structure of the studied CP is characterized by the presence of thin two-dimensional plates (microcrystals) with lateral size of 5–8 μm. Judging by the size of the end faces and transparency of the plates, their thickness does not exceed 5–10 nm, indicating that the microcrystals consist of only a few polymer layers. As the accelerating voltage of electron beam intensity increases (Fig. 1,*b*), silver

nanoparticles (light objects) localized both between microcrystals and on polymer planes become distinguishable. Ag particles are arranged in rows framing the edge of the polymer plates. Most Ag particles are tens of nanometers in size.

The conductivity and the Seebeck coefficient of the samples were measured simultaneously on the Netzsch SBA 458 Nemesis in the temperature range from 293 to 393 K. Electrical conductivity was measured using the four-point method. Specific electrical conductivity was determined using samples pressed into tablets with a diameter of 16 mm and a thickness of 1.5–2 mm using a hydraulic press. Three series of samples were made (three samples per each series) at different compressing pressures. Sufficiently strong and measurable samples were already obtained at a pressure of approx. 3 MPa.

a) *b*)

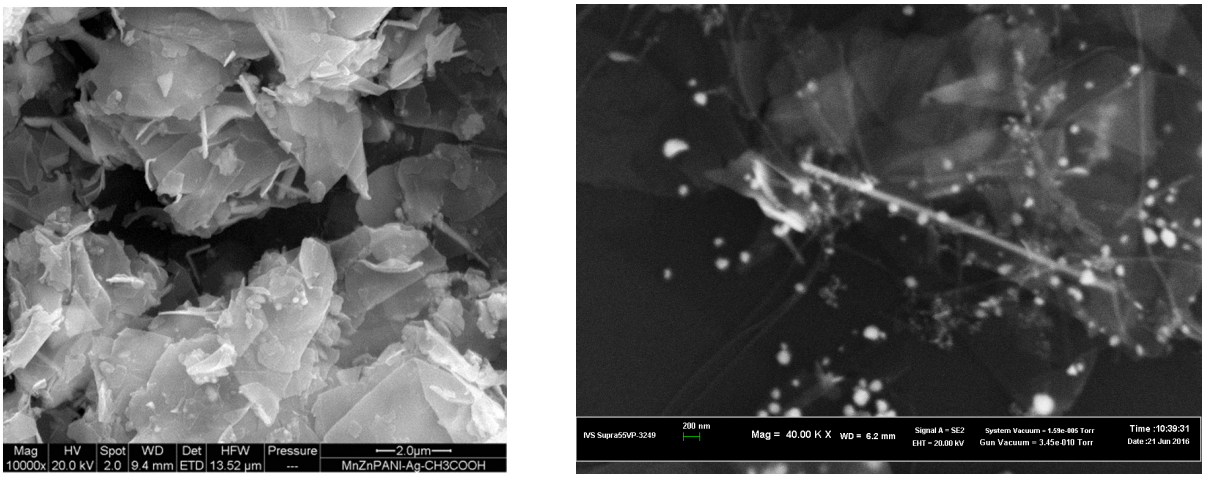

Fig. 1. SEM images of Phz-Ag morphology taken in standard mode (*a*) and at maximum electron beam intensity (*b*)

To measure the electrical impedance modulus Z and the phase angle φ, we used impedance meters E7-20 (in the frequency range from 25 to $5\cdot10^4$ Hz) and E7-29 (in the frequency range from $5\cdot10^4$ to $1.5\cdot10^7$ Hz) imminence meters. Measurements were carried out at alternative voltage amplitude of 1 V using flat clamping electrodes made of polished copper.

Results and discussion

The table shows the average values of density ρ, conductivity σ and Seebeck coefficient S measured at room temperature for the Phz-Ag samples made at different pressures. As follows from the presented data, with increasing compression pressure the Seebeck coefficient tends to decrease insignificantly, and the conductivity of samples increases in proportion to increasing pressure, however, even at the highest pressure used in this experiment, the conductivity of Phz-Ag samples is ~500 times lower than that of pure silver ($6.7\cdot10^5$ S/cm). The density of the samples increases until the pressing pressure exceeds 17.7 MPa. At higher pressures, its value seems to stabilize and is 2.4–2.5 g/cm^3. This density value corresponds to the theoretically calculated Phz-Ag density if we take the silver density to be 10.5 g/cm^3 at 63 wt. % and the phenazine density to be 1.2 g/cm^3 at 37 wt. %.

Table

Dependence of Phz-Ag parameter values on pressure

Pressure, MPa	ρ, g/cm^3	σ, S/cm	S, µV/K
38.0	2.4±0.1	1300±10	2.1±0.1
17.7	2.5±0.1	550±4	1.9±0.1
1.9	1.9±0.1	30±1	2.8±0.1

Fig. 2,*a* shows the temperature dependence of specific conductivity for two series of Phz-Ag samples prepared at pressures of 1.9 and 17.7 MPa. It can be seen that with increasing temperature their conductivity decreases approximately by a linear law, i.e., $d\sigma/dT$ = const, which allows us to simply calculate the temperature coefficient of resistance (TCR), defined as

$$\mathrm{TCR} = (1/\rho_0)d\rho/dT,$$

where ρ_0 is the specific resistance of the studied samples at $T = 296$ K. It turned out that its values are $1.6\cdot10^{-3}$ and $2.0\cdot10^{-3}$ K^{-1}, for samples pressed at lower and higher pressures, respectively. The TCR of pure silver is $4.3\cdot10^{-3}$ K^{-1} [13], so the TCRs of Phz-Ag and Ag are values of the same order, while the specific conductivities of these materials differ by 2–3 orders of magnitude.

Fig. 2,*b* presents the temperature dependence of the Seebeck coefficient for the studied samples. From the data presented, we can see that at room temperature, it is a small positive value, and it increases linearly with temperature. The determined values of *S* and the linear character of the dependence *S*(*T*) for Phz-Ag correspond to *S* and *S*(*T*) for pure silver [14].

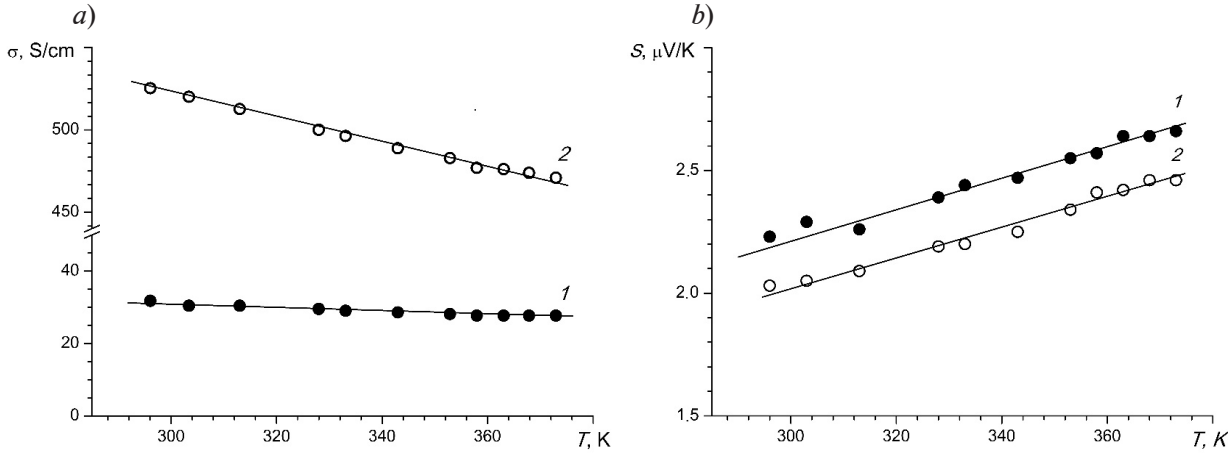

Fig. 2. Temperature dependence of electrical conductivity (*a*) and Seebeck coefficient (*b*) for the samples of Phz-Ag metal-organic coordination polymer pressed at 1.9 MPa (*1*) and 17.7 MPa (*2*)

Thus, the decrease of the specific conductivity with increasing temperature, the value of the TCR of Phz-Ag close to the TCS of silver, as well as the value of the Seebeck coefficient and its temperature dependence give reason to assume that in the investigated Phz-Ag CP the metallic type of conductivity is realized.

To clarify its features, impedance spectroscopy was used, which is sensitive to charge transfer in heterogeneous systems including phase boundaries, electrode interfaces and microstructure elements.

Fig. 3 shows the frequency dependences of the phase angle φ (*a*), the electrical impedance modulus *Z* (*b*), and the impedance diagram (*c*) of the Phz-Ag CP sample compressed at 38 MPa. It can be seen that in the entire frequency range studied $0 \le \varphi \le 90°$. At a frequency of less than 1 kHz the value of $\varphi \approx 0°$, and the electric impedance modulus is nearly independent of frequency and equal to ~ 8 mOhm, i.e. the conductivity of the sample is ohmic and is ~125 S. The frequency range from 1 to 100 kHz can be considered an intermediary. There is a sharp and non-linear increase in φ and *Z*, and, as it follows from Fig. 3,*c*, the increase in *Z* with rising frequency is mainly due to the increase in the imaginary part of the impedance Im*Z*. Finally, in the high-frequency region, the value of φ stabilizes near 90°, but the value of Z grows linearly with increasing frequency. This behavior of the *Z*(*f*) dependence in the high-frequency region indicates the inductive type of conductivity, because $Z = 2\pi fL$, where *L* is the inductance of the sample. Using this relation, we obtain that at frequencies above 100 kHz the value of *L* will be ~ 60 nH. The linear, close to vertical shape of the impedance diagram of the studied sample indicates that its conductivity is not related to any diffusion processes or to the influence of interphase boundaries (in this situation, these are the boundaries of microcrystallites in contact with each other) [15].

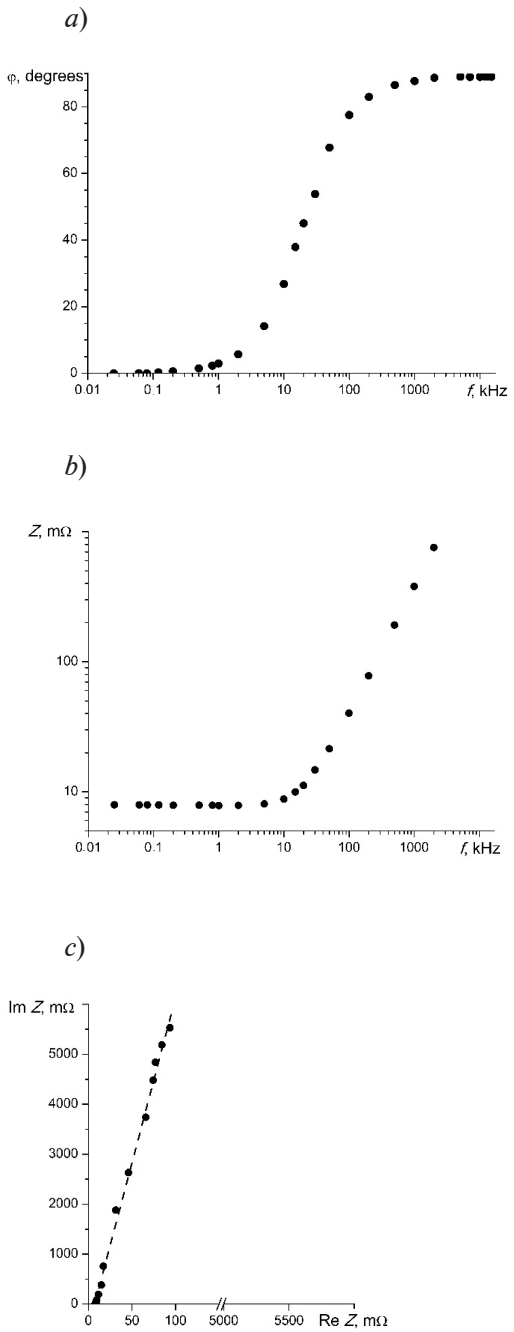

Fig. 3. Frequency dependences of electrical impedance modulus Z (*a*), phase angle φ (*b*) and impedance diagram (*c*) of Phz-Ag sample produced at a pressure of 38 MPa (data at room temperature)

The electrical equivalent circuit of this sample can be represented as a series-connected active resistance and inductance.

Let us consider the possible reasons for the appearance of metallic conductivity in the studied Phz-Ag CP samples, as well as the ohmic and inductive nature of their conductivity in the low- and high-frequency regions, respectively. In our opinion, the formation of thin silver films on the surface of microcrystals can be considered as one of the reasons.

We noted above that there are conglomerates of metallic silver ~10 nm in size on the surface of Phz-Ag microcrystals. Therefore, the presence of smaller silver clusters, not recorded by SEM, but forming conductive metal films in the shape of individual strips, seems very likely. Note that the authors [15] point to the possibility of formation of silver interlayers also between individual phenazine ligands that form a microcrystallite. Here it should be emphasized that the conductive properties of metal clusters are retained even when their size is reduced down to 1 nm [16]. It is known that the conductivity of metallic films formed from nanoscale clusters is significantly lower than that of their bulk analogues. For film thickness less than 40 nm, it is estimated to be no more than 10^4 S/cm and weakly dependent on the film thickness [17, 18]. With regard to the considered situation, we can assume that during pressing the plates of Phz-Ag microcrystals are stacked laterally on each other, providing a good overlap of the metal strips and a sufficiently high level of conductivity. As the compression pressure increases, the number of overlaps increases, which leads to the emergence of conductive wire-like microchannels piercing through the polymer sample. Such channels can be considered as microwires connecting the opposite sides of the tablet. They are characterized by a finite value of conductivity and inductance.

Let us consider the possible causes of metallic conductivity in the investigated Phz-Ag samples, as well as the ohmic and inductive nature of their conductivity, respectively in the low- and high-frequency regions.

The most likely cause is the formation of thin films of silver on the surfaces of the microcrystals. It was noted above that conglomerates of silver metal about 10 nm in size are present on the surfaces of Phz-Ag microcrystals. Therefore, the presence of smaller silver clusters that are not fixed by SEM but form conductive metal films in the form of individual stripes seems very likely. It should be noted that the authors of [16] point out that silver interlayers can also occur between the individual phenazine ligands that form the microcrystallite. It should be emphasised here that the conductive properties of metal clusters are retained when their size is reduced down to 1 nm [17]. It is known that the specific electrical conductivity of metal films formed from nanoscale clusters is significantly lower than that of their bulk counterparts. For film

thicknesses below 40 nm, it is estimated to be no more than 10^4 S/cm and weakly dependent on film thickness [18, 19]. In the situation under consideration, it can be assumed that during the pressing process the plates of Phz-Ag microcrystals stack laterally on top of each other, ensuring good overlapping of the metal stripes and a sufficiently high level of conductivity. As the pressure increases, the number of overlaps also increases, creating conductive filament-like microchannels that penetrate the polymer sample. Such channels can be thought of as microwires connecting opposite sides of the tablet, and it is these that determine the conductivity and inductance of the samples under investigation.

Conclusion

We carried out an experimental study of the effect of temperature on the specific conductivity and the Seebeck coefficient of a novel phenazine-silver coordination polymer, which demonstrates that the conductivity of this CP is of metallic nature. The conductivity value depends on the pressure at which the Phz-Ag tablet is prepared, and reaches a value of ~ 1300 S/cm, which is comparable to the highest CP conductivity value achieved to date. The metallic nature of the conductivity is due to the release of atomic silver during the synthesis of CP, its deposition on the surface of microcrystals and the formation of metallized strips on their surface. When the samples are pressed, electrical contact emerges between the individual microcrystals and conductive channels are formed inside the CP sample.

REFERENCES

1. **James S. L.,** Metal-organic frameworks, Chem. Soc. Rev. 32 (11) (2003) 276–288.
2. **Yutkin M. P., Dybtsev D. N., Fedin V. P.,** Homochiral porous metal-organic coordination polymers: synthesis, structure and functional properties, Rus. Chem. Rev. 80 (11) (2011) 1009–1034.
3. **Xie L. S., Skorupskii G., Dincă** M., Electrically conductive metal-organic frameworks, Chem. Rev. 120 (16) (2020) 8536–8580.
4. **Wang C., Liu D., Lin W.,** Metal-organic frameworks as a tunable platform for designing functional molecular materials, J. Am. Chem. Soc. 135 (36) (2013) 13222–13234.
5. **Huang X., Sheng P., Tu Z., et al.,** A two-dimensional π–d conjugated coordination polymer with extremely high electrical conductivity and ambipolar transport behavior, Nat. Commun. 6 (1) (2015) 7408.
6. **Dou J. H., Sun L., Ge Y., et al.,** Signature of metallic behavior in the metal-organic frameworks M_3(hexaiminobenzene)$_2$ (M = Ni, Cu), J. Am. Chem. Soc. 139 (39) (2017) 13608–13611.
7. **Kung C. W., Otake K., Buru C. T., et al.,** Increased electrical conductivity in a mesoporous metal-organic framework featuring metallacarboranes guests, J. Am. Chem. Soc. 140 (11) (2018) 3871–3875.
8. **Wu Z., Adekoya D., Huang X., et al.,** Highly conductive two-dimensional metal-organic frameworks for resilient lithium storage with superb rate capability, ACS Nano. 14 (9) (2020) 12016–12026.
9. **Sengupta A., Datta S., Su C., et al.,** Tunable electrical conductivity and magnetic property of the two dimensional metal organic framework [Cu(TPyP)$Cu_2(O_2CCH_3)_4$], ACS Appl. Mater. Interfaces. 8 (25) (2016) 16154–16159.
10. **Aubrey M. L., Kapelewski M. T., Melville J. F., et al.,** Chemiresistive detection of gaseous hydrocarbons and interrogation of charge transport in Cu[Ni(2,3-Pyrazinedithiolate)$_2$] by gas adsorption, J. Am. Chem. Soc. 141 (12) (2019) 5005–5013.
11. **Sapurina I. Y., Shishov M. A., Bursian A. E., et al.,** Coordination polymer based on phenazine ligands and silver with two-dimensional organization and high conductivity, Biointerface Res. Appl. Chem. 13 (6) (2023) 6577–6592.
12. **Seth K., Roy S. R., Chakraborti A. K.,** Synchronous double C–N bond formation via C–H activation for a novel synthetic route to phenazine, Chem. Commun. 52 (5) (2016) 922–925.
13. **Grigoriev I. S., Meilikhov, E. Z.,** Handbook of physical quantities, 1st edition, CRC Press, Boca Raton, Florida, USA, 1997.
14. **Kurelchuk U. N., Vasiliev O. S., Borisyuk P. V.,** *Ab initio* calculation of the thermoelectric coefficients for nanocluster lattices of noble metals, Nuclear Physics and Engineering. 9 (1) (2018) 99–102 (in Russian).
15. **Macdonald R. J., Johnson W. B.,** Fundamental of impedance spectroscopy, In book: Barsukov E., Macdonald R. J. (Eds.) Impedance spectroscopy: Theory, experiment and applications. 2nd Edition, John Wiley & Sons, Inc., New Jersey, USA, 2005.

16. **Itaya T., Ichihara M., Sugibayashi M., et al.,** Very unique liquid crystalline phase structures having two-dimensional silver sheet for the adducts of phenazine and silver alkylsulfonates, Mol. Cryst. Liq. Cryst. 503 (1) (2009) 69–80.

17. **Borman V. D., Borisyuk P. V., Vasiliev O. S., et al.,** Observation of electron localization in rough gold nanoclusters on the graphite surface, JETP Lett., 86 (6) (2007) 393–397.

18. **Antonets I. V., Kotov L. N., Nekipelov S. V., Golubev Y. A.,** Nanostructure and conductivity of thin metal films, Technical Physics. 49 (3) (2004) 306–309.

19. **Bennett H. E., Peck R. L., Burge D. K., Bennett J. M.,** Formation and growth of tarnish on evaporated silver films, J. Appl. Phys. 40 (8) (1969) 3351–3360.

СПИСОК ЛИТЕРАТУРЫ

1. **James S. L.** Metal-organic frameworks // Chemical Society Reviews. 2003. Vol. 32. No. 11. Pp. 276–288.

2. **Юткин М. П., Дыбцев Д. Н., Федин В. П.** Пористые гомохиральные металл-органические координационные полимеры: синтез, строение и функциональные свойства // Успехи химии. 2011. Т. 80. № 11. С. 1061–1096.

3. **Xie L. S., Skorupskii G., Dincă**, M. Electrically conductive metal-organic frameworks // Chemical Reviews. 2020. Vol. 120. No. 16. Pp. 8536–8580.

4. **Wang C., Liu D., Lin W.** Metal-organic frameworks as a tunable platform for designing functional molecular materials // Journal of the American Chemical Society. 2013. Vol. 135. No. 36. Pp. 13222–13234.

5. **Huang X., Sheng P., Tu Z., et al.** A two-dimensional π–d conjugated coordination polymer with extremely high electrical conductivity and ambipolar transport behavior // Nature Communications 2015. Vol. 6. No. 1. P. 7408.

6. **Dou J. H., Sun L., Ge Y., Li W., Hendon C. H., Li J., Dincă** M. Signature of metallic behavior in the metal-organic frameworks M_3 (hexaiminobenzene)$_2$ (M = Ni, Cu) // Journal of the American Chemical Society. 2017. Vol. 139. No. 39. Pp. 13608–13611.

7. **Kung C. W., Otake K., Buru C. T., Goswami S., Cui Y., Hupp J. T., Farha O. K.** Increased electrical conductivity in a mesoporous metal-organic framework featuring metallacarboranes guests // Journal of the American Chemical Society. 2018. Vol. 140. No. 11. Pp. 3871–3875.

8. **Wu Z., Adekoya D., Huang X., Kiefel M. J., Xie J., Xu W., Zhang S.** Highly conductive two-dimensional metal-organic frameworks for resilient lithium storage with superb rate capability // ACS Nano. 2020. Vol. 14. No. 9. Pp. 12016–12026.

9. **Sengupta A., Datta S., Su C., Herng T. S., Ding J., Vittal J. J., Loh K. P.** Tunable electrical conductivity and magnetic property of the two dimensional metal organic framework [Cu(TPyP) $Cu_2(O_2CCH_3)_4$] // ACS Applied Materials and Interfaces. 2016. Vol. 8. No. 25. Pp. 16154–16159.

10. **Aubrey M. L., Kapelewski M. T., Melville J. F., Oktawiec J., Presti D., Gagliardi L., Long J. R.** Chemiresistive detection of gaseous hydrocarbons and interrogation of charge transport in Cu[Ni(2,3-Pyrazinedithiolate)$_2$] by gas adsorption // Journal of the American Chemical Society. 2019. Vol. 141. No. 12. Pp. 5005–5013.

11. **Sapurina I. Y., Shishov M. A., Bursian A. E., Kompan M. E., Malyshkin V. G., Pizurova N.** Coordination polymer based on phenazine ligands and silver with two-dimensional organization and high conductivity // Biointerface Research in Applied Chemistry. 2023. Vol. 13. No. 6. Pp. 6577–6592.

12. **Seth K., Roy S. R., Chakraborti A. K.** Synchronous double C–N bond formation via C–H activation for a novel synthetic route to phenazine // Chemical Communications. 2016. Vol. 52. No. 5. Pp. 922–925.

13. **Григорьев И. С., Мейлихов Е. З.** Физические величины. Справочник М.: Энергоатомиздат. 1991. 1232 с.

14. **Курельчук У. Н., Васильев О. С., Борисюк П. В.** Первопринципный расчет термоэлектрических коэффициентов для нанокластерных решеток благородных металлов // Ядерная физика и инжиниринг. 2018. Т. 9. № 1. С. 99 –102.

15. **Macdonald R. J., Johnson W. B.** Fundamental of impedance spectroscopy // Barsukov E., Macdonald R. J. (Eds.) Impedance spectroscopy: Theory, experiment and applications. 2nd Edition, New Jersey, USA: John Wiley & Sons, Inc., 2005.

16. **Itaya T., Ichihara M., Sugibayashi M., Tai L. H., Ohta K.** Very unique liquid crystalline phase structures having two-dimensional silver sheet for the adducts of phenazine and silver alkylsulfonates // Molecular Crystals and Liquid Crystals. 2009. Vol. 503. No. 1. Pp. 69–80.

17. **Борман В. Д., Борисюк П. В., Васильев О. С., Пушкин М. А., Тронин В. Н., Тронин И. В., Троян В. И., Скородумова Н. В., Йоханссон Б.** Наблюдение локализации электронов в шероховатых нанокластерах золота на поверхности графита // Письма в Журнал экспериментальной и теоретической физики. 2007. Т. 86. № 6. С. 450–455.

18. **Антонец И. В., Котов Л. Н., Некипелов С. В., Голубев Е. А.** Особенности наноструктуры и удельной проводимости тонких пленок различных металлов // Журнал технической физики. 2004. Т. 74. № 3. С. 24–27.

19. **Bennett H. E., Peck R. L., Burge D. K., Bennett J. M.** Formation and growth of tarnish on evaporated silver films // Journal of Applied Physics. 1969. Vol. 40. No. 8. Pp. 3351–3360.

THE AUTHORS

TRETYAKOV Artem A.
Peter the Great St. Petersburg Polytechnic University
29 Politechnicheskaya St., St. Petersburg, 195251, Russia
tretartem@gmail.com
ORCID: 0000-0001-9050-4453

KAPRALOVA Viktoria M.
Peter the Great St. Petersburg Polytechnic University
29 Politechnicheskaya St., St. Petersburg, 195251, Russia
kapralova2006@yandex.ru
ORCID: 0000-0001-9050-4453

SAPURINA Irina Yu.
Institute of Macromolecular Compounds of RAS
31 Bolshoy Ave. V.O., St. Petersburg, 199004, Russia
sapurina@mail.ru
ORCID: 0000-0001-9050-4453

SUDAR Nicolay T.
Peter the Great St. Petersburg Polytechnic University
29 Politechnicheskaya St., St. Petersburg, 195251, Russia
sudar53@mail.ru
ORCID: 0000-0001-9050-4453

SHISHOV Mikhail A.
Peter the Great St. Petersburg Polytechnic University
29 Politechnicheskaya St., St. Petersburg, 195251, Russia
shv_misha@mail.ru
ORCID: 0000-0001-5100-2565

СВЕДЕНИЯ ОБ АВТОРАХ

ТРЕТЬЯКОВ Артём Александрович – *аспирант Высшей школы электроники и микросистемной техники Санкт-Петербургского политехнического университета Петра Великого.*
195251, Россия, г. Санкт-Петербург, Политехническая ул., 29
tretartem@gmail.com
ORCID: 0000-0001-9050-4453

КАПРАЛОВА Виктория Маратовна – *кандидат физико-математических наук, доцент Высшей школы электроники и микросистемной техники Санкт-Петербургского политехнического университета Петра Великого.*
195251, Россия, г. Санкт-Петербург, Политехническая ул., 29
kapralova2006@yandex.ru
ORCID: 0000-0001-9050-4453

САПУРИНА Ирина Юрьевна – *доктор химических наук, старший научный сотрудник Института высокомолекулярных соединений РАН, Санкт-Петербург, Россия.*
199004, Россия, г. Санкт-Петербург, Большой пр. В.О., 31
sapurina@mail.ru
ORCID: 0000-0001-9050-4453

СУДАРЬ Николай Тобисович – *доктор физико-математических наук, профессор Высшей школы электроники и микросистемной техники Санкт-Петербургского политехнического университета Петра Великого.*
195251, Россия, г. Санкт-Петербург, Политехническая ул., 29
sudar53@mail.ru
ORCID: 0000-0001-9050-4453

ШИШОВ Михаил Александрович – *кандидат технических наук, старший научный сотрудник научно-исследовательской лаборатории «Полимерные материалы для тканевой инженерии и трансплантологии» Санкт-Петербургского политехнического университета Петра Великого.*
195251, Россия, г. Санкт-Петербург, Политехническая ул., 29
shv_misha@mail.ru
ORCID: 0000-0001-5100-2565

Received 16.01.2023. Approved after reviewing 06.02.2023. Accepted 09.02.2023.
Статья поступила в редакцию 16.01.2023. Одобрена после рецензирования 06.02.2023. Принята 09.02.2023.

© Peter the Great St. Petersburg Polytechnic University, 2023

Original article
UDC 621.52
DOI: https://doi.org/10.18721/JPM.16207

FORMATION OF Mn_4Si7 FILMS BY MAGNETRON SPUTTERING AND A WIDE RANGE OF THEIR THERMOELECTRIC PROPERTIES

I. R. Bekpulatov[1]✉, *V. V. Loboda*[2], *M. T. Normuradov*[3], *B. D. Donaev*[4], *I. Kh. Turapov*[1]

[1] Tashkent State Technical University, Tashkent, Uzbekistan;

[2] Peter the Great St. Petersburg Polytechnic University, St. Petersburg, Russia;

[3] Karshi State University, Karshi, Uzbekistan;

[4] Karshi Engineering-Economics Institute, Karshi, Uzbekistan

✉ bekpulatov85@rambler.ru

Abstract. In the paper, films of higher manganese silicide Mn_4Si_7 have been made and a lot of their properties have been investigated. The composition and structure of the films formed by ion-plasma magnetron sputtering were examined by scanning electron microscopy and X-ray analysis. The temperature dependences of film resistivity (by the four-probe method), of their Seebeck coefficient (by the two-probe method), as well as their Hall constant and optical reflectivity spectra (at room temperature). Their thermoelectric figure of merit, the energy-gap width (0.66 eV), charged-particle density and mobility, etc., were calculated. The properties of the films in the amorphous and polycrystalline phases were compared. The thermopower of the Mn_4Si_7 film was established to increase by about 6 times during the transition from the amorphous phase to the polycrystalline one. The results obtained indicate that it is possible to use this film in heat wave detectors.

Keywords: magnetron sputtering, cleaning of silicon wafer, resistivity, silicon, thermoelectric properties

Funding: The studies are being done within the Fundamental Scientific Project No. F-OT-2021-422 of The Republic of Uzbekistan and The Ministry of Science and Higher Education of the Russian Federation. The research is funded by the Ministry of Science and Higher Education of the Russian Federation within the framework of the program "The World-Class Research Centre: Advanced Digital Technologies" (Contract No. 075-15-2022-311 dated April 20, 2022).

Citation: Bekpulatov I. R., Loboda V. V., Normuradov M. T., Donaev B. D., Turapov I. Kh., Formation of Mn_4Si_7 films by magnetron sputtering and a wide range of their thermoelectric properties, St. Petersburg State Polytechnical University Journal. Physics and Mathematics. 16 (2) (2023) 78–88. DOI: https://doi.org/10.18721/JPM.16207

This is an open access article under the CC BY-NC 4.0 license (https://creativecommons.org/licenses/by-nc/4.0/)

Научная статья
УДК 621.52
DOI: https://doi.org/10.18721/JPM.16207

ПОЛУЧЕНИЕ ПЛЕНОК Mn_4Si_7 МЕТОДОМ МАГНЕТРОННОГО РАСПЫЛЕНИЯ И ШИРОКИЙ СПЕКТР ИХ ТЕРМОЭЛЕКТРИЧЕСКИХ СВОЙСТВ

И. Р. Бекпулатов[1]✉, *В. В. Лобода*[2], *М. Т. Нормурадов*[3], *Б. Д. Донаев*[4], *И. Х. Турапов*[1]

© Bekpulatov I. R., Loboda V. V., Normuradov M. T., Donaev B. D., Turapov I. Kh., 2023. Published by Peter the Great St. Petersburg Polytechnic University.

[1] Ташкентский государственный технический университет, г. Ташкент, Узбекистан;
[2] Санкт-Петербургский политехнический университет Петра Великого, Санкт-Петербург, Россия;
[3] Каршинский государственный университет, г. Карши, Узбекистан;
[4] Каршинский инженерно-экономический институт, г. Карши, Узбекистан
✉ bekpulatov85@rambler.ru

Аннотация. В работе были изготовлены пленки высшего силицида марганца Mn_4Si_7 и изучен широкий спектр их свойств. Состав и структура пленок, полученных методом ионно-плазменного магнетронного распыления, исследовались методами сканирующей электронной микроскопии и рентгенофазового анализа. Были измерены температурные зависимости удельного сопротивления пленок (четырехзондовый метод), их коэффициента Зеебека (двухзондовый метод), а также постоянная Холла и спектры оптического отражения (при комнатной температуре). Рассчитаны термоэлектрическая добротность, ширина запрещенной зоны (0,66 эВ), концентрация и подвижность заряженных частиц и др. параметры. Проведено сравнение свойств пленок, находящихся в аморфной и поликристаллической фазах. Установлено, что термоэдс пленки при переходе из аморфного состояния в поликристаллическое увеличивается примерно в 6 раз. Полученные результаты доказывают, что пленку можно применять в детекторах тепловолнового излучения.

Ключевые слова: магнетронные распыление, высший силицид марганца, удельное сопротивление, коэффициент Зеебека, термоэлектрические свойства

Финансирование: Работа осуществляется в рамках Фундаментального научного проекта № Ф-ОТ-2021-422 Республики Узбекистан и Министерства науки и образования Российской Федерации. Исследование финансируется Министерством науки и образования Российской Федерации в рамках программы «Исследовательский класс мирового уровня: передовые цифровые технологии» (контракт № 075-15-2022-311 от 20 апреля 2022 года).

Ссылка для цитирования: Бекпулатов И. Р., Лобода В. В., Нормурадов М. Т., Донаев Б. Д., Турапов И. Х. Получение пленок Mn_4Si_7 с методом магнетронного распыления и широкий спектр их термоэлектрических свойств // Научно-технические ведомости СПбГПУ. Физико-математические науки. 2023. Т. 16. № 2. С. 78–88. DOI: https://doi.org/10.18721/ JPM.16207

Статья открытого доступа, распространяемая по лицензии CC BY-NC 4.0 (https://creativecommons.org/licenses/by-nc/4.0/)

Introduction

Many research centers around the world are currently conducting studies on the creation of environmentally friendly and low-cost energy sources. In this regard, great results have been achieved in the conversion of wind, light and heat energy into electrical one, which has led to an increase in the efficiency of the generated photovoltaic and thermoelectric elements [1 – 8]. In addition, scientific research on the creation of new types of photo- and thermoelectric films has been constantly developing [9 – 14]. Among these materials, the most promising one is a film based on a higher manganese silicide (HMS), whose thermoelectric figure of merit can reach 0.4 in the temperature range of 20 – 700 °C [15 – 21]. A Mn_4Si_7 thin film can be used for fabrication high-quality thermal elements and show the possibility of creating nanostructures with high thermal properties based on fundamental research on various physical properties, quantum effects, and size factors. Sensitivity cells based on HMS structures are also promising when using highly sensitive receivers of electromagnetic waves in visible and IR fields.

The goal of the present paper is to form the Mn_4Si_7 film by the ion-plasma magnetron sputtering method and to study its thermoelectric properties.

© Бекпулатов И. Р., Лобода В. В., Нормурадов М. Т., Донаев Б. Д., Турапов И. Х., 2023. Издатель: Санкт-Петербургский политехнический университет Петра Великого.

Material and methods

Magnetron sputtering synthesis of HMS films is carried out using SiO_2/Si substrate. Before the formation of the HMS film, the SiO_2/Si substrate was cleaned in two stages:

1. The cleaning of the silicon wafers surface SiO_2/Si (d = 60 mm) was carried out using an ammonia-peroxide mixture at a temperature of 60 – 70 °C, washing in deionized water, drying in a centrifuge;

2. The vacuum treatment (cleaning) of the silicon wafer surface was carried out using an argon plasma flow on EPOS-PVD-DESK-PRO magnetron sputtering machine. The plasma flow was created by a source of ions with a cold cathode at a voltage of 2 – 3 kV and a current of up to 100 mA during 3 – 5 min. A group of plates (2 – 4 pieces) was located on a rotating tool during the treatment.

HMS films were formed using an EPOS-PVD-DESK-PRO magnetron sputtering machine at a pressure of 10^{-4} Pa and room temperature. The purity of Mn_4Si_7 target was 99,5 %. The diameter and the thickness of the target were 76 mm and 6 mm, respectively [22, 23].

The composition and structure of the target were studied by Quanta 200 3D scanning electron microscope (SEM) from the Dutch Company FEI before placing the target into the magnetron machine (Fig. 1).

a) *b*)

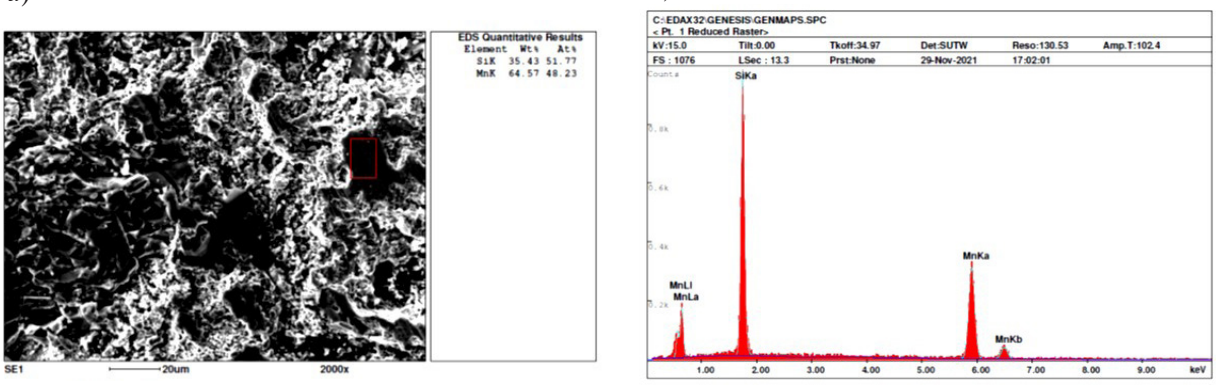

Fig. 1. The results of studying the Mn4Si7 target with a scanning electron microscope (SEM): the surface image (*a*) and energy dispersive *X*-ray spectrum (*b*)

The thermoelectric properties (the resistivity and Seebeck coefficient) of the manufactured Mn4Si7 film were determined by placing it in a vacuum of 10 Pa, using the four-probe method and two-probe one, respectively [24].

It is known that the thermoelectric figure of merit ZT of thermoelectric materials is a dimensionless quantity determining by the following formula:

$$ZT = \alpha^2 \sigma T / \kappa, \quad (1)$$

where α, μV/K, is the Seebeck coefficient; σ, S/cm, is the electrical conductivity; κ, W/(m·K), is the thermal conductivity; T, K, is the temperature [25 – 27].

Results and discussion

The Mn_4Si_7 film formed by magnetron sputtering is in an amorphous phase before thermal annealing; this was identified by electron microscope. Fig. 2 presents the SEM-images of the Mn_4Si_7 film before and after annealing. Silicon and manganese atoms deposited on silicon oxide almost completely cover the substrate. The annealing of the Mn_4Si_7 film was carried out at 620 K for 1 h. at a pressure of 10^{-3} Pa using an equipment. The annealed film was cooled in vacuum to room temperature.

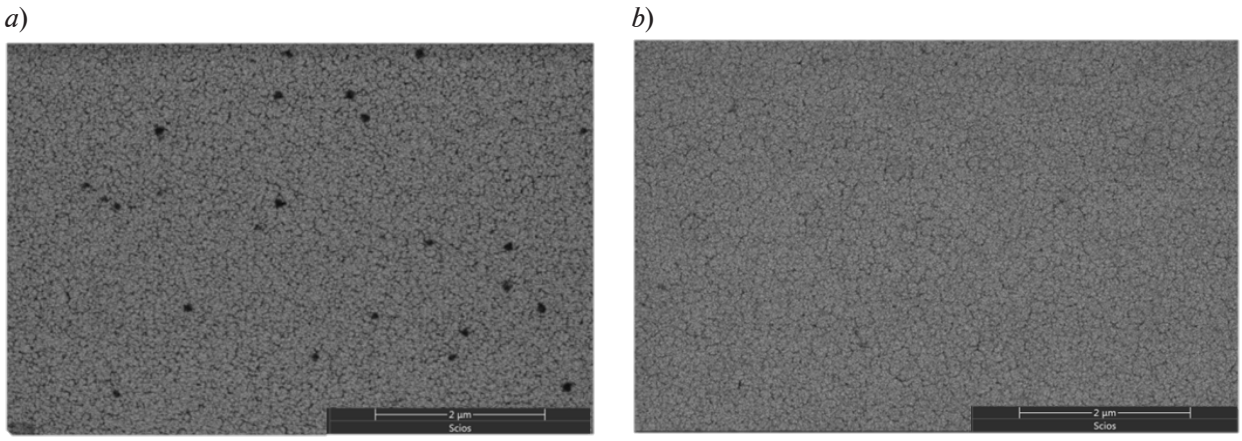

Fig. 2. SEM-images of the Mn4Si7 film surface before (*a*) and after (*b*) annealing at 620 K and 10^{-3} Pa

The resistivity of the formed Mn_4Si_7 film was $2\cdot10^{-5}$ Ω·cm at room temperature; when heated to a temperature of 750 K, its resistivity rose to $5\cdot10^{-5}$ Ω·cm (see Fig. 3, *a*). The electrical conductivity of this film was $5.0\cdot10^4$ S/cm at room temperature. As evident from Fig. 3, *b*, its electrical conductivity dropped to $1.2\cdot10^4$ S/cm when heated to 750 K.

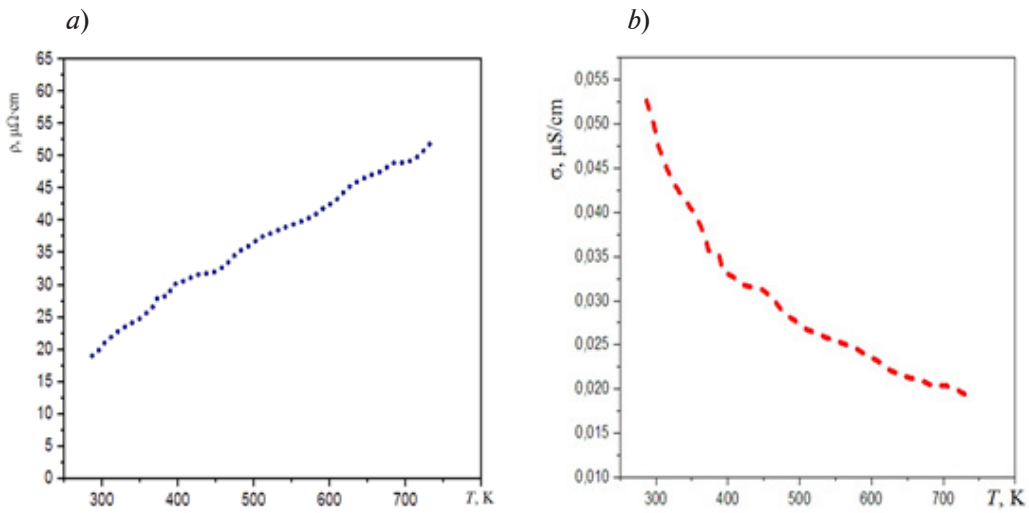

Fig. 3. Temperature dependences of the resistivity (*a*)
and electrical conductivity (*b*) for the Mn_4Si_7 film in amorphous phase

The graphs of the resistivity and electrical conductivity versus temperature for the Mn_4Si_7 annealed film are presented in Fig. 4. It was $7.86\cdot10^{-6}$ Ω·cm at room temperature, and when heated to 700 K, its resistivity dropped to $3.90\cdot10^{-6}$ Ω·cm (see Fig. 4, *a*). The electrical conductivity of this film was $1.2\cdot10^5$ S/cm at room temperature. When heated to 700 K, it rose to $2.7\cdot10^5$ S/cm (see Fig. 4, *b*).

As can be seen from this graphs, a decrease in resistivity with increasing temperature (see Fig. 4, *a*) and an increase in electrical conductivity (see Fig. 4, *b*) confirm that the film has a polycrystalline structure.

Fig. 5 presents temperature dependences of the Seebeck coefficient for the Mn_4Si_7 film in amorphous and polycrystalline phases. As evident from these graphs, the Seebeck coefficient in the case of the polycrystalline phase turned out to be approximately 6 times higher than that in the case of the amorphous one.

The thermoelectric figure of merit of the Mn_4Si_7 film was calculated by Eq. (1). Thermal conductivity value of the Mn_4Si_7 film was taken from Ref. [28].

The purification process concurrently enhances the σ and *S* values, and decreases the κ value for the Mn_4Si_7 samples, leading to an extraordinarily high thermoelectric figure of merit *ZT*. The

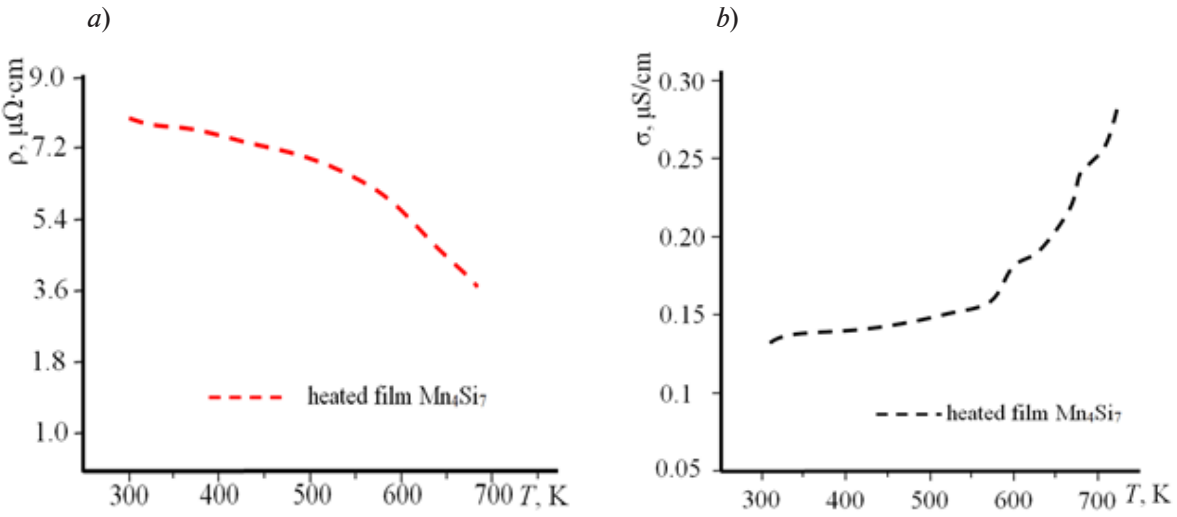

Fig. 4. Temperature dependences of the resistivity (*a*) and electrical conductivity (*b*) of the Mn_4Si_7 annealed film in polycrystalline phase

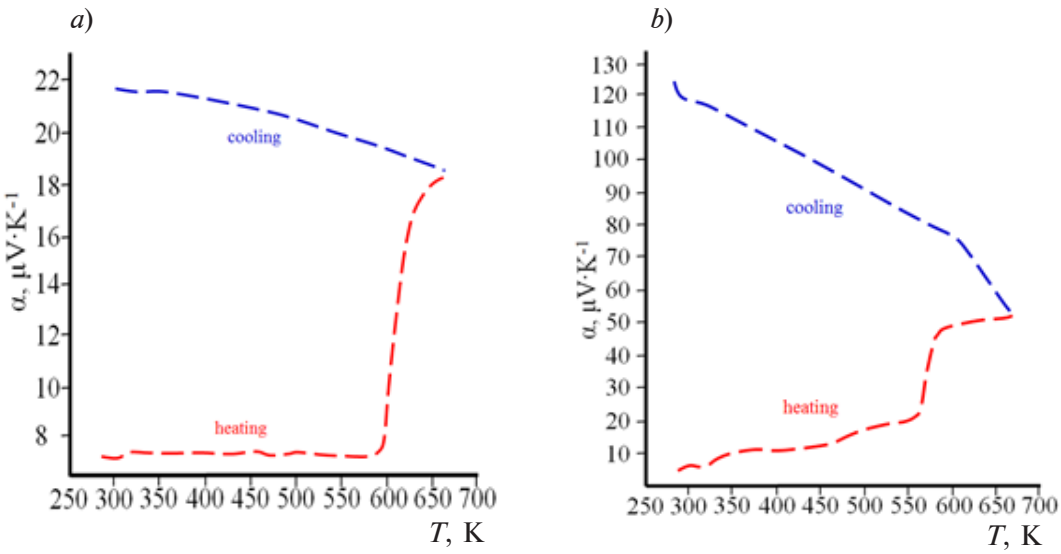

Fig. 5. Temperature dependences of the Seebeck coefficient for the Mn_4Si_7 film in amorphous (*a*) and polycrystalline (*b*) phases

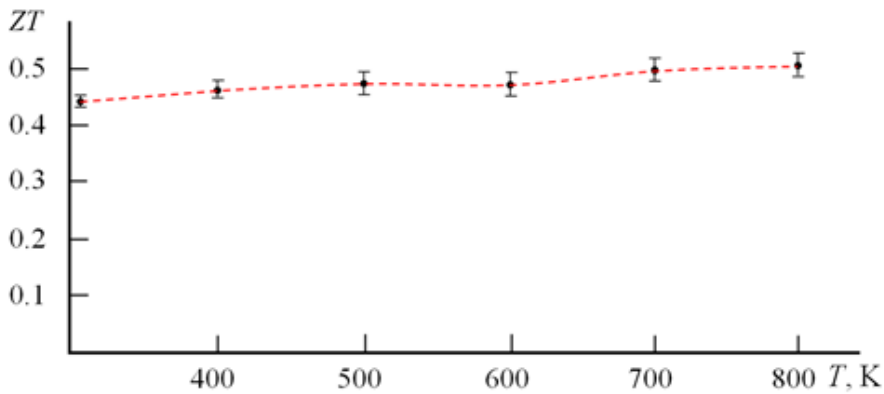

Fig. 6. Temperature dependence of *ZT* for the Mn_4Si_7 film in polycrystalline phase

corresponding curve for the Mn_4Si_7 film exhibits the maximum ZT ($(ZT)_{max}$), namely, about 0.5 at 800 K, and this is the highest value currently known and reported for thermoelectric systems (Fig. 6).

As a result of the experiments conducted with the HMS film, it was found that the thermoelectric properties of the film are better in the crystalline phase than in the amorphous one. This is due to the fact that the bond between manganese and silicon atoms is very weak and there are surface defects on the areas that are not completely covered of material. Surface defects of the film are disappeared as a result of structural relaxation and forming new bonds between the manganese and silicon atoms during the annealing, and the total structure acquires semiconductor properties.

Optical properties of the Mn_4Si_7/SiO_2 film were measured using an HR-4000 high-precision spectrometer according to the law of light reflection (Fig. 7). The graphs showed that the Mn_4Si_7 film had a high sensitivity in the visible and IR regions for the corresponding wavelengths. In addition, it is possible to determine the band gap of the Mn4Si7 silicide film from these data, using the Kubelka – Munk equation. The band gap of the film is 0.66 eV. Here α is the absorption coefficient, $h\nu$ (eV) is the photon energy, R (%) is the reflection coefficient, λ (nm) is the light wavelength [29, 30].

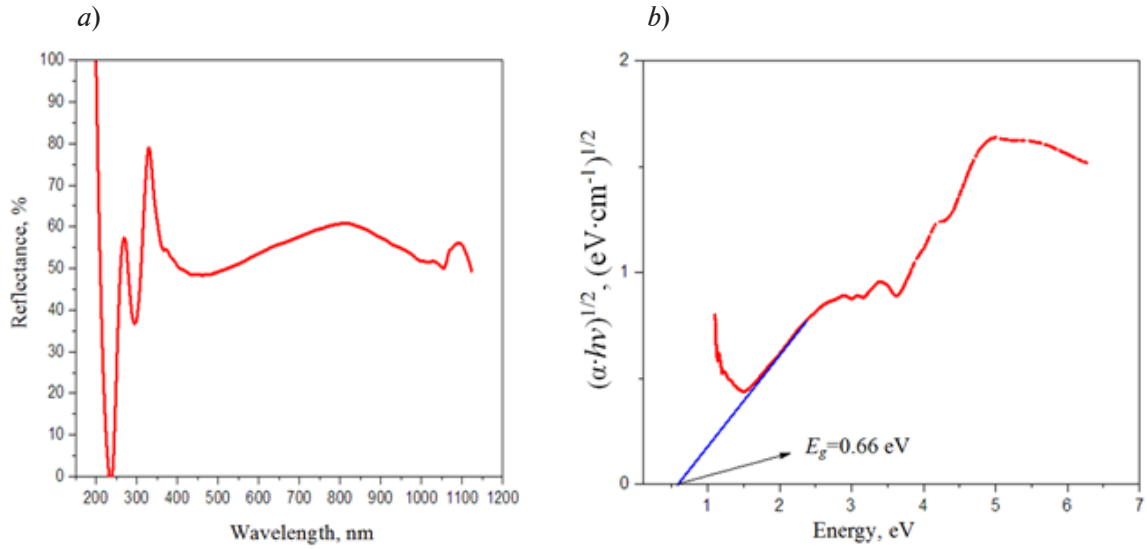

Fig. 7. The Mn_4Si_7 film: the graphs of the light reflection coefficient versus the light wavelength (*a*) and of the absorbed photon energy versus the incident photon one (*b*)

The probability of absorbing a photon depends on the likelihood of having a photon and an electron interact in such a way as to move from one energy band to another. For photons which have an energy very close to that of the band gap, the absorption is relatively low since only those electrons directly at the valence band edge can interact with the photon to cause absorption. As the photon energy increases, not just the electrons already having energy close to that of the band gap can interact with the photon. Therefore, a larger number of electrons can interact with the photon and result in the photon being absorbed.

The absorption coefficient α is related to the extinction coefficient k by the following formula:

$$\alpha = 4\pi k/\lambda, \quad (2)$$

Electrophysical properties of the Mn_4Si_7/SiO_2 film were measured on HMS-3000 Hall Measurement System. Obtained electrophysical parameters of the Mn_4Si_7 thin film are listed in Table.

Table

The obtained results on electrophysical properties of the Mn_4Si_7 film

Parameter	Unit	Value
Volumetric concentration of charged particles	cm^{-3}	$4.5 \cdot 10^{21}$
Mobility of charged particles	$cm^2/(V \cdot s)$	1.65
Surface resistance	Ω	313
Resistivity	Ω·cm	$7.83 \cdot 10^{-4}$
Hall coefficient	cm^3/C	$1.28 \cdot 10^{-3}$
Magnetoresistance	Ω	$1.73 \cdot 10^{-1}$
Surface concentration of charged particles	cm^{-2}	$1.2 \cdot 10^{17}$
Electrical conductivity	S/cm	$1.28 \cdot 10^{3}$

Summary

The paper has been studied a formation of Mn_4Si_7 (higher manganese silicide) films and their electrophysical properties. It was established that the thermoelectric power (the Seebeck coefficient) of the film increased during the transition from the amorphous phase to the nanocrystalline one. This effect is associated with the selective scattering of charge carriers at the boundaries of nanoclusters. The Seebeck coefficient of the film in the polycrystalline phase turned out to be approximately 6 times higher than that in the amorphous phase. The thermoelectric efficiency of Mn_4Si_7 film exhibited the maximum value ZT_{max} of approximately 0.5 at 800 K.

Moreover, it was revealed that Mn_4Si_7 films grown on a SiO_2/Si substrate had the highest conversion coefficient, and this is explained by the low thermal conductivity κ = 149 W/mK of SiO_2/Si. The films of Mn_4Si_7 on SiO_2/Si exhibited the high response speed, high sensitivity.

The results obtained indicate that the Mn_4Si_7 films can be recommended for use in thermal wave radiation detectors in the visible and infrared electromagnetic ranges.

REFERENCES

1. **Deng T., Xu Zh., Yamashita Y., et al.,** Modeling the effects of defect parameters on the performance of a *p*-$BaSi_2$/*n*-Si heterojunction solar cell, Sol. Energy Mater. Sol. Cells. 205 (February) (2020) 110244.

2. **Todorov T. K., Bishop D. M., Lee Y. S.,** Materials perspectives for next-generation low-cost tandem solar cells, Sol. Energy Mater. Sol. Cells. 180 (15 June) (2018) 350–357.

3. **Matsui T., Sai H., Saito K., Kondo M.,** High-efficiency thin-film silicon solar cells with improved light-soaking stability, Prog. Photovolt. 21 (6) (2013) 1363–1369.

4. **Müller J., Rech B., Springer J., Vanecek M.,** TCO and light trapping in silicon thin film solar cells, Sol. Energy. 77 (6) (2004) 917–930.

5. **Chopra K. L., Paulson P. D., Dutta V.,** Thin-film solar cells: an overview, Prog. Photovolt. 12 (2–3) (2004) 69–92.

6. **Shah A. V., Schade H., Vanecek M., et al.,** Thin-film silicon solar cell technology, Prog. Photovolt. 12 (2–3) (2004) 113–142.

7. **Nakamura T., Suemasu T., Takakura K., et al.,** Investigation of the energy band structure of orthorhombic $BaSi_2$ by optical and electrical measurements and theoretical calculations, Appl. Phys. Lett. 81 (6) (2002) 1032–1034.

8. **Kishino S., Imai T., Iida T., et al.,** Electronic and optical properties of bulk crystals of semiconducting orthorhombic BaSi2 prepared by the vertical Bridgman method, J. Alloys Compd. 428 (1–2) (2007) 22–27.

9. **Donaev S. B., Tashatov A. K., Umirzakov B. E.,** Effect of Ar^+-ion bombardment on the composition and structure of the surface of $CoSi_2$ / Si(111) nanofilms, J. Surf. Investig. 9 (2) (2015) 406–409.

10. **Lu Z., Zhou H., Ye C., et al.,** Fabrication of iron pyrite thin films and photovoltaic devices by sulfurization in electrodeposition method, Nanomaterials. 11 (11) (2021) 2844.

11. **Donaev S. B., Umirzakov B. E., Mustafaeva N. M.,** Emissivity of laser-activated Pd-Ba alloy, Tech. Phys. 64 (10) (2019) 1541–1543.

12. **Isakhanov Z. A., Umirzakov Y. E., Ruzibaeva M. K., Donaev S. B.,** Effect of the O^{2+}-ion bombardment on the TiN composition and structure, Tech. Phys. 60 (2) (2015) 313–315.

13. **Donaev S. B., Djurabekova F., Tashmukhamedova D. A., Umirzakov B. E.,** Formation of nanodimensional structures on surfaces of GaAs and Si by means of ion implantation, Phys. Status Solidi C. 12 (1–2) (2015) 89–93.

14. **Normuradov M. T., Rysbaev A. S., Bekpulatov I. R., et al.,** Formation and electronic structure of barium-monosilicide and barium-disilicide films, J. Surf. Investig. 15 (Suppl. 1) (2021) S211–S215.

15. **Saleemi M., Famengo A., Fiameni S., Toprak M.,** Thermoelectric performance of higher manganese silicide nanocomposites, J. Alloys Compd. 619. (15 January) (2015) 31–37.

16. **Joo S., Lee H., Jang J.,** Thermoelectric properties of higher manganese silicide films deposited by radio frequency magnetron co-sputtering, J. Alloys Compd. 747 (30 May) (2018) 603–610.

17. **Rysbaev A. S., Khuzhaniyazov Z. B., Rakhimov A. M., Bekpulatov I. R.**, Formation of nanosize silicides films on the Si (111) and Si (100) surfaces by low-energy ion implantation, Techn. Phys. 59 (10) (2014) 1526–1530.

18. **Bekpulatov I. R., Imanova G. T., Kamilov T. S., et al.,** Formation of *n*-type CoSi monosilicide film which can be used in instrumentation, Int. J. Mod. Phys. B. 36 (32) (2022) 2350164.

19. **Orekhov A. S., Kamilov T. S., Ibragimova B. V., Ivakin G. I., Klechkovskaya V. V.,** Structure of thermoelectric films of higher manganese silicide on silicon according to electron microscopy data, Semiconductors. 51 (6) (2017) 706–709.

20. **Kamilov T. S., Rysbaev A. S., Klechkovskaya V. V., et al.,** Influence of structural defects in silicon on formation of photosensitive heterostructures Mn_4Si_7-Si-Mn_4Si_7 and Mn_4Si_7-Si-M, Eurasian J. Phys. Funct. Mater. 2 (4) (2018) 360–366.

21. **Kamilov T. S., Rysbaev A. S., Klechkovskaya V. V., et al.,** The influence of structural defects in silicon on the formation of photosensitive Mn_4Si_7-Si(Mn)-Mn_4Si_7 and Mn_4Si_7-Si(Mn)-M heterostructures, Appl. Sol. Energy. 55 (6) (2019) 380–384.

22. **Liu H., She G., Huang X., et al.,** Synthesis and magnetic properties of Mn_4Si_7 and Si-Mn_4Si_7 axial heterostructure nanowire arrays, J. Phys. Chem. C. 117 (5) (2013) 2377–2381.

23. **Zolotarev V. M., Nikonorov N. V., Ignatiev A. I.,** Sovremennyye metody issledovaniya opticheskikh materialov. Chast II. Metody issledovaniya poverkhnosti opticheskikh materialov i tonkikh plenok [Modern methods of studying optical materials. Part II. Methods of studying the surface of optical materials and thin films], NIU ITMO, St. Petersburg, 2013 (in Russian).

24. **Mavrokefalos A., Pettes M. T., Zhou F., Shi L.,** Four-probe measurements of the in-plane thermoelectric properties of nanofilms, Rev. Sci. Instrum. 78 (3) (2007) 034901.

25. **Pitarch B. B., Gonjal J. P., Powell A., et al.,** Thermal conductivity, electrical resistivity, and dimensionless figure of merit (ZT) determination of thermoelectric materials by impedance spectroscopy up to 250 °C, J. Appl. Phys. 124 (2) (2018) 025105.

26. **Stevens K. R., Kanatzidis M. G., Johnsen S., Girard S. N.,** Investigation of the thermoelectric properties of metal chalcogenides with SnSe, Nanoscape. 7 (1) (2010) 52–57.

27. **Yin Y., Tiwari A.,** Understanding the effect of thickness on the thermoelectric properties of $Ca_3Co_4O_9$ thin films, Sci. Rep. 11 (2021) 6324.

28. **Choia S., Kuboa K., Uchiyamaa N., Takeuchi T.,** Thermoelectric properties of higher manganese silicide consolidated by flash spark plasma sintering technique, J. Alloys Compds. 921 (15 November) (2022) 166104.

29. **Riungu G. G., Mugo S. W., Ngaruiya J. M., et al.,** Optical band energy, Urbach energy and associated band tails of nano crystalline TiO_2 films at different annealing rates, Am. J. Nanosci. 7 (1) (2021) 28–34.

30. **Salah K. H.,** The determination of optical band and optical constants of MnO2 thin films prepared by spray pyrolysis, Berk. Fis. Indones. 5 (1) (2013) 1–6.

СПИСОК ЛИТЕРАТУРЫ

1. **Deng T., Xu Zh., Yamashita Y., Sato T., Toko K., Suemasu T.** Modeling the effects of defect parameters on the performance of a *p*-$BaSi_2$/*n*-Si heterojunction solar cell // Solar Energy Materials & Solar Cells. 2020. Vol. 205. February. P. 110244.

2. **Todorov T. K., Bishop D. M., Lee Y. S.** Materials perspectives for next-generation low-cost tandem solar cells // Solar Energy Materials & Solar Cells. 2018. Vol. 180. 15 June. Pp. 350–357.

3. **Matsui T., Sai H., Saito K., Kondo M.** High-efficiency thin-film silicon solar cells with improved light-soaking stability // Progress in Photovoltaics. 2013. Vol. 21. No. 6. Pp. 1363–1369.

4. **Müller J., Rech B., Springer J., Vanecek M.** TCO and light trapping in silicon thin film solar cells // Solar Energy. 2004. Vol. 77. No. 6. Pp. 917–930.

5. **Chopra K. L., Paulson P. D., Dutta V.** Thin-film solar cells: an overview // Progress in Photovoltaics. 2004. Vol. 12. No. 2–3. Pp. 69–92.

6. **Shah A. V., Schade H., Vanecek M., Meier J., Sauvain E. V., Wyrsch N., Kroll U., Droz C., Bailat J.** Thin-film silicon solar cell technology // Progress in Photovoltaics. 2004. Vol. 12. No. 2–3. Pp. 113–142.

7. **Nakamura T., Suemasu T., Takakura K., Hasegawa F., Wakahara A., Imai M.** Investigation of the energy band structure of orthorhombic $BaSi_2$ by optical and electrical measurements and theoretical calculations // Applied Physics Letters. 2002. Vol. 81. No. 6. Pp. 1032–1034.

8. **Kishino S., Imai T., Iida T., Nakaishi Y., Shinada M., Takanashi Y., Hamada N.** Electronic and optical properties of bulk crystals of semiconducting orthorhombic $BaSi_2$ prepared by the vertical Bridgman method // Journal of Alloys and Compounds. 2007. Vol. 428. No. 1–2. Pp. 22–27.

9. **Донаев С. Б., Ташатов А. К., Умирзаков Б. Е.** Влияние бомбардировки ионами Ar^+ на состав и структуру поверхности нанопленок $CoSi_2$ / Si(111) // Поверхность. Рентгеновские, синхротронные и нейтронные исследования. 2015. № 4. С. 95–98.

10. **Lu Z., Zhou H., Ye C., Chen S., Ning J., Halim M. A., Donaev S. B., Wang S.** Fabrication of iron pyrite thin films and photovoltaic devices by sulfurization in electrodeposition method // Nanomaterials. 2021. Vol. 11. No. 11. P. 2844.

11. **Донаев С. Б., Умирзаков Б. Е., Мустафаева Н. М.** Эмиссионные свойства сплава Pd-Ba, активированного лазерным облучением // Журнал технической физики. 2015. Т. 89. № 10. С. 1589–1591.

12. **Исаханов З. А., Умирзаков Ю. Е., Рузибаева М. К., Донаев С. Б.** Влияние бомбардировки ионов O^{2+} на состав и структуру TiN // Журнал технической физики. 2015. Т. 85. № 2. С. 156–158.

13. **Donaev S. B., Djurabekova F., Tashmukhamedova D. A., Umirzakov B. E.** Formation of nanodimensional structures on surfaces of GaAs and Si by means of ion implantation // Physica Status Solidi C. 2015. Vol. 12. No. 1–2. Pp. 89–93.

14. **Normuradov M. T., Rysbaev A. S., Bekpulatov I. R., Normuradov D. A., Tursunmetova Z. A.** Formation and electronic structure of barium-monosilicide- and barium-disilicide films // Journal of Surface Investigation. 2021. Vol. 15. No. 1 (Supplement). Pp. S211–S215.

15. **Saleemi M., Famengo A., Fiameni S., Toprak M.** Thermoelectric performance of higher manganese silicide nanocomposites. // Journal of Alloys and Compounds. 2015. Vol. 619. 15 January. Pp. 31–37.

16. **Joo S., Lee H., Jang J.** Thermoelectric properties of higher manganese silicide films deposited by radio frequency magnetron co-sputtering // Journal of Alloys and Compounds. 2018. Vol. 747. 30 May. Pp. 603–610.

17. **Рысбаев А. С., Хужаниязов Ж. Б., Рахимов А. М., Бекпулатов И. Р.** Формирование наноразмерных пленок силицидов на поверхности Si(111) и Si(100) методом низкоэнергетической ионной имплантации // Журнал технической физики. 2014. Т. 84. № 10. С. 107–111.

18. **Bekpulatov I. R., Imanova G. T., Kamilov T. S., Igamov B. D., Turapov I. K.** Formation of *n*-type CoSi monosilicide film which can be used in instrumentation // International Journal of Modern Physics B. 2022. Vol. 36. No. 32. P. 2350164.

19. **Орехов А. С., Камилов Т. С., Ибрагимова Б. В., Ивакин Г. И., Клечковская В. В.** Структура термоэлектрических пленок высшего силицида марганца на кремнии по данным электронной микроскопии // Физика и техника полупроводников. 2017. Т. 51. № 6. С. 740–743.

20. **Kamilov T. S., Rysbaev A. S., Klechkovskaya V. V., Orekhov A. S., Dzhuraev Sh. Kh., Kasymov A. S.** Influence of structural defects in silicon on formation of photosensitive heterostructures Mn_4Si_7-Si-Mn_4Si_7 and Mn_4Si_7-Si-M // Eurasian Journal of Physics and Functional Materials. 2018. Vol. 2. No. 4. Pp. 360–366.

21. **Kamilov T. S., Rysbaev A. S., Klechkovskaya V. V., Orekhov A. S., Igamov B. D., Bekpulatov I. R.** The influence of structural defects in silicon on the formation of photosensitive Mn_4Si_7-Si(Mn)-Mn_4Si_7 and Mn_4Si_7-Si(Mn)-M heterostructures // Applied Solar Energy. 2019. Vol. 55. No. 6. Pp. 380–384.

22. **Liu H., She G., Huang X., Qi X., Mu L., Meng X., Shi W.** Synthesis and magnetic properties of Mn_4Si_7 and Si-Mn_4Si_7 axial heterostructure nanowire arrays // The Journal of Physical Chemistry C. 2013. Vol. 117 No. 5. Pp. 2377–2381.

23. **Золотарев В. М., Никоноров Н. В., Игнатьев А. И.** Современные методы исследования оптических материалов. Часть II. Методы исследования поверхности оптических материалов и тонких пленок. СПб.: НИУ ИТМО, 2013. 166 с.

24. **Mavrokefalos A., Pettes M.T., Zhou F., Shi L.** Four-probe measurements of the in-plane thermoelectric properties of nanofilms // Review of Scientific Instruments. 2007. Vol. 78. No. 3. P. 034901.

25. **Pitarch B. B., Gonjal J. P., Powell A., Ziolkowski P., Canadas J. G.** Thermal conductivity, electrical resistivity, and dimensionless figure of merit (ZT) determination of thermoelectric materials by impedance spectroscopy up to 250 °C // Journal of Applied Physics. 2018. Vol. 124. No. 2. P. 025105.

26. **Stevens K. R., Kanatzidis M. G., Johnsen S., Girard S. N.** Investigation of the thermoelectric properties of metal chalcogenides with SnSe // Nanoscape. 2010. Vol. 7. No. 1. Pp. 52–57.

27. **Yin Y., Tiwari A.** Understanding the effect of thickness on the thermoelectric properties of $Ca_3Co_4O_9$ thin films // Scientific Reports. 2021. Vol. 11. P. 6324.

28. **Choia S., Kuboa K., Uchiyamaa N., Takeuchi T.** Thermoelectric properties of higher manganese silicide consolidated by flash spark plasma sintering technique // Journal of Alloys and Compounds. 2022. Vol. 921. 15 November. P. 166104.

29. **Riungu G. G., Mugo S. W., Ngaruiya J. M., John G. M., Mugambi N.** Optical band energy, Urbach energy and associated band tails of nano crystalline TiO_2 films at different annealing rates // American Journal of Nanosciences. 2021. Vol. 7. No. 1. Pp. 28–34.

30. **Salah K. H.** The determination of optical band and optical constants of MnO_2 thin films prepared by spray pyrolysis // Berkala Fisika Indonesia. 2013. Vol. 5. No. 1. Pp. 1–6.

THE AUTHORS

BEKPULATOV Ilkhom R.
Tashkent State Technical University
2 Universitetskaya St., Tashkent, 100095, Uzbekistan
bekpulatov85@rambler.ru
ORCID: 0000-0001-6311-6631

LOBODA Vera V.
Peter the Great St. Petersburg Polytechnic University
29 Politechnicheskaya St., St. Petersburg, 195251, Russia
vera_loboda@mail.ru
ORCID: 0000-0003-3103-7060

NORMURADOV Muradulla T.
Karshi State University
17 Kuchabog St., Karshi, 180103, Uzbekistan
m.normuradov@mail.ru
ORCID: 0000-0003-1771-0853

DONAEV Burkhon D.
Karshi Engineering-Economics Institute
225 Mustakillik Sqr., Karshi, 180100, Uzbekistan
donaev.sardor@gmail.com
ORCID: 0000-0001-7152-1610

TURAPOV Ilkhom Kh.
Tashkent State Technical University
2 Universitetskaya St., Tashkent, 100095, Uzbekistan
turapov_19_86@mail.ru
ORCID: 0000-0001-8946-4079

СВЕДЕНИЯ ОБ АВТОРАХ

БЕКПУЛАТОВ Ильхом Рустамович – *PhD, доцент кафедры общей физики Ташкентского государственного технического университета, г. Ташкент, Узбекистан.*
100095, Узбекистан, г. Ташкент, Университетская ул., 2.
bekpulatov85@rambler.ru
ORCID: 0000-0001-6311-6631

ЛОБОДА Вера Владимировна – *кандидат физико-математических наук, директор Высшей школы электроники и микросистемной техники Санкт-Петербургского политехнического университета Петра Великого, Санкт-Петербург, Россия.*
195251, Россия, г. Санкт-Петербург, Политехническая ул., 29
vera_loboda@mail.ru
ORCID: 0000-0003-3103-7060

НОРМУРАДОВ Мурадулла Тогаевич – *доктор физико-математических наук, профессор кафедры экспериментальной и теоретической физики Каршинского государственного университета, г. Карши, Узбекистан.*
180103, Узбекистан, г. Карши, ул. Кучабог, 17
m.normuradov@mail.ru
ORCID: 0000-0003-1771-0853

ДОНАЕВ Бурхон Донаевич – *кандидат физико-математических наук, доцент кафедры теоретической механики Каршинского инженерно-экономического института, г. Карши, Узбекистан.*
180100, Узбекистан, г. Карши, пл. Мустакиллик, 225
donaev.sardor@gmail.com
ORCID: 0000-0001-7152-1610

ТУРАПОВ Ильхом Химматалиевич – *кандидат физико-математических наук, доцент кафедры общей физики Ташкентского государственного технического университета, г. Ташкент, Узбекистан.*
100095, Узбекистан, г. Ташкент, Университетская ул., 2.
turapov_19_86@mail.ru
ORCID: 0000-0001-8946-4079

Received 16.01.2023. Approved after reviewing 25.01.2023. Accepted 26.01.2023.
Статья поступила в редакцию 16.01.2023. Одобрена после рецензирования 25.01.2023. Принята 26.01.2023.

© Peter the Great St. Petersburg Polytechnic University, 2023

Original article
UDC 621.52
DOI: https://doi.org/10.18721/JPM.16208

EMISSION, OPTICAL AND ELECTRICAL PROPERTIES OF GaInP/GaP NANOFILMS

G. M. Shirinov[1], *S. B. Donaev*[1]✉, *B. Y. Umirzakov*[1], *V. V. Loboda*[2]

[1] Tashkent State Technical University Named after Islam Karimov, Tashkent, Uzbekistan;

[2] Peter the Great St. Petersburg Polytechnic University, St. Petersburg, Russia

✉ sardor.donaev@gmail.com

Abstract. In order to search for materials with improved semiconductor properties, thin films of GaInP have been fabricated on the GaP surface (the molecular beam epitaxy and ion implantation procedures were used). These films were investigated by the Auger electron spectroscopy, ultraviolet photoelectron and light absorption ones. The energy and angle dependences of the secondary-electron-emission coefficient (SEEC) were obtained as well. An analysis of the experimental data allowed for the first time to determine the main energy-band and emission parameters of the $Ga_{0.6}In_{0.4}P$/GaP(111) nanofilm. The energy-gap width was found to be 1.85 eV, which was significantly less than that of the substrate GaP, and thus, the maximum value σ_{max} of the SEEC and the quantum yield K of photoelectrons (at $h\nu$ = 10.8 eV) values of the $Ga_{0.6}In_{0.4}P$/GaP system decreased slightly relative to the pure GaP.

Keywords: band gap, photoabsorption, energy-band parameter, nanofilm, heterostructure

Citation: Shirinov G. M., Donaev S. B., Umirzakov B. Y., Loboda V. V., Emission, optical and electrical properties of GaInP/GaP nanofilms, St. Petersburg State Polytechnical University Journal. Physics and Mathematics. 16 (2) (2023) 89–97. DOI: https://doi.org/10.18721/JPM.16208

This is an open access article under the CC BY-NC 4.0 license (https://creativecommons.org/licenses/by-nc/4.0/)

Научная статья
УДК 621.52
DOI: https://doi.org/10.18721/JPM.16208

ЭМИССИОННЫЕ, ОПТИЧЕСКИЕ И ЭЛЕКТРОФИЗИЧЕСКИЕ СВОЙСТВА НАНОПЛЕНОК GaInP/GaP

Г. М. Ширинов[1], *С. Б. Донаев*[1]✉, *Б. Е. Умирзаков*[1], *В. В. Лобода*[2]

[1] Ташкентский государственный технический университет им. Ислама Каримова, г. Ташкент, Узбекистан;

[2] Санкт-Петербургский политехнический университет Петра Великого, Санкт-Петербург, Россия

✉ sardor.donaev@gmail.com

Аннотация. С целью поиска материала с улучшенными полупроводниковыми свойствами были изготовлены тонкие пленки GaInP на поверхности GaP (использованы методы молекулярно-лучевой эпитаксии и ионной имплантации). Эти пленки были изучены методами оже-электронной спектроскопии, ультрафиолетовой фотоэлектронной спектроскопии, а также оптической спектроскопии поглощения

© Shirinov G. M., Donaev S. B., Umirzakov B. Y., Loboda V. V., 2023. Published by Peter the Great St. Petersburg Polytechnic University.

света. Были также получены энергетические и угловые зависимости коэффициентов вторичной электронной эмиссии. Анализ полученных экспериментальных данных позволил впервые определить основные параметры энергетических зон и эмиссионные параметры нанопленки $Ga_{0,6}In_{0,4}P/GaP$ (111). Установлено, что ширина запрещенной зоны пленки равна 1,85 эВ, что существенно меньше, чем таковая у подложки GaP; следовательно, максимальное значение коэффициента вторичной электронной эмиссии σ_{max} и квантовый выход фотоэлектронов K (при $h\nu$ = 10,8 эВ) системы $Ga_{0,6}In_{0,4}P/GaP$ немного уменьшаются относительно чистого GaP.

Ключевые слова: ширина запрещенной зоны, фотопоглощение, зонно-энергетические параметры, нанопленка, гетероструктура

Ссылка для цитирования: Ширинов Г. М., Донаев С. Б., Умирзаков Б. Е., Лобода В. В. Эмиссионные, оптические и электрофизические свойства нанопленок GaInP/GaP // Научно-технические ведомости СПбГПУ. Физико-математические науки. 2023. Т. 16. № 2. С. 89–97. DOI: https://doi.org/10.18721/ JPM.16208

Статья открытого доступа, распространяемая по лицензии CC BY-NC 4.0 (https://creativecommons.org/licenses/by-nc/4.0/)

Introduction

$A^{III}B^{V}$ binary semiconductors and multicomponent heterostructures based on them are widely used in the creation of various opto-, micro-, and nanoelectronic devices. In particular, multilayer structures with GaP, GaInP, AlGaInP layers are used and hold promise for the manufacture of laser diodes, solar cells, photovoltaic and optoelectronic devices. Particular interest is the preparation of ternary solid solutions such as $Ga_{1-x}Al_xAs$, $Ga_xIn_{1-x}P$ with an adjustable band gap [1 – 4]. At present, the composition, structure, optical and electronic properties of $Ga_{1-x}Al_xAs$ / GaAs multilayer structures fabricated by various epitaxy methods are well studied, which is associated with their wide use in various micro- and optoelectronic devices [5 – 10].

$Ga_xIn_{1-}xP$ alloys with a large band gap can potentially be used for high junction in tandem solar cells and yellow-green light emitting diodes [5, 6]. Due to the weak luminescence emission, studies of the optical properties of $Ga_xIn_{1-x}P$ alloys near the intersection of straight and indirect bands and in the region of indirect bands are more difficult than those for straight bands [5 – 7]. In addition, the absence of lattice-matched substrates and the ordering of effects complicate the studies. The authors of Ref. [8, 9] provided detailed information on the electronic structure of $Ga_xIn_{1-x}P$ ($0 \le x \le 1$).

Experimental results obtained in Ref. [10] showed that the luminescence efficiency of LEDs based on $Ga_xIn_{1-x}P$ significantly decreases at an emission wavelength shorter than 590 nm (< 2.1 eV). Despite the problems of carrier confinement for $Ga_xIn_{1-x}P$ alloys with a large band gap [11, 12], a simplified approach has been developed to simulate the degradation of luminescence intensity depending on the energy separation between direct and indirect bands [13].

In Ref. [14], $Ga_xIn_{1-x}P$ films were doped with tellurium ions with a concentration from $7\cdot10^{16}$ to $2\cdot10^{18}$ cm^{-2}. The study of the photoluminescence spectra showed that the transition from the indirect band to the direct one occurs at the temperatures between 40 and 100 K, and the direct emission of the band dominates in the photoluminescence (PL) spectra at room temperature.

In recent years, the most common method of fabrication nanofilms on the surfaces of semiconductor and dielectric films has been the low-energy ion implantation in an annealing test [15 – 19]. It has been established in private studies that when high-dose bombarded with argon ions Ar+, the surface is enriched with gallium (Ga) atoms, and when bombarded with metal ions (Me = Ba^{++} and Na^{+}), Ga and Me atoms are enriched. However, such studies have not yet been practically carried out for the case of gallium phosphide (GaP) implanted with low-energy In^{+} ions [20 – 22].

This paper is devoted to investigation of physical properties of GaInP/GaP(111) nanofilms formed by means of implantation of In^{+} ions into GaP.

© Ширинов Г. М., Донаев С. Б., Умирзаков Б. Е., Лобода В. В., 2023. Издатель: Санкт-Петербургский политехнический университет Петра Великого.

Materials and research methods

GaP(111) single-crystal samples were chosen as target of research. Prior to ion implantation, they were degassed under conditions of ultrahigh vacuum: the pressure $P = 10^{-7}$ Pa at the temperature $T = 900$ K for about 4 hours.

Molecular beam epitaxy (MBE) is the most promising method for growing these structures. In the process of MBE being a vacuum deposition, the film growth is determined mainly by the kinetic interaction of beams with the crystal surface, in contrast to other methods. Prior to MBE, the GaP(111) samples were degassed under conditions of ultrahigh vacuum ($P = 10^{-7}$ Pa).

Ultraviolet photoelectron spectroscopy (UVPS) was used, and the energy and angular dependences of the secondary electron emission (SEE) coefficients were obtained. Ultraviolet photoelectron spectra were recorded at photon energies $h\nu \approx 10.8$ eV. The photon source was a standard hydrogen-discharge lamp.

Results and discussion

The GaInP thin films with a thickness of 30 – 50 Å were formed by implanting In^+ ions into GaP(111) followed by annealing at $T \approx 950$ K. Fig. 1 shows the photoelectron spectra of GaP implanted with In^+ ions with an energy E_0 of 1 keV at a dose of $6 \cdot 10^{16}$ cm^{-2} and annealed at $T = 950$ K for 40 min. In this case, a nanocrystalline film of the $Ga_{0.6}In_{0.4}P$ type with a thickness of $d \approx 30 - 35$ Å was formed. These spectra reflect well the density distributions of electronic state in the valence band. One can see that the pure GaP spectrum exhibits maxima at binding energies $E_b \approx -0.8$, –2.2 and −4.0 eV, probably due to the excitation of electrons from the 4*p* and (4*p* + 4*s*) states of Ga, as well as the hybridization of the 4*s* state of Ga with the 3*s* one of P (see Fig. 1, curve *1*). In the case of the GaInP film, the spectrum (see Fig. 1, curve *2*) contains intense peaks with $E_b = -1.2$, –3.3 and −5.6 eV, apparently associated with the excitation of electrons from the hybridized electronic states of 4*s*(Ga) + 5*p*(In), 4*s*(Ga) + 5*p*(In) + 3*d*(P), and 4*s*(Ga) + 5*s*(In) + 3*d*(P).

Fig. 2 presents optical absorption spectra (graphs of the relative intensity *I* of the light passing through the sample versus the photon energy $h\nu$) for GaP(111) and GaP(111) with a $Ga_{0.6}In_{0.4}P$ film with a thickness of $d \approx 50$ Å.

As Fig. 2 suggests, at first the *I* value does not change practically with an increase in $h\nu$, and then sharply decreases approaching zero. For the GaP(111) and GaInP/GaP nanofilms, a decrease in the *I* value is observed from $h\nu \approx 2.2$ eV and $h\nu \approx 1.7$ eV, respectively. Extrapolation of the sharply decreasing parts of the curves to the $h\nu$ axis gives the value of the band gap E_g of

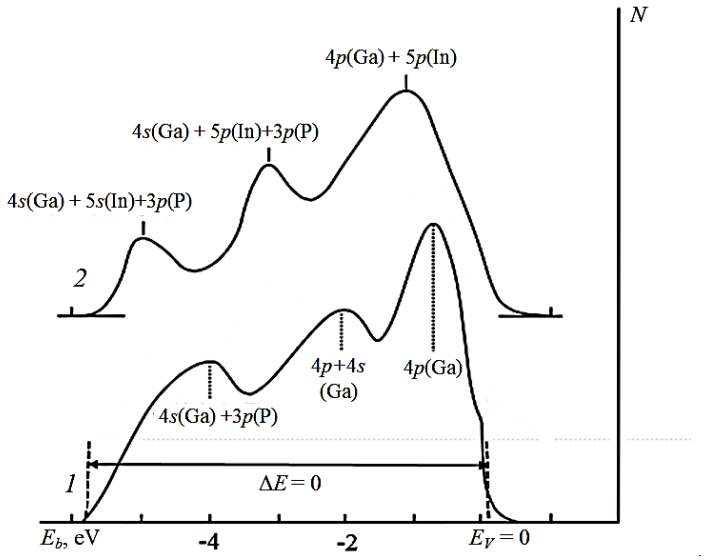

Fig. 1. Photoelectron spectra of the samples under study:
GaP(111) (curve *1*); GaP(111) with the $Ga_{0.6}In_{0.4}P$ film about 50 Å thick (curve *2*)
Identification of peaks is given

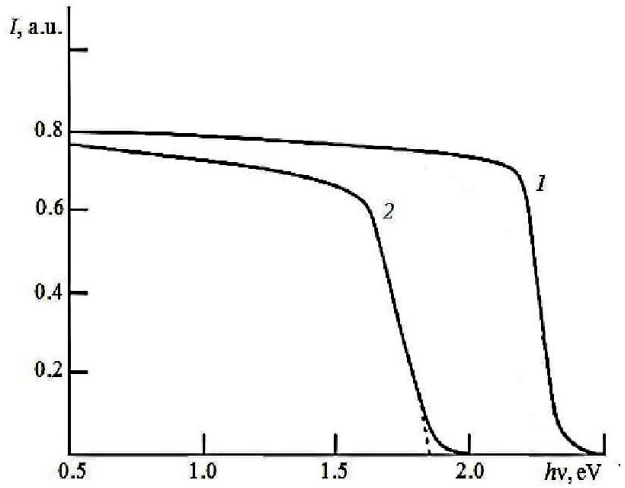

Fig. 2. Optical absorption spectra of GaP(111) (*1*) and GaP(111) with the $Ga_{0.6}In_{0.4}P$ nanofilm about 50 Å thick (*2*)

the material. As can be seen from Fig. 2, the E_g value for GaP(111) is approximately equal to 2.36 eV, and for the $Ga_{0.6}In_{0.4}P$ film it is about 1.85 eV.

Table presents the obtained values of main energy band parameters and emission characteristics of the samples under study. The photoelectric work function and electron affinity are determined by the formulas:

$$\Phi = h\nu - \Delta E,$$

where ΔE is the width of the photoelectron spectra, and

$$\varkappa = \Phi - \mathrm{Eg}.$$

In heterostructural systems, the degree of crystallinity and epitaxiality of a nanofilm is of particular interest. For the film thickness $d < \lambda$ (λ is the photon wavelength), the degree of epitaxiality can be estimated from the angular dependences of the secondary electron emission (SEE) coefficients. Fig. 3 shows the dependences $\sigma_{800}(\varphi)$ for pure GaP(111) and for GaP with a GaInP film 50 E thick formed by ion implantation in combination with annealing and MBE. Here σ_{800} is the value of σ at electron energy E_p = 800 eV. The angle φ was determined with respect to the normal of the sample.

Table

The obtained values of main energy-band parameters and emission characteristics of the samples under study

Parameter	Notation	Unit	Parameter value	
			GaP(111)	$Ga_{0.6}In_{0.4}P$
Photoelectric work function	Φ	eV	5.3	5.5
Band gap	E_g		2.36	1.85
Electron affinity	$\varkappa$		2.94	3.65
Coefficient of secondary electron emission (max)	σ_{max}	–	1.95	1.70
Quantum yield of photoelectrons (at $h\nu$=10.8 eV)	K		$6\cdot10^{-3}$	$4\cdot10^{-3}$

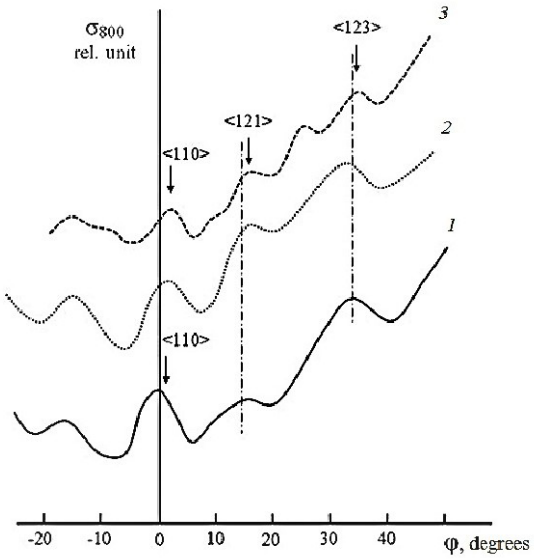

Fig. 3. The angular dependences of the secondary electron emission coefficient for pure GaAs (*1*), for GaP with the $Ga_{0.5}Al_{0.5}As$ film (50 Å thick) formed by ion implantation (*2*) and MBE (*3*). Crystallographic directions are shown

As evident from Fig. 3, a nonmonotonic increase in the value of σ_{800} with increasing φ occurs in all cases. Maxima and minima are observed on the $\sigma_{800}(\varphi)$ curves, and their positions are related by certain crystallographic directions.

The angular positions of the peaks for GaP and the GaInP nanofilms formed by ion implementation are in well arrangement with each other. From this observation, we can conclude that a strict epitaxial growth of the $Ga_{0.6}In_{0.4}P$ film takes place in this case. As for the MBE case (see Fig. 3, curve 3), The peak intensity on the $\sigma_{800}(\varphi)$ curve significantly decreases as compared to the corresponding GaP one, and new peaks appear near these peaks. The processing of the σ(φ) dependences taken at different Ep values made it possible to establish that the exit depth was about 50 Å at $E_p \approx 200$ eV. In this case, the GaP peaks completely disappeared on the σ(*d*) curve, while the intensity of the GaInP peaks increased significantly.

Conclusions

The information about the state density of valence electrons and the energy bands parameters of $Ga_{0.6}In_{0.4}P$ nanofilms has been presented. The nanofilms were fabricated by In^+ implantation in GaP with subsequent annealing; in this case, a strict epitaxial growth of the film took place. The crystallographic orientations of GaInP and GaP were established to coincide completely at the interface. Moreover, the energy gap of the GaInP nanofilm was found to be 1.85 eV.

REFERENCES

1. **Fedorchenko I. V., Kushkov A. R., Gaev D. S., et al.,** Growth method for $A^{III}B^{V}$ and $A^{IV}B^{VI}$ heterostructures, J. Cryst. Growth. 483 (1 February) (2018) 245–250.

2. **Spirina A. A., Nastovjak A. G., Usenkov S.V., Shvarts N. L.,** Lattice Monte Carlo model of Langmuir evaporation of AIIIBV semiconductors, J. Comput. Technol. 23 (6) (2018) 81–94 (in Russian).

3. **Blokhin E. E.,** Simulation QD-InAs/GaAs heterostructure for near infrared photodetectors, Fundamental Research. (9) (2015) 39–43 (in Russian).

4. **Krasil'nikova L. M., Ivonin I. V., Yakubenya M. P., et al.,** Solid-state recrystallization processes in Ni-GaAs and Pd-GaAs structures // Soviet Physics Journal. 32 (3) (1989) 207–211.

5. **Chang L. L., Ploog K.** (Eds.), Molecular beam epitaxy and heterostructures, Springer, Dordrecht, 2012.

6. **Laref S., Мезаbih S., Abbar B., et al.,** First-principle calculations of electronic and positronic properties of $AlGaAs_2$, Physica B Condens. 396 (1–2) (2007) 169–176.

7. **Zolotarev V. V., Leshko A. Y., Lyutetskii A. V., et al.,** Semiconductor lasers with internal wavelength selection, Semiconductors. 47 (1) (2013) 122–126.

8. **Seredin P. V., Domashevskaya E. P., Arsentyev I. N., et al.,** Superstructured ordering in $Al_xGa_{1-x}As$ and $Ga_xIn_{1-x}P$ alloys, Semiconductors. 47 (1) (2013) 1–6.

9. **Chaldyshev V. V., Shkol'nik A. S., Evtikhiyev V. P., Holden T.,** Optical reflection and contactless electroreflection from GaAlAs layers with periodically arranged GaAs quantum wells, Semiconductors. 40 (12) (2006) 1432–1435.

10. **Seredin P. V., Glotov A. V., Domashevskaya E. P., et al.,** Structural and optical properties of low-temperature hydride-MOCVD AlGaAs/GaAs(100) heterostructures based on omission solid solutions, Semiconductors. 43 (12) (2009) 1610–1616.

11. **Mori M. J.,** Lattice mismatched epitaxy of heterostructures for non-nitride green light emitting devices, Thesis for the Degree of Doctor of Philosophy in Electronic Materials, Massachusetts Institute of Technology, USA. June, 2008.

12. **Chang S. J., Chang C. S., Su Y. K., et al.,** AlGaInP yellow-green light-emitting diodes with a tensile strain barrier cladding layer, IEEE Photon. Technol. Lett. 9 (9) (1997) 1199–1201.

13. **Oelgart G., Schwabe R., Heider M., Jacobs B.,** Photoluminescence of $AlxGa_{1-x}As$ near the Γ-X crossover, Semicond. Sci. Technol. 2 (7) (1987) 468–474.

14. **Wang C., Wang B., Made R. I., et al.,** Direct bandgap photoluminescence from *n*-type indirect GaInP alloys, Photonics Res. 5 (3) (2017) 239–244.

15. **Umirzakov B. E., Donaev S. B.,** On the creation of ordered nuclei by ion bombardment for obtaining nanoscale Si structures on the surface of CaF_2 films, J. Surface Investig. 11(4) (2017) 746–748.

16. **Umirzakov D. A., Tashmukhamedova D. A., Muradkabilov D. M., Boltaev K. K.,** Electron spectroscopy of the nanostructures created in Si, GaAs, and CaF2 surface layers using low-energy ion implantation, Tech. Phys. 58 (6) (2013) 841–844.

17. **Umirzakov B. E., Tashmukhamedova D. A., Ruzibaeva D. A., et al.,** Investigation of change of the composition and structure of the CaF_2/Si films surface at the low-energy bombardment, Nucl. Instrum. Methods Phys. Res. B. 2014. Vol. 326. 1 May. Pp. 322–325.

18. **Ergashov Y. S., Tashmukhamedova D. A., Umirzakov B. E.,** On the synthesis of nanoscale phases of metal silicides in the near-surface region of silicon and the study of their electronic structures by passing light, J. Surf. Investig. 11 (2) (2017) 480–484.

19. **Danaev S. B., Umirzakov B. E., Tashmukhamedova D. A.,** Electronic structure of $Ga_{1-x}Al_xAs$ nanostructures grown on the GaAs surface by ion implantation, Techn. Phys. 60 (10) (2015) 1563–1566.

20. **Normuradov M. T., Rysbaev A. S., Bekpulatov I. R., et al.,** Formation and electronic structure of barium-monosilicide and barium-disilicide films, J. Surf. Investig. 15 (Suppl. 1) (2021) S211–S215.

21. **Rysbaev A. S., Khuzhaniyazov Z. B., Normuradov M. T., et al.,** Peculiarities of the electron structure of nanosized ion-implanted layers in silicon, Techn. Phys. 59 (11) (2014) 1705–1710.

22. **Rysbaev A. S., Khuzhaniyazov Z. B., Rakhimov A. M., Bekpulatov I. R.,** Formation of nanosize silicides films on the Si (111) and Si (100) surfaces by low-energy ion implantation, Techn. Phys. 59 (10) (2014) 1526–1530.

СПИСОК ЛИТЕРАТУРЫ

1. **Fedorchenko I. V., Kushkov A. R., Gaev D. S., Rabinovich O. I., Marenkin S. F., Didenko S. I., Legotin S. A., Orlova M. N., Krasnov A. A.** Growth method for $A^{III}B^{V}$ and $A^{IV}B^{VI}$ heterostructures // Journal of Crystal Growth. 2018. Vol. 483. 1 February. Pp. 245–250.

2. **Спирина А. А., Настовьяк А. Г., Усенков С. В., Шварц Н. Л.** Решеточная Монте-Карло модель ленгмюровского испарения полупроводников AIIIBV // Вычислительные технологии. 2018. Т. 23. № 6. С. 80–93.

3. **Блохин Э. Е.** Моделирование QD-InAs/GaAs гетероструктур для фотодетекторов ближнего ИК-диапазона // Фундаментальные исследования. 2015. № 11-1. С. 39–43.

4. **Красильникова Л. М., Ивонин И. В., Якубеня М. П., Максимова И. К., Арбузова Г. К.** Процессы твердотельной перекристаллизации в структурах Ni-GaAs, Pd-GaAs // Известия вузов. Физика. 1989. Т. 32. № 3. С. 60–65.

5. **Эсаки Л., Мёнх У., Джойс Б. А., Хекингботтом Р., Менх У., Фэрроу Р. Ф. К., Сарис Ф. У., Кремер Г., Бастар Г.** Молекулярно-лучевая эпитаксия и гетероструктуры. Пер. с англ. под ред. Алфёрова Ж. И., Шмарцева Ю. В. М.: Мир, 1989. 582 с.

6. **Laref S., Mezabih S., Abbar B., Bouhafs B., Laref A.** First-principle calculations of electronic and positronic properties of $AlGaAs_2$ // Physica B: Condensed Matter. 2007. Vol. 396. No. 1–2. Pp. 169–176.

7. **Золотарев В. В., Лешко А. Ю., Лютецкий А. В. и др.** Полупроводниковые лазеры с внутренней селекцией излучения // Физика и техника полупроводников. 2013. Т. 47. № 1. С. 124–128.

8. **Середин П. В., Домашевская Е. П., Арсенть.ев И. Н., Винокуров Д. А., Станкевич А. Л., Prutskij T.** Сверхструктурное упорядочение в твердых растворах AlxGa1–xAs и GaxIn1–xP // Физика и техника полупроводников. 2013. Т. 47. № 1. С. 3–8.

9. **Чалдышев В. В., Школьник А. С., Евтихиев В. П., Holden T.** Оптическое отражение и бесконтактное электроотражение от слоев GaAlAs с периодически расположенными квантовыми ямами GaAs // Физика и техника полупроводников. 2006. Т. 40. № 12. С. 1466–1469.

10. **Середин П. В., Глотов А. В., Домашевская Е. П., Арсентьев И. Н., Винокуров Д. А., Станкевич А. Л., Тарасов И. С.** Структурные и оптические свойства низкотемпературных МОС-гибридных гетероструктур AlGaAs/GaAs(100) на основе твердых растворов вычитания // Физика и техника полупроводников. 2009. Т. 43. № 12. С. 1654–1661.

11. **Mori M. J.** Lattice mismatched epitaxy of heterostructures for non-nitride green light emitting devices. Thesis for the Degree of Doctor of Philosophy in Electronic Materials. Massachusetts Institute of Technology, USA. June, 2008. 165 p.

12. **Chang S. J., Chang C. S., Su Y. K., Chang P. T., Wu Y. R., Huang K. H., Chen T. P.** AlGaInP yellow-green light-emitting diodes with a tensile strain barrier cladding layer // IEEE Photonic Technology Letters. 1997. Vol. 9. No. 9. Pp. 1199–1201.

13. **Oelgart G., Schwabe R., Heider M., Jacobs B.** Photoluminescence of $Al_xGa_{1-x}As$ near the Γ-X crossover // Semiconductor Science and Technology. 1987. Vol. 2. No 7. Pp. 468–474.

14. **Wang C., Wang B., Made R. I., Yoon S.-F., Michel J.** Direct bandgap photoluminescence from *n*-type indirect GaInP alloys // Photonics Research. 2017. Vol. 5. No. 3. Pp. 239–244.

15. **Умирзаков Б. Е., Донаев С. Б.** Создание ионной бомбардировкой упорядоченных зародышей для получения наноразмерных структур Si на поверхности пленок CaF_2 // Поверхность. Рентгеновские, синхротронные и рентгеновские исследования. 2017. № 7. С. 70–73.

16. **Умирзаков Б. Е., Ташмухамедова Д. А., Мурадкабилов Д. М., Болтаев Х. Х.** Электронная спектроскопия наноструктур, созданных в поверхностных слоях Si, GaAs и CaF_2 методом низкоэнергетической ионной имплантации // Журнал технической физики. 2013. Т. 83. № 6. С. 66–70.

17. **Umirzakov B. E., Tashmukhamedova D. A., Ruzibaeva D. A., Djurabekova F. G., Donaev S. B.** Investigation of change of the composition and structure of the CaF2/Si films surface at the low-energy bombardment // Nuclear Instruments and Methods in Physics Research B. 2014. Vol. 326. 1 May. Pp. 322–325.

18. **Эргашов Е. С., Ташмухамедова Д. А., Умирзаков Б. Е.** Получение наноразмерных фаз силицидов металлов в приповерхностной области кремния и изучение их электронных структур методом прохождения света // Поверхность. 2017. № 4. С. 104–108.

19. **Данаев С. Б., Умирзаков Б. Е., Ташмухамедова Д. А.** Электронная структура наноразмерных структур $Ga_{1-x}Al_xAs$, созданных на поверхности GaAs методом ионной имплантации // Журнал технической физики. 2015. Т. 85. № 10. С. 148–151.

20. **Normuradov M. T., Rysbaev A. S., Bekpulatov I. R., Normuradov D. A., Tursunmetova Z. A.** Formation and electronic structure of barium-monosilicide- and barium-disilicide films // Journal of Surface Investigation. 2021. Vol. 15. No. 1 (Supplement). Pp. S211–S215.

21. **Рысбаев А. С., Хужаниязов Ж. Б., Нормурадов М. Т., Рахимов А. М., Бекпулатов И. Р.** Особенности электронной структуры наноразмерных ионно-имплантированных слоев в кремнии // Журнал технической физики. 2014. Т. 84. № 11. С. 128–133.

22. **Рысбаев А. С., Хужаниязов Ж. Б., Рахимов А. М., Бекпулатов И. Р.** Формирование наноразмерных пленок силицидов на поверхности Si(111) и Si(100) методом низкоэнергетической ионной имплантации // Журнал технической физики. 2014. Т. 84. № 10. С. 107–111.

THE AUTHORS

SHIRINOV Ganjimurod M.
Tashkent State Technical University Named after Islam Karimov
2, Universitetskaya St., Tashkent,100095, Uzbekistan
ganjimurod777@gmail.com
ORCID: 0000-0002-7188-2560

DONAEV Sardor B.
Tashkent State Technical University Named after Islam Karimov
2, Universitetskaya St., Tashkent,100095, Uzbekistan
sardor.donaev@gmail.com
ORCID: 0000-0001-5656-126X

UMIRZAKOV Baltokhodja Y.
Tashkent State Technical University Named after Islam Karimov
2, Universitetskaya St., Tashkent,100095, Uzbekistan
be.umirzakov@gmail.com
ORCID: 0000-0002-9815-2111

LOBODA Vera V.
Peter the Great St. Petersburg Polytechnic University
29 Politechnicheskaya St., St. Petersburg, 195251, Russia
vera_loboda@mail.ru
ORCID: 0000-0003-3103-7060

СВЕДЕНИЯ ОБ АВТОРАХ

ШИРИНОВ Ганжимурад Мамир угли – *докторант кафедры общей физики Ташкентского государственного технического университета имени Ислама Каримова, г. Ташкент, Узбекистан.*
100095, Узбекистан, г. Ташкент, Университетская ул., 2
ganjimurod777@gmail.com
ORCID: 0000-0002-7188-2560

ДОНАЕВ Сардор Бурханович – *доктор физико-математических наук, проректор по науке и инновациям Ташкентского государственного технического университета имени Ислама Каримова, г. Ташкент, Узбекистан.*
100095, Узбекистан, г. Ташкент, Университетская ул., 2
sardor.donaev@gmail.com
ORCID: 0000-0001-5656-126X

УМИРЗАКОВ Балтоходжа Ерматович – *доктор физико-математических наук, профессор кафедры общей физики Ташкентского государственного технического университета имени Ислама Каримова, г. Ташкент, Узбекистан.*
100095, Узбекистан, г. Ташкент, Университетская ул., 2
be.umirzakov@gmail.com
ORCID: 0000-0002-9815-2111

ЛОБОДА Вера Владимировна – *кандидат физико-математических наук, директор Высшей школы электроники и микросистемной техники Санкт-Петербургского политехнического университета Петра Великого, Санкт-Петербург, Россия.*
195251, Россия, г. Санкт-Петербург, Политехническая ул., 29
vera_loboda@mail.ru
ORCID: 0000-0003-3103-7060

Received 25.01.2023. Approved after reviewing 01.02.2023. Accepted 01.02.2023.
Статья поступила в редакцию 25.01.2023. Одобрена после рецензирования 01.02.2023. Принята 01.02.2023.

© Peter the Great St. Petersburg Polytechnic University, 2023

BIOPHYSICS AND MEDICAL PHYSICS

Original article
DOI: https://doi.org/10.18721/JPM16209

DETERMINATION OF CONDITIONS FOR OBTAINING RADIOACTIVITY OF NITROGEN-13 ISOTOPE FOR MEDICAL USE BY NX2 DENSE PLASMA FOCUS DEVICE

A. Nassif[1]✉, *W. Sahyouni*[2], *O. Zeidan*[2], *N. Kafa*[2]

[1] Al-Wataniya Private University, Hama, Syrian Arab Republic;

[2] Al-Baath University, Homs, Syrian Arab Republic

✉ alaa.nassif.85@hotmail.com

Abstract. In the paper, a theoretical study to calculate the value of the radioactivity of nitrogen-13 isotope required for use in positron emission tomography (PET) has been presented. The isotope is produced by deuteron beams from NX2 dense plasma focus device. First the effect of three factors was studied, namely, the deuterium gas density, exposure time and the repetition rate of the device. The results showed an increase in radioactivity as deuterium gas pressure decreased. It was next possible to obtain four radioactivity values, suitable for use in PET, by varying the two rest factors.

Keywords: nitrogen-13 isotope, NX2 dense plasma focus device, radioactivity

Citation: Nassif A., Sahyouni W., Zeidan O., Kafa N., Determination of conditions for obtaining radioactivity of nitrogen-13 isotope for medical use by NX2 dense plasma focus device, St. Petersburg State Polytechnical University Journal. Physics and Mathematics. 16 (2) (2023) 98–110. DOI: https://doi.org/10.18721/JPM.16209

Научная статья
УДК 533.9.07
DOI: https://doi.org/10.18721/JPM.16209

ОПРЕДЕЛЕНИЕ УСЛОВИЙ ПОЛУЧЕНИЯ РАДИОАКТИВНОСТИ ИЗОТОПА АЗОТ-13, ТРЕБУЕМОЙ ДЛЯ МЕДИЦИНСКОГО ПРИМЕНЕНИЯ ПРИ ИСПОЛЬЗОВАНИИ УСТРОЙСТВА ПЛАЗМЕННОЙ ФОКУСИРОВКИ NX2

А. Нассиф[1]✉, *В. Сахьюни*[2], *О. Зейдан*[2], *Н. Кафа*[2]

[1] Частный университет Аль-Ватания, г. Хама, Сирийская Арабская Республика;

[2] Университет Аль-Баас, г. Хомс, Сирийская Арабская Республика

✉ alaa.nassif.85@hotmail.com

Аннотация. В работе представлено теоретическое исследование, направленное на расчет значений радиоактивности изотопа ^{13}N, необходимых для медицинского применения в позитронно-эмиссионной томографии (ПЭТ). Изотоп можно получать путем ядерной реакции ^{12}C(d, n)^{13}N, реализуемой пучками дейтронов из устройства фокусировки плотной плазмы NX2. На первой стадии исследования изучалось влияние на уровень радиоактивности трех параметров устройства NX2: давления газообразного дейтерия (ДГД), времени экспозиции и частоты следования импульсов. Результаты показали рост уровня радиоактивности по мере снижения ДГД. На второй стадии удалось получить четыре значения радиоактивности, пригодные для использования в ПЭТ, путем подбора значений двух других факторов.

© Nassif A., Sahyouni W., Zeidan O., Kafa N., 2023. Published by Peter the Great St. Petersburg Polytechnic University.

Ключевые слова: изотоп азот-13, радиоактивность, устройство плазменной фокусировки NX2, пучок дейтронов

Ссылка для цитирования: Нассиф А., Сахьюни В., Зейдан О., Кафа Н. Определение условий получения радиоактивности изотопа азот-13, требуемой для медицинского применения при использовании устройства плазменной фокусировки NX2 // Научно-технические ведомости СПбГПУ. Физико-математические науки. 2023. Т. 16. № 2. С. 98–110. DOI: https://doi.org/10.18721/ JPM.16209

Introduction

Since the initial design of the dense plasma focus devices by J. W. Mather [1] and N. V. Filippov et al. [2], a large number of studies have been conducted on this phenomenon due to its distinction in terms of obtaining very hot, very dense plasma that constitutes a source for a large number of radioactive emissions and ion beams and electrons, depending on the type of gas used in the operation process [3].

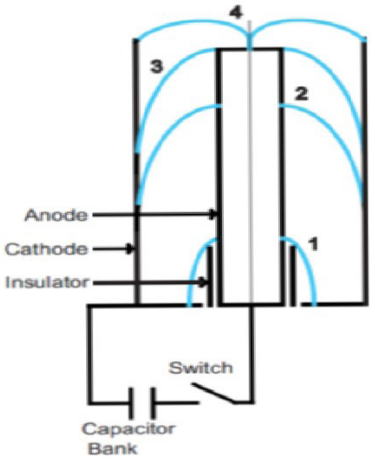

Fig. 1. Scheme of the dense plasma focus device able to cause the nuclear reaction required for the production of short-lived radioactive isotopes, e. g. ^{13}N

In Fig. 1 one can see an elementary scheme of this device. In the process of evolving plasma, a focus known as "pinch" is formed; it is a small column of plasma that collapses after a very short period (ns) due to the instability of the plasma [4, 5], leading to beams of ions and electrons moving in opposite directions [6]. The properties of these beams have been studied and characterized with a view to their practical application such as thin film deposition [7 – 11], material synthesis [12 – 15] and the production of short-lived radioisotopes [16, 17].

In the case when deuterium gas is used in a dense plasma device, it is possible to take advantage of the energy ion beams produced after the collapse of the plasma pinch and its collision with a suitable target in order to cause the desired reaction. For this purpose, many researches have been conducted experimental and computational studies aimed at the possibility of benefiting from the ion beams emitted by the collapse of a plasma column formed in the dense plasma focus device, especially when using deuterium as working gas in order to bring about the nuclear reaction required for the production of short-lived radioactive isotopes. M. Sumini et al. [18] designed a 150 kJ dense plasma focus device operating in a 1 Hz frequency mode to produce the ^{18}F radioactive isotope (1 Ci in a time of 2 hrs) and put the engineering designs of the electrodes and the parameters of the electrical circuit, and 128 shots were carried out. B. Shirani et al. [19] also studied the possibility of obtaining the radioactive isotope ^{13}N from a low-energy dense plasma focus device, and a radioactivity value of 10 kBq for one shot was obtained. In the process, the radioactivity value increased to several tens of MBq at an operating rate of $f = 1$ Hz with an operating time of 600 s. Since the medically required radioactivity is about 4 GBq, the idea to change the design of the electrodes or the pressure of deuterium gas was put forward. In order to increase the energy of the outgoing deuterons spectrum, M. Akel et al. [20] conducted numerical experiments using the Lee code for calculating the characteristics of the ion beams emitted by a number of dense plasma devices with different operating energies and for calculating the radioactivity of the $^{12}C(d, n)^{13}N$ reaction. As a result, they found that the device should operate in a repetitive mode (the repetition rate was $f = 25$ Hz for an operation period of 600 s) to reach the value of the medically required radioactivity and came to the conclusion that this possibility of operation was not available in the current devices. In addition, there was a problem of endurance of targets to resulting thermal loads.

© Нассиф А., Сахьюни В., Зейдан О., Кафа Н., 2023. Издатель: Санкт-Петербургский политехнический университет Петра Великого.

In 2019, H. Sadeghi et al. [21] developed the idea of adding magnetic lenses in order to focus and direct the outgoing ion beams, as well as to reduce the scattering ratio. Simulations were carried out on 16 different plasma incinerators with different energies (from 400 J to 500 kJ) and a radioactivity value of 0.016–7.71 GBq was reached. It was established that 9 of the devices studied were able to achieve the medically required radioactivity value of the isotope ^{13}N by using this technique.

Research technique

Firstly, the number of deuterium ions emitting from the collapse of the plasma pinch was found, then the radioactivity of the isotope was calculated for the 3 Torr pressure deuterium gas. Secondly, the effect of changing the pressure of deuterium gas on the value of radioactivity was calculated. Thirdly, the advantage of repetitive operation of the studied plasma focus device NX2 was taken in order to explore the effect of the exposure time and repetition rate on radioactivity. The results obtained are presented next.

Results and discussion

Finding deuterons beam properties emitted by a NX2 dense plasma focus device. The number of generated ions was calculated by taking advantage of the parameters of the plasma pinch (the source) that were found using the Lee code, by taking advantage of the following device features [22]:

Operating potential V = 14 kV;

Capacitor bank capacity C_0 = 28 μF;

Inductance L_0 = 20 nH.

The value of the total discharge current produced by the capacitor bank can be calculated as follows:

$$I_0 = \frac{V_0}{\sqrt{\frac{L_0}{C_0}}} = \frac{4\cdot 10^3}{\sqrt{\frac{20\cdot 10^{-9}}{28\cdot 10^{-6}}}} = 523.83kA. \quad (1)$$

The capacitor bank discharge time is

$$t_0 = \sqrt{L_0 C_0} = \sqrt{20\cdot 10^{-9}\cdot 28\cdot 10^{-6}} = 74.8\mu s; \quad (2)$$

$$T = 2\pi t_0 = 2\pi\cdot 74.8\cdot 10^{-6} = 469.98\ \mu s. \quad (3)$$

The time of movement of the plasma sheath through the axial phase is given by Ref. [23]:

$$t_a = \sqrt{\left[\frac{2\pi^2\left(c^2-1\right)}{\mu_0 \ln c}\right]}\left[\frac{\sqrt{f_m\cdot Z_0\sqrt{\rho}}}{f_c\left(\frac{I_0}{a}\right)}\right], \quad (4)$$

where c is the ratio of the cathode radius b to the anode one a ($c = b/a = 4.1/1.9 = 2.2$); μ_0 is the permeability of the plasma, $\mu_0 = 4\pi\cdot 10^{-7}\ H/(m\cdot Z_0)$; Z_0 is the anode length; f_m, f_c are the factors of mass and current losses in the axial phase, relatively, $f_m = 0.06$, $f_c = 0.70$ [22].

The time of movement of the plasma sheath radially at the top of anode until reaching the stage of pinching is given by Ref. [23]:

$$t_r = \sqrt{\frac{4\pi}{\mu_0\left(\gamma+1\right)}}\left[\frac{\sqrt{f_m\sqrt{\rho}}}{f_c\left(\frac{I_0}{a}\right)}\right]a, \quad (5)$$

where γ is the specific heat capacity of deuterium plasma, $\gamma = 5/3$.

The density ρ (kg/m^3) of deuterium gas is calculated by the formula

$$\rho = P \cdot M / (R \cdot T). \tag{6}$$

Our studies showed that about 60 % of the total discharge current will form the peak current I_{peak} which continues to push the plasma sheath until reaching the stage of the formation of the plasma pinch [24]. Deuterium gas has $P = 3$ Torr where this condition is met by Lee code. Thus, we get that the pressure is

$$P = 3 \cdot 1.013 \cdot 10^5/760 = 400 \text{ Pa}.$$

The temperature $T = 273 + 20 = 293$ K; the gas constant $R = 8.31$ J/(K·mol); the molar mass of deuterium gas $M = 4.027$ kg/mol.

Substituting these values into Eq. (6) for the deuterium gas density, we obtain that

$$\rho = 0.661 \text{ kg/m}^3. \tag{7}$$

The values obtained were taken to calculate the velocity values of the plasma sheath in the axial and radial phases by using Lee code. The following are the results obtained:

The axial velocity $v_a = 1290$ km/s, (8)

The radial velocity $v_r = 327$ km/s, (9)

The ion current density is calculated using the Langmuir – Child formula [25]:

$$J_i = 1.86 \cdot \left(\frac{4}{9}\right) \varepsilon_0 \sqrt{\frac{2e}{m_i}} \cdot \frac{\Phi^{3/2}}{d^2}, \tag{10}$$

where ε_0 is the permittivity of free space, $\varepsilon_0 = 8.854 \cdot 10^{-12}$; e is the electric charge, $e = 1.6 \cdot 10^{-19}$ C; m_i is the mass of the deuterium ion, $m_i = 3{,}34 \cdot 10^{-27}$ kg; d is the width of the formed plasma sheath; Φ is the induced voltage within the plasma pinch,

$$\Phi = I_0 \, (dL_p/dt). \tag{11}$$

We calculate the induction within the plasma pinch dL_p/dt by using Ref. [26]:

$$\frac{dL_p}{dt} = \frac{\mu_0}{2\pi} \left[\ln\left(\frac{b}{r_p}\right) v_a + \left(\frac{z}{r_p}\right) v_r \right], \tag{12}$$

where b, r_p are the radii of the cathode and plasma pinch, relatively, $b = 4.100$ cm, $r_p = 0.302$ cm; z is the length of the plasma pinch, $z = 2.806$ cm.

Substituting these values, we get that $dL_p/dt = 0.674$.

Thus, according to Eq. (11), the induced potential within plasma pinch is

$$\Phi = 523.83 \cdot 10^3 \cdot 0.674 = 353 \text{ kV}.$$

Now let us calculate ion current density:

$$J_i = 1.86 \cdot \left(\frac{4}{9}\right) \varepsilon_0 \sqrt{\frac{2e}{m_i}} \cdot \frac{\Phi^{3/2}}{d^2} = 19 kA / m^2.$$

Thus we get the number of deuterium ions ejected from the plasma pinch:

$$N_i = \pi \frac{r_p^2}{e} J_i \tau_p = 6.5 \cdot 10^{12} \left(\text{ions}\right). \tag{13}$$

Calculation of the radiative yield. The energy distribution $f(E)$ of the ions emitted from the plasma pinch is given by Ref. [20]:

$$f(E) = dN_i / dE = C \cdot E^{-m}, \tag{14}$$

where C is the constant, power coefficient m takes values within the range $2.0 < m < 3.5$;

$$N_i = \int_{E_{\min}}^{E_{\max}} CE^{-m} dE = C\left[\frac{E^{1-m}}{1-m}\right]_{E_{\min}}^{E_{\max}}.$$

Consequently, the function $f(E)$ is of the form

$$f(E) = N_i\left(\frac{1-m}{E_{\max}^{1-m} - E_{\min}^{1-m}}\right)E^{-m}. \quad (15)$$

where E_{max}, E_{min} are the maximum and minimum energies of the emitting deuterons.

The radiative yield of the reaction is given by Ref. [27]:

$$\langle y \rangle = \frac{\Omega_1}{\Omega_2}\left(\frac{1-m}{E_{\max}^{1-m} - E_{\min}^{1-m}}\right)\int_{E_{\min}}^{E_{\max}} n\frac{E^{-m}\sigma(E)}{\frac{dE}{dx}}dE. \quad (16)$$

where Ω_1, Ω_2 are the solid angles of the source (the pinch) and of the target, relatively; n is the density of graphite target, $n = 1.129 \cdot 10^{29}$ m^{-3}; dE/dx is the stopping power of the graphite target; $\sigma(E)$ is the experimental cross-section of the reaction $^{12}C(d, n)^{13}N$.

There are two angles Ω_1 and Ω_2 that need to be calculated: the former is the angle of emission of ions from the pinch, and the latter is the angle of arrival of ions to the target.

Deuterium ions are emitted in the form of a cone whose top rests on the grip and its base does on the target. The solid angle of a cone is given by

$$\Omega_1 = 2\pi(1 - \cos\theta_1). \quad (17)$$

If we assume that the angle $\theta_1 = 25° = 0.436$ rad, then $\Omega_1 = 0.587$ sr.

The portion of the released ions falls on the graphite target. The angle of arrival of ions to the target is proportional to the surface area and is given by the following relationship:

$$\Omega_2 = \pi\theta_2 = \pi(r/R)^2, \quad (18)$$

where r is the radius of the source, R is the distance between the target and the source (the grip).

If we assume that $r = 1$ cm and $R = 20$ cm, then $\Omega_2 = 0.0078$ sr.

Calculation of the stopping power *dE/dx* of a graphite target. The 2013 SRIM (The Stopping and Range of Ions in Matter) program (see Ref. [28]) was used to find the stopping power of deuterium ions within the energy range 0.6 – 3 MeV within the graphite target. By drawing the matching curve, we obtained the formula for the stopping power: $dE/dx = 51408E^{-0.691}$.

The results obtained are shown in Table 1 and Fig. 2.

Table 1

The ion energy – the stopping power relationship obtained using SRIM

Ion kinetic energy, MeV	Stopping power, GeV/m
0.60	71.6
0.70	65.0
0.90	55.5
1.00	51.9
1.10	49.0
1.50	39.4
1.70	36.0
1.80	34.5
2.00	32.0
2.50	27.1
2.75	25.3
3.00	23.7

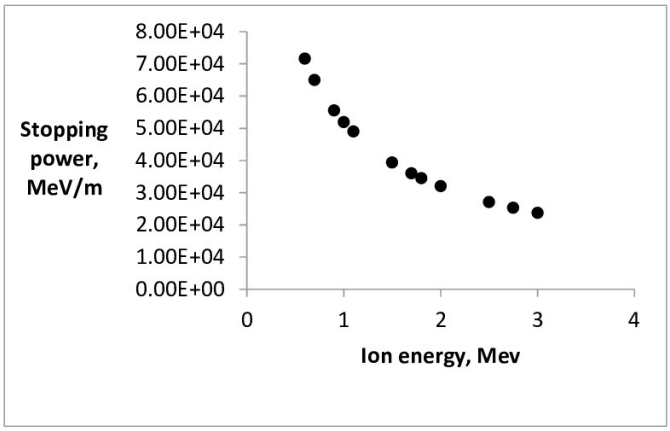

Fig. 2. The dependence of the stopping power of deuterium ions within the graphite target on their kinetic energy

Finding the experimental cross-section σ(E) for the reaction $^{12}C(d, n)^{13}N$. To find this cross-section, the Experimental Nuclear Reaction Data (EXFOR) of the International Atomic Energy Agency (IAEA) (see Ref. [29]) was used. This result is presented in Fig. 3 and Table 2. Thus, we obtained the formula giving the cross-section:

$$\sigma(E) = -72.771E^2 + 314E - 164.78.$$

Table 2

Experimental dependence of cross-section values on the ion energy for the $^{12}C(d, n)^{13}N$ reaction taken from EXFOR database

Ion kinetic energy E, Mev	σ, mb
0.65	12.37
1.04	82.29
1.52	130.2
2.00	186.5
3.00	119.9

Substituting the previous relations to calculate the yield value at the values m = 2.0, 3.0, 3.5, we can find three $\langle y \rangle$ values. They are equal respectively:

$$9.3100 \cdot 10^{-5},\ 1.4534 \cdot 10^{-5},\ 3.1420 \cdot 10^{-5}.$$

The radioactivity is calculated by Ref. [20]:

$$A = N_i \langle y \rangle \ln 2/T_{1/2}, \tag{19}$$

where $T_{1/2}$ is the half-life of the radioactive isotope ^{13}N, $T_{1/2}$ = 10 min = 600 s.

Therefore, the value of the radioactivity for $m = 2$ is: $A = 6.99 \cdot 10^5$ Bq.

The effect of the density of deuterium gas on the value of radioactivity. The density of deuterium gas is considered as one of the factors affecting the formation of the plasma sheath, its axial and radial velocity, and the parameters of the plasma pinch formed at the end of radial phase, and thus, its effect on the induction generated within the pinch and the voltage generated within it, and later on the current density and the number of ions emitting from the collapse of the pinch.

The calculations of the density of the gas when changing the pressure of deuterium gas from the value $P = 1$ Torr to the value at which focusing does not occur, and then finding the values of the velocities of the axial and radial plasma sheath, the dimensions and the duration of the formed plasma pinch using the Lee code were performed. The results obtained are presented in Table 3.

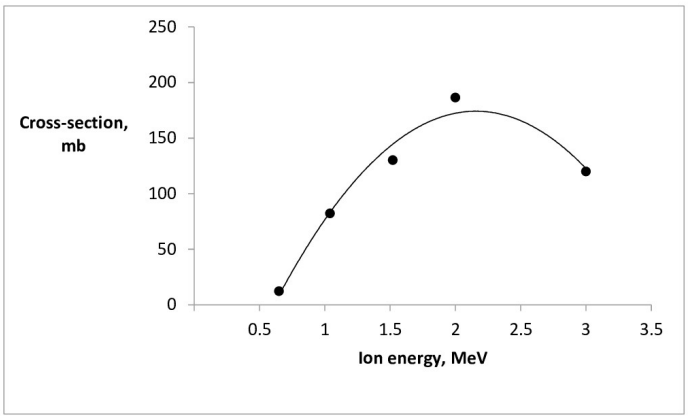

Fig. 3. Cross-section of the $^{12}C(d, n)^{13}N$ reaction taken from (EXFOR) database

Table 3

The dependence of some key plasma parameters on the deuterium gas pressure and density using the Lee code

Deuterium gas		Plasma sheath velocity		Plasma pinch		
Pressure, Torr	Density, g/m^3	Axial, km/s	Radial, km/s	Radius, mm	Length, mm	Duration, ns
1	220	176	457	3.01	28.06	13.5
2	440	145	371	3.02	28.04	16.7
3	661	129	327	3.04	28.06	19.1
4	881	118	297	3.05	28.04	21.0
5	1102	111	274	3.06	28.05	22.8
6	1322	105	257	3.08	28.03	24.3
7	1543	100	243	3.09	28.02	25.8
8	1763	95	231	3.11	28.05	27.3
9	1984	92	221	3.12	28.03	28.6
10	2204	89	211	3.13	28.03	30.0
11	2424	86	203	3.15	28.05	31.4
12	2645	83	195	3.17	28.02	32.6
13	2865	81	189	3.18	28.04	33.9
14	3086	79	183	3.20	28.03	35.2
15	3306	77	176	3.22	28.04	36.5
16	3527	75	171	3.24	28.05	37.7
17	3747	74	166	3.26	28.04	39.0
18	3968	72	161	3.28	28.04	40.3
19	41885	71	157	3.30	28.02	41.6

The value of the plasma pinch induction, the voltage generated within it, the density of the ion current and the number of the ejected ions were calculated using the Eqs. (10) – (13) (see Table 4). Then, using Eq. (19), the value of the radioactivity was calculated with changing in the deuterium gas pressure. The results are shown in Fig. 4.

Table 4

The dependence of some plasma pinch and deuterium ion beam parameters on the deuterium gas pressure using the Lee code

Deuteriun gas pressure, Torr	Plasma pinch		Deuteriun ion beam	
	Induction	Voltage in it, kV	Current density, kA/m^2	Number of ejected ions
1	0.9439	494.5	31.64	660
2	0.7645	400.5	23.09	595
3	0.6707	351.4	18.95	559
4	0.6074	318.2	16.35	530
5	0.5599	293.3	14.46	509
6	0.5221	273.5	13.04	489
7	0.4924	257.9	11.95	475
8	0.4656	243.9	10.97	462
9	0.4444	232.8	10.24	452
10	0.4237	221.9	9.534	441
11	0.4056	212.5	8.919	432
12	0.3872	202.8	8.336	419
13	0.3747	196.3	7.924	414
14	0.3608	189.0	7.495	407
15	0.3457	181.1	7.022	395
16	0.3341	175.0	6.668	388
17	0.3230	169.2	6.342	382
18	0.3116	163.2	6.010	374
19	0.3023	158.4	5.753	369

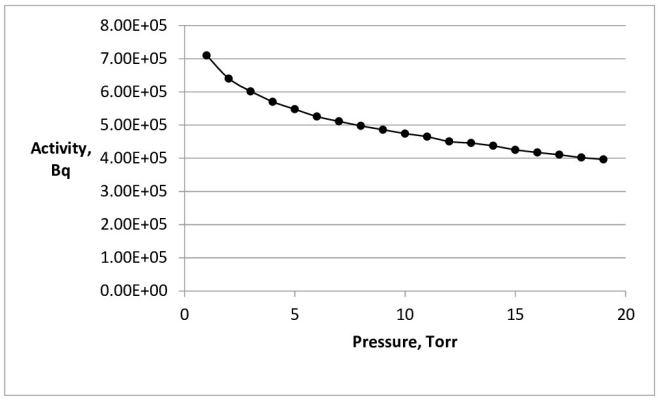

Fig. 4. The plots of the radioactivity values versus the deuterium gas pressure

An analysis of the obtained results allows us to note that an increase in the pressure of deuterium gas has led to an increase in the time of movement of the plasma sheath both axially and radially and consequently decreasing of axial velocity of the plasma from 176 km/s at a pressure of 1 Torr to 71 km/s at the highest pressure value (19 Torr), and the plasma velocity at the top of

the anode radially decreased from 457 km/s to 157 km/s, and thus, the decrease in the value of the energy coming from the capacitor bank to the plasma pinch, and as a result the decrease in the value of the induction inside the plasma pinch and the voltage generated within it, and thus, the number of ions ejected from the plasma pinch according to Eqs. (11) – (13), the value of the radioactivity of the isotope ^{13}N decreases, as shown in Fig. 3, from 710 kBq to 397 kBq. So, decreasing the gas pressure led to an increase in the radioactivity value of the isotope 13N, but in order to make it suitable for use in medicine, rather in PET, the radioactivity value must be within the range 370 – 740 MBq [30] and therefore it is necessary to search for additional methods for increasing the value of radioactivity, apart from the low pressure of deuterium gas, such as increasing the device's operating rate, i. e., exposure of the target to a number of successive shots (i. e., increasing reaction yield) or by increasing the operating power of the device.

Calculation of the radioactivity value when changing the frequency of operation and exposure time. The value of the radioactivity of the isotope ^{13}N was found at repetition rates equal to 1, 5, 10, 16 Hz and the exposure time of the graphite target to deuterium ions equal to 30, 60, 100, 200, 300, 400, 500 s.

The value of the radioactivity was calculated according to the formula given in Ref. [20]:

$$A_\nu = N_i \cdot \langle y \rangle \, \nu[1 - \exp(-\lambda t)], \tag{20}$$

where ν is the frequency of shots, $\lambda = (\ln 2)/T_{1/2}$ ($T_{1/2}$ is the radioactive half-period); t is the exposure time.

The calculation results are presented in Table 5 and Fig. 5.

Table 5

The dependence of the radioactivity values on the exposure time at different values of the repetition rate

Exposure time, s	Radioactivity value, MBq			
	1 Hz	5 Hz	10 Hz	16 Hz
30	18.9	94.3	189	302
60	34.9	174	349	**558**
100	53.8	269	**538**	861
200	97.8	**489**	978	1560
300	133.0	**666**	1330	2130
400	164.0	818	1640	2620
500	189.0	944	1890	3020

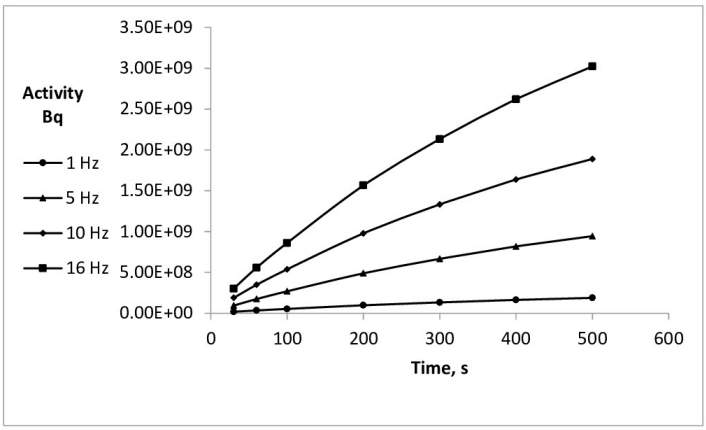

Fig. 5. Plots of the radioactivity values versus the exposure time at different repetition rates

Table 6

The radioactivity values that meet the requirements for use in PET

Radioactivity value, MBq	Exposure time, s	Repetition rate, Hz
489	200	5
538	100	10
558	60	16
666	300	5

It is evident from the results shown in the Table 5 and Fig. 5, that there are four values for the radioactivity of the isotope for use in a PET technique. We specially listed these values in ascending order in the separate Table 6.

Conclusions

This study presents a visualization of the operational conditions that should be met in the NX2 dense plasma focus device as a medium-energy apparatus for the possibility of producing ^{13}N isotope suitable for use in PET. The results also determined the values of the repetition rate and the exposure time required in order to obtain the value of the required radioactivity, where four values were obtained.

This study can be expanded in order to study the effect of the geometric dimensions of the vacuum chamber and the possibility of modifying them for increasing the radioactivity.

We expect that in the current operational conditions, the operating energy of the dense plasma focus device should not be less than 100 kJ in order to obtain the required radioactivity of 13N isotope.

REFERENCES

1. **Mather J. W.,** Formation of a high-density deuterium plasma focus, Phys. Fluids. 8 (2) (1965) 366–377.

2. **Filippov N. V., Filippova T. I., Vinogradov V. P.,** Dense high-temperature plasma in a non-cylindrical Z-pinch compression, Nucl. Fusion, Suppl. Part 2 (January) (1962) 577.

3. **Haines M. G.,** A review of the dense Z-pinch, Plasma Phys. Control. Fusion. 53 (9) (2011) 093001.

4. **Al-Hawat S., Akel M., Lee S., Saw S. H.,** Model parameters versus gas pressure in two different plasma focus devices operated in argon and neon, J. Fusion Energy. 31 (1) (2012) 13–20.

5. **Lee S., Saw S. H.,** Plasma focus ion beam fluence and flux – For various gases, Phys. Plasmas. 20 (6) (2013) 062702.

6. **Mohamed A. E. S.,** A dense plasma focus device as a pulsed neutron source for material identification, A dissertation for the degree of Ph.D., Kansas State University, Kansas, USA, 2015.

7. **Feugeas J. N., Llonch E. C., De González C. O., Galambos G.,** Nitrogen implantation of AISI 304 stainless steel with a coaxial plasma gun, J. Appl. Phys. 64 (5) (1988) 2648–2651.

8. **Rawat R. S., Srivastava M. P., Tandon S., Mansingh A.,** Crystallization of an amorphous lead zirconate titanate thin film with a dense-plasma-focus device, Phys. Rev. B. 47 (9) (1993) 4858–4862.

9. **Kant C. R., Srivastava M. P., Rawat R. S.,** Thin carbon film deposition using energetic ions of a dense plasma focus, Phys. Lett. A. 226 (3–4) (1997) 212–216.

10. **Tan K. S.,** High growth rate synthesis of zinc oxide and carbon based nanostructured materials using dense plasma focus device, A dissertation for the degree Ph.D, Nanyang Technological University, Singapore, 2017.

11. **Rawat R. S.,** Dense plasma focus – High-energy-density pulsed plasma device based novel facility for controlled material processing and synthesis, In book: Plasma Science and Technology for Emerging Economies, Springer, Singapore (2017) 39–112.

12. **Zhang T., Lin J., Patran A., et al.,** Optimization of a plasma focus device as an electron beam source for thin film deposition, Plasma Sources Sci. Technol. 16 (2) (2007) 250–256.

13. **Pimenov V. N., Demina E. V., Ivanov L. I., et al.,** Damage and modification of materials produced by pulsed ion and plasma streams in Dense Plasma Focus device, Nukleonika. 53 (3) (2008) 111–121.

14. **Gribkov V. A.,** Physical processes taking place in dense plasma focus devices at the interaction of hot plasma and fast ion streams with materials under test, Plasma Phys. Control. Fusion. 57 (6) (2015) 065010.

15. **Roshan M. V., Lee P., Lee S., et al.,** Backward high energy ion beams from plasma focus, Phys. Plasmas. 16 (7) (2009) 074506.

16. **Brzosko J. S., Nardi V.,** High yield of ^{12}C (*d*, *n*) ^{13}N and ^{14}N (*d*, *n*) ^{15}O reactions in the plasma focus pinch, Phys. Lett. A. 155 (2–3) (1991) 162–168.

17. **Roshan M. V., Razaghi S., Asghari F., et al.,** Potential medical applications of the plasma focus in the radioisotope production for PET imaging, Phys. Lett. A. 378 (30–31) (2014) 2168–2170.

18. **Sumini M., Mostacci D., Rocchi F., et al.,** Preliminary design of a 150 kJ repetitive plasma focus for the production of 18-F, Nucl. Instrum. Methods Phys. Res. A. 562 (2) (2006) 1068–1071.

19. **Shirani B., Abbasi F.,** Prospects for ^{13}N production in a small plasma focus device, J. Fusion Energy. 32 (2) (2013) 235–241.

20. **Akel M., Alsheikh Salo S., Ismael S., et al.,** Interaction of the high energy deuterons with the graphite target in the plasma focus devices based on Lee model, Phys. Plasmas. 21 (7) (2014) 072507.

21. **Sadeghi H., Amrollahi R., Fazelpour S., Omrani M.,** Simulation of dense plasma focus devices to produce N-13 efficiently, Laser Part. 37 (2) (2019) 209–216.

22. **Lee S., Saw S. H.,** Plasma focus ion beam fluence and flux – Scaling with stored energy, Phys. Plasmas. 19 (11) (2012) 112703.

23. **Lee S., Saw S. H.,** The plasma focus – Numerical experiments, insights and application, In book: Plasma Science and Technology for Emerging Economies: An AAAPT Experience, Rawat R. S. (Editor), Springer, Singapore, 2017. 811 p. Pp. 131–137.

24. **Soto L.,** New trends and future perspectives on plasma focus research, Plasma Phys. Control. Fusion. 47 (5A) (2005) A361.

25. **Carlqvist P.,** Current limitation and solar flares, Sol. Phys. 7 (3) (1969) 377–392.

26. **Talaei A., Sadat Kiai S. M.,** Study the influence of the bank energy on the dynamical pinch in plasma focus, J. Fusion Energy. 28 (3) (2009) 304–313.

27. **Young F. C., Golden J., Kapetanakos C. A.,** Diagnostics for intense pulsed ion beams, Rev. Sci. Instrum. 48 (4) (1977) 432–443.

28. www.srim.org for the stopping and range of ions in matter.

29. **Michelmann R.,** https://www-nds.iaea.org/exfor/exfor.htm.

30. **Castillo S.,** Medical and statistical review of N-13 ammonia Positron Emission Tomography, 1999, Florence Houn, MD MPH FACP, Medical Office.

СПИСОК ЛИТЕРАТУРЫ

1. **Mather J. W.** Formation of a high-density deuterium plasma focus // Physics of Fluids. 1965. Vol. 8. No. 2. Pp. 366–377.

2. **Filippov N. V., Filippova T. I., Vinogradov V. P.** Dense high-temperature plasma in a non-cylindrical Z-pinch compression // Nuclear Fusion. Supplement. 1962. Part 2. January. P. 577.

3. **Haines M. G.** A review of the dense Z-pinch // Plasma Physics and Controlled Fusion. 2011. Vol. 53. No. 9. P. 093001.

4. **Al-Hawat S., Akel M., Lee S., Saw S. H.** Model parameters versus gas pressure in two different plasma focus devices operated in argon and neon // Journal of Fusion Energy. 2012. Vol. 31. No. 1. Pp. 13–20.

5. **Lee S., Saw S. H.** Plasma focus ion beam fluence and flux – For various gases // Physics of Plasmas. 2013. Vol. 20. No. 6. P. 062702.

6. **Mohamed A. E. S.** A dense plasma focus device as a pulsed neutron source for material identification. A dissertation for the degree of Ph.D. Kansas, USA: Kansas State University, 2015. 168 p.

7. **Feugeas J. N., Llonch E. C., De González C. O., Galambos G.** Nitrogen implantation of AISI 304 stainless steel with a coaxial plasma gun // Journal of Applied Physics. 1988. Vol. 64. No. 5. Pp. 2648–2651.

8. **Rawat R. S., Srivastava M. P., Tandon S., Mansingh A.** Crystallization of an amorphous lead zirconate titanate thin film with a dense-plasma-focus device // Physical Review B. 1993. Vol. 47. No. 9. Pp. 4858–4862.

9. **Kant C. R., Srivastava M. P., Rawat R. S.** Thin carbon film deposition using energetic ions of a dense plasma focus // Physics Letters A. 1997. Vol. 226. No. 3–4. Pp. 212–216.

10. **Tan K. S.** High growth rate synthesis of zinc oxide and carbon based nanostructured materials using dense plasma focus device. A dissertation for the degree of Ph.D. Singapore: Nanyang Technological University, 2017.

11. **Rawat R. S.** Dense plasma focus – high-energy-density pulsed plasma device based novel facility for controlled material processing and synthesis // Plasma Science and Technology for Emerging Economies: An AAAPT Experience. Rawat R. S. (Editor). Singapore: Springer, 2017. 811 p. Pp. 39–112.

12. **Zhang T., Lin J., Patran A., Wong D., Hassan S. M., Mahmood S., Rawat R. S.** Optimization of a plasma focus device as an electron beam source for thin film deposition // Plasma Sources Science and Technology. 2007. Vol. 16. No. 2. Pp. 250–256.

13. **Pimenov V. N., Demina E. V., Ivanov L. I., Gribkov V. A., Dubrovsky A. V., Ugaste U., Tartari A.** Damage and modification of materials produced by pulsed ion and plasma streams in Dense Plasma Focus device // Nukleonika. 2008. Vol. 53. No. 3. Pp. 111–121.

14. **Gribkov V. A.** Physical processes taking place in dense plasma focus devices at the interaction of hot plasma and fast ion streams with materials under test // Plasma Physics and Controlled Fusion. 2015. Vol. 57. No. 6. P. 065010.

15. **Roshan M. V., Lee P., Lee S., Talebitaher A., Rawat R. S., Springham S. V.** Backward high energy ion beams from plasma focus // Physics of Plasmas. 2009. Vol. 16. No. 7. P. 074506.

16. **Brzosko J. S., Nardi V.** High yield of ^{12}C (d, n) ^{13}N and ^{14}N (d, n) ^{15}O reactions in the plasma focus pinch // Physics Letters A. 1991. Vol. 155. No. 2–3. Pp. 162–168.

17. **Roshan M. V., Razaghi S., Asghari F., Rawat R. S., Springham S. V., Lee P., Tan T. L.** Potential medical applications of the plasma focus in the radioisotope production for PET imaging // Physics Letters A. 2014. Vol. 378. No. 30–31. Pp. 2168–2170.

18. **Sumini M., Mostacci D., Rocchi F., Frignani M., Tartari A., Angeli E., Cucchi G.** Preliminary design of a 150 kJ repetitive plasma focus for the production of 18-F // Nuclear Instruments and Methods in Physics Research. Section A: Accelerators, Spectrometers, Detectors and Associated Equipment. 2006. Vol. 562. No. 2. Pp. 1068–1071.

19. **Shirani B., Abbasi F.** Prospects for 13N production in a small plasma focus device // Journal of Fusion Energy. 2013. Vol. 32. No. 2. Pp. 235–241.

20. **Akel M., Alsheikh Salo S., Ismael S., Saw S. H., Lee S.** Interaction of the high energy deuterons with the graphite target in the plasma focus devices based on Lee model // Physics of Plasmas. 2014. Vol. 21. No. 7. P. 072507.

21. **Sadeghi H., Amrollahi R., Fazelpour S., Omrani M.** Simulation of dense plasma focus devices to produce N-13 efficiently // Laser and Particle Beams. 2019. Vol. 37. No. 2. Pp. 209–216.

22. **Lee S., Saw S. H.** Plasma focus ion beam fluence and flux – Scaling with stored energy // Physics of Plasmas. 2012. Vol. 19. No. 11. P. 112703.

23. **Lee S., Saw S. H.** The plasma focus – Numerical experiments, insights and application // Plasma Science and Technology for Emerging Economies: An AAAPT Experience. Rawat R. S. (Editor). Singapore: Springer, 2017. 811 p. Pp. 131–137.

24. **Soto L.** New trends and future perspectives on plasma focus research // Plasma Physics and Controlled Fusion. 2005. Vol. 47. No. 5A. P. A361.

25. **Carlqvist P.** Current limitation and solar flares // Solar Physics. 1969. Vol. 7. No. 3. Pp. 377–392.

26. **Talaei A., Sadat Kiai S. M.** Study the influence of the bank energy on the dynamical pinch in plasma focus // Journal of Fusion Energy. 2009. Vol. 28. No. 3. Pp. 304–313.

27. **Young F. C., Golden J., Kapetanakos C. A.** Diagnostics for intense pulsed ion beams // Review of Scientific Instruments. 1977. Vol. 48. No. 4. Pp. 432–443.

28. www.srim.org for the stopping and range of ions in matter

29. **Michelmann R.** https://www-nds.iaea.org/exfor/exfor.htm

30. **Castillo S.** Medical and Statistical Review of N-13 Ammonia Positron Emission Tomography. 1999. Florence Houn, MD MPH FACP, Medical Office.

THE AUTHORS

NASSIF Alaa
Al-Wataniya Private University
Al-Wataniya Private University, International Hama–Homs Highway, Hama, XQ92+PMC, Syrian Arab Republic
alaa.nassif.85@hotmail.com

SAHYOUNI Walid
Al-Baath University
Al-Baath University, Damascus – Aleppo Highway, Homs, PP75+5VC, Syrian Arab Republic
wsahyouni@albaath-univ.edu.sy

ZEIDAN Ola
Al-Baath University
Al-Baath University, Damascus – Aleppo Highway, Homs, PP75+5VC, Syrian Arab Republic
ozedan@albaath-univ.edu.sy

KAFA Noha
Al-Baath University
Al-Baath University, Damascus – Aleppo Highway, Homs, PP75+5VC, Syrian Arab Republic
nohakafa10@gmail.com

СВЕДЕНИЯ ОБ АВТОРАХ

НАССИФ Алаа – *доктор военных наук, профессор инженерного факультета Частного университета Аль-Ватания, г. Хама, Сирийская Арабская Республика.*
XQ92+PMC, Syrian Arab Republic, Hama, Al-Wataniya Private University
alaa.nassif.85@hotmail.com

САХЬЮНИ Валид – *Ph.D., профессор кафедры физики (исследовательский отдел физики плазмы) Университета Аль-Баас, г. Хомс, Сирийская Арабская Республика.*
PP75+5VC, Syrian Arab Republic, Homs, Damascus – Aleppo Highway
wsahyouni@albaath-univ.edu.sy

ЗЕЙДАН Ола – *Ph.D., профессор кафедры физики (исследовательский отдел физики плазмы) Университета Аль-Баас, г. Хомс, Сирийская Арабская Республика.*
PP75+5VC, Syrian Arab Republic, Homs, Damascus – Aleppo Highway
ozedan@albaath-univ.edu.sy

КАФА Ноха – *сотрудник кафедры физики Университета Аль-Баас, г. Хомс, Сирийская Арабская Республика.*
PP75+5VC, Syrian Arab Republic, Homs, Damascus – Aleppo Highway
nohakafa10@gmail.com

Received 25.02.2023. Approved after reviewing 20.03.2023. Accepted 20.03.2023.
Статья поступила в редакцию 25.02.2023. Одобрена после рецензирования 20.03.2023. Принята 20.03.2023.

© Peter the Great St. Petersburg Polytechnic University, 2023

NUCLEAR PHYSICS

Original article
DOI: https://doi.org/10.18721/JPM.16210

MACHINE LEARNING MODELS TO DETERMINE UNOBSERVABLE CENTRALITY-RELATED PARAMETER VALUES FOR A WIDE RANGE OF NUCLEAR COLLISIONS AT THE ENERGY OF 200 GeV

A. A. Lobanov✉, *Ya. A. Berdnikov, Iu. M. Mitrankov*

Peter the Great St. Petersburg Polytechnic University, St. Petersburg, Russia

✉ lobanov2.aa@edu.spbstu.ru

Abstract. In the paper, a comparative analysis and a search for the optimal machine learning model have been conducted. The model should predict the values of unobservable centrality-related quantities based on the experimental data for observable quantities, namely, the number of charged particles and the number of neutral ones born in the interactions of both heavy and light ultrarelativistic nuclei. The sought-for unobservable values were the numbers of wounded nucleons involved in the interactions and of the binary nucleon-nucleon collisions. Linear and polynomial regressions of various degrees, a decision tree (DT), a random forest (RF), and a multilayer perceptron (MP) were chosen and considered as machine learning models. The prediction accuracy of the models was characterized and tested by the coefficient of determination. The DT, RF, and MP models were found to predict the desired values with the highest accuracy, i.e., they gave equally good results.

Keywords: machine learning, nuclei collisions, regression, decision tree, random forest, multilayer perceptron

Citation: Lobanov A. A., Berdnikov Ya. A., Mitrankov Iu. M., Machine learning models to determine unobservable centrality-related parameter values for a wide range of nuclear collisions at the energy of 200 GeV, St. Petersburg State Polytechnical University Journal. Physics and Mathematics. 16 (2) (2023) 111–120. DOI: https://doi.org/10.18721/JPM.16210

This is an open access article under the CC BY-NC 4.0 license (https://creativecommons.org/licenses/by-nc/4.0/)

© Lobanov A. A., Berdnikov Ya. A., Mitrankov Iu. M., 2023. Published by Peter the Great St. Petersburg Polytechnic University.

Научная статья
УДК 539.12
DOI: https://doi.org/10.18721/JPM.16210

МОДЕЛИ МАШИННОГО ОБУЧЕНИЯ ДЛЯ ОПРЕДЕЛЕНИЯ ЗНАЧЕНИЙ НЕНАБЛЮДАЕМЫХ ПАРАМЕТРОВ, СВЯЗАННЫХ С ЦЕНТРАЛЬНОСТЬЮ, ДЛЯ ШИРОКОГО СПЕКТРА ЯДЕРНЫХ СИСТЕМ ПРИ ЭНЕРГИИ 200 ГЭВ

А. А. Лобанов✉, *Я. А. Бердников*, *Ю. М. Митранков*

Санкт-Петербургский политехнический университет Петра Великого,

Санкт-Петербург, Россия

✉ lobanov2.aa@edu.spbstu.ru

Аннотация. В работе проведен сравнительный анализ и поиск оптимальной модели машинного обучения, которая позволила бы предсказывать значения ненаблюдаемых величин, характеризующих центральность, основываясь на экспериментальных данных для наблюдаемых величин: числа заряженных частиц и числа нейтральных частиц, рождающихся во взаимодействии как тяжелых, так и легких ультрарелятивистских ядер. Искомыми ненаблюдаемыми величинами были число раненых нуклонов, участвующих во взаимодействии, и число бинарных нуклон-нуклонных столкновений. В качестве моделей машинного обучения были выбраны и рассмотрены линейная и полиномиальные регрессии различных степеней, дерево решений (ДР), случайный лес (СЛ) и многослойный перцептрон (МП). Точность предсказания моделей характеризовалась и проверялась—коэффициентом детерминации. Установлено, что модели ДР, СЛ и МП с наибольшей точностью предсказывают искомые значения, т. е. дают одинаково хорошие результаты.

Ключевые слова: машинное обучение, столкновение ядер, регрессия, дерево решений, случайный лес, многослойный перцептрон

Ссылка для цитирования: Лобанов А. А., Бердников Я. А., Митранков Ю. М. Модели машинного обучения для определения значений ненаблюдаемых параметров, связанных с центральностью, для широкого спектра ядерных столкновений при энергии 200 ГэВ // Научно-технические ведомости СПбГПУ. Физико-математические науки. 2023. Т. 16. № 2. С. 111–120. DOI: https://doi.org/10.18721/ JPM.16210

Статья открытого доступа, распространяемая по лицензии CC BY-NC 4.0 (https://creativecommons.org/licenses/by-nc/4.0/)

Introduction

There is much interest towards machine learning methods, as they yield good results in diverse fields ranging from speech models to image generation.

For this reason, it seems worthwhile to apply existing machine learning algorithms in nuclear physics, elementary particle physics and high-energy physics, as well as develop new algorithms.

The physics of ultrarelativistic heavy-ion collisions is a fascinating field of research, holding immense potential for exploring the unusual state of matter that is quark-gluon plasma [1].

The high-energy interactions of nuclei are generally studied in collider experiments, measuring the characteristics of particles produced in ion beam collisions [2].

The energy of an ion beam is commonly expressed by the amount of energy per nucleon. This allows comparing the nucleus–nucleus collisions with proton-proton ones; it is assumed that the moving nuclei are a nucleon beam, while the collision of nuclei is a combination of nucleon pair collisions from different nuclei.

© Лобанов А. А., Бердников Я. А., Митранков Ю. М., 2023. Издатель: Санкт-Петербургский политехнический университет Петра Великого.

It was established in [3] that an important property of nucleus–nucleus collisions is a significant increase in the average multiplicity (calculated per colliding nucleon pair inside the nucleus) relative to the average multiplicity observed in a collision of free nucleon pairs (outside the nucleus).

The number of interacting nucleon pairs N_{coll} and the number of wounded nucleons N_{part} in nucleus–nucleus collisions characterizes the collision centrality [4]. Centrality determines the overlap volume of colliding nuclei and is related to the impact parameter of the collision (Fig. 1).

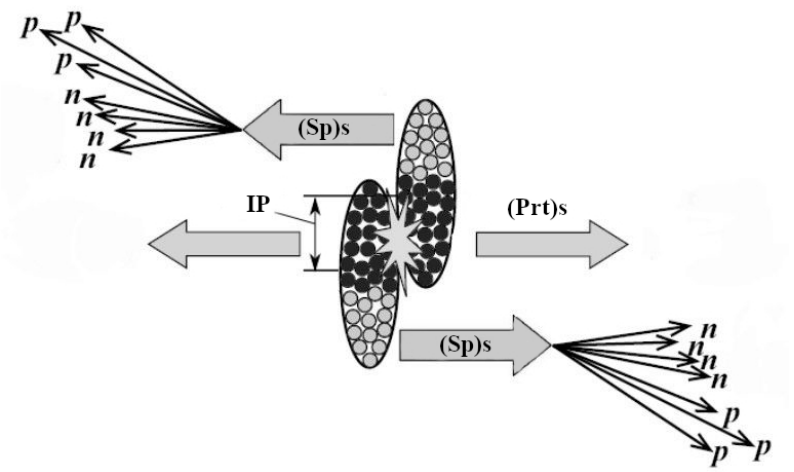

Fig. 1. Schematic representation of nuclear reaction:
spectators (Sp)s; participants (Prt)s; impact parameter IP
Interacting nucleons (black circles) and non-interacting
nucleons (gray circles) are shown; *p* are protons, *n* are neutrons

The overlap volume is in turn related to the number of nucleons participating in the interaction N_{coll} and the number of wounded nucleons N_{part} located in this volume and experiencing inelastic scattering. The values of N_{coll} and N_{part} cannot be determined experimentally for each collision of nuclei (event). However, even earlier data obtained at the RHIC (Relativistic Heavy Ion Collider) and SPS (Super Proton Synchrotron) accelerators [5, 6] showed that the multiplicities of particles (or their total transverse energies) are directly proportional to N_{coll} and N_{part}. This means that N_{coll} and N_{part} can be determined for the given multiplicities (or total transverse energies).

The goal of this study was to develop an optimal machine learning model allowing to predict the unobservables characterizing centrality.

These unobservable quantities are the number of wounded nucleons involved in the interaction and the number of binary nucleon–nucleon collisions.

The prediction should be based on the quantities observed in the experiment: the number of charged particles and the number of neutrons generated in each individual nucleus–nucleus interaction.

Simulation and computational technique

The machine learning model should predict the number of wounded nucleons N_{part} and the number of binary nucleon–nucleon collisions N_{coll} in a nucleus–nucleus collision at a given initial energy. The numbers of charged and neutral particles in each event in the pseudo-rapidity ranges $3 < |\eta| < 4$ and $5 < |\eta| < 8$, respectively, were chosen as the model parameters. The ranges were selected based on the experimental data, taken close to those used in experiments [2, 7]. The number of protons and the number of neutral particles in interacting nuclei were added to the above parameters to extend the functionality of the model for various collision systems.

Because it is impossible to determine the quantities N_{part} and N_{coll} experimentally, N_{part} and N_{coll} taken for training were preliminarily obtained in this study using the PYTHIA8/Angantyr 8.307 Monte Carlo generator [8].

The center-of-mass energy per nucleon pair was chosen equal to $\sqrt{s_{NN}}$ = 200 GeV for all nucleus–nucleus collisions considered. This energy is used in a large number of experiments at the RHIC collider [2].

The number of nucleus–nucleus collisions generated was 100,000.

From the standpoint of machine learning, prediction of N_{part} and N_{coll} depending on the multiplicity of charged particles N_{ch} and neutrons N_{neut} is a regression problem [9] (supervised training). For this reason, the methods most commonly used for this type of problems were selected and considered as machine learning models: linear regression [10], polynomial regressions of different degrees [10], decision tree [11], random forest [12] and multilayer perceptron [13].

Hyperparameters of the models (the parameters that are not determined during training) were selected using the Optuna library [14]. Tree Parzen Estimators was chosen as the algorithm [15].

The determination coefficient R^2 [16] characterized the prediction accuracy of the models, following the expression

$$R^2 = 1 - \frac{\sum_{i=1}^{N} (y_i - \hat{y}_i)^2}{\sum_{i=1}^{N} y_i^2},$$

where y_i are the reference values (for example, N_{coll}), $\hat{y}_i$ are the values of N_{coll} predicted by the model, N is the number of values.

The maximum value of the determination coefficient R^2 is equal to 1. The closer it is to 1, the closer the values obtained using the model are to the reference values. The model's prediction quality for N_{coll} and N_{part} was characterized by the arithmetic mean of their determination coefficients (since we intended to predict the values of two quantities). R^2 refers to this arithmetic mean from now on.

The confidence intervals and errors of the determination coefficient R^2 were found by the bootstrap method [17].

This numerical method allows to analyze statistical distributions. It is based on repeated Monte Carlo generation based on the available sample (introduced in 1977 by Bradley Efron and consisting in generating an empirical distribution [18] based on the available sample). Using the empirical distribution as a theoretical probability distribution allows generating a large number of pseudo-samples of arbitrary size via a random number generator. The resulting set of pseudo-samples is used to estimate the mean value and the error, constructing a confidence interval for the considered random variable with a confidence probability $p = 0.997$.

N_{coll}, N_{part}, N_{ch} values can be obtained for each nucleus–nucleus interaction (100,000 collisions generated in PYTHIA8/Angantyr were taken). This is used to construct the dependence of N_{coll}, N_{part} on the multiplicity of charged particles N_{ch} for the collision of gold nuclei (Au + Au) at an energy $\sqrt{s_{NN}} = 200$ GeV (initial data).

Fig. 2,*a* shows the dependence of N_{coll} on N_{ch}, obtained in the manner described here. Evidently, N_{coll}, N_{ch} have certain distributions that occur during simulation in the PYTHIA8/Angantyr package. To accelerate the training and optimize the performance of the models, these distributions of quantities were divided into 50 intervals, each characterized by a specific average value of a physical quantity. Fig. 2,*b* shows such an averaged dependence for the number of nucleon–nucleon collisions $\langle N_{coll} \rangle$ on the average multiplicity of charged particles $\langle N_{ch} \rangle$.

The resulting 50 intervals were randomly divided into 80% for training the models and 20% for testing them.

A similar computational pattern appears for the dependence of N_{part} on N_{ch}.

Comparison of linear and polynomial machine learning models for predicting the dependence $N_{coll}(N_{ch})$ in Au+Au collisions

As mentioned above, the following machine learning models were used: linear regression, polynomial regressions of various degrees, decision tree, random forest and multilayer perceptron.

Linear and polynomial regression. Let us start our consideration with the simplest of the above models. Quadratic and cubic functions were chosen as models of polynomial regression to avoid overfitting the model at higher degrees of the polynomial [19]. For comparison, a collision system of gold nuclei (Au+Au) was considered at the interaction energy $\sqrt{s_{NN}} = 200$ GeV.

Fig. 2,*a* shows the dependence of the number of nucleon–nucleon collisions on the multiplicity of charged particles approximated by linear, quadratic and cubic functions. Fig. 2,*b* shows the dependence of the average number of wounded nucleons $<N_{coll}>$ on the average multiplicity of charged particles $<N_{ch}>$ approximated by the same three functions.

Analyzing the data in Fig. 2, we can conclude that the approximation by a linear function systematically overestimates the number of wounded nucleons at high multiplicities of charged particles. For this reason, we only consider the computational results for polynomials of the 2nd and 3rd degrees.

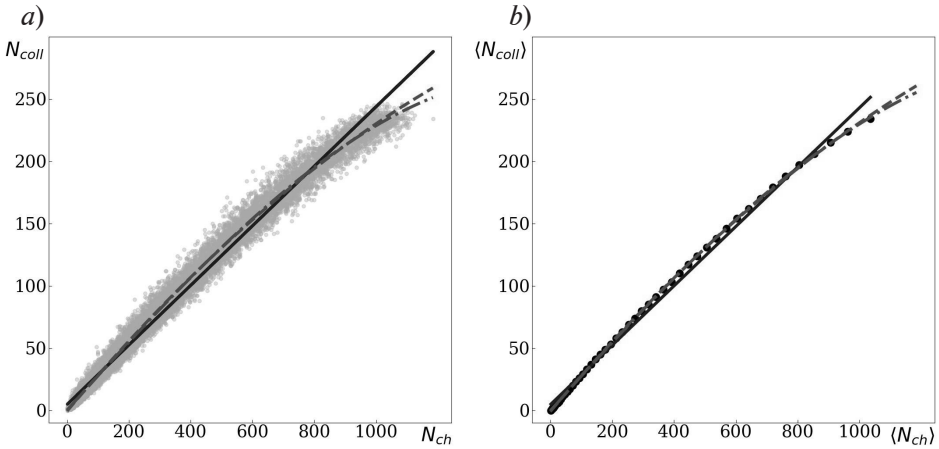

Fig. 2. Initial (gray area) (*a*) and averaged (symbols) (*b*) computational dependences for the number of nucleon–nucleon collisions of gold nuclei versus the initial (*a*) and averaged (*b*) multiplicity of charged particles; data approximation by various functions: linear (solid lines), quadratic (dashes) and cubic (dash-dotted lines)

Predictions made by machine learning models for the N_{coll} (N_{ch}) dependence for heavy ion collisions

To estimate the capabilities that the models have for generalizing the dependences and determining them, let us consider training on symmetric collision systems: copper (Cu + Cu), xenon (Xe + Xe), gold (Au + Au), lead (Pb + Pb) and uranium (U + U), subsequently testing them on asymmetric systems (see Table 1).

Here we give a dependence of R^2 for various models and various collisions systems on which the models were not trained. As follows from analysis of the data in Table 1, the results produced by the 3rd degree polynomial dependence are noticeable worse for most heavy ion collision systems, and differ from those given by other models. The determination coefficient R^2 in many systems is significantly less than unity for such a model. Therefore, it seems ill-advised to further consider this model.

The obtained values of the determination coefficient coincide within the error for all models (except for the 3rd degree polynomial) within the same system (see Table 1). An exception is observed for polynomial regression of the 3rd degree, for which the value of R^2 is statistically significantly different from other models.

Predictions for collisions of light-heavy nuclei

This section considers training of the models on light-heavy ion collisions

$$p + \text{Au},\ p + \text{Cu},\ d + \text{Au},\ d + \text{Cu},\ \text{He} + \text{Au},\ \text{He} + \text{Cu},$$

where *p* are protons, *d* are deuterium nuclei.

The models are also verified on asymmetric systems given in Table 2. This situation is interesting as it allows to carry out further generalization to various (different from the ones previously considered) collision systems and to check how well the models can perform in this case.

Table 1

Determination coefficients for various models and non-symmetric collision systems

Collision system	Determination coefficient R^2				
	Polynomial		Decision tree	Random forest	Multilayer perceptron
	2nd degree	3rd degree			
Cu + Xe	0.990±0.025	0.175±0.005	0.979±0.030	0.981±0.021	0.967±0.023
Cu + Au	0.986±0.023	–2.301±0.328	0.963±0.024	0.969±0.028	0.934±0.025
Cu + Pb	0.984±0.026	–0.087±0.442	0.960±0.027	0.963±0.026	0.926±0.024
Cu + U	0.982±0.029	0.460±0.769	0.960±0.026	0.961±0.031	0.921±0.024
Xe + Au	0.997±0.028	0.155±0.004	0.991±0.027	0.992±0.030	0.987±0.029
Xe + Pb	0.996±0.026	–0.284±0.013	0.990±0.026	0.991±0.027	0.984±0.029
Xe + U	0.996±0.028	–0.224±0.119	0.987±0.029	0.989±0.026	0.977±0.022
Au + Pb	1.000±0.031	0.999±0.025	0.998±0.024	0.999±0.026	0.999±0.030
Au + U	0.999±0.024	0.901±0.024	0.998±0.030	0.998±0.027	0.996±0.027
Pb + U	0.999±0.027	0.963±0.026	0.998±0.027	0.998±0.031	0.997±0.028

Note. Data are given for verification of the models for collision systems on which the models were not trained.

Table 2

Determination coefficients for four models and for systems of light-heavy ion collisions

Collision system	Determination coefficient R^2			
	2nd degree polynomial	Decision tree	Random forest	Multilayer perceptron
p + U	0.511±0.016	0.988±0.031	0.965±0.026	0.953±0.026
p + Xe	0.978±0.029	0.990±0.028	0.973±0.026	0.947±0.026
d + Pb	0.856±0.022	0.996±0.028	0.987±0.027	0.983±0.027
d + U	0.507±0.015	0.996±0.023	0.983±0.027	0.983±0.026
d + Xe	0.990±0.031	0.988±0.024	0.982±0.024	0.973±0.022
He + Pb	0.863±0.023	0.996±0.033	0.990±0.026	0.991±0.024
He + U	0.597±0.016	0.993±0.026	0.977±0.026	0.992±0.024
He + Xe	0.989±0.030	0.989±0.026	0.982±0.024	0.983±0.023

Note. Data are given for verification of the models for collision systems on which the models were not trained.

Table 2 shows the dependence of the determination coefficient for the models considered in this paper and various nuclear systems on which the models were not trained. It follows from the data in the table that the 2nd degree polynomial dependence gives noticeably worse (statistically validated) results, unlike other models. The determination coefficient for this model is significantly different from unity in many systems. As in the first case, it seems impractical to consider it further.

The obtained values of the determination coefficient coincide within the error for all other models (except for the results for the 2nd degree polynomial) within the same system.

Generalized case

It is of the greatest interest to apply the models to interactions of both light-heavy and heavy-heavy nuclei. The models were trained for such situations on a range of collision systems of both light and heavy nuclei, considered in the previous two sections:

Cu + Cu, Xe + Xe, Au + Au, Pb + Pb, U + U;

p + Au, *p* + Cu, *d* + Au, *d* + Cu, He + Au, He + Cu.

The prediction accuracy was verified on the collision systems listed in Table 3. The Table also gives values of R^2 for different models, depending on the collision system. Analyzing the obtained results, we can conclude that all models yield similar values of the dtermination coefficient within the error.

Table 3

Generalized computations of determination coefficients for three models and various collision systems that did not participate in the training

Collision system	Determination coefficient R^2		
	Decision tree	Random forest	Multilayer perceptron
p + U	0.984±0.030	0.954±0.026	0.955±0.026
p + Xe	0.984±0.029	0.960±0.024	0.956±0.025
d + Pb	0.996±0.027	0.982±0.024	0.990±0.026
d + U	0.990±0.024	0.974±0.025	0.987±0.025
d + Xe	0.984±0.022	0.971±0.023	0.971±0.026
He + Pb	0.997±0.026	0.985±0.024	0.991±0.029
He + U	0.993±0.026	0.981±0.029	0.990±0.030
He + Xe	0.985±0.024	0.987±0.032	0.987±0.026
Cu + Xe	0.980±0.025	0.982±0.031	0.990±0.027
Cu + Au	0.969±0.023	0.965±0.025	0.983±0.023
Cu + Pb	0.965±0.027	0.961±0.025	0.981±0.029
Cu + U	0.959±0.024	0.959±0.023	0.980±0.027
Xe + Au	0.991±0.023	0.992±0.029	0.996±0.024
Xe + Pb	0.991±0.027	0.991±0.029	0.995±0.028
Xe + U	0.988±0.026	0.987±0.025	0.993±0.026
Au + Pb	0.999±0.027	0.999±0.027	0.999±0.023
Au + U	0.997±0.028	0.998±0.026	0.998±0.025
Pb + U	0.998±0.025	0.999±0.030	0.999±0.028

Conclusion

We carried out a comparative analysis of machine learning models to determine the optimal algorithm for obtaining experimentally unobservable parameters characterizing the collision centrality, specifically, the number of wounded nucleons and the number of binary nucleon collisions, based observable quantities, i.e., the multiplicity of charged particles and the number of neutrons produced in the collision. We adopted models of polynomial regression of different degrees, decision tree, random forest and multilayer perceptron.

It was established in the analysis that the decision tree, the random forest and the multilayer perceptron predict the values of N_{part} and N_{coll} with the greatest accuracy ($R^2 \gtrsim 0.95$), which is to say that these models yield equally good results (within uncertainty) for a fixed initial energy.

We propose an additional parameter that is the initial energy of colliding nuclei $\sqrt{s_{NN}}$ to be introduced as a natural continuation of this study to expand the applicability range of the considered models to an arbitrary range of initial energies.

The computations were run on an Intel® Core™ i9-9980XE processor and an NVIDIA GeForce RTX™ 2080 Ti video card. RAM was 64 GB.

REFERENCES

1. **Shurjak E. V.,** The quark-glyuon plasma, Phys. Usp. 25 (10) (1982) 760– 761.

2. **Morrison D. P., Akiba Y., Alford O., et al.,** The PHENIX experiment at RHIC, Nucl. Phys. A. 638 (1–2) (1998) 565c–569c.

3. ATLAS Collaboration**, Aad G., Abbott B., et al.,** Measurement of the centrality dependence of the charged particle pseudorapidity distribution in lead-lead collisions at $\sqrt{s_{NN}}$ = 2.76 TeV with the ATLAS detector, Phys. Lett. B. 710 (3) (2012) 363–382.

4. **Aguiar C. E., Andrade R., Grassi F., et al.,** Comparison between classification using impact parameter and using number of participants in relativistic nuclear collisions, Braz. J. Phys. 34 (1a) (2004) 319–321.

5. **Adcox K., Adler S. S., Ajitanand N. N., et al.** Centrality dependence of charged particle multiplicity in Au-Au collisions at $\sqrt{s_{NN}}$ = 130 GeV, Phys. Rev. Lett. 86 (16) (2001) 3500–3505.

6. UAS Collaboration, **Alpgerd K., Ansorge R. E., et al.,** Charged particle multiplicities at the CERN SPS collider, Phys. Lett. B. 107 (4) (1981) 315–319.

7. **Harris J. W.,** STAR Collaboration, **Adams D. L., et al.,** The STAR experiment at the relativistic heavy ion collider, Nucl. Phys. A. 566 (3 January) (1994) 277–285.

8. **Sjöstrand T., Mrenna S., Skands P.,** A brief introduction to PYTHIA 8.1, Comp. Phys. Commun. 178 (11) (2008) 852–867.

9. **Förster E., Rönz B.,** Methoden der Korrelations- und Regressionanalyse, Verlag Die Wirtschaft, Berlin, 1979.

10. **Yan X., Su X.,** Linear regression analysis: Theory and computing, World Scientific, Singapore, 2009.

11. **Quinlan J. R.,** Induction of decision trees, Mach. Learn. 1 (1) (1986) 81–106.

12. **Ho T. K.,** Random decision forests, Proc. 3rd Int. Conf. Document Analysis and Recognition, Montreal, QC, Canada. 14–16 Aug. 1995. IEEE. 1 (1995) 278– 282.

13. **Haykin S.** Neural networks. A comprehensive foundation. Prentice Hall, New Jersey, USA, 1998.

14. **Akiba T., Sano S., Yanase T., et al.,** Optuna: A next-generation hyperparameter optimization framework, Proc. 25th ACM SIGKDD Int. Conf. Knowledge Discovery & Data Mining (2019) 2623–2631.

15. **Bergstra J., Bardenet R., Bengio Y., Kégl B.,** Algorithms for hyper-parameter optimization, In book: Advances in Neural Information Processing Systems 24 (NIPS 2011). Edited by J. Shawe-Taylor, R. Zemel, P. Bartlett, F. Pereira, K. Q. Weinberger. 24 (2011) 1–6.

16. **Barten A. P.,** The coefficient of determination for regression without a constant term, In book: Heijmans R., Neudecker H. (Eds.) The practice of econometrics, (International Studies in Economics and Econometrics. Vol. 15). Springer, Dordrecht (1987) 181–189.

17. **Efron B.,** Bootstrap methods: Another look at the jackknife, Ann. Stat. 7 (1) (1979) 1–26.

18. **Shorack G. R., Wellner J. A.,** Empirical processes with applications to statistics (Classics in Applied Mathematics, Ser. No. 59). Publ. by SIAM, Philadelphia, USA, 2009.

19. **Tetko I. V., Livingstone D. J., Luik A. I.,** Neural network studies. 1. Comparison of overfitting and overtraining, J. Chem. Inf. Comput. Sci. 35 (5) (1995) 826–833.

СПИСОК ЛИТЕРАТУРЫ

1. **Шуряк Э. В.** Кварк-глюонная плазма // Успехи физических наук. 1982. Т. 138. № 2. С. 327–328.

2. **Morrison D. P., Akiba Y., Alford O., et al.** The PHENIX experiment at RHIC // Nuclear Physics A. 1998. Vol. 638. No. 1–2. Pp. 565c–569c.

3. **ATLAS Collaboration, Aad G., Abbott B., et al.** Measurement of the centrality dependence of the charged particle pseudorapidity distribution in lead-lead collisions at $\sqrt{s_{NN}}$ = 2.76 TeV with the ATLAS detector // Physics Letters B. 2012. Vol. 710. No. 3. Pp. 363–382.

4. **Aguiar C. E., Andrade R., Grassi F., Hama Y., Kodama T., Osada T., Socolowski Jr. O.** Comparison between classification using impact parameter and using number of participants in relativistic nuclear collisions // Brazilian Journal of Physics. 2004. Vol. 34. No. 1a. Pp. 319–321.

5. **Adcox K., Adler S. S., Ajitanand N. N., et al.** Centrality dependence of charged particle

multiplicity in Au-Au collisions at $\sqrt{s_{NN}}$ = 130 GeV // Physical Review Letters. 2001. Vol. 86. No. 16. Pp. 3500–3505.

6. **UAS Collaboration, Alpgerd K., Ansorge R. E., et al.** Charged particle multiplicities at the CERN SPS collider // Physics Letters B. 1981. Vol. 107. No. 4. Pp. 315–319.

7. **Harris J. W., STAR Collaboration, Adams D. L., et al.** The STAR experiment at the relativistic heavy ion collider // Nuclear Physics A. 1994. Vol. 566. 3 January. Pp. 277–285.

8. **Sjöstrand T., Mrenna S., Skands P.** A brief introduction to PYTHIA 8.1 // Computer Physics Communications. 2008. Vol. 178. No. 11. Pp. 852–867.

9. **Фёрстер Э., Рёнц Б.** Методы корреляционного и регрессионного анализа. Пер. с нем. М.: Финансы и статистика, 1983. 303 с.

10. **Yan X., Su X.** Linear regression analysis: Theory and computing. Singapore: World Scientific, 2009. 348 p.

11. **Quinlan J. R.** Induction of decision trees // Machine Learning. 1986. Vol. 1. No. 1. Pp. 81–106.

12. **Ho T. K.** Random decision forests // Proceedings of 3rd International Conference on Document Analysis and Recognition. Montreal, QC, Canada. 14–16 August, 1995. Vol. 1. Pp. 278– 282.

13. **Хайкин С.** Нейронные сети. Полный курс. Пер. с англ. -2е изд. М.: Изд-во «Вильямс», 2019. 1104 с.

14. **Akiba T., Sano S., Yanase T., Ohta T., Koyama M.** Optuna: A next-generation hyperparameter optimization framework // Proceedings of the 25th ACM SIGKDD International Conference on Knowledge Discovery & Data Mining. 2019. Pp. 2623–2631.

15. **Bergstra J., Bardenet R., Bengio Y., Kégl B.** Algorithms for hyper-parameter optimization // Advances in Neural Information Processing Systems 24 (NIPS 2011). Edited by J. Shawe-Taylor, R. Zemel, P. Bartlett, F. Pereira, K. Q. Weinberger. 2011. Vol. 24. Pp. 1–6.

16. **Barten A. P.** The coefficient of determination for regression without a constant term // Heijmans R., Neudecker H. (Eds.) The practice of econometrics. International Studies in Economics and Econometrics. Vol. 15. Dordrecht: Springer, 1987. Pp. 181– 189.

17. **Efron B.** Bootstrap methods: Another look at the jackknife // The Annals of Statistics. 1979. Vol. 7. No. 1. Pp. 1–26.

18. **Shorack G. R., Wellner J. A.** Empirical processes with applications to statistics (Classics in Applied Mathematics, Series No. 59). Published by Society for Industrial and Applied Mathematics, Philadelphia, USA, 2009. 348 p.

19. **Tetko I. V., Livingstone D. J., Luik A. I.** Neural network studies. 1. Comparison of overfitting and overtraining // Journal of Chemical Information and Computer Sciences. 1995. Vol. 35. No. 5. Pp. 826 –833.

THE AUTHORS

LOBANOV Andrey A.
Peter the Great St. Petersburg Polytechnic University
29 Politechnicheskaya St., St. Petersburg, 195251, Russia
lobanov2.aa@edu.spbstu.ru
ORCID: 0000-0002-8910-4775

BERDNIKOV Yaroslav A.
Peter the Great St. Petersburg Polytechnic University
29 Politechnicheskaya St., St. Petersburg, 195251, Russia
berdnikov@spbstu.ru
ORCID: 0000-0003-0309-5917

MITRANKOV Iurii M.
Peter the Great St. Petersburg Polytechnic University
29 Politechnicheskaya St., St. Petersburg, 195251, Russia
mitrankovy@gmail.com
ORCID: 0000-0002-9774-2339

СВЕДЕНИЯ ОБ АВТОРАХ

ЛОБАНОВ Андрей Александрович – *студент Физико-механического института Санкт-Петербургского политехнического университета Петра Великого.*
195251, Россия, г. Санкт-Петербург, Политехническая ул., 29
lobanov2.aa@edu.spbstu.ru
ORCID: 0000-0002-8910-4775

БЕРДНИКОВ Ярослав Александрович – *доктор физико-математических наук, профессор Высшей школы фундаментальных физических исследований Санкт-Петербургского политехнического университета Петра Великого.*
195251, Россия, г. Санкт-Петербург, Политехническая ул., 29
berdnikov@spbstu.ru
ORCID: 0000-0003-0309-5917

МИТРАНКОВ Юрий Михайлович – *ассистент Высшей школы фундаментальных физических исследований Санкт-Петербургского политехнического университета Петра Великого.*
195251, Россия, г. Санкт-Петербург, Политехническая ул., 29
mitrankovy@gmail.com
ORCID: 0000-0002-9774-2339

Received 18.01.2023. Approved after reviewing 30.01.2023. Accepted 31.01.2023.
Статья поступила в редакцию 18.01.2023. Одобрена после рецензирования 30.01.2023. Принята 31.01.2023.

© Peter the Great St. Petersburg Polytechnic University, 2023

Original article
DOI: https://doi.org/10.18721/JPM.16211

MACHINE LEARNING MODELS TO FIND UNOBSERVABLE CENTRALITY-RELATED PARAMETER VALUES IN COLLISIONS OF DIFFERENT NUCLEI IN THE INITIAL ENERGY RANGE FROM 40 TO 200 GEV

A. A. Lobanov✉, *A. Ya. Berdnikov*, *M. M. Mitrankova*

Peter the Great St. Petersburg Polytechnic University, St. Petersburg, Russia

✉ lobanov2.aa@edu.spbstu.ru

Abstract. This paper continues studies in machine learning models capabilities aimed to finding the best way to predict the values of unobservable quantities that characterize centrality, based on experimental data for observable quantities: the number of charged particles and the number of neutrons produced in ultrarelativistic nuclear interactions. The sought-for unobservable quantities were the number of wounded nucleons involved in the interaction and the number of binary nucleon-nucleon collisions. A decision tree, a random forest, and a multilayer perceptron (MP) were tested as machine learning models. The prediction accuracy of the models was characterized by the coefficient of determination R^2. Dependences of R^2 values on initial energies (40–200 GeV) for different systems of colliding nuclei were obtained. The MP model was found to be able to predict the values of unknown quantities in a wide range of initial energies for different systems of nuclear interactions with good accuracy.

Keywords: machine learning, nuclei collisions, initial energy, *R*-squared, multilayer perceptron

Citation: Lobanov A. A., Berdnikov A. Ya., Mitrankova M. M., Machine learning models to find unobservable centrality-related parameter values in collisions of different nuclei in the initial energy range from 40 to 200 GeV, St. Petersburg State Polytechnical University Journal. Physics and Mathematics. 16 (2) (2023) 121–131. DOI: https://doi.org/10.18721/JPM.16211

This is an open access article under the CC BY-NC 4.0 license (https://creativecommons.org/licenses/by-nc/4.0/)

© Lobanov A. A., Berdnikov A. Ya, Mitrankova M. M., 2023. Published by Peter the Great St. Petersburg Polytechnic University.

Научная статья
УДК 539.12
DOI: https://doi.org/10.18721/JPM.16211

МОДЕЛИ МАШИННОГО ОБУЧЕНИЯ ДЛЯ НАХОЖДЕНИЯ ЗНАЧЕНИЙ НЕНАБЛЮДАЕМЫХ ПАРАМЕТРОВ, ОПИСЫВАЮЩИХ ЦЕНТРАЛЬНОСТЬ, ПРИ СТОЛКНОВЕНИЯХ РАЗЛИЧНЫХ ЯДЕР В ЭНЕРГЕТИЧЕСКОМ ДИАПАЗОНЕ ОТ 40 ДО 200 ГЭВ

А. А. Лобанов✉, *А. Я. Бердников*, *М. М. Митранкова*

Санкт-Петербургский политехнический университет Петра Великого,

Санкт-Петербург, Россия

✉ lobanov2.aa@edu.spbstu.ru

Аннотация. Данная работа продолжает исследования возможностей моделей машинного обучения, направленные на поиск оптимального пути предсказания значений ненаблюдаемых величин, характеризующих центральность, основываясь на экспериментальных данных для наблюдаемых величин: числа заряженных частиц и числа нейтронов, рождающихся во взаимодействии ультрарелятивистских ядер. Искомыми ненаблюдаемыми величинами были число раненых нуклонов, участвующих во взаимодействии, и число бинарных нуклон-нуклонных столкновений. В качестве моделей машинного обучения были протестированы дерево решений, случайный лес и многослойный перцептрон (МП). Точность предсказания моделей характеризовалась коэффициентом детерминации (R^2). Получены зависимости значений R^2 от начальных энергий (200 – 40 ГэВ) для разных систем сталкивающихся ядер. Установлено, что модель МП способна с хорошей точностью предсказывать значения искомых величин в широком диапазоне начальных энергий для различных систем ядерных взаимодействий.

Ключевые слова: машинное обучение, столкновение ядер, начальная энергия, коэффициент детерминации, многослойный перцептрон

Ссылка для цитирования: Лобанов А. А., Бердников А. Я., Митранкова М. М. Модели машинного обучения для нахождения значений ненаблюдаемых параметров, описывающих с центральность, при столкновениях различных ядер в энергетическом диапазоне от 40 до 200 ГэВ // Научно-технические ведомости СПбГПУ. Физико-математические науки. 2023. Т. 16. № 2. С. 121–131. DOI: https://doi.org/10.18721/ JPM.16211

Статья открытого доступа, распространяемая по лицензии CC BY-NC 4.0 (https://creativecommons.org/licenses/by-nc/4.0/)

Introduction

Algorithms based on machine learning methods have long yielded good results in various fields of science and technology, often surpassing standard algorithms [1]. In fiew of this, it seems reasonable to apply machine learning to physics of ultrarelativistic collisions of nuclei.

This paper intends to continue and expand the studies in [2]. This initial study applied machine learning methods to determine the values of unobservable experimental quantities from the observed ones. The former include the number of binary nucleon–nucleon collisions N_{coll} in a nucleus–nucleus collision at a given initial energy and the number of wounded nucleons N_{part} produced in a nucleus–nucleus collision. The latter are the number of charged particles N_{ch} and the number of neutrons N_{neut} produced in each individual nucleus–nucleus interaction.

We have found that three models, namely, a decision tree, a random forest and a multilayer perceptron, are capable of predicting the values of N_{coll} and N_{part} with good accuracy in a wide range of collision systems [2].

© Лобанов А. А., Бердников А. Я., Митранкова М. М., 2023. Издатель: Санкт-Петербургский политехнический университет Петра Великого.

However, the above-mentioned study was limited to considering the applicability of the models only for a given initial center-of-mass energy $\sqrt{s_{NN}}$ = 200 GeV.

As the next stage in our research, we intend to find out whether these models are applicable for varying values of the initial energy $\sqrt{s_{NN}}$. In fact, the initial energy can determine the nature of the processes occurring during the collision of nuclei [3].

This paper analyzes the applicability of machine learning models to predicting the number of wounded nucleons N_{part} involved in the interaction and the number of binary nucleon–nucleon collisions N_{coll} (parameters characterizing centrality) at initial energies in the range of 40–200 GeV.

The basis for the models are the quantities observed experimentally: the number of charged particles and the number of neutrons produced in each individual nucleus–nucleus interaction for various systems of colliding nuclei.

Computational technique

The input parameters of the models (decision tree, random forest and multilayer perceptron) are the multiplicities of charged particles N_{ch} and neutrons N_{neut}.

The multiplicity of charged particles was set in the range of pseudorapidities $3 < |\eta| < 4$, and the number of neutral particles in the range of pseudorapidities $5 < |\eta| < 8$. These ranges were selected based on the experimental data from [4]. Additional input parameters of the models were the number of protons and neutrons in colliding nuclei and the center-of-mass energy $\sqrt{s_{NN}}$ [5]. These parameters allow simulating collisions of nuclei of different nature at different initial energies.

We considered collision events for a wide variety of nuclei used by researchers in a large number of very diverse experiments [4]. These nuclei are hydrogen H (protons) *p*, helium He, copper Cu, xenon Xe, gold Au, lead Pb and uranium U.

The models were trained on the following binary systems, randomly selected from the above nuclei:

$$p + \mathrm{Cu},\ p + \mathrm{U},\ \mathrm{He} + \mathrm{Xe},\ \mathrm{He} + \mathrm{U},\ \mathrm{Cu} + \mathrm{Cu},\ \mathrm{Cu} + \mathrm{Xe},\ \mathrm{Xe} + \mathrm{Pb},\ \mathrm{Au} + \mathrm{Au}.$$

The predictions of the models were verified on the following binary systems:

$$p + \mathrm{Pb},\ p + \mathrm{Xe},\ p + \mathrm{Au},\ \mathrm{He} + \mathrm{Cu},\ \mathrm{He} + \mathrm{Au},\ \mathrm{He} + \mathrm{Pb}$$
(light-heavy collision systems);

$$\mathrm{Cu} + \mathrm{Au},\ \mathrm{Cu} + \mathrm{Pb},\ \mathrm{Cu} + \mathrm{U},\ \mathrm{Xe} + \mathrm{U},\ \mathrm{Au} + \mathrm{Pb},\ \mathrm{Au} + \mathrm{U},\ \mathrm{Pb} + \mathrm{U}$$
(asymmetric heavy collisions)

$$\mathrm{Xe} + \mathrm{Xe},\ \mathrm{Pb} + \mathrm{Pb},\ \mathrm{U} + \mathrm{U}$$
(symmetric heavy collision systems).

The selected initial energies $\sqrt{s_{NN}}$ lay in the range from 40 to 200 GeV [4].

The models were trained at energies in the range of 40–200 GeV with a step of 40 GeV, and verified in the extended energy range of 20–260 GeV with a step of 20 GeV. The tables below give only part of the data obtained (not for all selected initial energies) for space considerations.

The same as in [2], training of the models and verification of their prediction accuracy were preceded by simulation (generation) of the above-mentioned binary collisions, but at different initial energies (see above). The PYTHIA8/Angantyr 8.307 software was used to generate collisions [5]. The number of generated events was 100,000. Numerical values of wounded nucleons N_{part} and binary nucleon–nucleon collisions N_{coll} were obtained from each event, as well as multiplicities of charged particles and neutrons (reference values).

The decision tree [6], random forest [7] and multilayer perceptron [8] were considered as machine learning models, as in the previous study [2], where these models produced the best results.

The model parameters that the program did not determine during training (hyperparameters) was selected with the Tree Parzen Estimators algorithm [9] from the Optuna library [10].

The details of the simulation were as follows. The decision tree model had a depth of 63. The random forest model included 37 estimators with a maximum depth of 84 each. The multilayer perceptron consisted of 7 input neurons, 5 hidden layers of 512 neurons each, with a ReLU activation function and an output layer of two neurons with a linear activation function. The number of epochs for training was 45, and Adam was chosen as the gradient descent optimizer [11].

The prediction accuracy provided by the models for N_{coll} and N_{part} was characterized by the determination coefficients R^2_{Ncoll} and R^2_{Npart} [12], which are determined by the following formula:

$$R^2 = 1 - \frac{\sum_{i=1}^{N}(y_i - \hat{y}_i)^2}{\sum_{i=1}^{N} y_i^2},$$

where R^2 includes R^2_{Ncoll} or R^2_{Npart}; y_i *are* the reference values of the given quantities; $\hat{y}_i$ *are* the values predicted by the model; N is the number of values [2].

The prediction accuracy of the parameters N_{coll} and N_{part} was characterized by the arithmetic mean R^2 of R^2_{Ncoll} for N_{coll} and R^2_{Npart} for N_{part} [13]:

$$\overline{R}^2 = \frac{R_{N_{coll}}{}^2 + R_{N_{part}}{}^2}{2}.$$

The closer R^2 to unity (the maximum value), the closer the computational values to the reference ones.

Confidence intervals and errors of the determination coefficient R^2 were found by the bootstrap method [14].

Computational results and discussion

Tables 1–9 present the computational results for the determination coefficients R^2 depending on the initial energy of colliding nuclei $\sqrt{s_{NN}}$, for three classes of collision systems on which the verification was performed.

The models that gave the best results are considered (see [2]): a multilayer perceptron, a decision tree and a random forest.

As follows from analysis of the data presented in the tables, all models used yield good results for any systems of colliding nuclei at initial energies of 40, 80, 120, 160 and 200 GeV (on which the models were trained), since the values of $R^2 > 0.95$.

Because one of our goals was to analyze the results of model predictions at points interpolated and extrapolated by energy, the tables show the determination coefficients at energies of 20, 60, 180 and 220 GeV.

Table 1

Determination coefficients of multilayer perceptron model as function of initial energies $\sqrt{s_{NN}}$ for light-heavy collision systems

$\sqrt{s_{NN}}$, GeV	Determination coefficient $\bar{R}^2$ for collision system				
	p + Xe	p + Au	p + Pb	He + Au	He + U
20	0.742±0.019	0.706±0.023	0.789±0.024	0.902±0.023	0.895±0.022
40	0.954±0.022	0.956±0.025	0.954±0.028	0.984±0.023	0.988±0.025
60	0.967±0.025	0.965±0.025	0.932±0.025	0.983±0.025	0.983±0.023
80	0.951±0.026	0.967±0.028	0.969±0.024	0.987±0.026	0.988±0.026
160	0.957±0.025	0.957±0.021	0.965±0.027	0.989±0.025	0.989±0.026
180	0.957±0.027	0.960±0.026	0.961±0.026	0.989±0.024	0.990±0.024
200	0.955±0.029	0.948±0.026	0.959±0.026	0.987±0.027	0.990±0.024
220	0.952±0.027	0.949±0.023	0.951±0.029	0.983±0.025	0.988±0.030

Table 2

Determination coefficients of multilayer perceptron model as function of initial energies $\sqrt{s_{NN}}$ for asymmetric heavy collision systems

$\sqrt{s_{NN}}$, GeV	Determination coefficient $\bar{R}^2$ for collision system						
	Cu + Au	Cu + Pb	Xe + Pb	Xe + U	Au + Pb	Au + U	Pb + U
20	0.860± ±0.023	0.846± ±0.021	0.725± ±0.019	0.733± ±0.018	0.679± ±0.014	0.689± ±0.019	0.685± ±0.016
40	0.978± ±0.023	0.978± ±0.024	0.988± ±0.023	0.994± ±0.023	0.999± ±0.024	0.998± ±0.028	0.999± ±0.029
60	0.969± ±0.028	0.949± ±0.024	0.995± ±0.026	0.951± ±0.024	0.980± ±0.025	0.971± ±0.025	0.975± ±0.028
80	0.993± ±0.029	0.990± ±0.026	0.998± ±0.025	0.993± ±0.028	0.998± ±0.027	0.994± ±0.024	0.994± ±0.028
160	0.996± ±0.028	0.994± ±0.023	0.999± ±0.025	0.998± ±0.027	0.998± ±0.025	0.998± ±0.031	0.998± ±0.030
180	0.995± ±0.030	0.994± ±0.028	0.999± ±0.022	0.998± ±0.033	0.999± ±0.026	0.998± ±0.028	0.998± ±0.023
200	0.994± ±0.024	0.994± ±0.024	0.999± ±0.024	0.997± ±0.025	0.999± ±0.035	0.998± ±0.026	0.998± ±0.029
220	0.996± ±0.028	0.993± ±0.030	0.999± ±0.027	0.997± ±0.028	0.999± ±0.026	0.998± ±0.025	0.998± ±0.028

Table 3

Determination coefficients of multilayer perceptron model as function of initial energies $\sqrt{s_{NN}}$ for symmetric heavy collision systems

$\sqrt{s_{NN}}$, GeV	Determination coefficient $\bar{R}^2$ for collision system		
	Xe + Xe	Pb + Pb	U + U
20	0.840±0.022	0.682±0.020	0.627±0.020
40	0.960±0.028	0.998±0.025	0.998±0.023
60	0.899±0.024	0.985±0.026	0.972±0.027
80	0.972±0.026	0.998±0.027	0.993±0.028
160	0.992±0.026	0.998±0.026	0.998±0.028
180	0.993±0.026	0.999±0.032	0.998±0.025
200	0.993±0.029	0.999±0.027	0.999±0.028
220	0.992±0.028	0.999±0.029	0.999±0.024

Table 4

Determination coefficients of decision tree model as function of initial energies $\sqrt{s_{NN}}$ for light-heavy collision systems

$\sqrt{s_{NN}}$, GeV	Determination coefficient $\bar{R}^2$ for collision system				
	p + Xe	p + Au	p + Pb	He + Au	He + U
20	0.399±0.009	0.151±0.004	0.251±0.007	0.228±0.006	0.328±0.008
40	0.978±0.025	0.978±0.027	0.986±0.025	0.975±0.028	0.983±0.029
60	0.577±0.014	0.672±0.019	0.454±0.014	0.502±0.013	0.611±0.019
80	0.969±0.034	0.973±0.026	0.964±0.023	0.972±0.025	0.970±0.027
160	0.985±0.026	0.995±0.028	0.988±0.027	0.983±0.030	0.997±0.024
180	0.971±0.024	0.983±0.024	0.985±0.026	0.964±0.026	0.980±0.036
200	0.982±0.027	0.980±0.029	0.989±0.029	0.966±0.028	0.969±0.030
220	0.993±0.028	0.988±0.031	0.980±0.027	0.974±0.026	0.953±0.029

Table 5

Determination coefficients of decision tree model as function of initial energies $\sqrt{s_{NN}}$ for asymmetric heavy collision systems

$\sqrt{s_{NN}}$, GeV	Determination coefficient $\bar{R}^2$ for collision system						
	Cu+Au	Cu+Pb	Xe+Pb	Xe+U	Au+Pb	Au+U	Pb+U
20	0.260± ±0.008	0.268± ±0.008	0.359± ±0.008	0.304± ±0.008	0.361± ±0.015	0.398± ±0.010	0.364± ±0.010
40	0.966± ±0.023	0.976± ±0.027	0.981± ±0.028	0.994± ±0.033	0.996± ±0.024	0.992± ±0.027	0.989± ±0.028
60	0.293± ±0.008	0.173± ±0.004	0.027± ±0.001	0.557± ±0.016	0.685± ±0.018	0.732± ±0.022	0.782± ±0.021
80	0.989± ±0.027	0.980± ±0.026	0.997± ±0.026	0.994± ±0.024	0.996± ±0.027	0.991± ±0.027	0.988± ±0.025
160	0.982± ±0.026	0.973± ±0.026	0.990± ±0.028	0.996± ±0.028	0.989± ±0.028	0.986± ±0.026	0.978± ±0.023
180	0.966± ±0.027	0.968± ±0.028	0.978± ±0.024	0.983± ±0.025	0.990± ±0.027	0.976± ±0.027	0.978± ±0.030
200	0.980± ±0.025	0.986± ±0.026	0.983± ±0.024	0.994± ±0.027	0.996± ±0.027	0.988± ±0.023	0.982± ±0.027
220	0.976± ±0.026	0.984± ±0.028	0.964± ±0.026	0.987± ±0.024	0.988± ±0.025	0.979± ±0.028	0.978± ±0.024

Table 6

Determination coefficients of decision tree model as function of initial energies $\sqrt{s_{NN}}$ for symmetric heavy collision systems

$\sqrt{s_{NN}}$, GeV	Determination coefficient $\bar{R}^2$ for collision system		
	Xe + Xe	Pb + Pb	U + U
20	0.275±0.007	0.383±0.010	0.329±0.009
40	0.983±0.025	0.996±0.029	0.983±0.027
60	0.169±0.005	0.715±0.020	0.757±0.021
80	0.981±0.027	0.994±0.028	0.970±0.025
160	0.965±0.023	0.994±0.026	0.965±0.025
180	0.971±0.025	0.984±0.028	0.973±0.027
200	0.978±0.025	0.995±0.023	0.978±0.025
220	0.979±0.023	0.989±0.028	0.977±0.028

Table 7

Determination coefficients of random forest model as function of initial energies $\sqrt{s_{NN}}$ for light-heavy collision systems

$\sqrt{s_{NN}}$, GeV	Determination coefficient $\bar{R}^2$ for collision system				
	p + Xe	*p* + Au	*p* + Pb	He + Au	He + U
20	0.311±0.008	0.098±0.002	0.205±0.006	0.192±0.006	0.302±0.009
40	0.979±0.026	0.980±0.024	0.985±0.025	0.980±0.025	0.980±0.025
60	0.628±0.016	0.705±0.015	0.508±0.012	0.589±0.016	0.661±0.019
80	0.973±0.024	0.989±0.032	0.988±0.028	0.983±0.025	0.979±0.030
160	0.990±0.023	0.991±0.029	0.987±0.025	0.981±0.027	0.992±0.028
180	0.989±0.028	0.994±0.031	0.993±0.025	0.990±0.029	0.992±0.032
200	0.994±0.029	0.993±0.027	0.997±0.025	0.984±0.02	0.984±0.030
220	0.986±0.030	0.994±0.027	0.990±0.030	0.980±0.027	0.970±0.024

Table 8

Determination coefficients of random forest model as function of initial energies $\sqrt{s_{NN}}$ for asymmetric heavy collision systems

$\sqrt{s_{NN}}$, GeV	Determination coefficient $\bar{R}^2$ for collision system						
	Cu+Au	Cu+Pb	Xe+Pb	Xe+U	Au+Pb	Au+U	Pb+U
20	0.270± ±0.007	0.274± ±0.007	0.343± ±0.012	0.290± ±0.007	0.338± ±0.010	0.378± ±0.010	0.352± ±0.008
40	0.983± ±0.027	0.986± ±0.026	0.992± ±0.029	0.995± ±0.027	0.994± ±0.024	0.972± ±0.025	0.967± ±0.028
60	0.501± ±0.012	0.393± ±0.011	0.282± ±0.007	0.709± ±0.018	0.754± ±0.020	0.793± ±0.021	0.806± ±0.020
80	0.988± ±0.025	0.984± ±0.028	0.997± ±0.026	0.994± ±0.028	0.992± ±0.031	0.974± ±0.025	0.968± ±0.025
160	0.988± ±0.031	0.987± ±0.024	0.996± ±0.033	0.998± ±0.025	0.995± ±0.028	0.985± ±0.031	0.981± ±0.026
180	0.985± ±0.027	0.984± ±0.027	0.983± ±0.026	0.995± ±0.023	0.992± ±0.025	0.984± ±0.027	0.983± ±0.027
200	0.986± ±0.025	0.988± ±0.025	0.983± ±0.024	0.997± ±0.028	0.993± ±0.028	0.987± ±0.024	0.983± ±0.029
220	0.977± ±0.026	0.980± ±0.024	0.962± ±0.026	0.987± ±0.026	0.984± ±0.027	0.976± ±0.028	0.975± ±0.023

Table 9

Determination coefficients of random forest model as function of initial energies $\sqrt{s_{NN}}$ for symmetric heavy collision systems

$\sqrt{s_{NN}}$, GeV	Determination coefficient $\bar{R}^2$ for collision system		
	Xe + Xe	Pb + Pb	U + U
20	0.277±0.008	0.379±0.010	0.311±0.008
40	0.986±0.023	0.990±0.029	0.947±0.027
60	0.456±0.014	0.759±0.022	0.768±0.022
80	0.977±0.030	0.986±0.030	0.952±0.027
160	0.985±0.026	0.995±0.029	0.968±0.027
180	0.986±0.032	0.991±0.028	0.977±0.027
200	0.988±0.027	0.992±0.025	0.973±0.025
220	0.978±0.028	0.981±0.029	0.971±0.027

Comparing the data obtained, we can conclude that the multilayer perceptron model showed the best results compared to the others with an interpolated initial energy of 60 GeV, since its R^2 values are closest to unity. We should also note that the value of R^2 for the decision tree and random forest models is noticeably less than unity (within the errors given in the tables).

Further analysis of these tables suggests that all models show good results for extrapolating the given values towards higher energies (220 GeV), $R^2 > 0.9$. However, all models proved incapable of fully describing the considered dependences at energies lower than the ones on which the training was conducted (20 GeV). The determination coefficient R^2 is much less than unity for all three models considered in this study. This is due to excessively low multiplicities of charged particles N_{ch} and neutrons N_{neut} at an initial energy of 20 GeV. Because of the strong differences in the values of N_{ch} and N_{neut} at 20 GeV, as well as at the energies on which the training was conducted, none of the models turned out to be capable of correctly predicting the required values of N_{coll} and N_{part}.

Conclusion

The studies carried out allowed to establish an optimal machine learning model capable of predicting the number of wounded nucleons N_{part} and the number of binary nucleon collisions N_{coll} characterizing the collision centrality, which are not observed in the experiment, based on the experimentally observed multiplicity of charged particles N_{ch} and the number of neutrons N_{neut} produced in the collision for a wide variety of collision systems with the initial energies $\sqrt{s_{NN}}$ ranging from 40 to 200 GeV.

We established for the initial conditions and the selected parameters (the energies and collision systems on which the training was conducted, as well as the energies of the interpolated and extrapolated points) that the multilayer perceptron model gives the best results compared to the decision tree and random forest models. Moreover, the multilayer perceptron can predict the values of N_{coll} and N_{part} with high accuracy ($R^2 > 0.9$) in collisions at higher (extrapolated) initial energies: 220, 240 and 260 GeV.

Intel® Core™ i9-9980XE processor, NVIDIA GeForce RTX™ 2080 Ti graphics card and 64 GB RAM were used for the computations.

REFERENCES

1. **Krizhevsky A., Sutskever I., Hinton G. E.,** Imagenet classification with deep convolutional neural networks, Commun. ACM. 60 (6) (2017) 84–90.
2. **Lobanov A. A., Berdnikov Ya. A, Mitrankov Iu. M.,** Machine learning models to determine unobservable centrality-related parameter values for a wide range of nuclear collisions at the energy of 200 GeV, St. Petersburg State Polytechnical University Journal. Physics and Mathematics. 16 (2) (2023) 111–120.
3. **Esumi S.** (STAR Collaboration), Results from beam energy scan program at RHIC-STAR, Proc. Int. Conf. on Critical Point and Onset of Deconfinement, CERN,15–19 Mar. 2021. (2021) 1–33.
4. **Morrison D. P., Akiba Y., Alford O., et al.,** The PHENIX experiment at RHIC, Nucl. Phys. A. 638 (1–2) (1998) 565c–569c.
5. **Sjöstrand T., Mrenna S., Skands P.,** A brief introduction to PYTHIA 8.1, Comp. Phys. Commun. 178 (11) (2008) 852–867.
6. **Quinlan J. R.,** Induction of decision trees, Mach. Learn. 1 (1) (1986) 81–106.
7. **Ho T. K.,** Random decision forests, Proc. 3rd Int. Conf. Document Analysis and Recognition, Montreal, QC, Canada, 14–16 Aug. 1995, IEEE. 1 (1995) 278– 282.
8. **Haykin S.,** Neural networks. A comprehensive foundation. Prentice Hall, New Jersey, USA, 1998.
9. **Bergstra J., Bardenet R., Bengio Y., Kégl B.,** Algorithms for hyper-parameter optimization, In book: Advances in Neural Information Processing Systems 24 (NIPS 2011). Edited by J. Shawe-Taylor, R. Zemel, P. Bartlett, F. Pereira, K. Q. Weinberger. 24 (2011) 1–6.
10. **Akiba T., Sano S., Yanase T., et al.,** Optuna: A next-generation hyperparameter optimization framework, Proc. 25th ACM SIGKDD Int. Conf. Knowledge Discovery & Data Mining (2019) 2623–2631.
11. **Kingma D. P., Ba J.,** Adam: A method for stochastic optimization, arXiv preprint arXiv:1412.6980. 2014.

12. **Barten A. P.,** The coefficient of determination for regression without a constant term, In book: Heijmans R., Neudecker H. (Eds.) The practice of econometrics, (International Studies in Economics and Econometrics. Vol. 15). Springer, Dordrecht (1987) 181–189.

13. **Mastelini S. M., Santana E. J., da Costa V. G. T., Barbon S.,** Benchmarking multi-target regression methods, Proc. 7th Brazilian Conf. on Intelligent Systems (BRACIS-2018), Sдо Paulo, Brazil, Oct. 22–25, 2018. (2018) 396–401.

14. **Efron B.,** Bootstrap methods: Another look at the jackknife, Ann. Stat. 7 (1) (1979) 1–26.

СПИСОК ЛИТЕРАТУРЫ

1. **Krizhevsky A., Sutskever I., Hinton G. E.** Imagenet classification with deep convolutional neural networks // Communications of the ACM (Association for Computing Machinery). 2017. Vol. 60. No. 6. Pp. 84–90.

2. **Лобанов А. А., Бердников Я. А., Митранков Ю. М.** Модели машинного обучения для определения значений ненаблюдаемых параметров, связанных с центральностью, для широкого спектра ядерных столкновений при энергии 200 ГэВ // Научно-технические ведомости СПбГПУ. Физико-математические науки. 2023. Т. 16. № 2. С. 111–120.

3. **Esumi S.** (STAR Collaboration). Results from beam energy scan program at RHIC-STAR // The International Conference on Critical Point and Onset of Deconfinement, CERN, 15–19 March 2021. Pp. 1–33.

4. **Morrison D. P., Akiba Y., Alford O., et al.** The PHENIX experiment at RHIC // Nuclear Physics A. 1998. Vol. 638. No. 1–2. Pp. 565c–569c.

5. **Sjöstrand T., Mrenna S., Skands P.** A brief introduction to PYTHIA 8.1 // Computer Physics Communications. 2008. Vol. 178. No. 11. Pp. 852–867.

6. **Quinlan J. R.** Induction of decision trees // Machine Learning. 1986. Vol. 1. No. 1. Pp. 81–106.

7. **Ho T. K.** Random decision forests // Proceedings of 3rd International Conference on Document Analysis and Recognition. Montreal, QC, Canada. 14–16 August, 1995. Vol. 1. Pp. 278– 282.

8. **Хайкин С.** Нейронные сети. Полный курс. Пер. с англ. 2-е изд. М.: Изд-во «Вильямс», 2019. 1104 с.

9. **Bergstra J., Bardenet R., Bengio Y., Kégl B.** Algorithms for hyper-parameter optimization // Advances in Neural Information Processing Systems 24 (NIPS 2011). Edited by J. Shawe-Taylor, R. Zemel, P. Bartlett, F. Pereira, K. Q. Weinberger. 2011. Vol. 24. Pp. 1–6.

10. **Akiba T., Sano S., Yanase T., Ohta T., Koyama M.** Optuna: A next-generation hyperparameter optimization framework // Proceedings of the 25th ACM SIGKDD International Conference on Knowledge Discovery & Data Mining. 2019. Pp. 2623–2631.

11. **Kingma D. P., Ba J**. Adam: A method for stochastic optimization // arXiv preprint arXiv:1412.6980. 2014.

12. **Barten A. P.** The coefficient of determination for regression without a constant term // Heijmans R., Neudecker H. (Eds.) The practice of econometrics. International Studies in Economics and Econometrics. Vol. 15. Dordrecht: Springer, 1987. Pp. 181– 189.

13. **Mastelini S. M., Santana E. J., da Costa V. G. T., Barbon S.** Benchmarking multi-target regression methods // Proceedings of the 7th Brazilian Conference on Intelligent Systems (BRACIS-2018), Sдо Paulo, Brazil, October 22–25, 2018. Pp. 396–401.

14. **Efron B.** Bootstrap methods: Another look at the jackknife // The Annals of Statistics. 1979. Vol. 7. No. 1. Pp. 1–26.

THE AUTHORS

LOBANOV Andrey A.
Peter the Great St. Petersburg Polytechnic University
29 Politechnicheskaya St., St. Petersburg, 195251, Russia
lobanov2.aa@edu.spbstu.ru
ORCID: 0000-0002-8910-4775

BERDNIKOV Alexander Ya.
Peter the Great St. Petersburg Polytechnic University
29 Politechnicheskaya St., St. Petersburg, 195251, Russia
alexber@phmf.spbstu.ru
ORCID: 0000-0002-0093-6875

MITRANKOVA Maria M.
Peter the Great St. Petersburg Polytechnic University
29 Politechnicheskaya St., St. Petersburg, 195251, Russia
mashalario@gmail.com
ORCID: 0000-0002-6798-6092

СВЕДЕНИЯ ОБ АВТОРАХ

ЛОБАНОВ Андрей Александрович – *студент Физико-механического института Санкт-Петербургского политехнического университета Петра Великого.*
195251, Россия, г. Санкт-Петербург, Политехническая ул., 29
lobanov2.aa@edu.spbstu.ru
ORCID: 0000-0002-8910-4775

БЕРДНИКОВ Александр Ярославич – *кандидат физико-математических наук, доцент Высшей школы фундаментальных физических исследований Санкт-Петербургского политехнического университета Петра Великого.*
195251, Россия, г. Санкт-Петербург, Политехническая ул., 29
alexber@phmf.spbstu.ru
ORCID: 0000-0002-0093-6875

МИТРАНКОВА Мария Максимовна – *аспирантка Высшей школы фундаментальных физических исследований Санкт-Петербургского политехнического университета Петра Великого.*
195251, Россия, г. Санкт-Петербург, Политехническая ул., 29
mashalario@gmail.com
ORCID: 0000-0002-6798-6092

Received 14.02.2023. Approved after reviewing 22.02.2023. Accepted 22.02.2023.
Статья поступила в редакцию 14.02.2023. Одобрена после рецензирования 22.02.2023. Принята 22.02.2023.

© Peter the Great St. Petersburg Polytechnic University, 2023

THEORETICAL PHYSICS

Original article
UDC 530.121
DOI: https://doi.org/10.18721/JPM.16212

THE MOTION OF AN UNCHARGED RELATIVISTIC PARTICLE: AN ANALYSIS OF ITS INTEGRABLE MOTION INTEGRALS DYNAMICS

N. S. Akintsov[1, 2], *A. P. Nevecheria*[3]✉, *A. A. Martynov*[3]

[1] Nantong University, Nantong, People's Republic of China;
[2] Ocean University of China, Nantong, People's Republic of China;
[3] Kuban State University, Krasnodar, Russia

✉ artiom1989@mail.ru

Abstract. In this study, the dynamics of a relativistic particle that does not have an electric charge and is under the action of an external force has been analyzed on the basis of the special theory of relativity. The accelerated motion of such a particle was also investigated in the absence of an external electromagnetic field specified by the scalar and vector potentials. An analytical method for efficient writing of classical equations of relativistic dynamics was developed, and an estimate of integrals of motion was carried out. The motion integral was established to be valid both for charged particles and uncharged ones. The use of motion integrals made it possible to describe the relationship between dynamic parameters. The dependence of the x space-time coordinate on the integral of motion was also obtained.

Keywords: motion integral, relativistic particle energy, radiative friction, radiation intensity

Funding: This study was partially supported by the Nantong Science and Technology Plan Project under Grant Nos. JC2020137 and JC2020138; the Key Research and Development Program of Jiangsu Province of China under Grant BE2021013-1.

For citation: Akintsov N. S., Nevecheria A. P., Martynov A. A., The motion of an uncharged relativistic particle: an analysis of its integrable motion integrals dynamics, St. Petersburg State Polytechnical University Journal. Physics and Mathematics. 16 (2) (2023) 132–145. DOI: https://doi.org/10.18721/JPM.16212

This is an open access article under the CC BY-NC 4.0 license (https://creativecommons.org/licenses/by-nc/4.0/)

Научная статья
УДК 530.121
DOI: https://doi.org/10.18721/JPM

АНАЛИЗ ДИНАМИКИ ИНТЕГРИРУЕМЫХ ИНТЕГРАЛОВ ДВИЖЕНИЯ НЕЗАРЯЖЕННОЙ РЕЛЯТИВИСТСКОЙ ЧАСТИЦЫ

Н. С. Акинцов[1, 2], *А. П. Невечеря*[3]✉, *А. А. Мартынов*[3]

[1] Наньтунский университет, г. Наньтун, Китайская Народная Республика;
[2] Китайский океанологический университет,
г. Наньтун, Китайская Народная Республика;
[3] Кубанский государственный университет, г. Краснодар, Россия

✉ artiom1989@mail.ru

Аннотация. На основе специальной теории относительности в работе проанализирована динамика релятивистской частицы, не имеющей электрического заряда, под действием внешней силы. Исследовано ускоренное движение такой частицы и в отсутствие внешнего электромагнитного поля, заданного скалярным и векторным потенциалами. Разработан аналитический метод эффективной записи классических уравнений релятивистской

© Akintsov N. S., Nevecheria A. P., Martynov A. A., 2023. Published by Peter the Great St. Petersburg Polytechnic University.

динамики и проведена оценка интегралов движения. Установлено, что интеграл движения справедлив и для заряженных частиц, и для незаряженных. Использование интегралов движения позволило описать связь динамических параметров. Получена также зависимость пространственно-временной координаты x от интеграла движения.

Ключевые слова: интеграл движения, энергия релятивистской частицы, радиационное трение, интенсивность излучения незаряженной частицы

Финансирование: Исследование выполнено при частичной финансовой поддержке грантов № JC2020137 и JC2020138 Проекта Наньтунгского научно-технического плана, а также гранта BE2021013-1 Ключевой программы исследований и разработок Китайской провинции Цзянсу.

Ссылка для цитирования: Акинцов Н. С., Невечеря А. П., Мартынов А. А. Анализ динамики интегрируемых интегралов движения незаряженной релятивистской частицы // Научно-технические ведомости СПбГПУ. Физико-математические науки. 2023. Т. 16. № 2. С. 132–145. DOI: https://doi.org/10.18721/ JPM.16212

Статья открытого доступа, распространяемая по лицензии CC BY-NC 4.0 (https://creativecommons.org/licenses/by-nc/4.0/)

Introduction

The motion equation of a particle of mass m and a charge q in the electromagnetic field has been studied extensively in classical relativistic electrodynamics, and has the following form [1]:

$$\frac{d\mathbf{p}}{dt} = q\mathbf{E} + \frac{q}{c}[\mathbf{V} \times \mathbf{H}], \tag{1}$$

where the momentum $\mathbf{p}$ of the particle and its velocity $\mathbf{V}$ are related as follows:

$$\mathbf{p} = \frac{m\mathbf{V}}{\sqrt{1 - \frac{V^2}{c^2}}}. \tag{2}$$

The change $d\varepsilon$ in the energy of the particle was widely established to be determined by the equation

$$\frac{d\varepsilon}{dt} = q\mathbf{E} \cdot \mathbf{V}, \tag{3}$$

where

$$\varepsilon = \frac{mc^2}{\sqrt{1 - \frac{V^2}{c^2}}} = \sqrt{m^2c^4 + c^2p^2}. \tag{4}$$

From Eqs. (1) and (4) the relationship between the energy ε and the longitudinal component $\mathbf{n}\cdot\mathbf{p}$ of the momentum $\mathbf{p}$ of the particle can be represented as an integral of motion in the following form:

$$\varepsilon - \mathbf{n}\cdot\mathbf{p}c = \gamma_0 c, \ \gamma_0 = \frac{mc\left(1 - \mathbf{n}\cdot\boldsymbol{\beta}\right)}{\sqrt{1 - \beta^2}}, \ \boldsymbol{\beta} = \frac{V}{c}, \tag{5}$$

where $\mathbf{n}$ is the normal vector directed along the particle's trajectory.

© Акинцов Н. С., Невечеря А. П., Мартынов А. А., 2023. Издатель: Санкт-Петербургский политехнический университет Петра Великого.

It was demonstrated in Ref. [2] that the integral (5) was the same for a plane monochromatic electromagnetic wave and a constant uniform magnetic field.

The acceleration and radiation of relativistic particles were explored in several works [3, 4]. However, generally, the dynamics of particle acceleration was considered under the action of external ponderomotive forces of electromagnetic nature [5 – 9].

In Refs. [2, 10 – 14], the motion integrals of a charged particle were obtained, and the particle momentum was demonstrated to be written as an explicit function of the zero coordinate ξ ($\xi = t - z/c$ where t, z are the laboratory time and coordinate respectively, and c is the velocity of light in vacuo).

In the absence of external forces acting on the particle, the particle's motion is free and obeys the basic dynamics equation. In this study, we focused on the non-electromagnetic 2D force action upon a particle. We intend to show that the motion integral (5) is valid for any particle motion in free space.

The objective of this study is to analyze the dynamics of an uncharged relativistic particle in the absence of external electromagnetic fields, i. e., $\mathbf{E} = \mathbf{H} = 0$, scalar $\varphi = 0$, and vector field potentials $\mathbf{F}$ for the following force acting $\mathbf{A} = 0$, on the particle is of the form

$$\mathbf{F} = \frac{d\mathbf{p}}{dt} \neq 0, \tag{6}$$

where $\mathbf{p}$ is the relativistic momentum of the particle (see Eq. (2)).

Eventually, we show that the integral of motion is also applicable in the absence of fields ($\mathbf{E} = \mathbf{H} = 0$, $\varphi = 0$, $\mathbf{A} = 0$). We consistently derive formulas for the space-time coordinate , coordinate $\mathbf{r}$, velocity $\boldsymbol{\beta}$, momentum $\mathbf{p}$, energy ε and radiation intensity $I = -d\varepsilon/dt$ of the particle, depending on the motion integrals Q_t and Q_ξ.

Finally, we demonstrate the dependence of the dynamic parameters (ξ, $\mathbf{r}$, $\boldsymbol{\beta}$, $\mathbf{p}$, ε and I) on the motion integral γ.

The main goal of this work is to obtain invariant forms of the integrals of motion

$$\gamma = \gamma(\mathbf{n}\cdot\mathbf{r}, t, Q_t) \text{ and } Q_t = Q_t(\mathbf{n}\cdot\mathbf{r}, t, \gamma)$$

in 1 + 1 dimensions, which are mutually expressed in terms of the coordinate $\mathbf{n}\cdot\mathbf{r} = \mathbf{n}\cdot\mathbf{r}(t, Q_t, \gamma)$ and proper time $t = t(\mathbf{n}\cdot\mathbf{r}, Q_t, \gamma)$ of the particle, based on the law of conservation of energy – momentum for a relativistic particle (4).

Moreover, the aim is to search for an invariant form as the motion integrals for energy $E = E(r, t, \gamma, Q_t)$ and momentum $\mathbf{n}\cdot\mathbf{P} = \mathbf{n}\cdot\mathbf{P}(\mathbf{r}, t, \gamma, Q_t)$ of the particle.

An analysis of the space – time coordinate ξ

We introduce the space – time coordinate ξ [1, 2, 10 – 15] such as

$$\xi = t - f\frac{\mathbf{n}\cdot\mathbf{r}}{c}, \tag{7}$$

where t is the laboratory time, $\mathbf{n}$ is the normal vector, $\mathbf{r}$ is the laboratory coordinate, c is the speed of light, and f characterizes the direction of motion of a particle or wave and takes a value of +1 or –1 when the particle moves to the right or left, respectively, relative to the observer located at the initial space – time point ($\mathbf{r}_0$, t_0).

Differentiating (7) with respect to time t, we obtain

$$\frac{d\xi}{dt} = \frac{dt}{dt} - f\frac{\mathbf{n}}{c}\frac{d\mathbf{r}}{dt} = 1 - f\mathbf{n}\frac{\mathbf{V}}{c} = 1 - f\mathbf{n}\cdot\boldsymbol{\beta}, \tag{8}$$

where $\boldsymbol{\beta} = \mathbf{V}/c$, $\mathbf{V} = d\mathbf{r}/dt$.

From Eq. (7), we can express t as follows:

$$t = \xi + f\frac{\mathbf{n}\cdot\mathbf{r}}{c}, \tag{9}$$

and by differentiating (9) with respect to ξ, we obtain

$$\frac{dt}{d\xi}=\frac{d\xi}{d\xi}+f\frac{\mathbf{n}}{c}\frac{d\mathbf{r}}{d\xi}=1+f\frac{\mathbf{n}}{c}\frac{d\mathbf{r}}{d\xi}. \tag{10}$$

Multiplying Eqs. (8) and (10), and considering that $\frac{d\xi}{dt}\frac{dt}{d\xi}=1$, we obtain:

$$\frac{d\mathbf{r}}{dt}-\frac{d\mathbf{r}}{d\text{ì}}+\frac{1}{c}f\mathbf{n}\frac{d\mathbf{r}}{dt}\frac{d\mathbf{r}}{d\text{ì}}=0. \tag{11}$$

By substituting $\frac{d\mathbf{r}}{dt}=\frac{d\mathbf{r}}{d\xi}\frac{d\xi}{dt}$ into Eq. (11), we can find out that the condition given by Eq. (8) is satisfied, and the following equalities are true:

$$\frac{d\mathbf{r}}{dt}=f\mathbf{n}c\left(1-\frac{d\xi}{dt}\right), \tag{12}$$

$$\frac{d\mathbf{r}}{d\xi}=\frac{\mathbf{V}}{1-f\mathbf{n}\cdot\boldsymbol{\beta}}, \tag{13}$$

$$\frac{d\xi}{dt}=f\mathbf{n}c\frac{d\xi}{d\mathbf{r}}\left(1-\frac{d\xi}{dt}\right), \tag{14}$$

$$\frac{d\xi}{dr}=\frac{\left(1-f\mathbf{n}\cdot\boldsymbol{\beta}\right)}{\mathbf{V}}. \tag{15}$$

Differentiating (11) with respect to d/dt gives the following:

$$\frac{d^2\mathbf{r}}{dt^2}\left(1+\frac{1}{c}f\mathbf{n}\frac{dr}{d\xi}\right)-\frac{d^2\mathbf{r}}{dtd\xi}\left(1-\frac{1}{c}f\mathbf{n}\frac{d\mathbf{r}}{dt}\right)=0, \tag{16}$$

and similarly, by differentiating (11) with respect to $d/d\xi$, we obtain

$$\frac{d^2\mathbf{r}}{d\xi dt}\left(1+\frac{1}{c}f\mathbf{n}\frac{d\mathbf{r}}{d\xi}\right)-\frac{d^2\mathbf{r}}{d\xi^2}\left(1-\frac{1}{c}f\mathbf{n}\frac{d\mathbf{r}}{dt}\right)=0. \tag{17}$$

Adding (16) and (17) gives

$$\left(\frac{d^2\mathbf{r}}{dt^2}+\frac{d^2\mathbf{r}}{d\xi dt}\right)\left(1+\frac{1}{c}f\mathbf{n}\frac{d\mathbf{r}}{d\xi}\right)-\left(\frac{d^2\mathbf{r}}{dtd\xi}+\frac{d^2\mathbf{r}}{d\xi^2}\right)\left(1-\frac{1}{c}f\mathbf{n}\frac{d\mathbf{r}}{dt}\right)=0. \tag{18}$$

We subsequently introduce new variables Q_t and Q_ξ, such as

$$Q_\xi=1+\frac{1}{c}f\mathbf{n}\frac{dr}{d\xi}=\frac{1}{1-f\mathbf{n}\cdot\boldsymbol{\beta}},\ Q_t=1-\frac{1}{c}f\mathbf{n}\frac{dr}{dt}=1-f\mathbf{n}\cdot\boldsymbol{\beta}=\frac{d\xi}{dt}. \tag{19}$$

Eqs. (19) show that Q_ξ and Q_t integrals of motion, have a one-to-one correspondence, i.e.,

$$Q_\xi Q_t=Q_t Q_\xi=1 \tag{20}$$

Invariant representation of Q_ξ and Q_t in the $Q_t^+Q_t^-$ and $Q_{\hat{\imath}}^+Q_{\hat{\imath}}^-$

From Eqs. (19), we propose the following notation for Q_t and Q_ξ:

$$Q_t^+Q_{\hat{\imath}}^+ = Q_t^-Q_{\hat{\imath}}^- = 1,$$

$$1 = \frac{Q_t^-Q_{\hat{\imath}}^-}{Q_t^+Q_{\hat{\imath}}^+} = Q_t^+Q_{\hat{\imath}}^+ = Q_t^-Q_{\hat{\imath}}^- = Q_t^-Q_{\hat{\imath}}^-Q_t^+Q_{\hat{\imath}}^+, \tag{21}$$

where

$$Q_t^+ = 1 - \mathbf{n}\cdot\boldsymbol{\beta},\ Q_\xi^+ = \frac{1}{1-\mathbf{n}\cdot\boldsymbol{\beta}}, \tag{22}$$

$$Q_t^- = 1 + \mathbf{n}\cdot\boldsymbol{\beta},\ Q_\xi^- = \frac{1}{1+\mathbf{n}\cdot\boldsymbol{\beta}}.$$

One can see from Eqs. (22) that

$$Q_t^+Q_t^- = 1-\beta^2 \text{ and } Q_\xi^+Q_\xi^- = \frac{1}{1-\beta^2}$$

are invariants and have direct and inverse representations, and that

$$Q_t^- + Q_t^+ = 2 \text{ or } Q_{\hat{\imath}}^- + Q_{\hat{\imath}}^+ = 2Q_{\hat{\imath}}^+Q_{\hat{\imath}}^-.$$

We can express $\boldsymbol{\beta}$ in terms of $Q_t^+Q_t^-$ to obtain

$$\boldsymbol{\beta} = \mathbf{n}\sqrt{1-Q_t^+Q_t^-}. \tag{23}$$

Relations of special relativity in the $Q_t^+Q_t^-$ and $Q_t^+Q_t^-$ representations

Let us introduce the dimensionless momentum of a particle $\mathbf{P} = \mathbf{p}/mc$, and the dimensionless energy of the particle $E = \varepsilon/mc$.

Thus, Eqs. (2) and (3) can be rewritten as

$$\mathbf{P} = \frac{\boldsymbol{\beta}}{\sqrt{1-\beta^2}}, \tag{24}$$

$$E^2 = \frac{1}{1-\beta^2} = 1 + P^2. \tag{25}$$

Substituting Eq. (23) into Eq. (24), we obtain the $\boldsymbol{\beta}$ representation of the momentum in terms of $Q_\xi^+Q_\xi^-$, i. e.,

$$\mathbf{P} = \mathbf{n}\sqrt{1-Q_t^+Q_t^-}\sqrt{Q_{\hat{\imath}}^+Q_{\hat{\imath}}^-} = \mathbf{n}\sqrt{Q_{\hat{\imath}}^+Q_{\hat{\imath}}^- - 1}, \tag{26}$$

and the corresponding representation for energy (following Eq. (25)) will be

$$E = \sqrt{Q_{\hat{\imath}}^+Q_{\hat{\imath}}^-}, \tag{27}$$

where $E \geq 0$.

The problem involving eigenfunctions and Q_t^+, Q_t^-, $Q_{\hat{\imath}}^+$, $Q_{\hat{\imath}}^-$, $Q_t^+Q_t^-$, $Q_{\hat{\imath}}^+Q_{\hat{\imath}}^-$, as well as $\boldsymbol{\beta} = n\sqrt{1-Q_t^+Q_t^-}$ from d/dt

We determine the eigenvalues with respect to time t. We obtain the following:

$$\frac{d}{dt}Q_t^+ = -\mathbf{n}\frac{d\boldsymbol{\beta}}{dt} = -\mathbf{n}\frac{d\boldsymbol{\beta}}{dt}Q_\xi^+Q_t^+ = q_t^+Q_t^+, \tag{28}$$

where

$$q_t^+ = -\mathbf{n}\frac{d\boldsymbol{\beta}}{dt}Q_\xi^+. \tag{29}$$

Similarly, we obtain the following eigenvalues for the Q_t^-, $Q_{\hat{\imath}}^+$, $Q_{\hat{\imath}}^-$, $Q_t^+Q_t^-$, $Q_{\hat{\imath}}^+Q_{\hat{\imath}}^-$ and $\boldsymbol{\beta} = \mathbf{n}\sqrt{1-Q_t^+Q_t^-}$:

$$\frac{d}{dt}Q_t^- = \mathbf{n}\frac{d\boldsymbol{\beta}}{dt} = \mathbf{n}\frac{d\boldsymbol{\beta}}{dt}Q_\xi^-Q_t^- = q_t^-Q_t^-, \tag{30}$$

$$q_t^- = \mathbf{n}\frac{d\boldsymbol{\beta}}{dt}Q_\xi^-. \tag{31}$$

$$\frac{d}{dt}Q_\xi^+ = \left(1-n\cdot\boldsymbol{\beta}\right)^{-2}\cdot n\frac{d\boldsymbol{\beta}}{dt} = n\frac{d\boldsymbol{\beta}}{dt}Q_\xi^+Q_\xi^+ = q_\xi^+Q_\xi^+, \tag{32}$$

$$q_\xi^+ = \mathbf{n}\frac{d\boldsymbol{\beta}}{dt}Q_\xi^+. \tag{33}$$

$$\frac{d}{dt}Q_\xi^- = -\left(1+\mathbf{n}\cdot\boldsymbol{\beta}\right)^{-2}\cdot \mathrm{n}\frac{d\boldsymbol{\beta}}{dt} = -\mathbf{n}\frac{d\boldsymbol{\beta}}{dt}Q_\xi^-Q_\xi^- = q_\xi^-Q_\xi^-, \tag{34}$$

$$q_\xi^- = -\mathbf{n}\frac{d\boldsymbol{\beta}}{dt}Q_\xi^-. \tag{35}$$

$$\frac{d}{dt}\left(Q_t^+Q_t^-\right) = q_t^+Q_t^+Q_t^- + Q_t^+q_t^-Q_t^- = -2\boldsymbol{\beta}\frac{d\boldsymbol{\beta}}{dt}. \tag{36}$$

$$\frac{d}{dt}\left(Q_\xi^+Q_\xi^-\right) = Q_\xi^+Q_\xi^-\left(q_\xi^- + q_\xi^+\right) = \frac{2\boldsymbol{\beta}}{\left(1-\beta^2\right)^2}\frac{d\boldsymbol{\beta}}{dt}. \tag{37}$$

$$\frac{d\boldsymbol{\beta}}{dt} = -\frac{1}{2}\mathbf{n}\left(1-Q_t^+Q_t^-\right)^{-\frac{1}{2}}\cdot\frac{d}{dt}\left(Q_t^+Q_t^-\right) = \frac{\mathbf{n}\dfrac{d\boldsymbol{\beta}}{dt}}{\sqrt{1-Q_t^+Q_t^-}}\boldsymbol{\beta}, \tag{38}$$

where the eigenvalue of the velocity modulus is determined by the expression

$$\boldsymbol{\beta} = \frac{\mathbf{n}\dfrac{d\boldsymbol{\beta}}{dt}}{\sqrt{1-Q_t^+Q_t^-}}. \tag{39}$$

Substituting the values from Eq. (39) into Eqs. (36) and (37), then taking into account that $\boldsymbol{\beta} = \mathbf{n}\beta$, we obtain:

$$\frac{d}{dt}\left(Q_t^+Q_t^-\right) = -2\left(1-Q_t^+Q_t^-\right)^{\frac{3}{2}}, \tag{40}$$

$$\frac{d}{dt}\left(Q_{\hat{\imath}}^+Q_{\hat{\imath}}^-\right) = 2\left(Q_{\hat{\imath}}^+Q_{\hat{\imath}}^- - 1\right)^{\frac{3}{2}}\left(Q_{\hat{\imath}}^+Q_{\hat{\imath}}^-\right)^{\frac{1}{2}}. \tag{41}$$

Variables ξ, $\dfrac{\mathbf{n}\cdot\mathbf{r}}{c}$ and t in the $Q_t^+Q_t^-$ representation. We now represent Eq. (23) by the following form:

$$\boldsymbol{\beta} = \frac{1}{\tilde{n}}\frac{d\mathbf{r}}{dt} = \frac{1}{\tilde{n}}\frac{d\mathbf{r}}{d\left(Q_t^+Q_t^-\right)}\frac{d\left(Q_t^+Q_t^-\right)}{dt} = \mathbf{n}\sqrt{1-Q_t^+Q_t^-}. \tag{42}$$

Substituting Eq. (40) into (42), and integrating over the $d\left(Q_t^+Q_t^-\right)$ from 0 to $Q_t^+Q_t^-$, we obtain

$$\frac{\mathbf{n}\cdot\mathbf{r}}{c}=\frac{1}{2}\ln\left(1-Q_t^+Q_t^-\right). \tag{43}$$

From Eq. (8), we now express dt as follows:

$$dt=d\xi+f\mathbf{n}\frac{d\mathbf{r}}{c}. \tag{44}$$

It is known that $d\xi=Q_t dt$, $Q_t=1-f\mathbf{n}\cdot\boldsymbol{\beta}$, and hence, substituting them into Eq. (44), we obtain

$$\left(1-Q_t\right)dt=f\mathbf{n}\frac{d\mathbf{r}}{c},\ \text{or}\ \boldsymbol{\beta}dt=\frac{d\mathbf{r}}{c}. \tag{45}$$

Substituting $\boldsymbol{\beta}$ from Eq. (23) and $d\mathbf{r}$ rom Eq. (42) into Eq. (45), we obtain

$$dt=\frac{1}{2}\frac{d\left(1-Q_t^+Q_t^-\right)}{\left(1-Q_t^+Q_t^-\right)^{\frac{3}{2}}}. \tag{46}$$

Subsequently, integrating this over $d\left(1-Q_t^+Q_t^-\right)$ from 0 to $Q_t^+Q_t^-$ results in

$$t=1-\frac{1}{\sqrt{\left(1-Q_t^+Q_t^-\right)}}. \tag{47}$$

Finally, substituting Eqs. (43) and (47) into Eq. (7) results in

$$\xi=1-\frac{1}{\sqrt{\left(1-Q_t^+Q_t^-\right)}}-f\frac{1}{2}\ln\left(1-Q_t^+Q_t^-\right); \tag{48}$$

then, differentiating Eq. (48) with respect to d/dt gives a relationship between $Q_t^+Q_t^-$ and Q_t as follows:

$$\frac{d\xi}{dt}=1-f\sqrt{1-Q_t^+Q_t^-}=1-f\mathbf{n}\cdot\boldsymbol{\beta}=Q_t. \tag{49}$$

The relationship between $Q_t^+Q_t^-$ and Q_t. Eq. (49) demonstrates the following relationship between $Q_t^+Q_t^-$ and Q_t:

$$\sqrt{1-Q_t^+Q_t^-}=f\left(1-Q_t\right). \tag{50}$$

By considering Eq. (50), we can represent the following formulas:

$$\boldsymbol{\beta}=\mathbf{n}\sqrt{1-Q_t^+Q_t^-}=f\mathbf{n}\left(1-Q_t\right), \tag{51}$$

$$\frac{d\boldsymbol{\beta}}{dt}=\boldsymbol{\beta}\sqrt{1-Q_t^+Q_t^-}=\mathbf{n}\left(1-Q_t\right)^2, \tag{52}$$

$$\frac{\mathbf{n}\cdot\mathbf{r}}{c}=\frac{1}{2}\ln\left(1-Q_t^+Q_t^-\right)=\frac{1}{2}\ln\left[\left(1-Q_t\right)^2\right], \tag{53}$$

$$t=1-\frac{1}{\sqrt{1-Q_t^+Q_t^-}}=1-\frac{1}{f\left(1-Q_t\right)}, \tag{54}$$

$$\xi=1-\frac{f}{\left(1-Q_t\right)}-f\frac{1}{2}\ln\left[\left(1-Q_t\right)^2\right]. \tag{55}$$

Eigenfunctions and eigenvalues of Q_t and Q_ξ. We now take the derivative of ξ from Eq. (55) with respect to time, i. e.,

$$\frac{d\xi}{dt} = -f\frac{Q_t}{\left(1-Q_t\right)^2}\frac{dQ_t}{dt}, \tag{56}$$

and substitute $\frac{d\xi}{dt} = Q_t$ into Eq. (56) to obtain

$$\frac{dQ_t}{dt} = -f\left(1-Q_t\right)^2 Q_{\text{i}} Q_t, \tag{57}$$

where

$$q_t = -f\left(1-Q_t\right)^2 Q_{\text{i}} = -f\left(Q_{\text{i}} - 2 + Q_t\right). \tag{58}$$

Using the relationship

$$\frac{d\left(Q_t Q_\xi\right)}{dt} = \frac{dQ_t}{dt}Q_\xi + Q_t\frac{dQ_\xi}{dt} = 0, \tag{59}$$

we can derive $\frac{dQ_\xi}{dt}$ as follows:

$$\frac{dQ_\xi}{dt} = -\frac{dQ_t}{dt}\left(Q_\xi\right)^2, \tag{60}$$

$$\frac{dQ_\xi}{dt} = f\left(1-Q_t\right)^2\left(Q_\xi\right)^2 = f\left(1-Q_t\right)^2 Q_\xi Q_\xi, \tag{61}$$

and finally,

$$q_\xi = f\left(1-Q_t\right)^2 Q_\xi = f\left(Q_\xi - 2 + Q_t\right). \tag{62}$$

Eqs. (58) and (62) show that

$$q_t + q_\xi = 0. \tag{63}$$

Differentiating Eq. (55) with respect to $\frac{d}{d\xi}$, we obtain the following:

$$\frac{dQ_t}{d\xi} = -f\frac{\left(1-Q_t\right)^2}{Q_t}Q_\xi Q_t, \tag{64}$$

where

$$p_t = -f\frac{\left(1-Q_t\right)^2}{Q_t}Q_\xi = -f\left(Q_\xi - 1\right)^2. \tag{65}$$

Using the following identity

$$\frac{d\left(Q_t Q_\xi\right)}{d\xi} = \frac{dQ_t}{d\xi}Q_\xi + Q_t\frac{dQ_\xi}{d\xi} = 0, \tag{66}$$

we find that $\frac{dQ_\xi}{d\xi}$ to be

$$\frac{dQ_\xi}{d\xi} = f\frac{\left(1-Q_t\right)^2}{Q_t}Q_\xi Q_\xi = p_\xi Q_\xi, \tag{67}$$

where

$$p_\xi = f\frac{\left(1-Q_t\right)^2}{Q_t}Q_\xi = f\left(Q_\xi - 1\right)^2, \tag{68}$$

$$p_t + p_\xi = 0. \tag{69}$$

Integrals of motion

From Eq. (5) we can introduce the dimensionless integral of motion $\gamma = \gamma_0/mc$, and then using Eq. (50) we obtain

$$\gamma = \frac{\left(1 - f\mathbf{n}\cdot\boldsymbol{\beta}\right)}{\sqrt{1-\beta^2}} = \sqrt{\frac{1 - f\mathbf{n}\cdot\boldsymbol{\beta}}{1 + f\mathbf{n}\cdot\boldsymbol{\beta}}} = \frac{Q_t}{\sqrt{Q_t^+ Q_t^-}} = \frac{Q_t}{\sqrt{2Q_t - \left(Q_t\right)^2}} = \frac{1}{\sqrt{2Q_\xi - 1}}. \tag{70}$$

Expressing Q_t and Q_ξ in terms of the motion integral γ, we obtain:

$$Q_t = \frac{2\gamma^2}{1+\gamma^2},\ Q_\xi = \frac{1+\gamma^2}{2\gamma^2}, \tag{71}$$

where

$$1 - Q_t = \frac{1-\gamma^2}{1+\gamma^2}. \tag{72}$$

Substituting Eq. (72) into the obtained definition for laboratory time t within Eq. (54), the laboratory coordinate $\mathbf{n}\cdot\mathbf{r}/c$ in Eq. (53), and space-time coordinate ξ in Eq. (55), we obtain the dependence of these parameters on the integral of motion γ:

$$t = 1 - \frac{1}{f\left(1 - Q_t\right)} = 1 - f\frac{1+\gamma^2}{1-\gamma^2}, \tag{73}$$

$$\frac{\mathbf{n}\cdot\mathbf{r}}{c} = \frac{1}{2}\ln\left(\left(1 - Q_t\right)^2\right) = \frac{1}{2}\ln\left[\left(\frac{1-\gamma^2}{1+\gamma^2}\right)^2\right], \tag{74}$$

$$\xi = t - f\frac{\mathbf{n}\cdot\mathbf{r}}{c} = 1 - f\frac{1+\gamma^2}{1-\gamma^2} - f\frac{1}{2}\ln\left[\left(\frac{1-\gamma^2}{1+\gamma^2}\right)^2\right]. \tag{75}$$

The dependences of energy and momentum on Q_ξ and γ. By considering Eqs. (21) and (50), the particle energy, as shown in Eq. (27) dependent on both Q_ξ and γ, takes the following form:

$$E = \sqrt{Q_\xi^+ Q_\xi^-} = \frac{Q_\xi}{\sqrt{2Q_\xi - 1}} = Q_\xi\gamma = \frac{1}{2\gamma}\left(1+\gamma^2\right). \tag{76}$$

In the absence of an initial velocity of the particle ($\boldsymbol{\beta} = 0$, $\gamma = 0$), the particle's energy is $E = 1$, i. e., equal to mc^2.

Following the particle momentum as given by Eq. (26), we can substitute Eqs. (21) and (50) to obtain

$$\mathbf{P} = \mathbf{n}\sqrt{Q_\xi^+ Q_\xi^- - 1} = \mathbf{n}\sqrt{\frac{Q_\xi^2}{\left(2Q_\xi - 1\right)} - 1} = f\mathbf{n}\left(Q_\xi - 1\right)\gamma = \frac{f\mathbf{n}}{2\gamma}\left(1-\gamma^2\right). \tag{77}$$

Subtracting the longitudinal component of momentum (as given in $\mathbf{n}\cdot\mathbf{P}$, Eq. (77)) from the energy E (see Eq. (76)), we obtain the integral of motion in the form

$$E - \mathbf{n}\cdot\mathbf{P} = \gamma^+, \tag{78}$$

where γ^+ , $\gamma^+\gamma^- = 1$.

Adding the energy E given by Eq. (76) and the longitudinal component of the momentum $\mathbf{n}\cdot\mathbf{P}$ into Eq. (77), we obtain the inverse integral of motion:

$$E + \mathbf{n}\cdot\mathbf{P} = \gamma^-. \tag{79}$$

We then use Eqs. (78) and (79) to conclude that

$$E - f\mathbf{n}\cdot\mathbf{P} = \gamma. \tag{80}$$

Assuming that the momentum **P** of the system is equal to the sum of the longitudinal and transverse components, we can see from Eqs. (25), (78) and (79) that the transverse component of the momentum is zero for this $\mathbf{P}_{\perp} = 0$ system.

For a freely moving particle with a sufficiently small change in energy and momentum, the particle velocity is determined by the following expression:

$$\frac{dE}{d\mathbf{P}} = \frac{d}{d\mathbf{P}}\left(\sqrt{1+P^2}\right) = \frac{\mathbf{P}}{E} = \boldsymbol{\beta} = f\mathbf{n}\left(1-Q_t\right) = f\mathbf{n}\left(\frac{1-\gamma^2}{1+\gamma^2}\right). \tag{81}$$

Acceleration of an uncharged relativistic particle in a force field and intensity of its radiation

We now investigate the dynamics of a relativistic charged particle in a force field (following Eq. (6)), i. e.,

$$\mathbf{n}\frac{d\mathbf{P}}{dt} = \frac{d}{dt}\left(\sqrt{Q_\xi^+ Q_\xi^- - 1}\right) = \sqrt{\left(Q_\xi^+ Q_\xi^- - 1\right)Q_\xi^+ Q_\xi^-}\,P = P_1 P, \tag{82}$$

where

$$P_1 = \sqrt{\left(Q_\xi^+ Q_\xi^- - 1\right)Q_\xi^+ Q_\xi^-} = P\sqrt{Q_\xi^+ Q_\xi^-} = PE;$$

$$P = \sqrt{Q_\xi^+ Q_\xi^- - 1}, \tag{83}$$

and

$$\mathbf{n}\cdot\mathbf{P}_1 = \sqrt{\left(Q_\xi^+ Q_\xi^- - 1\right)Q_\xi^+ Q_\xi^-} = P\sqrt{Q_\xi^+ Q_\xi^-} = PE. \tag{84}$$

Differentiating Eq. (82) with respect to time and using Eq. (25), we obtain the radiative friction acting on an uncharged particle as follows:

$$\mathbf{F}_{rad} = \frac{d^2\mathbf{P}}{dt^2} = \left(2+3P^2\right)P^2\mathbf{P}. \tag{85}$$

The radiation intensity of an uncharged particle is determined from the total energy (see Eq. (27)), and without considering the radiative friction force in Eq. (85), the radiation intensity takes the form

$$I = -\frac{dE}{dt} = -\frac{d}{dt}\left(\sqrt{Q_\xi^+ Q_\xi^-}\right) = -\left(Q_\xi^+ Q_\xi^- - 1\right)^{\frac{3}{2}} = -P^3 = -\frac{f}{8\gamma^3}\left(1-\gamma^2\right)^3, \tag{86}$$

where $I \geq 0$.

Generalization of the obtained results

To generalize the above results to electrons accelerated by the transverse electromagnetic field of an incident laser pulse on the frontal surface of the target and estimate the temperature of fast electrons, similar to the authors of Ref. [16], we substitute the expression for the amplitude of an electron oscillating in a field of a plane monochromatic wave, i. e.,

$$P^2 = Q_\xi^+ Q_\xi^- - 1 = \frac{q^2 E_0^2}{m^2 c^2 \omega^2}, \tag{87}$$

and obtain a formula for the kinetic energy of an electron oscillating in the transverse field of an incident light wave as follows,

$$\bar{K}_e = m_e c^2\left(\sqrt{1+\left(\frac{q^2 E_0^2}{m^2 c^2 \omega^2}\right)^2} - 1\right) = m_e c^2\left(\sqrt{1+\frac{I\lambda^2}{1.37\cdot 10^{18}}} - 1\right), \tag{88}$$

where m_e, g, is the electron mass; c, km/s, is the speed of light; E_0, V/m, is the amplitude of the electric field of the incident electromagnetic wave; ω, s^{-1}, is the carrier frequency; I, W/cm^2, is the intensity of the incident wave; λ, μm, is the wavelength.

A similar formula has been used to theoretically estimate the temperature of fast electrons on the frontal surface of the target and to analyze experimental results [17 – 20].

Further, it is of interest to use this method to describe the dynamics of a relativistic particle in stationary electrical, magnetic and electromagnetic fields [1 – 23], and to study the Doppler effect of a particle displacement in high-intensity fields.

Conclusion

In this study, we have obtained the direct and inverse integrals of the particle motion and demonstrated the advantage of using these approaches to investigate the dynamics of relativistic particle dynamics. It was demonstrated that the relativistic root can be represented by the form $\sqrt{1-\beta^2} = \sqrt{Q_t^+ Q_t^-}$, and further calculation of the arbitrary partial in Q_t^+ and Q_t^- considerably simplifies calculations in relativistic particle dynamics. The total energy of a particle is related to its momentum (25) through $Q_i^+ Q_i^-$ also simplifies the calculations since the total energy and momentum can be represented as $E = \sqrt{Q_\xi^+ Q_\xi^-}$ and $\mathbf{P} = \mathbf{n}\sqrt{Q_\xi^+ Q_\xi^- - 1}$, respectively. It was shown that the energy (76) and momentum (77) could be separately expressed in terms of the integral of motion γ, and their difference gave the direct integral of motion (78), while the sum did the inverse integral of motion (79). Additionally, a relationship between $Q_t^+ Q_t^-$ and Q_t was obtained. A detailed analysis is given for the space-time coordinate ξ and its dependence on $Q_t^+ Q_t^-$, Q_t and the integral of motion γ.

Furthermore, we demonstrated that as $|\mathbf{V}| \to c$, $t \to 0$, to interpret the dependence of the physical quantities t (47) and $\mathbf{n}\cdot\mathbf{r}$ / c (43) on $|\boldsymbol{\beta}|$, it is necessary to apply the following gauge transformations, $-t \to t$ and $-\mathbf{n}\cdot\mathbf{r} / c \to \mathbf{n}\cdot\mathbf{r} / c$, its dependence on $Q_\xi^+ Q_\xi^-$. The radiation intensity of a particle in the far-field was obtained, and its dependence of γ on $Q_\xi^+ Q_\xi^-$ was shown. The results appeared from the special theory of relativity. This approach can also be generalized for tensor use, allowing a more detailed description of the dynamics of relativistic particles in a medium.

The proposed approach has all the limitations of the special theory of relativity.

Further, the generalization of this approach to the Lagrangian and Hamiltonian formalism is significant.

The future scope of this work will be to investigate the spectral-angular characteristics of particle radiation and particle dynamics in a force field in the presence of radiative friction forces.

Acknowledgment

The authors would like to thank Prof. Young-Jie Yang, Prof. V. A. Isaev, Prof. E. N. Tumaev and Prof. Kopytov G. F. for their enlightening comments.

REFERENCES

1. **Landau L. D., Lifshitz E. M.,** The classical theory of fields, Second English Edition. Course of Theoretical Physics, Vol. 2, Pergamon Press, Oxford, New York, 1962.

2. **Ternov I. M., Khapaev A. M., Volodin B. A.,** The relativistic charged particles dynamics in the field of the flat electromagnetic wave and in the Redmond's field, Moscow Univ. Phys. Bull. 21 (4) (1980) 70–74 (in Russian).

3. **Bagrov V. G., Gitman D. M.** (Eds.), Exact solutions of relativistic wave equations (Book Series "Mathematics and its Applications", Vol. 39), Kluwer Academic Publishers, Amsterdam, 1990.

4. **Bagrov V. G., Bisnovatyi-Kogan G. S., Bordovitsin V. A., et. al.,** Teoriya izlucheniya relyativistskikh chastits [Theory of emission by relativistic particles], Fizmatlit Publishing, Moscow, 2002 (in Russian).

5. **Kaplan A. E., Pokrovsky A. L.,** Fully relativistic theory of the ponderomotive force in an ultraintense standing wave, Phys. Rev. Lett. 95 (5) (2005) 053601.

6. **Zhu S., Shen W.,** General relativistic ponderomotive force in a moving medium, J. Opt. Soc. Am. B. 4 (5) (1987) 739–742.

7. **Quesnel B., Mora P.,** Theory and simulation of the interaction of ultraintense laser pulses with electrons in vacuum, Phys. Rev. E. 58 (3) (1998) 3719–3732.

8. **Axelrod J. J., Campbell S. L., Schwartz O., et al.,** Observation of the relativistic reversal of the ponderomotive potential, Phys. Rev. Lett. 124 (13) (2020) 174801.

9. **Buts V. A., Zagorodny A. G.,** New cyclotron resonances and features of charged-particle dynamics in the presence of an intense electromagnetic wave, Phys. Plasmas. 28 (2) (2021) 022311.

10. **Volodin B. A., Ponomarev I. V., Khapaev A. M.,** On electron motion in the Redmond field, Sov. Phys. J. 27 (3) (1984) 113–115 (in Russian).

11. **Kopytov G. F., Tlyachev V. B., Oksuzyan S. S.,** On the radiation of an electron in a non-monochromatic Redmon field, Sov. Phys. J. 28 (2) (1986) 110–111 (in Russian).

12. **Qian B.-L.,** Relativistic motion of a charged particle in a superposition of circularly polarized plane electromagnetic waves and a uniform magnetic field, Phys. Plasmas. 7 (2) (2002) 573–543.

13. **Kong L.-B., Liu P.-K.,** Analytical solution for relativistic charged particle motion in a circularly polarized electromagnetic wave, Phys. Plasmas. 14 (6) (2007) 063101.

14. **Andreev S. N., Makarov V. P., Rukhadze A. A.,** On the motion of a charged particle in a plane monochromatic electromagnetic wave, Quantum Electron. 39 (1) (2009) 68–72.

15. **Akintsov N. S., Nevecheria A. P.,** Acceleration of a charged particle in the Redmond field, AIP Adv. 12 (3) (2022) 035212.

16. **Wilks S. C., Kruer W. L., Tabak M., Langdon A. B.,** Absorption of ultraintense laser pulses, Phys. Rev. Lett. 69 (9) (1992) 1382 –1386.

17. **Sentoku Y., Cowan T. E., Kemp A., Ruhl H.,** High energy proton acceleration in interaction of short laser pulse with dense plasma target, Phys. Plasmas. 10 (5) (2003) 2009–2015.

18. **D'Humieres E., Lefebvre E., Gremillet L., Malka V.,** Proton acceleration mechanisms in high-intensity laser interaction with thin foils, Phys. Plasmas. 12 (6) (2005) 056401.

19. **Mora P.,** Thin-foil expansion into a vacuum, Phys. Rev. E. 72 (5) (2005) 056401.

20. **Oishi Y., Nayuki T., Fujii T., et al.,** Dependence on laser intensity and pulse duration in proton acceleration by irradiation of ultrashort laser pulses on a Cu foil target, Phys. Plasmas. 12 (7) (2005) 073102.

21. **Shebalin J. V.,** An exact solution to the relativistic equation of motion of a charged particle driven by a linearly polarized electromagnetic wave, IEEE Trans. Plasma Sci. 16 (3) (1988) 390–392.

22. **Acharya S., Saxena A. C.,** The exact solution of the relativistic equation of motion of a charged particle driven by an elliptically polarized electromagnetic wave, IEEE Trans. Plasma Sci. 21 (2) (1993) 257–259.

23. **Ondarza R., Gomez F.,** Exact solution of the relativistic equation of motion of a charged particle driven by an elliptically polarized electromagnetic shaped pulse propagating along a static and homogeneous magnetic field, IEEE Trans. Plasma Sci. 32 (2) (2004) 808–812.

СПИСОК ЛИТЕРАТУРЫ

1. **Ландау Л. Д., Лифшиц Е. М.** Теоретическая физика. В 10 тт. Т. 2. Теория поля. М.: Физматлит. 1962. 424 с.

2. **Тернов И. М., Хапаев А. М., Володин В. А.** Динамика релятивистских заряженных частиц в поле плоской электромагнитной волны и в поле Редмонда // Вестник Московского университета. Физика. Астрономия. 1980. Т. 21. № 4. С. 70–74.

3. **Багров В. Г., Гитман Д. М., Тернов И. М., Халилов В. Р., Шаповалов В. Н.** Точные решения релятивистских волновых уравнений. Новосибирск: Академиздатцентр «Наука», 1982. 144 с.

4. **Багров В. Г., Бисноватый-Коган Г. С., Бордовицын В. А. Борисов А. В., Дорофеев О. Ф., Жуковский В. Ч., Пивоваров Ю. Л., Шорохов О. В., Эпп В. Я.** Теория излучения релятивистских частиц. М.: Физматлит. 2002. 576 с.

5. **Kaplan A. E., Pokrovsky A. L.** Fully relativistic theory of the ponderomotive force in an ultraintense standing wave // Physical Review Letters. 2005. Vol. 95. No. 5. P. 053601.

6. **Zhu S., Shen W.** General relativistic ponderomotive force in a moving medium // Journal of the Optical Society of America B. 1987. Vol. 4. No. 5. Pp. 739–742.

7. **Quesnel B., Mora P.** Theory and simulation of the interaction of ultraintense laser pulses with electrons in vacuum // Physical Review E. 1998. Vol. 58. No. 3. Pp. 3719–3732.

8. **Axelrod J. J., Campbell S. L., Schwartz O., Turnbaugh C., Glaeser R. M., Müller H.** Observation of the relativistic reversal of the ponderomotive potential // Physical Review Letters. 2020. Vol. 124. No. 13. P. 174801.

9. **Buts V. A., Zagorodny A. G.** New cyclotron resonances and features of charged-particle dynamics in the presence of an intense electromagnetic wave // Physics of Plasmas. 2021. Vol. 28. No. 2. P. 022311.

10. **Володин Б. А., Пономарев И. В., Хапаев А. М.** К вопросу о движении электрона в поле Редмонда // Известия вузов. Физика. 1984. Т. 27. № 3. С. 113–115.

11. **Копытов Г. Ф., Тлячев В. Б., Оксузян С. С.** Об излучении электрона в немонохроматическом поле Редмонда // Известия вузов. Физика. 1986. Т. 29. № 2. С. 110–111.

12. **Qian B.-L.** Relativistic motion of a charged particle in a superposition of circularly polarized plane electromagnetic waves and a uniform magnetic field // Physics of Plasmas. 2002. Vol. 7. No. 2. Pp. 573–543.

13. **Kong L.-B., Liu P.-K.** Analytical solution for relativistic charged particle motion in a circularly polarized electromagnetic wave // Physics of Plasmas. 2007. Vol. 14. No. 6. P. 063101.

14. **Андреев С. Н., Макаров В. П., Рухадзе А. А.** О движении заряженной частицы в плоской монохроматической электромагнитной волне // Квантовая электроника. 2009. Т. 39. № 1. С. 68–72.

15. **Akintsov N. S., Nevecheria A. P.** Acceleration of a charged particle in the Redmond field // AIP Advances. 2022. Vol. 12. No. 3. P. 035212.

16. **Wilks S. C., Kruer W. L., Tabak M., Langdon A. B.** Absorption of ultraintense laser pulses // Physical Review Letters. 1992. Vol. 69. No. 9. Pp. 1382 –1386.

17. **Sentoku Y., Cowan T.E., Kemp A., Ruhl H.** High energy proton acceleration in interaction of short laser pulse with dense plasma target // Physics of Plasmas. 2003. Vol. 10. No. 5. Pp. 2009–2015.

18. **D'Humieres E., Lefebvre E., Gremillet L., Malka V.** Proton acceleration mechanisms in high-intensity laser interaction with thin foils // Physics of Plasmas. 2005. Vol. 12. No. 6. P. 056401.

19. **Mora P.** Thin-foil expansion into a vacuum // Physical Review E. 2005. Vol. 72. No. 5. P. 056401.

20. **Oishi Y., Nayuki T., Fujii T., et al.** Dependence on laser intensity and pulse duration in proton acceleration by irradiation of ultrashort laser pulses on a Cu foil target // Physics of Plasmas. 2005. Vol. 12. No. 7. P. 073102.

21. **Shebalin J. V.** An exact solution to the relativistic equation of motion of a charged particle driven by a linearly polarized electromagnetic wave // IEEE Transactions on Plasma Science. 1988. Vol. 16. No. 3. Pp. 390–392.

22. **Acharya S., Saxena A. C.** The exact solution of the relativistic equation of motion of a charged particle driven by an elliptically polarized electromagnetic wave // IEEE Transactions on Plasma Science. 1993. Vol. 21. No. 2. Pp. 257–259.

23. **Ondarza R., Gomez F.** Exact solution of the relativistic equation of motion of a charged particle driven by an elliptically polarized electromagnetic shaped pulse propagating along a static and homogeneous magnetic field // IEEE Transactions on Plasma Science. 2004. Vol. 32. No. 2. Pp. 808–812.

THE AUTHORS

AKINTSOV Nikolai S.
Nantong University, Ocean University of China
40 Qing Nian Dong Lu, Chongchuan Qu, Nantong Shi, Jiangsu Sheng,
Nantong University, Nantong, 226019, People's Republic of China
akintsov777@mail.ru
ORCID: 0000-0002-1040-1292

NEVECHERIA Artem P.
Kuban State University
149 Stavropolskaya St., Krasnodar, 350040, Russia
artiom1989@mail.ru
ORCID: 0000-0001-6736-4691

MARTYNOV Alexander A.
Kuban State University
149 Stavropolskaya St., Krasnodar, 350040, Russia
martynov159@yandex.ru
ORCID: 0009-0000-7673-966X

СВЕДЕНИЯ ОБ АВТОРАХ

АКИНЦОВ Николай Сергеевич – *кандидат физико-математических наук, научный исследователь (постдокторант) Наньтунского университета, научный сотрудник Китайского океанологического университета, г. Наньтун, Китайская Народная Республика.*
226019, People's Republic of China, 40 Qing Nian Dong Lu, Chongchuan Qu, Nantong Shi, Jiangsu Sheng, Nantong University, Nantong
akintsov777@mail.ru
ORCID: 0000-0002-1040-1292

НЕВЕЧЕРЯ Артём Павлович – *преподаватель кафедры математических и компьютерных методов Кубанского государственного университета, г. Краснодар, Россия.*
350040, Россия, г. Краснодар, Ставропольская ул., 149
artiom1989@mail.ru
ORCID: 0000-0001-6736-4691

МАРТЫНОВ Александр Алексеевич – *кандидат физико-математических наук, доцент кафедры теоретической физики и компьютерных технологий Кубанского государственного университета, г. Краснодар, Россия.*
350040, Россия, г. Краснодар, Ставропольская ул., 149
martynov159@yandex.ru
ORCID: 0009-0000-7673-966X

Received 15.12.2022. Approved after reviewing 20.04.2023. Accepted 20.04.2023.
Статья поступила в редакцию 15.12.2022. Одобрена после рецензирования 20.04.2023. Принята 20.04.2023.

© Peter the Great St. Petersburg Polytechnic University, 2023

MATHEMATICS

Original article
DOI: https://doi.org/10.18721/JPM.16213

A NUMERICAL ALGORITHM FOR SYNTHESIZING THE POLYNOMIALS DEVIATING LEAST FROM ZERO WITH A GIVEN WEIGHT

A. S. Berdnikov[1]✉, *K. V. Solovyev*[2, 1]

[1] Institute for Analytical Instrumentation RAS, St. Petersburg, Russia;

[2] Peter the Great St. Petersburg Polytechnic University, St. Petersburg, Russia

✉ asberd@yandex.ru

Abstract. The article considers numerical algorithms for determining the coefficients of polynomials with a fixed leading coefficient, the algorithms supplying a minimum deviation from zero in a minimax norm with a given weight function. The polynomials serve as a useful tool in many numerical methods, in particular, in the Lanczos' tau method which provides an approximate numerical analytic solution of ordinary differential equations with coefficients as polynomials in the independent variable. The well-known Chebyshev polynomials determined analytically are the special case of such polynomials, however, in most cases of weight functions, such polynomials can only be determined and tabulated numerically.

Keywords: minimax norm, Chebyshev polynomial, optimal approximation, interpolation, numerical algorithm

Funding: The reported study was carried out at Institute for Analytical Instrumentation, RAS (St. Petersburg, Russia) within the framework of the theme FFZM-2022-0009 (State registration No. 122040600002-3) of the State Assignment of the Ministry of Science and Higher Education of the Russian Federation, 075-01157-23-00 dated 29.12.2022.

Citation: Berdnikov A. S., Solovyev K. V., A numerical algorithm for synthesizing the polynomials deviating least from zero with a given weight. St. Petersburg State Polytechnical University Journal. Physics and Mathematics. 16 (2) (2023) 146–160. DOI: https://doi.org/10.18721/JPM.16213

This is an open access article under the CC BY-NC 4.0 license (https://creativecommons.org/licenses/by-nc/4.0/)

© Berdnikov A. S., Solovyev K. V., 2023. Published by Peter the Great St. Petersburg Polytechnic University.

Научная статья
УДК 537.213, 537.612, 517.5
DOI: https://doi.org/10.18721/JPM.16213

ЧИСЛЕННЫЙ АЛГОРИТМ ДЛЯ КОНСТРУИРОВАНИЯ МНОГОЧЛЕНОВ, НАИМЕНЕЕ ОТКЛОНЯЮЩИХСЯ ОТ НУЛЯ С ЗАДАННЫМ ВЕСОМ

А. С. Бердников[1]✉, *К. В. Соловьев*[2, 1]

[1] Институт аналитического приборостроения РАН, Санкт-Петербург, Россия;

[2] Санкт-Петербургский политехнический университет Петра Великого, Санкт-Петербург, Россия

✉ asberd@yandex.ru

Аннотация. В статье рассматриваются численные алгоритмы для определения коэффициентов многочленов с фиксированным старшим коэффициентом, которые обеспечивают на заданном интервале минимальное отклонение от нуля в минимаксной норме с заданной весовой функцией. Указанные многочлены служат полезным инструментом во многих численных методах, в частности в тау-методе Ланцоша, обеспечивающего нахождение приближенного численно-аналитического решения обыкновенных дифференциальных уравнений с коэффициентами в виде многочленов от независимой переменной. Частным случаем таких многочленов являются хорошо известные многочлены Чебышева, определяемые аналитически, однако в большинстве случаев весовых функций такие многочлены можно определить и табулировать только численно.

Ключевые слова: минимаксная норма, многочлен Чебышева, оптимальная аппроксимация, интерполяция, численный алгоритм

Финансирование: Работа выполнена в Институте аналитического приборостроения РАН (г. Санкт-Петербург, Россия) в рамках темы FFZM-2022-0009 (номер гос. регистрации 122040600002-3) государственного задания Министерства науки и высшего образования Российской Федерации № 075-01157-23-00 от 29.12.2022.

Ссылка для цитирования: Бердников А. С., Соловьев К. В. Численный алгоритм для конструирования многочленов, наименее отклоняющихся от нуля с заданным весом // Научно-технические ведомости СПбГПУ. Физико-математические науки. 2023. Т. 16. № 2. С. 146–160. DOI: https://doi.org/10.18721/JPM.16213

Статья открытого доступа, распространяемая по лицензии CC BY-NC 4.0 (https://creativecommons.org/licenses/by-nc/4.0/)

Introduction

Approximations of functions that are optimal by the minimax (uniform) norm offer significant advantages over the simpler approximation of functions by the least squares method [1]. Expansion of a function into a truncated series consisting of polynomials of least deviation from zero is commonly used to construct such approximations [2, 3, 5–7]. In addition, the polynomials of least deviation from zero are useful for making an optimal choice of collocation points for interpolation of functions by polynomials (these points are zeros of the corresponding polynomials [1]), as well as for constructing approximate solutions for linear ordinary differential equations (ODE) with coefficients in the form of polynomials with respect to an independent variable [1, 2, 4].

Unfortunately, there are not many polynomials of least deviation from zero at a given interval, for which there is an explicit algebraic representation in analytical form. In this paper, we consider a refined version of a rapidly convergent numerical algorithm for calculating the coefficients of polynomials of least deviation from zero over a given interval with a given weight, which was partially discussed in [8].

© Бердников А. С., Соловьев К. В., 2023. Издатель: Санкт-Петербургский политехнический университет Петра Великого.

Polynomials of least deviation from zero

The problem on constructing a polynomial of a given degree that deviates least from zero in a given interval with a given weight is formulated as follows. Let there be a continuous function $f(x)$ and a finite interval $[a, b]$ for which a continuous weight function $q(x)$ is strictly positive in this interval; however, the ends of the interval where the function $q(x)$ can vanish[1] may be the exceptions. It is required to find a polynomial of degree n of the form

$$p(x) = a_0 + a_1x + a_2x^2 + \ldots + a_{n-1}x^{n-1} + a_nx^n \tag{1}$$

with previously undetermined coefficients $a_0, a_1, a_2, \ldots, a_{n-1}$ and the leading coefficient $a_n = 1$, which is the solution to the optimization problem

$$\max |q(x)p(x)| \to \min. \tag{2}$$

Here, maximization is performed with respect to the variable $x \in [a, b]$, and minimization with respect to the coefficients $a_0, a_1, a_2, \ldots, a_{n-1}$. Such a polynomial is called the polynomial of least deviation from zero in the interval $[a, b]$ with the weight $q(x)$.

First-kind Chebyshev polynomials taking the following form provide the smallest deviation from zero in the interval $[-1, +1]$ with the weight $q(x) = 1$:

$$T_n(x) = \cos[n \arccos(x)];$$

the polynomials are scaled using a 2^{-n} multiplier so that the leading coefficient of the polynomial is equal to unity. Scaled second-kind Chebyshev polynomials of the second kind taking the following form provide the smallest deviation from zero in the interval $[-1, +1]$ with the weight $q(x) = (1 - x^2)^{1/2}$:

$$U_n(x) = \sin[(n + 1) \arccos(x)] / (1 - x^2)^{1/2}.$$

Polynomials of degree n, providing the smallest deviation from zero in the interval $[0, 1]$ with the weight $q(x) = x$, are obtained by separating a multiplier in the form of a weight function from first-kind Chebyshev polynomials of degree $n + 1$, for which such an argument substitution $x \to ax + b$ should be performed that the interval $[x_a + 1]$ of argument values be mapped to the interval $[0, 1]$, where

$$x_a = \cos[\pi(2n + 1)/(2n + 2)]$$

is the minimum zero of the function $T_{n+1}(x)$.

Polynomials of degree n, providing the smallest deviation from zero in the interval $[0, 1]$ with the weight $q(x) = x(1 - x)$, are obtained by separating a multiplier in the form of a weight function from first-kind Chebyshev polynomials oof degree $n + 2$, for which such an argument substitution $x \to ax + b$ should be performed that the interval $[x_b, x_c]$ of argument values is mapped to the interval $[0, 1]$, where

$$x_b = \cos[\pi(2n + 3) / (2n + 4)] \text{ and } x_c = \cos[\pi/(2n+4)]$$

are the minimum and maximum zeros of the function $T_{n+2}(x)$.

Other examples of polynomials of least deviation from zero are given in monographs [6, 7], but in general, very few such polynomials for which there are explicit algebraic expressions are known.

Chebyshev criterion

The fundamental properties of polynomials of least deviation from zero are determined by the following statement.

[1] A weight function with zeros in the interval $[a, b]$ requires that the Chebyshev maxima and minima (and the test points for the numerical algorithm) do not coincide with the zeros of the weight function, and the signs of alternating maxima and minima change in accordance with the sign of the weight function. Furthermore, the interval $[a, b]$ can be infinite on the right and/or on the left-hand sides, but the weight function $q(x)$ should tend to zero at infinity no slower than the power function $1/x^k$ [5–7].

Statement 1 (Chebyshev criterion for polynomials of least deviation from zero). *In order for a polynomial p(x) of degree n with the leading coefficient equal to unity to be a solution to problem (2), it is necessary and sufficient that there exist such a set of n + 1 points* $x_0 < x_1 < x_2 < \ldots < x_n$ *belonging to the interval [a,b], and such a number* ε*(positive or negative) that the following conditions are satisfied:*

$$-|\varepsilon| \le q(x)p(x) \le |\varepsilon| \text{ for } x \in [a, b], \tag{3}$$

$$q(x_k)p(x_k) = (-1)^k\varepsilon \text{ for } k = 0, 1, 2, \ldots, n. \tag{4}$$

This criterion is a special case of a more general statement about uniform approximations by rational functions, considered by Pafnuty Chebyshev in his mémoire [17] (see also [6, 7]). The mémoire was not published, so it is difficult to establish the exact date when this result was obtained. Notably, Chebyshev also turned to the problem of the best uniform approximation by polynomials in his earlier works (see, for example, [16]), frequently revisiting the statements formulated in [17] later (see, for example, [18]).

Below we present the modern proof of the Chebyshev criterion for polynomials deviating least from zero, divided for convenience of presentation into several auxiliary statements 2–6: lower and upper bound estimate of norm (2), existence of optimal solution, sufficiency of Chebyshev criterion, necessity of Chebyshev criterion, uniqueness of solution.

Evidently, provided that conditions (3), (4) are satisfied, the equality $\max |q(x)p(x)| = |\varepsilon|$ holds true. The points $x_0 < x_1 < x_2 < \ldots < x_{n+1}$ of the interval $[a, b]$ with alternating positive minima and negative maxima equal in absolute value to the maximum absolute value of the function considered are called the Chebyshev alternation. According to Chebyshev's alternation theorem ([6, 7] and [16–20]), the condition under consideration is necessary and sufficient for the polynomial $p(x)$ to be a solution to optimization problem (2), so that such a solution always exists and is unique.

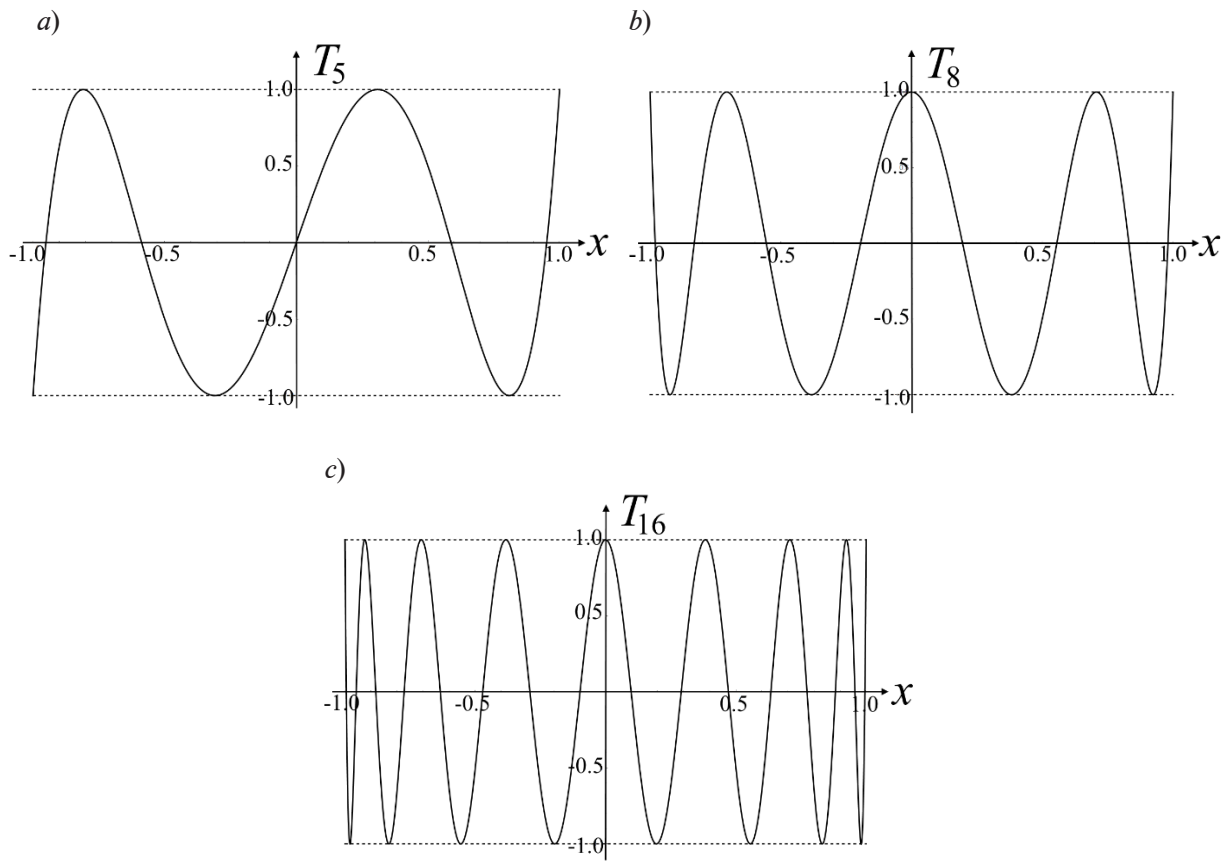

Fig. 1. Chebyshev polynomials $T_n(x)$ for $n = 5$ (*a*), 8 (*b*) and 16 (*c*), deviating least from zero in the segment [–1, +1]

Fig. 1 shows graphs of first-kind Chebyshev polynomials [1–3], illustrating that this condition is satisfied in the interval [−1, +1] with weight $q(x) = 1$.

In accordance with conditions (3), (4) for an optimal polynomial $p(x)$ with a coefficient at the highest degree equal to unity, there is a set of $n + 1$ test points x_k in which the deviation from zero $q(x)p(x)$ has alternating local negative minima and positive maxima, equal to $\pm|\varepsilon|$, and the values of these minima and maxima are global in the interval $[a, b]$.

This criterion is a special case of Chebyshev's theory of minimax approximation using rational functions [6, 7], however, the proof of the corresponding statements is simplified for polynomials of least deviation from zero.

Statement 2 (de la Vallée Poussin theorem [6, 7, 21–23]). *If the function q(x)p(x) takes values* $\lambda_0, \lambda_1, ..., \lambda_{N-1}$ *different than zero with alternating signs, where* $N \geq n + 1$, *at N consecutive points* $x_0 < x_1 < ... < x_{N-1}$ *of the interval [a,b] for some polynomial p(x) of degree n with the leading coefficient equal to unity, then the following relation holds true for any other polynomial r(x) of degree n with the leading coefficient equal to unity:*

$\max |q(x)r(x)| \geq \min \{|\lambda_0|, |\lambda_1|, ..., |\lambda_{N-1}|\}$.

Proof. Suppose there is a polynomial $r(x)$ for which the condition $\max |q(x)r(x)| < \min (|\lambda_0|, |\lambda_1|, ..., |\lambda_{N-1}|)$ is satisfied. We assume that the values of $q(x_k)p(x_k)$ in the sequence x_k are strictly positive for even points, and strictly negative for odd points. (The reasoning is similar when the values are positive for odd points and negative for even points). This means that the following condition is satisfied at even points x_k:

$$q(x_k)r(x_k) < |\lambda_k| = q(x_k)p(x_k),$$

and the following condition is satisfied at odd points x_k:

$$q(x_k)r(x_k) > -|\lambda_k| = q(x_k)p(x_k).$$

As a result, the quantity $q(x)[p(x) - r(x)]$ is strictly positive at even points x_k and strictly negative at odd points x_k. The values of $q(x_k)$ do not vanish and, therefore, are strictly positive. The polynomial $p(x) - r(x)$ of degree $n - 1$, which is not identically zero, alternately takes positive and negative values for at least $n + 1$ points and, therefore, has at least n zeros. Consequently, the polynomial $r(x)$ for which

$$\max |q(x)r(x)| < \min (|\lambda_0|, |\lambda_1|, \ldots, |\lambda_{N-1}|),$$

does not exist.

Statement 2 is proved.

Remark. De la Vallée Poussin theorem allows to obtain a lower-bound estimate for solving optimization problem (2). If $\lambda_0, \lambda_1, ..., \lambda_{N-1}$ are local maxima and minima of the function $q(x)$ $r(x)$ with alternating signs, then such a structure is called the de la Vallée Poussin alternation; it gives not only the lower-bound estimate for the solution to optimization problem (2), but also the upper-bound estimate, equal to $\max \{|\lambda_0|, |\lambda_1|, ..., |\lambda_{N-1}|\}$.

Statement 3. *There is a polynomial p(x) that provides a solution to optimization problem (2).*

This statement is important because it excludes the case when there are polynomials $p_k(x)$ with progressively decreasing values $P_k = \max |q(x)p_k(x)|$, while the minimum of this quantity is never reached in the set of polynomials of fixed degree. In particular, there is no solution to optimization problem (2) without imposing an a priori restriction on the degree of the polynomial $p(x)$.

Proof. The values of the quantities $P_k = \max |q(x)p_k(x)|$ are bounded from below by zero, so there is an exact lower bound $P$for the values of P_k in the set of polynomials. According to the definition of the exact lower bound, there is a sequence of polynomials $p_k(x)$ of degree n:

$$p_k(x) = a_{0,k} + a_{1,k}x + a_{2,k}x^2 + \ldots + a_{n-1,k}x^{n-1} + x^n,$$

for which $P \leq P_k \leq 2P$ and $\lim P_k = P$ with $k \to \infty$.

Consequently, the values of the polynomials $p_k(x)$ in the interval $[a + \delta, b - \delta]$ (where δ is sufficiently small) starting from some number k are bounded from above and from below (an offset had to be made from the ends of the interval to take into account the case when the continuous weight function $q(x)$ at the ends of the interval can equal zero). It follows from the Lagrange formula [15] for a polynomial $p(x)$ of degree n, taking the values y_k at the given $n + 1$ points x_k, of the form

$$p(x) = \sum_{j=1,n+1} \left(y_j \prod_{i=1,n+1,i\neq j} \frac{(x - x_i)}{(x_j - x_i)} \right),$$

that when the values of the polynomial y_k are bounded from above and from below at $n + 1$ fixed points x_k, each individual coefficient of the polynomial is also bounded from above and from below. According to the Bolzano–Weierstrass theorem (lemma) on the limit point, each infinite bounded sequence of points in the space R^n has an infinite subsequence with a limit. Therefore, a subsequence with a limit for each of the polynomial coefficients can be selected in the considered sequence of polynomials $p_k(x)$ (represented as vectors of length $n + 1$, consisting of the polynomial coefficients bounded from above and from below).

In other words, there is a sequence of polynomials $p_k(x)$ for which $\lim P_k = P$ for $k \to \infty$, and the coefficients of the polynomials $p_k(x)$ have limit values $b_j = \lim a_{j,k}$ при $k \to \infty$. Evidently, this condition also holds true for the higher coefficients of the polynomials $p_k(x)$, by definition equal to unity.

Consider a polynomial $r(x)$ with the coefficients b_j:

$$r(x) = b_0 + b_1x + b_2x^2 + \ldots + b_{n-1}x^{n-1} + x^n.$$

Since $b_j = \lim a_{jk}$, the following condition is satisfied for any fixed value of x:

$$\lim p_k(x) = r(x) \text{ for } k \to \infty,$$

so that convergence to the limit is uniform over the considered finite interval of values of x. It follows from the inequality

$$\max |q(x)r(x)| = \max |q(x)\{p_k(x) + [r(x) - p_k(x)]\}| \leq$$

$$\leq \max |q(x)p_k(x)| + \max |q(x)| \cdot \max |r(x) - p_k(x)|$$

that $\max |q(x)r(x)| = P$. Indeed, $\max |q(x)r(x)|$ cannot be less than P; at the same time, the first term on the right-hand side of the inequality tends to P for $k \to \infty$, and the second term tends to zero. Thus, quantity (2) reaches its lower bound P for the polynomial $r(x)$.

Statement 3 is proved.

Statement 4. *If conditions (3), (4) of the Chebyshev criterion are satisfied for the polynomial p(x), then the optimal value for the right-hand side of optimization problem (2) is equal to* $|\varepsilon|$*, and the polynomial p(x) (possibly one of many) ensures that this optimum is achieved.*

Proof. The condition $\max|q(x)p(x)| = |\varepsilon|$ is satisfied for a polynomial $p(x)$ satisfying the Chebyshev criterion, so that the solution of optimization problem (2) does not exceed $|\varepsilon|$. However, since the Chebyshev alternation is a special case of the de la Vallée Poussin alternation, then, according to the de la Vallée Poussin theorem (see Statement 2), the solution to optimization problem (2) cannot be less than $|\varepsilon|$. Therefore, the solution of optimization problem (2) is equal to $|\varepsilon|$, and the polynomial $p(x)$ ensures that this optimum is achieved.

Statement 4 is proved.

Statement 5. *The polynomial p(x) providing a solution to optimization problem (2) must satisfy the Chebyshev criterion (see Statement 1).*

Proof. Consider the behavior of the function $F(x) = q(x)p(x)$ in the segment $[a, b]$. The function $q(x)$ can vanish only at the ends of the interval, so the number of zeros of the function $F(x)$ within the interval certainly does not exceed n, and all zeros are isolated points.

Let $y_1, y_2, \ldots, y_m$ be an ordered set of zeros of odd multiplicity for this continuous function (that might not contain a single point). The points $y_1, y_2, \ldots, y_m$ divide the segment $[a, b]$ into $m + 1$ intervals, so that the function $F(x)$ takes alternately a positive or a negative value in each of them. If the function $F(x)$ has no zeros, then the entire segment $[a, b]$ is an interval where the function $F(x)$ is either positive or negative.

For intervals with positive values of $F(x)$, we select a point with the maximum value of the function in this interval (it might not be the only one in this interval), and for intervals with negative values of $F(x)$, we select a point with the minimum value of the function in this interval. We obtain a set of points $y_1, y_2, \ldots, y_m$, dividing the segment $[a, b]$ into $m + 1$ intervals, where the

function $F(x)$ preserves its sign, but changes it upon intersecting the interval boundary. The set of points $x_0, x_1, x_2, ..., x_m, x_{m+1}$, belonging to these intervals, which do not coincide with the ends of the intervals, consists of alternating positive maxima and negative minima $\lambda_0, \lambda_1, \lambda_2, ..., \lambda_{m+1}$ of the function $F(x)$.

Let $\lambda = \max|\lambda_k|$. If the maximum is equal to λ in any interval, and the minimum modulus is less than λ in the adjacent (subsequent or preceding) interval, then this interval is attached to the current interval together with the subsequent interval with a positive maximum, regardless of its value (Fig. 2,*a*). The resulting interval has the following property: such a positive constant can be subtracted from the function $F(x)$ that the positive maximum of the function in the interval decreases, but the negative minimum modulus of the function in the interval does not increase sufficiently to exceed the new positive maximum.

Similarly, if the minimum is equal to $-\lambda$ in some interval, and the maximum is less than λ in the neighboring interval, then this first interval is attached the current interval together with the subsequent interval containing a negative minimum (see Fig. 2,*b*). A positive constant can be added to the function $F(x)$ for this interval, which would reduce the negative minimum modulus of the function in the interval and simultaneously increase the positive maximum of the function in the interval so as not to exceed the new negative minimum modulus.

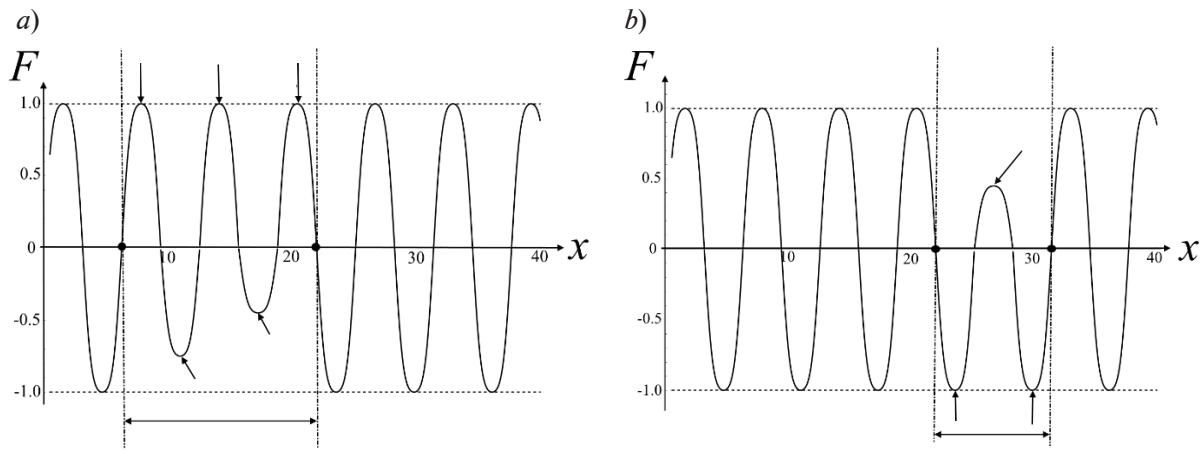

Fig. 2. Procedure for combining segments with alternating maxima and minima to construct the Chebyshev alternation (the length of the combined segments is marked by the extension lines): single or several sequentially located minima lie above the minimum level of the function $F(x)$ (*a*); single or several sequentially located maxima lie below its maximum level (*b*). The extrema are shown by arrows

Ultimately, a set of N intervals is obtained in the interval $[a, b]$ for a given polynomial $p(x)$, containing points $x_0, x_1, x_2, ..., x_{N-1}$ with alternating positive maxima and negative minima of the function $F(x)$ equal to $\pm\varepsilon$, where $\varepsilon = \max |q(x)p(x)|$. On the other hand, if N is greater than or equal to $n + 1$, then such a polynomial $p(x)$ satisfies the Chebyshev criterion and, in accordance with statement 2, is the solution to optimization problem (2).

Now let N be less than or equal to n. At the stage when the intervals were combined, the boundaries of the new intervals were determined, i.e., a set of points $y_1, y_2, ..., y_{N-1}$, where the function $F(x)$ vanishes and changes its sign. There are also constants $\delta_k > 0$ and a universal constant $\delta = \min \delta_k$. These constants can be subtracted from the function $F(x)$ in intervals with positive maxima or added to the function $F(x)$ in intervals with negative minima, reducing the minimax norm in the corresponding interval.

Let the function $F(x)$ take positive values in the first interval (the reasoning is similar if the function $F(x)$ takes negative values in the first interval). Consider the function $Q(x)$, which is the product of a polynomial of degree no higher than $n - 1$ and the weight function $q(x)$:

$$Q(x) = q(x)(y_1 - x)(y_2 - x) \cdots (y_{N-1} - x).$$

The function $Q(x)$ is strictly positive in the intervals where there is a Chebyshev maximum of the function $F(x)$, and strictly negative in those where there is a Chebyshev minimum of this function.

Let $R = \max |Q(x)|$. If we subtract the function $sQ(x)$ with a sufficiently small positive factor s from the function $F(x)$ (for example, we can choose $s = (\delta/R)$), then this should safely reduce the positive maxima of the function $F(x)$ and reduce its negative minima, thus also serving to reduce $\max |F(x)|$. Therefore, the considered polynomial $p(x)$ cannot serve as a solution to optimization problem (2), since an even smaller value for $\max |F(x)|$ can be obtained to replace the current polynomial $p(x)$ of degree n (its leading coefficient is unity) with a new polynomial $r(x)$ of degree n, where the leading coefficient is also equal to unity:

$$G(x) = F(x) - (\delta/R)Q(x) = q(x)p(x) - (\delta/R)q(x)(y_1 - x) \cdots (y_{N-1} - x) =$$

$$= q(x)[p(x) - (\delta/R)(y_1 - x) \cdots (y_{N-1} - x)] = q(x)r(x),$$

$$\max |G(x)| < \max |F(x)|.$$

Thus, the optimal polynomial of degree n, considered in statement 3, must satisfy the Chebyshev criterion.

Statement 5 is proved.

Statement 6. *The polynomial p(x) satisfying the Chebyshev criterion and providing a solution to optimization problem (2) is unique.*

Proof. Let there be two polynomials $p(x)$ and $r(x)$ of degree n, whose higher coefficients are equal to unity and which are the solution to optimization problem (2). Since the polynomials $p(x)$ and $r(x)$ are not identically zero, the expressions $q(x)p(x)$ and $q(x)r(x)$ have non-zero maxima and minima in the interval $[a, b]$.

According to statement 5, each of the polynomials $p(x)$ and $r(x)$ satisfies the Chebyshev criterion, and the value $\varepsilon \neq 0$ is the same for them. Polynomials of the form

$$s(x,\alpha) = (1 - \alpha)p(x) + \alpha r(x)$$

are polynomials of degree n with a unit coefficient for the highest degree. These polynomials are also solutions to optimization problem (2) for $0 < \alpha < 1$: the chain of inequalities

$$|q(x)s(x,\alpha)| = |q(x)[(1 - \alpha)p(x) + \alpha r(x)]| \leq (1 - \alpha)|q(x)p(x)| + \alpha|q(x)r(x))| \leq |\varepsilon|$$

implies that $\max |q(x)s(x,\alpha)| \leq |\varepsilon|$, and since the case $\max |q(x)s(x,\alpha)| < |\varepsilon|$ is impossible because $|\varepsilon|$ is the solution to optimization problem (2), we obtain that $\max |q(x)s(x,\alpha)| = |\varepsilon|$.

Let $x_1, x_2, \ldots, x_{n+1}$ be Chebyshev inflection points with alternating maxima and minima of the function $q(x)s(x,\alpha)$, equal to $\pm\varepsilon$. If x_k is the point of the negative minimum of the function $q(x)s(x,\alpha)$, equal to $-|\varepsilon|$, then the conditions

$$q(x_k)s(x_k,\alpha) = (1 - \alpha)q(x_k)p(x_k) + \alpha q(x_k)r(x_k)) = -|\varepsilon|,$$

$$q(x_k)p(x_k) \geq -|\varepsilon|,\ q(x_k)r(x_k) \geq -|\varepsilon|,\ 0 < \alpha < 1$$

imply that the case when

$$q(x_k)p(x_k) = -|\varepsilon| \text{ and } q(x_k)r(x_k) = -|\varepsilon|,$$

is the only possible one.

Similarly, if x_k is the point of the positive maximum of the function $q(x)s(x,\alpha)$, equal to $|\varepsilon|$, then the conditions

$$q(x_k)s(x_k,\alpha) = (1 - \alpha)q(x_k)p(x_k) + \alpha q(x_k)r(x_k)) = |\varepsilon|,$$

$$q(x_k)p(x_k) \leq |\varepsilon|,\ q(x_k)r(x_k) \leq |\varepsilon|,\ 0 < \alpha < 1,$$

imply that

$$q(x_k)p(x_k) = |\varepsilon| \text{ and } q(x_k)r(x_k) = |\varepsilon|.$$

Since the values of the polynomials $p(x)$ and $r(x)$ of degree n with the leading coefficient equal to unity are the same at $n + 1$ different points $x_1, x_2, ..., x_{n+1}$, these polynomials are identically equal to each other.

Algorithm for constructing a polynomial of least deviation from zero

An algorithm for numerically constructing polynomials of least deviation from zero, which is a modified and optimized Remez algorithm [9–14], follows from the above Chebyshev criterion (Statement 1).

Step 1. The initial set of points $x_0 < x_1 < x_2 < ... < x_n$ belonging to the interval $[a, b]$ is chosen arbitrarily.

Step 2. For the current set of points,

$$a \le x_0 < x_1 < x_2 < \ldots < x_n \le b$$

a polynomial $p(x)$ of degree n is constructed for which the conditions

$$q(x_k)p(x_k) = (-1)^k \text{ for } k = 0, 1, 2, ..., n$$

are satisfied.

Evidently, such a polynomial exists, is defined uniquely and can be calculated explicitly by the Lagrange formula [15].

Step 3. The roots belonging to the interval $[a, b]$ are found for the polynomial $p(x)$. Since the values of the polynomial $p(x)$ have different signs at the ends of the intervals $[x_k, x_{k+1}]$, there is at least one root of the polynomial $p(x)$ inside each such interval. There are exactly n such intervals, so there is exactly one root in each of the intervals $[x_k, x_{k+1}]$, and all the roots of the polynomial $p(x)$ are real, belong to the interval $[a, b]$ and are not multiples. It is not difficult to find these roots using a suitable numerical method.

Step 4. The list of roots

$$a < y_1 < y_2 < \ldots < y_n < b,$$

belonging to the interval $[a, b]$, which were found in Step 3, are supplemented by the beginning and end of the interval $y_0 = a$ and $y_{n+1} = b$. Since the polynomial $p(x)$ of degree n preserves the sign in the intervals $[y_k, y_{k+1}]$, either a global maximum (for positive values of the polynomial) or a global minimum (for negative values of the polynomial) exists in each of the intervals $[y_k, y_{k+1}]$ for the function $q(x)p(x)$. If the function $q(x)$ varies slowly enough that it can be assumed to be constant in a narrow interval $[y_k, y_{k+1}]$ (a typical case), then there is exactly one local maximum or minimum in each of the intervals $[y_k, y_{k+1}]$, thus coinciding with the global maximum or minimum in this interval, since the derivative of the polynomial $p(x)$ has degree $n - 1$ and therefore cannot have more than $n - 1$ zeros.

Step 5. Let $a \le z_0 < z_1 < z_2 < ... < z_n \le b$ be a list of alternating positive maxima and negative minima of the function $q(x)p(x)$, which were found in Step 4. Let us consider the values

$$q(z_k)p(z_k) = (-1)^k \varepsilon_k \text{ with } k = 0, 1, 2, ..., n$$

in these points, which, according to Step 4, must be either positive or negative extrema for intervals $[y_k, y_{k+1}]$ with purely positive or purely negative values of the function $q(x)p(x)$. If the condition $\varepsilon_k \approx$ const is satisfied within the given accuracy, then a polynomial $p(x)$ is obtained, deviating least from zero and satisfying the Chebyshev criterion. At the same time, it follows from the de la Vallée Poussin theorem on the best approximation of a function by polynomials (see the Statement 2) [6, 7] that the exact optimum for problem (2) lies in the range between $\min|\varepsilon_k|$ and $\max|\varepsilon_k|$ (adjusted for the current multiplier before the leading coefficient of the polynomial replacing unity). If the values of ε_k are considerably different from each other, we replace the test points

$$a \le x_0 < x_1 < x_2 < \ldots < x_n \le b$$

with the points

$$a \le z_0 < z_1 < z_2 < \ldots < z_n \le b$$

and return to Step 2.

Step 6. The remaining step is to normalize the polynomial $p(x)$ so that its leading coefficient becomes equal to unity. Since the polynomial $p(x)$ has n roots, and the polynomial itself is not identical to zero, its leading coefficient cannot be zero and, therefore, such normalization can be performed. An additional useful result is applying a list of n real roots of the polynomial $p(x)$ located in the interval $[a, b]$ (found in Step 3) to the polynomial.

The algorithm has a geometrical convergence rate in the following sense: there are numbers $C > 0$ and $0 < \lambda < 1$ for any continuous weight function and for any degree n, for which

$$\max |q(x)p_i(x)| \leq 1 + C\lambda^i,$$

where i is the iteration number.

Convergence of the given algorithm is proved similarly to that of the Remez algorithm in monograph [11]. Numerical experiments established that our algorithm converged very quickly in all practically verified cases.

Fig. 3 illustrates the verification of the algorithm's performance for the case

$$a = 0,\ b = 1,\ q(x) = x^3,\ p(x) = a_0 + a_1x + a_2x^2 + a_3x^3 + a_4x^4 + x^5.$$

Evidently, it is already the third iteration that provides a completely acceptable deviation from zero. The algorithm finally converges in the fifth iteration.

The solution is a polynomial with the coefficients

$$a_0 = -0.018464,\ a_1 = 0.712942,\ a_2 = -2.851981,$$

$$a_3 = 4.650795,\ a_4 = -3.493237$$

The deviation from zero is $5.5 \cdot 10^{-5}$. Fig. 4 shows a comparison between the deviations from zero of the polynomial $q(x)p(x)$ and the first-kind Chebyshev polynomial of the same degree.

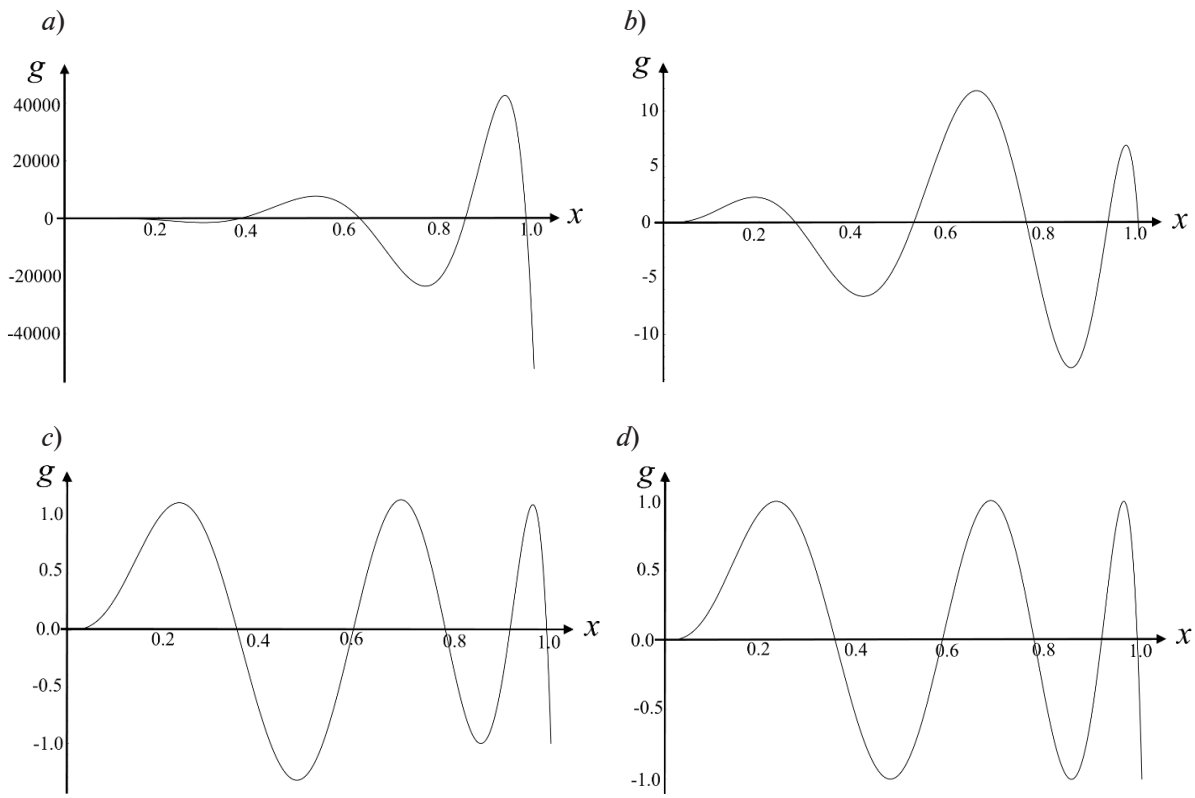

Fig. 3. Iterations $g(x) = q(x)p(x)$ for calculated fifth-degree polynomial $p(x)$ of least deviation from zero in the interval [0, 1] with weight $q(x) = x^3$: initial state after Step 1 of algorithm (*a*), as well as the first (*b*), second (*c*) and third (*d*) iterations

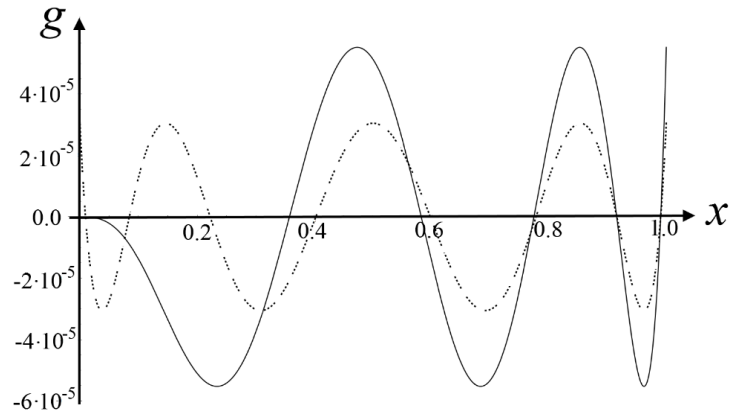

Fig. 4. Oscillations of function $g(x) = q(x)p(x)$ of least deviation from zero in the interval [0, 1] at $n = 5$ and $q(x) = x^3$ (solid line)
Scaled Chebyshev polynomial of degree 5 + 3 = 8, shifted from the interval [-1, +1] to the interval [0, 1], which has 1 as the leading coefficient, is shown by a dashed line

Since the weight function $q(x)$ can vanish at some of the ends of the interval $[a, b]$, the test points selected at Step 1 must lie strictly within the interval $[a, b]$ to ensure that Step 2 can be taken:

$$a < x_0 < x_1 < x_2 < \ldots < x_n < b. \quad (5)$$

Apparently, if $q(a) = 0$ or $q(b) = 0$ and requirement (5) is preserved, the points z_k satisfy the following condition at step 5:

$$a < z_0 < z_1 < z_2 < \ldots < z_n < b,$$

consequently, condition (5) is preserved both in the next iteration and in all subsequent ones. For this reason, it is sufficient to ensure that condition (5) is satisfied at the first step of the algorithm.

To improve the performance of the algorithm at Step 1, it is recommended to choose either the zeros of the first-kind Chebyshev polynomial of degree $n + 1$, or the minima and maxima of the second-kind Chebyshev polynomial of degree n, shifted and scaled from the interval $[-1, +1]$ to the interval $[a, b]$, as the starting points in (5). It is recommended to use the condition $q(x_k)p(x_k) = (-1)^k \cdot [(b - a)/4]^n$ instead of the condition $q(x_k)p(x_k) = (-1)^k$ at Step 2 to avoid unnecessarily large coefficients for the polynomial $p(x)$. This choice of scale corresponds to the oscillations of the first-kind Chebyshev polynomial of degree n (least deviating from zero in the segment $[-1, +1]$ with the weight $q(x) \equiv 1$), recalculated from the interval $[-1, +1]$ to the interval $[a, b]$ and scaled so that the leading coefficient is equal to unity[2].

It is not recommended to use a direct solution of the system of linear equations $q(x_k)p(x_k) = (-1)^k$ with respect to unknown coefficients a_j to find the polynomial $p(x)$, taking the given values at the given points, at Step 2. The matrix of such linear equations for large n (the Vandermonde matrix) is characterized by a high condition number, which is why the solution of the equations is very sensitive to errors in rounding floating-point numbers [15]. The Lagrange formula [15] for a polynomial of degree n, taking given values at given $n + 1$ points, is free from such instability. Aitken's iterative process [15] can be used in practice instead of the explicit Lagrange formula for large degrees of the polynomial, allowing to sequentially add a new degree and a new interpolation point to a pre-existing interpolation

[2] Strictly speaking, this estimate is not entirely accurate, since it does not take into account the form of the weight function $q(x)$. In particular, $n = 5$ and $q(x) = x^3$ for the example considered, so $q(x)p(x)$ is an eighth degree polynomial, and the scale of oscillations for Chebyshev polynomials of degree $n = 8$ instead of $n = 5$ should be considered. The refined estimate of the oscillation amplitude has the form $(4/(b - a))^{-n-m}$, where m is the effective degree of the weight function $q(x)$ (it can be found by approximating $q(x)$ by a minimax norm polynomial with a unit weight function).

polynomial. However, it seems to be best to use one of Newton's finite difference schemes [15] instead of the explicit Lagrange formula at Step 2. Since the algorithm only requires that the value of the polynomial $p(x)$ be calculated at a given point x, there is no need to recalculate the form of Newton's finite differences into a polynomial represented explicitly (1) before the algorithm stops.

We should also note that all calculations should be performed with high accuracy if possible, since rounding errors introduced at intermediate stages can distort the calculation results to an unacceptable degree, causing the algorithm to become unstable.

The Wolfram Mathematica 11 software system was used to perform the calculations [24].

REFERENCES

1. **Lántczos K.,** Prakticheskiye metody prikladnogo analiza [Practical methods of an applied analysis], GIFML Publishing, Moscow, 1961 (in Russian).
2. **Pashkovskii S.,** Vychislitelnyye primeneniya mnogochlenov i ryadov Chebysheva [Chebyshev polynomials and series used for calculations], Nauka, Moscow, 1983 (in Russian).
3. **Danilov Yu. A.,** Mnogochleny Chebysheva [Chebyshev polynomials], Vysheyshaya shkola, Minsk, 1984 (in Russian).
4. **Chaplygin S. A.,** Novyy metod priblizhennogo integrirovaniya differentsialnykh uravneniy [A new method of approximate integration of differential equations], State Publishing House of Technical and Theoretical Literature, Moscow, Leningrad, 1950 (in Russian).
5. **Goncharov V. L.,** Teoriya interpolirovaniya i priblizheniya funktsiy [Theory of interpolation and approximation of functions], GTTI Publishing, Moscow, Leningrad, 1934 (in Russian).
6. **Akhiezer N. I.,** Lektsii po teorii approksimatsii [Lectures on approximation theory], OGIZ Publishing, Moscow, Leningrad, 1947 (in Russian).
7. **Akhiezer N. I.,** Lektsii po teorii approksimatsii, 2-ye izd. [Lectures on approximation theory, 2nd edition], Nauka Publishing, Moscow, 1965 (in Russian).
8. **Berdnikov A., Solovyev K., Krasnova N., et al.,** Algorithm for constructing the Chebyshev-type polynomials and the Chebyshev-type approximations with a given weight, Proc. 2022 Int. Conf. on Electrical Engin. & Photonics (EExPolytech), 20–21 Oct. 2022, St. Petersburg, Russia (2022) 143–145.
9. **Remez E.,** Sur un procédé convergent d'approximations successives pour determiner les polynomes d'appproximation, C. R. Acad. Sci. Paris. 198 (1934) 2063–2065.
10. **Remez E. Ya.,** Sur le calcul effectif des polynomes d'approximation de Tschebyscheff, C. R. Acad. Sci. Paris. 199 (1934) 337–340.
11. **Dzyadyk V. K.,** Vvedeniye v teoriyu ravnomernogo priblizheniya funktsiy polinomami [Introduction to the theory of uniform approximation of functions by polynomials], Nauka, Moscow, 1977 (in Russian).
12. **Remez E. Ya.,** Osnovy chislennykh metodov chebyshevskogo priblizheniya [Fundamentals of numerical methods for Chebyshev approximation], Naukova Dumka Publishing, Kiev, 1969 (in Russian).
13. **Laurent P. J.,** Approximations et optimisation, Hermann, Paris, 1972.
14. **Gribkova V. P.,** Effektivnyye metody ravnomernykh priblizheniy, osnovannyye na polinomakh Chebysheva [Effective methods of uniform approximations based on Chebyshev polynomials]. Sputnik Publishing, 2017 (in Russian).
15. **Berezin I. S., Zhidkov N. P.,** Computing methods, Vol. 1, Pergamon Press, Oxford, London, New York, Paris, 2014.
16. **Chebyshev P. L.,** Teoriya mekhanizmov, izvestnykh pod imenem parallelogrammov [Theory of the mechanisms known as parallelograms], In book: P. L. Chebyshev. Izbrannyye Trudy [Selectas]. Publishing house of the Academy of Sciences of the USSR, Moscow (1955) 611–648.
17. **Chebyshev P. L.,** Voprosy o naimenshikh priblizheniyakh, svyazannykh s priblizhennym predstavleniyem funktsiy [Issues on the least approximations related to the approximate representation of functions], In book: P. L. Chebyshev. Izbrannyye Trudy [Selectas]. Publishing house of the Academy of Sciences of the USSR, Moscow (1955) 462–578.

18. **Chebyshev P. L.**, O funktsiyakh, naimeneye uklonyayushchikhsya ot nulya [About functions deviating least from zero], In book: P. L. Chebyshev. Izbrannyye Trudy [Selectas]. Publishing house of the Academy of Sciences of the USSR, Moscow (1955) 579– 608.

19. **Bernstein S. N.,** O nailuchshem priblizhenii nepreryvnykh funktsiy posredstvom mnogochlenov dannoy stepeni [On the best approximation of the continuous functions by means of polynomials of a given degree], Communications de la Société Mathematique de 2-ume Série, Kharkow. XIII (2–3) (1912) 49–144.

20. **Bernstein S. N.,** On the best approximation of functions of several variables by means of polynomials or trigonometric sums. Collection of articles. To the 60-th birthday of academician Ivan Matveevich Vinogradov, Proceedings of the Steklov Institute of Mathematics 38 (1951) 24–29.

21. **de la Vallée Poussin Ch. J.,** Sur les polynomes d'approximation et la représentation approchée d'un angle, Bull. Cl. Sci., Acad. R. (12) (1910) 808–844.

22. **de la Vallée Poussin Ch. J.,** Leзons sur l'approximation des fonctions d'une variable réelle, Gauthier-Villars, Paris, 1919.

23. **Butzer P. L., Nessel R. J.,** Aspects of de La Vallée Poussin's work in approximation and its influence, Archi. Hist. Exact Sci. 46 (1) (1993) 67–95.

24. Wolfram Mathematica: Naiboleye polnaya sistema dlya matematicheskikh i tekhnicheskikh vychisleniy [The most complete system for mathematical and technical calculations], URL: https://www.wolfram.com/mathematica/ (Access on 21.03.2023).

СПИСОК ЛИТЕРАТУРЫ

1. **Ланцош К.** Практические методы прикладного анализа. Пер. с англ. М.: Гос. изд-во физ.-мат. лит-ры, 1961. 524 с.

2. **Пашковский С.** Вычислительные применения многочленов и рядов Чебышева. Пер. с польского. М.: Наука, 1983. 384 с.

3. **Данилов Ю. А.** Многочлены Чебышева. Минск: Вышэйшая школа, 1984. 157 с.

4. **Чаплыгин С. А.** Новый метод приближенного интегрирования дифференциальных уравнений. М.–Л.: Гос. изд-во технико-теоретической лит-ры, 1950. 102 с.

5. **Гончаров В. Л.** Теория интерполирования и приближения функций. М.–Л.: Гос. технико-теоретическое изд-во, 1934. 316 с.

6. **Ахиезер Н. И.** Лекции по теории аппроксимации. М.–Л.: Объединение государственных книжно-журнальных издательств, 1947. 324 с.

7. **Ахиезер Н. И.** Лекции по теории аппроксимации. 2-е изд. М.: Наука, 1965. 407 с.

8. **Berdnikov A., Solovyev K., Krasnova N., Golovitski A., Syasko M.** Algorithm for constructing the Chebyshev-type polynomials and the Chebyshev-type approximations with a given weight // Proceedings of 2022 International Conference on Electrical Engineering and Photonics (EExPolytech). 20–21 October 2022, St. Petersburg, Russia. Pp. 143–145.

9. **Remez E.** Sur un, Procédé convergent d'approximations successives pour determiner les polynomes d'appproximation // Comptes Rendus l' Académie des Sciences. Paris. 1934. Vol. 198. No. Pp. 2063–2065.

10. **Remez E. Ya.** Sur le calcul effectif des polynomes d'approximation de Tschebyscheff // Comptes Rendus l' Académie des Sciences. Paris. 1934. Vol. 199. No. Pp. 337–340.

11. **Дзядык В. К.** Введение в теорию равномерного приближения функций полиномами. М.: Наука. Гл. редакция физ.-мат. лит-ры, 1977. 508 с.

12. **Ремез Е. Я.** Основы численных методов чебышёвского приближения. Киев: Наукова думка, 1969. 624 с.

13. **Лоран П.-Ж.** Аппроксимация и оптимизация. М.: Мир, 1975. 496 с.

14. **Грибкова В. П.** Эффективные методы равномерных приближений, основанные на полиномах Чебышева. М.: Изд-во «Спутник», 2017. 193 с.

15. **Березин И. С., Жидков Н. П.** Методы вычислений. В 2 тт. Т. 1. М.: Гос. изд-во физ.-мат. лит-ры, 1962. 464 с.

16. **Чебышев П. Л.** Теория механизмов, известных под именем параллелограммов // П. Л. Чебышев. Избранные труды. Отв. редактор акад. И. М. Виноградов. М.: Изд-во Академии наук СССР, 1955. С. 611–648.

17. **Чебышев П. Л.** Вопросы о наименьших приближениях, связанных с приближенным представлением функций // П. Л. Чебышев. Избранные труды. Отв. редактор акад. И. М. Виноградов. М.: Изд-во Академии наук СССР, 1955. С. 462–578.

18. **Чебышев П. Л.** О функциях, наименее уклоняющихся от нуля // П. Л. Чебышев. Избранные труды. Отв. редактор акад. И. М. Виноградов. М.: Изд-во Академии наук СССР, 1955. С. 579–608.

19. **Бернштейн С. Н.** О наилучшем приближении непрерывных функций посредством многочленов данной степени // Сообщения Харьковского математического общества. 2-я серия. 1912. Т. XIII. Вып. 2–3. С. 49–144.

20. **Бернштейн С. Н.** О наилучшем приближении функций нескольких переменных посредством многочленов или тригонометрических сумм. Сб. статей. Посвящается академику И. М. Виноградову к его 60-летию. Труды Математического института им. В. А. Стеклова. 1951. Т. 38. М.: Изд-во АН СССР, 1951. С. 24–29.

21. **de la Vallée Poussin Ch. J.** Sur les polynomes d'approximation et la représentation approchée d'un angle // Bulletin de la Classe des Sciences (Académie Royale de Belgique). 1910. No. 12. Pp. 808–844.

22. **de la Vallée Poussin Ch. J.** Leзons sur l'approximation des fonctions d'une variable réelle. Paris: Gauthier-Villars, 1919. 150 p.

23. **Butzer P. L., Nessel R. J.** Aspects of de La Vallée Poussin's work in approximation and its influence // Archive for History of Exact Sciences. 1993. Vol. 46. No. 1. Pp. 67–95.

24. Wolfram Mathematica: наиболее полная система для математических и технических вычислений. URL: https://www.wolfram.com/mathematica/ (Обращение 21.03.2023).

THE AUTHORS

BERDNIKOV Alexander S.
Institute for Analytical Instrumentation, RAS
31–33, Ivan Chernykh St., St. Petersburg, 198095, Russia
asberd@yandex.ru
ORCID: 0000-0003-0985-5964

SOLOVYEV Konstantin V.
Peter the Great St. Petersburg Polytechnic University
Institute for Analytical Instrumentation, RAS
29 Politechnicheskaya St., St. Petersburg, 195251, Russia
k-solovyev@mail.ru
ORCID: 0000-0003-3514-8577

СВЕДЕНИЯ ОБ АВТОРАХ

БЕРДНИКОВ Александр Сергеевич – *доктор физико-математических наук, ведущий научный сотрудник Института аналитического приборостроения Российской академии наук.*
198095, Россия, г. Санкт-Петербург, ул. Ивана Черных, 31–33, лит. А.
asberd@yandex.ru
ORCID: 0000-0003-0985-5964

СОЛОВЬЕВ Константин Вячеславович – *кандидат физико-математических наук, доцент Высшей инженерно-физической школы Санкт-Петербургского политехнического университета Петра Великого, младший научный сотрудник Института аналитического приборостроения Российской академии наук.*
195251, Россия, г. Санкт-Петербург, Политехническая ул., 29
k-solovyev@mail.ru
ORCID: 0000-0003-3514-8577

Received 30.03.2023. Approved after reviewing 17.04.2023. Accepted 17.04.2023.
Статья поступила в редакцию 30.03.2023. Одобрена после рецензирования 17.04.2023. Принята 17.04.2023.

© Peter the Great St. Petersburg Polytechnic University, 2023

Journal

**ST. PETERSBURG STATE POLYTECHNICAL UNIVERSITY JOURNAL:
PHYSICS AND MATHEMATICS**

Vol. 16, No. 2, 2023

Founder and publisher: Peter the Great St. Petersburg Polytechnic University

The journal is registered with the Federal Service for Supervision of Communications,
Information Technology and Mass Media (Roskomnadzor).
Certificate ПИ ФС77-51457 issued 19.10.2012.

Editorial Office

Dr. Prof. *V.K. Ivanov*, Editor-in-Chief
Dr. Prof. *A.E. Fotiadi*, Deputy Editor-in-Chief
Dr. Prof.*V.V. Dubov*
Dr. Prof. *P.A. Karaseov*
Dr. Assoc. Prof. *V.M. Kapralova*
A.S. Kolgatina, translator
N.A. Bushmanova, editorial manager

Phone 8 (812) 294-22-85

Website https://physmath.spbstu.ru/

E-mail: physics@spbstu.ru

Typesetting by A.S. Kolgatina

Published 30.06.2023. Format 60x84/8. Digital print.
Printer's sheets Print circulation 1000. Order ID